

**TOWARDS AN IMPROVED RUPTURE POTENTIAL INDEX FOR ABDOMINAL
AORTIC ANEURYSMS: ANISOTROPIC CONSTITUTIVE MODELING AND
NONINVASIVE WALL STRENGTH ESTIMATION**

by

Jonathan Pieter Vande Geest

BS, University of Iowa, 2000

Submitted to the Graduate Faculty of

School of Engineering in partial fulfillment

of the requirements for the degree of

Doctor of Philosophy

University of Pittsburgh

2005

UNIVERSITY OF PITTSBURGH

SCHOOL OF ENGINEERING

This dissertation was presented

by

Jonathan Pieter Vande Geest

It was defended on

July 20, 2005

and approved by

Michael S. Sacks, PhD, William Kepler Whiteford Professor, Department of Bioengineering

Richard Debski, PhD, Assistant Professor, Department of Bioengineering

Anne Robertson, PhD, Associate Professor, Department of Mechanical Engineering

Navyash Gupta, MD, Department of Surgery, Division of Vascular Surgery, University of
Pittsburgh Medical Center

David A. Vorp, PhD, Associate Professor, Departments of Surgery and Bioengineering
Dissertation Director

TOWARDS AN IMPROVED RUPTURE POTENTIAL INDEX FOR ABDOMINAL AORTIC ANEURYSMS: ANISOTROPIC CONSTITUTIVE MODELING AND NONINVASIVE WALL STRENGTH ESTIMATION

Jonathan Pieter Vande Geest, PhD

University of Pittsburgh, 2005

Abdominal aortic aneurysm (AAA), a localized dilation of the infrarenal aorta, represents a significant disease in the western population. There are approximately 200,000 patients in the US and 500,000 patients worldwide diagnosed with AAAs every year, and rupture of AAAs currently ranks as the 13th leading cause of death in the US. The formation of aneurysm within the abdominal aorta presents a unique clinical dilemma, requiring surgeons to offer intervention when the risks of rupture outweigh those associated with the repairing the AAA. The gold standard for quantitatively assessing a AAAs risk of rupture is the maximum transverse diameter – with intervention typically recommended at a diameter of 5.5cm. This criterion, however, is not based on the sound physical properties governing the mechanical failure of the AAA wall – the stresses acting on the wall and the ability to withstand those stresses (its strength). The current work describes the continued improvement of a rupture potential index (RPI) which is defined as the ratio of local wall stress and strength.

The effect of mechanical anisotropy on the constitutive modeling and finite element analyses of AAA has been neglected in the literature. In order to address the assumption of isotropy, planar biaxial tensile testing was performed on AAA wall and intraluminal thrombus (ILT) tissue excised from patients undergoing elective open repair of their AAA. The peak stretch values and maximum tangential moduli for AAA versus nonaneurysmal tissue indicate a preferential circumferential stiffening of the abdominal aorta in the presence of aneurysm. It was concluded that aneurysmal degeneration of the abdominal aorta is associated with an increase in mechanical anisotropy, with preferential stiffening in the circumferential direction. This anisotropy was modeled using an exponential strain energy function which was able to minimize the covariance between model parameters. Implementation of this relation into a commercially available finite element code (ABAQUS) resulted in a more realistic estimation of in-vivo wall stress. There was a significant increase in peak wall stress in AAAs utilizing the anisotropic

constitutive relation versus those using the previously derived isotropic relation (38.30 ± 3.04 , 36.06 ± 2.73 , $p < 0.001$). This result was not universal, however, indicating the presence of anisotropy on peak wall stress may be patient-specific.

Previous work in our laboratory resulted in an initial statistical model for noninvasively estimating AAA wall strength. This model has currently been improved with several notable enhancements some of which include a larger construction data set and a CT-based method of local diameter measurement. This model contains four, non-invasively measurable predictors: the square root of local ILT thickness, normalized local diameter, patient's sex, and the patient's family history of AAA. The noninvasive statistical model for predicting AAA wall strength derived here predicted a statistically weaker wall for ruptured AAAs than for non-ruptured AAAs (119.41 ± 4.48 and 137.06 ± 1.49 N/cm², $p = 0.02$). In fact, the current model performed better than either the previously derived AAA wall strength model or the clinically utilized maximum cross sectional diameter in identifying ruptured AAAs. The currently developed rupture potential index resulted in an increased peak value of RPI for a set of electively repaired AAAs in comparison to the previously developed RPI technique (0.34 ± 0.03 vs. 0.22 ± 0.03 , $p < 0.001$). In addition, comparisons of peak RPI values for ruptured and non-ruptured AAAs suggest an improvement in rupture prediction utilizing the current methodology ($p = 0.10$) as opposed to the previously developed RPI ($p = 0.79$) as well as the maximum diameter criterion ($p = 0.17$).

The locally acting AAA wall stress divided by the local AAA wall strength, termed the rupture potential index, has been introduced as an alternative to the maximum diameter criterion for AAA rupture assessment. The clinical relevance of this method for rupture assessment has yet to be validated, however its success will undoubtedly aid surgeons in clinical decision making and AAA patient management.

TABLE OF CONTENTS

| | |
|--|-----|
| PREFACE | xxi |
| 1.0 INTRODUCTION AND BACKGROUND | 1 |
| 1.1 DEMOGRAPHICS | 2 |
| 1.2 CLINICAL TREATMENT..... | 3 |
| 1.2.1 Open AAA Repair..... | 3 |
| 1.2.2 Endovascular Repair of AAA | 5 |
| 1.3 A BIOMECHANICAL APPROACH..... | 7 |
| 1.3.1 The Surgeon’s Dilemma | 7 |
| 1.3.2 Rupture Potential Index | 8 |
| 1.4 HYPOTHESIS AND SPECIFIC AIMS | 9 |
| 2.0 BIAXIAL TESTING OF AAA AND NONANEURYSMAL AORTIC TISSUE | 13 |
| 2.1 INTRODUCTION | 13 |
| 2.2 METHODS | 15 |
| 2.2.1 Biaxial Tensile Testing Device..... | 15 |
| 2.2.2 Specimen Procurement | 17 |
| 2.2.2.1 Specimen Source..... | 17 |
| 2.2.2.2 Specimen Storage..... | 19 |
| 2.2.3 Biaxial Protocol | 20 |

| | | |
|---------|---|----|
| 2.2.4 | Data Analysis | 22 |
| 2.2.4.1 | Stress | 22 |
| 2.2.4.2 | Strain | 22 |
| 2.2.4.3 | Stiffness..... | 23 |
| 2.2.5 | Statistical Analyses | 23 |
| 2.3 | RESULTS AND DISCUSSION | 24 |
| 2.3.1 | Nonaneurysmal Abdominal Aorta | 24 |
| 2.3.1.1 | Results..... | 24 |
| 2.3.1.2 | Discussion..... | 27 |
| 2.3.2 | Descending Thoracic Aorta | 29 |
| 2.3.2.1 | Results..... | 29 |
| 2.3.2.2 | Discussion..... | 31 |
| 2.3.3 | Abdominal Aortic Aneurysmal Wall..... | 33 |
| 2.3.3.1 | Results..... | 33 |
| 2.3.3.2 | Discussion..... | 37 |
| 2.3.4 | Intraluminal Thrombus | 39 |
| 2.3.4.1 | Results..... | 39 |
| 2.3.4.2 | Discussion..... | 41 |
| 2.3.5 | Limitations | 42 |
| 3.0 | ANISOTROPIC CONSTITUTIVE MODEL DEVELOPMENT..... | 47 |
| 3.1 | INTRODUCTION | 47 |
| 3.2 | METHODS | 48 |
| 3.2.1 | Assumptions..... | 48 |

| | | |
|---------|--|----|
| 3.2.1.1 | Homogeneity..... | 48 |
| 3.2.1.2 | Large Deformation..... | 48 |
| 3.2.1.3 | Incompressibility..... | 49 |
| 3.2.2 | Assessment of Anisotropy | 50 |
| 3.2.2.1 | Peak Stretch | 50 |
| 3.2.2.2 | Maximum Tangential Modulus..... | 51 |
| 3.2.2.3 | Response Functions | 51 |
| 3.2.3 | Population-wide Constitutive Modeling..... | 52 |
| 3.3 | RESULTS AND DISCUSSION..... | 54 |
| 3.3.1 | Nonaneurysmal Abdominal Aorta | 54 |
| 3.3.1.1 | Results..... | 54 |
| 3.3.1.2 | Discussion..... | 63 |
| 3.3.2 | Descending Thoracic Aorta | 64 |
| 3.3.3 | Abdominal Aortic Aneurysmal Wall..... | 66 |
| 3.3.3.1 | Results..... | 66 |
| 3.3.3.2 | Discussion..... | 74 |
| 3.3.4 | Intraluminal Thrombus | 77 |
| 3.3.4.1 | Results..... | 77 |
| 3.3.4.2 | Discussion..... | 81 |
| 3.3.5 | Limitations | 83 |
| 4.0 | 3D RECONSTRUCTION AND MESHING OF AAA | 90 |
| 4.1 | INTRODUCTION | 90 |
| 4.1.1 | Reconstruction of Biological Tissues | 90 |

| | | |
|---------|---|-----|
| 4.1.2 | Current Reconstruction Protocol..... | 91 |
| 4.2 | Methods..... | 93 |
| 4.2.1 | Computed Tomography of AAA | 93 |
| 4.2.2 | Segmentation..... | 94 |
| 4.2.3 | Preprocessing for 3D Smoothing..... | 96 |
| 4.2.4 | 3D Smoothing..... | 97 |
| 4.2.5 | Surface and Solid Modeling..... | 98 |
| 4.2.6 | Hexahedral Meshing..... | 100 |
| 4.2.6.1 | Wall..... | 100 |
| 4.2.6.2 | Intra-luminal Thrombus | 102 |
| 4.2.7 | Preprocessing for ABAQUS Input File Creation..... | 102 |
| 4.2.8 | Summary of New Protocol Changes..... | 103 |
| 4.3 | RESULTS AND DISCUSSION..... | 105 |
| 4.3.1 | Meshing Results..... | 105 |
| 4.3.1.1 | AAA Wall..... | 105 |
| 4.3.1.2 | Intra-luminal Thrombus | 108 |
| 4.3.2 | Visual Inspection of Smoothed 3D Mesh..... | 111 |
| 4.3.3 | Discussion..... | 112 |
| 5.0 | ANISOTROPIC FINITE ELEMENT SIMULATIONS..... | 117 |
| 5.1 | INTRODUCTION | 117 |
| 5.2 | METHODS | 119 |
| 5.2.1 | Boundary Conditions | 119 |
| 5.2.1.1 | Blood Pressure | 120 |

| | | |
|---------|---|-----|
| 5.2.1.2 | Longitudinal Tethering | 121 |
| 5.2.1.3 | Reference Configuration..... | 121 |
| 5.2.1.4 | Shear Stresses..... | 123 |
| 5.2.2 | Implementation of the Anisotropic Constitutive Relation into ABAQUS | 123 |
| 5.2.2.1 | Solving a Nonlinear Problem Using Newton’s Method | 124 |
| 5.2.2.2 | User-Defined Material Properties | 129 |
| 5.2.2.3 | Definition of Local Material Coordinates..... | 131 |
| 5.2.3 | Biaxial Simulations..... | 134 |
| 5.2.4 | Cylindrical Simulation..... | 137 |
| 5.2.5 | Anisotropic AAA Finite Element Simulations | 137 |
| 5.2.6 | Stress Concentration Quantification | 139 |
| 5.3 | RESULTS AND DISCUSSION..... | 140 |
| 5.3.1 | Biaxial Simulations..... | 140 |
| 5.3.2 | Cylindrical Simulation..... | 143 |
| 5.3.3 | Anisotropic Versus Isotropic AAA Simulations..... | 144 |
| 5.3.4 | Ruptured Versus Electively-Repaired AAA Simulations..... | 154 |
| 5.3.5 | Discussion..... | 158 |
| 6.0 | NONINVASIVE ESTIMATION OF AAA WALL STRENGTH | 167 |
| 6.1 | INTRODUCTION | 167 |
| 6.2 | SUMMARY OF SHORTCOMINGS OF PREVIOUS APPROACH | 168 |
| 6.3 | METHODS | 172 |
| 6.3.1 | Initial Selection of Variables Predicting AAA Wall Strength..... | 172 |
| 6.3.1.1 | Smoking..... | 173 |

| | | |
|---------|---|-----|
| 6.3.1.2 | Family History | 174 |
| 6.3.1.3 | Gender..... | 175 |
| 6.3.1.4 | Age..... | 176 |
| 6.3.1.5 | Intraluminal Thrombus Thickness | 177 |
| 6.3.1.6 | Maximum and Local Transverse Diameter..... | 179 |
| 6.3.2 | Specimen Procurement and Variable Recording | 179 |
| 6.3.2.1 | Demographical Data Collection..... | 180 |
| 6.3.2.2 | Local Variable Measurement..... | 181 |
| 6.3.3 | Uniaxial Tensile Testing..... | 183 |
| 6.3.4 | Statistical Modeling of AAA Wall Strength..... | 184 |
| 6.3.4.1 | The Initial Wall Strength Model..... | 184 |
| 6.3.4.2 | Assumptions for Linear Regression..... | 185 |
| 6.3.4.3 | Outliers and High Influential Points | 190 |
| 6.3.4.4 | Variable Selection Technique – Backwards Stepwise Regression..... | 191 |
| 6.3.4.5 | Linear Mixed-Effects Modeling | 192 |
| 6.4 | RESULTS AND DISCUSSION..... | 193 |
| 6.4.1 | Assumptions for Linear Regression..... | 193 |
| 6.4.2 | Outliers and Highly Influential Points | 198 |
| 6.4.3 | Backwards Stepwise Regression – Variable Selection..... | 200 |
| 6.4.4 | Mixed-Effects Modeling..... | 200 |
| 6.4.5 | Model Application | 202 |
| 6.4.6 | Electively Repaired AAAs..... | 206 |
| 6.4.7 | Ruptured Versus Non-ruptured AAAs..... | 208 |

| | | |
|-------|--|-----|
| 6.4.8 | Discussion..... | 210 |
| 7.0 | RUPTURE POTENTIAL INDEX..... | 217 |
| 7.1 | INTRODUCTION..... | 217 |
| 7.2 | METHODS..... | 219 |
| 7.2.1 | Rupture Potential Index Calculation..... | 219 |
| 7.2.2 | Comparison of Old versus New RPI Techniques..... | 219 |
| 7.2.3 | Ruptured versus Electively Repaired AAAs..... | 219 |
| 7.3 | RESULTS AND DISCUSSION..... | 220 |
| 7.3.1 | Comparison of Old versus New RPI Techniques..... | 220 |
| 7.3.2 | Ruptured versus Non-ruptured AAAs..... | 222 |
| 7.3.3 | Summary..... | 224 |
| 8.0 | DISCUSSION..... | 226 |
| 8.1 | RELATION TO PREVIOUS WORK..... | 226 |
| 8.2 | LIMITATIONS AND FUTURE WORK..... | 233 |
| 8.2.1 | Estimation of Wall Stress..... | 233 |
| 8.2.2 | Estimation of Wall Strength..... | 234 |
| 8.2.3 | RPI in the Clinic..... | 236 |
| 8.3 | CONCLUSION..... | 236 |
| | APPENDIX A..... | 237 |
| | AVERAGING OF BIAxIAL TENSILE TESTING DATA..... | 237 |
| | APPENDIX B..... | 248 |
| | PREPROCESSING OF 2D SLICE DATA..... | 248 |

| | |
|---|-----|
| APPENDIX C | 253 |
| ILD TO 3D SMOOTHING MATLAB FUNCTION | 253 |
| APPENDIX D..... | 255 |
| 3D SMOOTHING TO IGES CREATION MATLAB SCRIPT..... | 255 |
| APPENDIX E | 259 |
| CREATION OF ABAQUS INPUT FILE FROM TRUE GRID FILE | 259 |
| APPENDIX F..... | 276 |
| EXERPTS FROM A SAMPLE INPUT FILE..... | 276 |
| APPENDIX G..... | 282 |
| ABAQUS UMAT SUBROUTINE FOR ANISOTROPIC IMPLEMENTATION | 282 |
| APPENDIX H..... | 288 |
| MATLAB FUNCTION TO CREATE BIAXIAL SPECIMEN SIMULATIONS..... | 288 |
| APPENDIX I | 291 |
| POST PROCESSING MATLAB FUNCTION FOR STRESS GRADIENTS | 291 |
| APPENDIX J | 295 |
| RESIDUALS VERSUS EACH INDEPENDENT VARIABLE | 295 |
| APPENDIX K..... | 297 |
| MATLAB FUNCTION CALCULATING RPI..... | 297 |
| BIBLIOGRAPHY..... | 299 |

LIST OF TABLES

| | |
|---|-----|
| Table 1-1: Patient demographical data from a random sampling in the US[7] | 3 |
| Table 1-2: Relationship of size to rupture in 473 nonresected AAA (adapted from Darling et al.[23])..... | 7 |
| Table 2-1: Age and source of death for Group 1 specimens..... | 17 |
| Table 2-2: Age and source of death for Group 2 specimens..... | 18 |
| Table 2-3: Age and source of death for Group 3 specimens..... | 18 |
| Table 2-4: Peak stretch, areal strain, and MTM for the luminal layer of ILT | 41 |
| Table 3-1: Constitutive model parameters for the Group 1 specimens. OD=organ donor; MOSF=multisystem organ failure; HT TX REJ=heart transplant rejection. | 60 |
| Table 3-2: Constitutive model parameters for the Group 2 specimens. CREP MEN=creptycoccal meningitis; SEP=sepsis. X indicates the regression did not converge. 61 | 61 |
| Table 3-3: Constitutive model parameters for the Group 3 specimens. MI=myocardial infarction; CEREB AN=cerebral aneurysm; MET CARC=Metastatic uterine carcinoma | 61 |
| Table 3-4: Constitutive model parameters for nonaneurysmal aorta fit to equation (3.4)..... | 65 |
| Table 3-5: Constitutive model parameters for nonaneurysmal descending thoracic aorta fit to equation (3.4) | 65 |
| Table 3-6: Constitutive model parameters for the nonaneurysmal abdominal aorta | 68 |
| Table 3-7. Constitutive model parameters for the AAA wall specimens | 68 |
| Table 3-8: Constitutive model parameters for the averaged AA and AAA datasets | 70 |
| Table 3-9: Constitutive model parameters for the luminal layer of ILT..... | 79 |
| Table 4-1: Summary of changes to the AAA reconstruction protocol | 105 |
| Table 4-2: Mesh densities for all AAA wall meshes. ‘N’=non-ruptured; ‘R’=ruptured | 106 |

| | |
|--|-----|
| Table 4-3: Mesh densities for all ILT meshes. NA denotes the AAA had no ILT..... | 109 |
| Table 5-1: Hoop stress for the analytical and computational solution of the pressurization of a thick walled cylinder..... | 143 |
| Table 5-2: Peak maximum principal stresses for the electively repaired AAA simulations. ANI ISO = anisotropic AAA wall + isotropic ILT; ISO ISO = isotropic AAA wall + isotropic ILT; ANI ANI = anisotropic AAA wall + biaxial derived luminal ILT; ANI NOILT = equivalent to ANI ISO excluding presence of ILT; ISO NOILT = equivalent to ISO ISO excluding presence of ILT | 146 |
| Table 5-3: Mean maximum principal stresses for the electively repaired AAA simulations.... | 148 |
| Table 5-4: Peak maximum principal strain for the electively repaired AAA simulations..... | 150 |
| Table 5-5: Mean maximum principal strain for the electively repaired AAA simulations | 151 |
| Table 5-6: Peak maximum principal stress gradient for the electively repaired AAA simulations | 153 |
| Table 5-7: Peak and mean maximum principal stresses and strains for the non-ruptured AAA simulations | 155 |
| Table 5-8: Peak and mean maximum principal stresses and strains for the ruptured AAA simulations | 155 |
| Table 5-9: Peak maximum principal stress gradients for the non-ruptured and ruptured AAA simulations (* p = 0.049) | 157 |
| Table 6-1: Improvements in model used to noninvasively estimate AAA wall strength | 172 |
| Table 6-2: Correlations between independent variables after regression of equation 6.7. Shaded cells represent high (>0.5) correlations..... | 197 |
| Table 6-3: Variance inflation factors (VIF) after regression of equation 6.7 | 197 |
| Table 6-4: Hat diagonal and studentized residuals for regressing Group A data to equation 6.8. Shaded cells represent outliers or highly influential points. Data points 6 and 35 were removed as highly influential outliers..... | 199 |
| Table 6-5: Parameter values for Group C linear mixed-effects regression | 201 |
| Table 6-6: Characteristics of four AAA patients used in the demonstration of AAA wall strength | 204 |
| Table 6-7: Strength values using the old and new methods for AAA strength prediction | 206 |
| Table 6-8: Strength values using the old statistical model for ruptured and non-ruptured AAAs | 209 |

| | |
|--|-----|
| Table 6-9: Strength values using the new statistical model for ruptured and non-ruptured AAAs (*,+,# p < 0.05) | 209 |
| Table 7-1: Peak and Mean RPI values for all electively repaired AAAs | 221 |
| Table 7-2: RPI values derived from the old stress and strength estimation techniques (* p = 0.79 ; + p = 0.58)..... | 223 |
| Table 7-3: RPI values derived from the new stress and strength estimation techniques (* p = 0.10; + p = 0.35)..... | 223 |

LIST OF FIGURES

| | |
|--|----|
| Figure 1-1: Anatomical depiction of an AAA displaying the dilation at the abdominal level (taken from www.endovascular.net) | 2 |
| Figure 1-2: Traditional open repair of AAA with large anterior incision (adapted from www.guidant.com)..... | 4 |
| Figure 1-3: Placement (left) and resulting endovascular graft (right) (adapted from www.medtronic.com) | 5 |
| Figure 2-1: Biaxial loading condition of abdominal aorta pronounced by aneurysmal dilation . | 15 |
| Figure 2-2: Biaxial tensile testing setup. Adapted from Sacks and Sun (2003)[58]..... | 16 |
| Figure 2-3: Typical AAA biaxial specimen..... | 16 |
| Figure 2-4: Biaxial specimen undeformed geometry (left) and tension-driven biaxial protocol (right) | 21 |
| Figure 2-5: Typical stress-strain plots for all protocols and age groups..... | 25 |
| Figure 2-6: Peak stretch values in both directions according to age group. $p < 0.001$ for Group 2 and 3 peak stretch values compared to Group 1 values in both directions | 26 |
| Figure 2-7: Areal strain as a function of age..... | 27 |
| Figure 2-8: Representative stress-strain plots for DTA and AA specimens..... | 30 |
| Figure 2-9: Maximum tangential modulus (MTM) for each age group and location..... | 31 |
| Figure 2-10: Areal strain for each age group and location | 31 |
| Figure 2-11: Stress-strain plots for a representative AAA and AA specimen..... | 35 |
| Figure 2-12: Peak strains (A) and areal strain (B) for AAA and AA tissue | 36 |
| Figure 2-13: AAA and AA maximum tangential modulus for both experimental directions | 37 |
| Figure 2-14: Representative stress-strain plot for the luminal layer of ILT | 40 |

| | |
|--|-----|
| Figure 2-15: Stress versus strain in the circumferential direction for a representative specimen for all preconditioning cycles..... | 43 |
| Figure 3-1: Circumferential stress contour plot for an idealized perfectly isotropic material..... | 52 |
| Figure 3-2: Circumferential and longitudinal stress contours for each age group..... | 58 |
| Figure 3-3: I_1 versus I_2 and $\partial W/\partial I_1$ versus I_1 for a representative AA specimen..... | 59 |
| Figure 3-4: Experimental data and model fits for representative Group 1-3 specimens..... | 62 |
| Figure 3-5: Representative AA and AAA stress contour plots..... | 71 |
| Figure 3-6: Averaged datasets and model fits for AA and AAA tissue..... | 72 |
| Figure 3-7: Strain energy as a function of equibiaxial strain for the isotropic [38] and anisotropic (equation 3.10) constitutive models..... | 73 |
| Figure 3-8: Representative stress contour plot for the luminal layer of ILT..... | 80 |
| Figure 3-9: I_1 versus I_2 and $\partial W/\partial I_1$ versus I_1 for a representative ILT specimen..... | 81 |
| Figure 3-10: Strain energy as a function of equibiaxial strain for the uniaxially[59] and biaxially-derived constitutive models of the luminal layer of ILT..... | 83 |
| Figure 3-11: Model parameter variability of the averaged AAA constitutive model using bootstrapping methods. Open circles are the bootstrapped parameter sets, while dashes correspond to the averaged AAA model in Table 3-8..... | 89 |
| Figure 4-1: Summary of current AAA reconstruction protocol..... | 92 |
| Figure 4-2: Typical image slice from an abdominal CT scan..... | 94 |
| Figure 4-3: Segmentation of AAA wall (yellow) and concentric (A) and crescent-shaped (B) ILT (red)..... | 95 |
| Figure 4-4: Lofting of IGES splines to create a smoothed 3D surface..... | 99 |
| Figure 4-5: Boolean operation on the AAA in order to create the solid ILT..... | 99 |
| Figure 4-6: Percent change in mean AAA wall stress with increasing mesh density..... | 107 |
| Figure 4-7: Representative mesh for AAA4, $f = 9.68$ | 108 |
| Figure 4-8: Percent change in mean ILT stress with increasing mesh density..... | 110 |
| Figure 4-9. Representative mesh for the ILT of AAA8, $f = 22.24$ | 111 |

| | |
|---|-----|
| Figure 4-10: Smoothed AAA7 wall mesh (black) and 3D point cloud resulting from the segmentation process (red) | 112 |
| Figure 5-1: Pictorial view of Newton’s method for solving nonlinear problems | 126 |
| Figure 5-2: Problems associated with low initial slopes when using Newton’s method..... | 128 |
| Figure 5-3: A) Differences in stress with the implementation of equation 5.1. B) Blown up view of A) | 128 |
| Figure 5-4: Outline of the purpose of UMAT subroutine within ABAQUS | 129 |
| Figure 5-5: Longitudinal center points and resulting 3D spline used to define local material coordinates | 132 |
| Figure 5-6: A representative AAA showing the definition of local material coordinates | 133 |
| Figure 5-7: Definition of the strain and modulus used in comparing biaxial simulations..... | 136 |
| Figure 5-8: Determination of stress gradients within a spherical region of interest (large red sphere) around a finite element node (small blue sphere) | 140 |
| Figure 5-9: Circumferential (A) and longitudinal (B) Cauchy stress versus stretch ratio for the PT ISO and PT ANI simulations and the corresponding biaxial experimental data..... | 141 |
| Figure 5-10: The strain values at $t = 60$ kPa for 14 biaxial simulations | 142 |
| Figure 5-11: The moduli at a strain of 3% for 14 biaxial simulations..... | 142 |
| Figure 5-12: Maximum principal stress distribution for the computational solution of the cylindrical simulation..... | 144 |
| Figure 5-13: Maximum principal stress distributions for AAA17. ANI ISO = anisotropic AAA wall + isotropic ILT; ISO ISO = isotropic AAA wall + isotropic ILT; ANI ANI = anisotropic AAA wall + biaxial derived luminal ILT; ANI NOILT = equivalent to ANI ISO excluding presence of ILT; ISO NOILT = equivalent to ISO ISO excluding presence of ILT | 147 |
| Figure 5-14: Maximum principal strain distributions for AAA17..... | 152 |
| Figure 5-15: Maximum principal stress gradient distribution for AAA17 | 154 |
| Figure 5-16: Maximum principal stress distributions for N5 and R7 | 156 |
| Figure 5-17: Maximum principal strain distributions for N5 and R7 | 156 |
| Figure 5-18. Maximum principal stress gradient distributions for N5 and R7 | 158 |

| | |
|---|-----|
| Figure 5-19: Comparison of anisotropic and isotropic simulations for ruptured and non-ruptured groups..... | 162 |
| Figure 5-20: Differences in stress values using the assumption that the CT configuration is the zero stress configuration | 165 |
| Figure 6-1: Schematic of AAA wall sample preparation and local parameter measurement using the pervious method. A wedge-shaped sample of ILT was cut and removed with a piece of wall attached (A). Then the whole thrombus was removed from the aneurysm as is routine in open surgical repair. The wedge-shaped ILT was put back in the whole thrombus and sliced longitudinally, as shown in (B). The local ILT thickness and local diameter was then measured on the cross-section. A slice of circumferentially-oriented wall specimen was harvested from the wedge-shaped sample edge (C). Taken from [40]. | 169 |
| Figure 6-2: Mean wall strength values for men (n=24) versus women (n=10) | 176 |
| Figure 6-3: Correlation between age (in years) and aortic matrix metalloproteinase-2 (MMP-2) activity. Taken from McNulty et al. [182]..... | 177 |
| Figure 6-4: Comparison of tensile strength for group I versus group II specimens. Significant difference was noted by means of the paired t test. Taken from Vorp et al. [31]..... | 178 |
| Figure 6-5: Depiction of improved method for determining local transverse diameter and ILT thickness for a uniaxial specimen. The longitudinal level of the IMA was used as a landmark on the excised specimen for determining the appropriate CT slice on which local ILT and diameter were measured..... | 182 |
| Figure 6-6: Residuals (on all y-axes) versus individual independent variables (X_i 's) for a set of hypothetical data. A) Data satisfy both the linearity and constant variance assumptions. B) Data depart from linearity. C) Residual variance increases with Y. D) Residual variance increases with Y. Adapted from [40, 194]. | 187 |
| Figure 6-7: Histograms of hypothetical data illustrating the meaning of skewness and kurtosis. A) Positive skewed distribution; B) Negative skewed distribution. C) Distribution with kurtosis = 4.25; D) Distribution with kurtosis = 1.75. C) and D) have approximately the same skewness. The dotted lines represent the normal distribution curve. Adapted from [40, 194]. | 189 |
| Figure 6-8: Residuals of S versus ILT displaying decreasing bow-tie appearance (red dotted lines)..... | 194 |
| Figure 6-9: Residuals of S versus corrected variable $ILT^{1/2}$ | 194 |
| Figure 6-10: Normal probability plot when regressing Group A data to equation 6.7 | 195 |
| Figure 6-11: Histogram of residuals when regressing Group A data to equation 6.7 | 196 |
| Figure 6-12: 95% CI's intervals for the mixed-effects model parameters for all Groups | 201 |

| | |
|--|-----|
| Figure 6-13: Predicted versus measured wall strength for Group C..... | 203 |
| Figure 6-14: Anterior (left) and posterior (right) view of the 3D distribution of AAA wall strength for four AAA patients using equation 6.10..... | 205 |
| Figure 6-15: A representative 3D distribution of AAA wall strength for the new and old methods for predicting AAA wall strength | 207 |
| Figure 6-16: 3D strength distribution on a representative ruptured and non-ruptured AAA using the current wall statistical model | 210 |
| Figure 6-17: Mean AAA wall strength using the old and new models for ruptured vs. non-ruptured AAAs..... | 213 |
| Figure 7-1: Noninvasively predicted stress, strength and RPI using the current techniques for stress and strength estimation | 220 |
| Figure 7-2: Comparison of old versus new techniques for RPI for a representative electively repaired AAA (AAA16) | 222 |
| Figure 7-3: Representative comparison of the current RPI between a ruptured (R8, maximum diameter = 5.20) and non-ruptured AAA (N4, maximum diameter = 5.23 cm)..... | 224 |
| Figure 7-4: Improvement in rupture potential prediction by using the currently developed RPI methodology (n=5 for non-ruptured, n=9 for ruptured)..... | 225 |
| Figure 8-1: Preliminary relationship between AAA wall strength and locally acting wall stress | 235 |

ACKNOWLEDGEMENTS

I would like to extend my deepest gratitude to my doctoral advisor, Dr. David Alan Vorp. Thank you for providing me with an exciting research atmosphere, guidance and support all along the way, and especially for taking a personal interest in my professional development as a teacher and researcher.

Thank you Dr. Harvey Borovetz for your guidance and support throughout my graduate student career. I would also like to acknowledge Lynette Spataro and Joan Williamson, who have always been supportive and extremely helpful in taking care of the ‘details’ of being a graduate student in the department of Bioengineering at the University of Pittsburgh.

I would also like to thank all of the members of my thesis committee for their time and effort with regards to my dissertation and this manuscript. Special thanks goes to Dr. Michael S. Sacks for the use of his biaxial tensile testing device as well as the endless insight he provided me on the mechanical testing, data analysis, and constitutive modeling of soft biological tissues. To Dr. Rich Debski, Dr. Anne Roberston, and Dr. Navyash Gupta, I extend a heartfelt thank you for your encouragement and thoughtful insights in to this work.

Special thanks to the team of vascular surgeons at UPMC including but not limited to Dr. Michel Makaroun, Dr. Robert Rhee, and Dr. Ellen Dillavou. Without all of your help this work would not be possible. Dr. Stephen R. Wisniewski also deserves a thank you for his guidance in

the statistical modeling of AAA wall strength presented in this work. I would also like to acknowledge Dr. David Smith for allowing the use of his biquintic surface smoothing software.

I have no doubt that I have been surrounded by some outstanding lab mates as a part of Dr. Vorp's vascular biomechanics research laboratory (VBRL). To Dr. David H. J. Wang and Dr. Madhavan L. Raghavan I extend my thanks for laying the groundwork that this thesis builds upon. My thanks to Dr. Elena S. Di Martino who spent endless hours teaching me the ins and outs of ABAQUS and serving as a computational mentor throughout my time in Pittsburgh. Others in the VBRL that deserve thanks include Mohammed El-Kurdi, Tim Maul, Rachelle Prantil, Ajay Bohra, Doug Chew, Charita Collins, Anil Thapa, Scott Van Epps, and Alessandro Nieponiece. Thanks to all of you for encouraging and helping me over the past five years.

I can't continue without thanking all of the friends I've had the privilege of getting to know while here in Pittsburgh: Tom Payne, David Merryman, Phil Marascalco, Susan Moore, Ed Lacis, Marnie Goldblum, B. J. and Katrina Woodworth, Dwight and Janet Fox, and Jan and Dave Van Dyke. Thank you all for your support and friendship.

Thank you mom, dad, Nic, Dawn, Lori, John, Lance, grandpa, Mike, Julie, Terry, Mark and all of my family back home in Moline, IL for your support as I started, continued and finished my graduate degree. Thanks to my 'new' parents Jack and Margaret Bellak for accepting me into your family! All of you are dear to me and I know I could not have finished this work without your support and prayers.

To my wife Susan: we did it! Thank you for your love and support during the stressful times and late nights. You truly are amazing and have always been supportive and encouraging to me. I pray God will continue to bless our marriage as we start a new chapter of our lives. I love you.

I would finally and most importantly like to thank my Lord and savior Jesus Christ, who brought me to Pittsburgh, walked along side me in my struggles and my successes. You have blessed me beyond belief, and I know that it is your love that gives my life meaning.

I dedicate this manuscript to you.

1.0 INTRODUCTION AND BACKGROUND

Abdominal aortic aneurysms (AAA) are the local dilation of the abdominal aorta, occurring in the region of the aortic tree distal to the renal arteries and proximal to the aortic bifurcation ([Figure 1-1](#)). This dilation of the aorta occurs over a time course of several years, with an average expansion rate of 2.6 mm/yr¹. Typically, a person's aorta is considered aneurysmal when its maximum transversal diameter increases by 50% of the expected diameter, which may vary according to the patients age, sex, and body weight.[1] Patients with AAA will often times be asymptomatic, making the detection and prevention of this disease difficult. AAAs will continue to grow until the vessel ruptures or the patient succumbs to a comorbid condition. Each year, approximately 15,000 people in the United States die of a ruptured abdominal aortic aneurysm, which makes it the 15th leading cause of death in this country[2, 3].

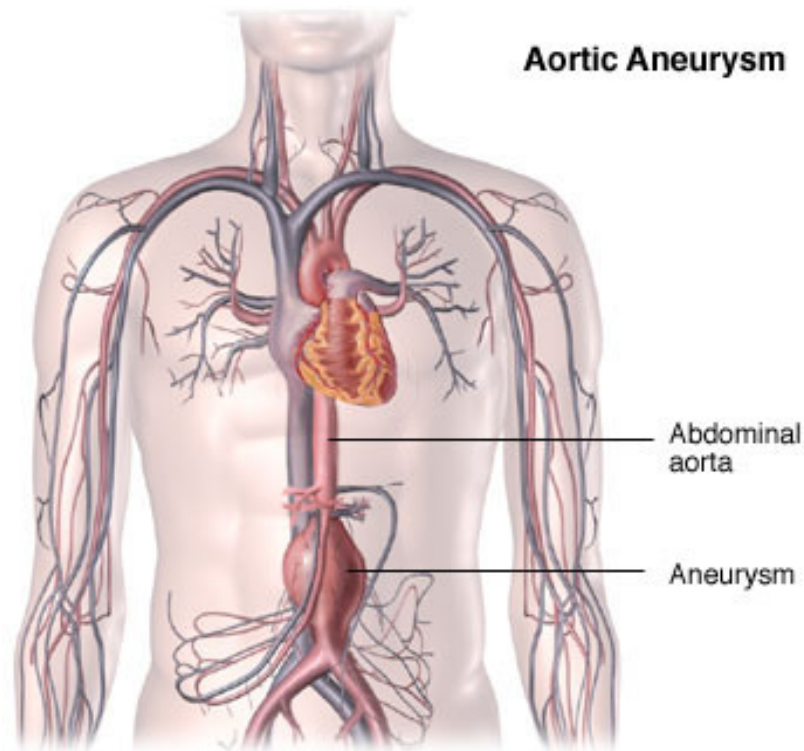


Figure 1-1: Anatomical depiction of an AAA displaying the dilation at the abdominal level (taken from www.endovascular.net)

1.1 DEMOGRAPHICS

The formation of abdominal aortic aneurysm is primarily a disease of the elder male ages 50 years and above. The incidence of AAA is 4 to 6 times greater in men than women, with this difference dissipating after the 8th decade of life [4, 5]. This being said, the annual risk of rupture for females was recently shown to be 3 times that for males [6]. Aneurysmal disease primarily occurs in the white race, as shown in a recent study utilizing the Nationwide Inpatient

Sample of 1994-1996 [7] ([Table 1](#)). This table also outlines the preference of this disease to the male aged 60 years and above.

Table 1-1: Patient demographical data from a random sampling in the US[7]

| <i>Patient Demographics</i> ⁷ | |
|---|-----------------|
| Age | |
| 50-59 y | 960 (5.8%) |
| 60-69 y | 5,228 (31.8%) |
| 70-79 y | 7,965 (48.4%) |
| Male | 13,114 (79.70%) |
| Female | 3,340 (20.3%) |
| White | 13,009 (94.7%) |
| Black | 286 (2.1%) |
| Other race | 450 (3.3%) |

1.2 CLINICAL TREATMENT

1.2.1 Open AAA Repair

DuBost et al. reported the first open surgical repair of AAA in 1952 [8]. This surgery involves a large anterior incision with the exclusion of the AAA via a graft sewn inside the intra-

aneurysmal sac ([Figure 1-2](#)). Once the body of the AAA is opened up, the intra-luminal thrombus (ILT), which occurs in 75% of AAAs, is removed. Either a straight tube or a bifurcated tube graft is then anastomosed to the proximal and distal interior of the abdominal aorta. Following the reestablishment of blood flow, the AAA wall is then sewn back around the graft and the patient is closed. Over the past 30 years, the elective repair of AAA via open surgical techniques has resulted in a decrease in mortality and morbidity rate from 20% to 5% [9], largely due to advances in surgical, anesthetic, and intensive care techniques. The emergent open repair of AAA, however, results in a much higher morbidity and mortality rate, typically around 50% [10-12]. Given the relative success of open AAA surgery in the elective setting, this remains the gold standard for treatment of AAAs larger than 5.5cm in diameter.

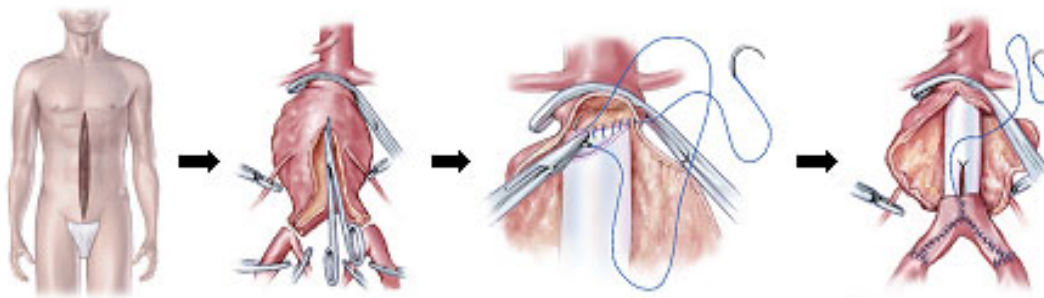


Figure 1-2: Traditional open repair of AAA with large anterior incision (adapted from www.guidant.com)

1.2.2 Endovascular Repair of AAA

A less invasive endovascular treatment for the exclusion of AAAs was introduced early in the last decade by Carlos Parodi in South America [13]. This procedure involves the insertion of an endoluminal graft into the femoral artery and its gradual advancement and deployment in the abdominal region ([Figure 1-3](#)). Endovascular repair (EVAR) has grown in

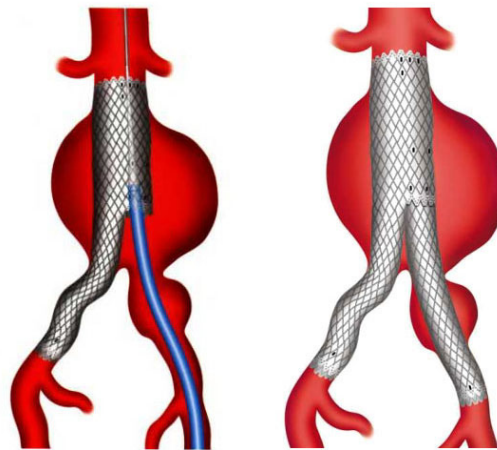


Figure 1-3: Placement (left) and resulting endovascular graft (right) (adapted from www.medtronic.com)

popularity due to its noninvasive nature [12]. The most commonly reported benefits of EVAR compared to the traditional open repair are a decrease in blood loss, a decrease in hospital stay, and fewer complications [14-16]. Indeed, for a recently reported clinical trial the average recovery times in the hospital for open repair were statistically larger than that for EVAR [17]. EVAR is not without its caveats, however. Because it is a relatively new procedure, the long-term benefits of this procedure are yet to be discovered [14-16]. In addition, currently available

endovascular grafts are also associated with several mechanisms of failure, including graft migration and endoleak. Type I endoleak occurs when the seal between the graft and the aorta is not complete, allowing blood to flow from the lumen to the aneurysmal sac. Type I endoleaks can occur at proximal or distal attachment sites, and have been correlated to short aneurysm neck [18], large vessel diameter [19], aneurysm neck angulation [20], and tortuosity of the iliac arteries [21]. Type II endoleaks are a result of retrograde flow from small arteries such as the lumbar or the inferior mesenteric artery (IMA). Type III endoleaks are due to a graft defect, either a separation of a modular graft or a hole in the graft. Type IV endoleaks are caused by fabric porosity and usually subside within 30 days [22]. All forms of endoleak result in endotension – the increase in pressure within the aneurysmal sac – which increases the risk of AAA rupture. In addition to the mechanisms of failure for EVAR, this procedure is limited to patients whose aortic geometry are amenable to this procedure. Specifically, those patients whose aortas are highly tortuous or who present with a very small neck region are typically declined the EVAR approach and offered the open surgical repair [18-21]. In addition to device complications and patient selection, the comparatively high cost of the endovascular graft is prohibiting this procedure from providing a large decrease in the cost of AAA repair. Despite its noted disadvantages, the design of new EVAR devices as well as the increasing experience of surgeons with EVAR over the next few decades may eventually render it the mainstay for the treatment of AAA.

1.3 A BIOMECHANICAL APPROACH

1.3.1 The Surgeon's Dilemma

Given the limitations and risks of current repair techniques, it is important to determine when, during the course of an aneurysm, the risk of rupture justifies repair. That is, only those patients who are of high risk of suffering AAA rupture should be offered repair. However, there is no currently accepted technique available to quantify the risk of rupture for individual AAA. Presently, the decision for elective repair of AAA is based on the maximum diameter of the aneurysm. Typically, when the AAA reaches 5-cm in diameter, it is thought that risk of rupture warrants repair [23-25]. This “5-cm diameter criterion” is only a rule-of-thumb and is, in general, unreliable ([Table 1-2](#)) [23, 25]. Autopsy studies have shown that up to 23% of AAAs rupture at a diameter less than 5 cm [26, 27], while up to 66% of the

Table 1-2: Relationship of size to rupture in 473 nonresected AAA (adapted from Darling et al.[23])

| Size (cm) | Ruptured | Unruptured | Total | % Ruptured |
|------------------|----------|------------|-------|------------|
| ≤ 5.0 | 34 | 231 | 265 | 12.8 |
| > 5.0 | 78 | 116 | 194 | 40.0 |
| No Size Recorded | 6 | 8 | 14 | 43.0 |
| Total | 118 | 355 | 473 | 24.9 |

aneurysms between 5 cm and 10 cm will not rupture, given the life expectancy of the patient. Therefore, surgery based on the 5-cm diameter criterion may be offered too late or may not be necessary for a certain group of patients. Clearly, the ability to reliably evaluate the susceptibility of a particular AAA to rupture on a patient-specific basis could vastly improve the clinical management of these patients.

1.3.2 Rupture Potential Index

The reason that the “5-cm diameter criterion” to evaluate AAA severity is so unreliable is that it does not take into account other individual characteristics of an aneurysm. AAA rupture assessment is not a “one-size-fits-all” process. From a purely mechanical point of view, rupture of AAA occurs when the mechanical stresses (internal forces per unit area) acting on the aneurysm exceed the ability of the wall tissue to withstand these stresses (i.e., the wall's failure strength). Our previous observations show that AAA formation is accompanied by an increase in wall stress [28, 29], as well as a corresponding decrease in wall strength [30-32]. Despite recent reports [33, 34], it should be noted that evaluation of rupture potential based on only one of these parameters – stress or strength – is not sufficient since a region of the AAA wall that is under elevated wall stress may also have higher wall strength, thus equalizing its rupture potential. Based on principles of material failure, rupture instead is most likely where the ratio of stress to strength is highest. Nonetheless, it is interesting to note from a recent retrospective study using an earlier version of our wall stress evaluation techniques that consideration of even peak wall stress alone suggests an improvement over the “5-cm diameter criterion” [33, 35]. Clearly, the ability to non-invasively predict the locally acting wall stress and wall strength for

AAAs on a patient-specific basis will provide a more appropriate diagnostic tool for isolating those AAAs who are at high risk of rupture. Our laboratory has proposed the use of a new index for the detection of high risk AAAs, which is based on the noninvasive prediction of patient-specific AAA wall stress and wall strength. The rupture potential index (RPI) of an AAA can be defined as the ratio of the locally varying wall stress to the wall strength:

$$\text{RPI} = \frac{\text{AAA Wall Stress}}{\text{AAA Wall Strength}} \quad (1.1)$$

The range of the RPI index is from zero to one, with one being zero chance of AAA rupture, and one being imminent rupture. It is important to note that both the stress and the strength acting on the AAA wall may vary spatially, so that the RPI inherently has the ability to determine not only high risk aneurysms, but also the region within the aneurysm that is at highest risk. The development of the RPI as an index for determining the risk of AAA rupture on a patient-specific basis may improve the diagnosis and treatment of this disease.

1.4 HYPOTHESIS AND SPECIFIC AIMS

The purpose of the proposed research is to improve the RPI calculation for patient-specific AAA models by the implementation of a biaxial constitutive relation for AAA wall and ILT into finite element simulations as well as the inclusion of a more robust wall strength model. Therefore, there are three primary hypotheses that will be addressed in the current work:

Hypothesis #1 – The utilization of a biaxially-derived constitutive relation for the AAA wall and intra-luminal thrombus into patient-specific finite element simulations of AAA will alter the peak stress as well as the distribution of stresses within a given AAA.

Hypothesis #2 – An increased dataset and more appropriate data collection and statistical analyses will improve the estimation of AAA wall strength.

Hypothesis #3 – The inclusion of the improved estimates of wall stress and wall strength will result in an RPI that can better identify those AAAs that are at high risk of rupture.

The above hypotheses will be tested with the following specific aims:

Specific Aim #1 - Determine an accurate biaxial hyperelastic constitutive equation for non-aneurysmal and aneurysmal human abdominal aorta, and intra-luminal thrombus.

To the author's knowledge, there has been no report of the biaxial mechanical properties of human nonaneurysmal and aneurysmal abdominal aorta in the literature. This deficiency prohibits the direct insertion of such data into 3D finite element simulations of these tissues. For these reasons, biaxial tensile testing of nonaneurysmal and aneurysmal abdominal aorta, as well as ILT will be performed using a well-documented and well-validated device [36, 37]. Nonaneurysmal aortic tissue will serve as age-matched controls for the AAA tissue. Assuming these tissues are incompressible and undergo large deformations in-vivo, a suitable strain energy function (W) will be chosen and applied to each material. Because it is desired to derive a constitutive relation for AAA wall and ILT that will be suitable to estimate the patient-wide multiaxial mechanical response of all AAA, a single (averaged) set of material parameters will be determined for each of these tissues.

Specific Aim #2 - Implement the new constitutive models into patient-specific finite element models of AAA.

The biaxial material model for AAA wall and ILT derived in Specific Aim #1 will be implemented into the finite element software Abaqus Inc. (HKS, 2003). The first step will be to simulate biaxial tensile tests from a specific AAA wall and ILT specimen using parameters derived experimentally from each specimen. The second step will be to compare these specimen-specific results to simulations in which the group AAA wall and ILT material parameters derived in Specific Aim #1 are used. The next step of this aim will be to assess the improvement of using the biaxial AAA wall and group material parameters as compared to the isotropic, uniaxially-derived material parameters used previously by our lab [38]. Finally, the population-wide biaxial constitutive relations for AAA wall and ILT will be taken from a 2D boundary condition setting and translated into a fully 3D constitutive relation applicable to 3D patient-specific AAA geometry.

Specific Aim #3 - Improve the mathematical model for the prediction of spatially-varying AAA wall strength.

Prior research by our laboratory has led to the formulation of a statistically-based mathematical model for the prediction of local wall strength [39, 40]. Using a step-down statistical procedure, it was found that the local ILT thickness, patient age, local normalized diameter, and patient family history of AAA disease each have a significant affect on local AAA wall strength. The previous approach, however, used an awkward and potentially inaccurate ex-vivo procedure to measure local ILT thickness. Moreover, this model is hard to build on, since the experimental

procedure previously used to calculate ILT thickness was extremely user-dependent. The relatively small range of variables used in the construction of the model also limits its clinical utilization to a wide range of AAAs. This specific aim, therefore, is designed to derive a new AAA wall strength model using similar statistical procedures as the previous approach but using a larger range of input variables, a more reliable calculation of local ILT thickness and local diameter, and a larger wall strength dataset.

Specific Aim #4 - Compare the RPI for AAAs using the previous estimation techniques of stress and strength distributions with that using the revised techniques

Once Specific Aims #1 through #3 above were completed, the final aim was to compare the RPI of patient specific AAAs using the previously derived stress and strength models with the RPI of the same patient specific AAAs using the new stress and strength distributions. The updated stress and strength distributions will be separately compared to their previous counterparts so the effect of each component on the RPI can be fully realized. The magnitude of the minimum, maximum, and average stress, strength, and RPI values that occur will be recorded and compared. Finally, the RPI distributions of patients undergoing elective AAA repair will be compared with the RPI distributions of a set of patients who's AAA eventually ruptured.

2.0 BIAXIAL TESTING OF AAA AND NONANEURYSMAL AORTIC TISSUE

2.1 INTRODUCTION

One of the first biaxial tensile testing experiments was performed by Lanir and Fung [41, 42] when they investigated the biaxial mechanical response of rabbit skin. Many other investigators have used biaxial tensile testing devices to study a wide variety of biological tissues including canine diaphragm[43], aorta[44], saphenous vein [45], pulmonary arteries [46], as well as porcine intestinal submucosa [47], heart valve [48], and rat bladder wall [49]. Sacks et al. was the first to include the measurement of in-plane shear strains in their biaxial tensile testing device. [36] This device is that being used in the current study. To the author's knowledge, the only ex-vivo biaxial tensile testing experiments reported for human aortic tissue were the biaxial inflation tests on descending thoracic aorta by Mohan et al. [50], the inflation tests on human iliac arteries by Schulze-Bauer et al. [51], and the planar biaxial testing of human ascending thoracic aneurysm tissue reported by Okamoto et al. [52] The Okamoto et al. manuscript represents the first report of the planar biaxial response of aneurysmal tissue. Given the small number of these initial studies, there clearly exists a large deficiency in the literature concerning the biaxial mechanical response of human aortic tissue, especially in the nonaneurysmal and

aneurysmal segment of human infrarenal abdominal aorta. The biaxial tensile testing reported for the current research will serve in part to complete this portion of the literature.

The biomechanical response of human AAA, as well as nonaneurysmal abdominal aorta (AA), to uniaxial loading conditions has been previously reported by our laboratory and others. [30, 38, 53, 54] However, mechanical data derived from uniaxial tensile testing is insufficient for the characterization of its multi-axial mechanical response. Yet, most 3D stress analysis models of AAA reported in the literature have been based on previous uniaxial tensile testing data.[28, 33-35, 55] Clearly, multi-axial mechanical evaluation would allow for more appropriate modeling of aneurysmal tissue, especially given the extent of mechanical anisotropy already quantified for human aortic tissue in the literature.[51, 52] The biaxial mechanical response of the human abdominal aorta may be even more important in the presence of aneurysm, in which the multi-axial loading of the vessel is pronounced due to its anterior bulging. ([Figure 2-1](#)) In addition, the inclusion of the biaxial mechanical response for aneurysmal aorta to the literature may lead to a better understanding of the progression and structural manifestations of this disease. Yet, to date there is no extant data on the biaxial mechanical response of AAA tissue. In the current investigation, biaxial tensile testing was performed on human AAA and AA tissue in order to characterize the biaxial mechanical response of both tissue types and to gain insight into differences between them. It should be noted that this work has previously been published (see Vande Geest et al. [56, 57]).

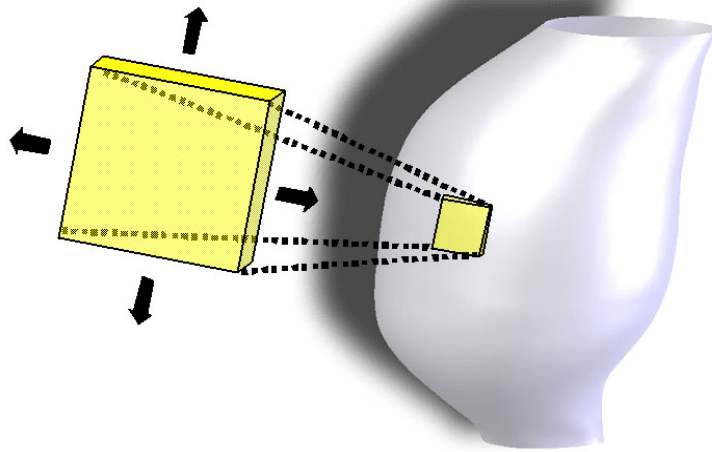


Figure 2-1: Biaxial loading condition of abdominal aorta pronounced by aneurysmal dilation

2.2 METHODS

2.2.1 Biaxial Tensile Testing Device

The biaxial tensile testing device utilized in the current study has been detailed previously. [36, 37] Simply stated, this device allows for the simultaneous recording of load and marker displacement on planar biological soft tissues. The device consists of two orthogonally placed load cells and motion carriages, a saline bath for specimen saturation, and a CCD camera for the simultaneous measurement of marker displacement. ([Figure 2-2](#)) The typical dimensions for a biaxial specimen are 15 mm along each orthogonal edge and a thickness of 2 mm, providing a state of plane stress within the specimen. The four markers used for strain

measurement typically make a 3 mm x 3 mm square at the center of the specimen. A typical AAA biaxial specimen is shown in [Figure 2-3](#).

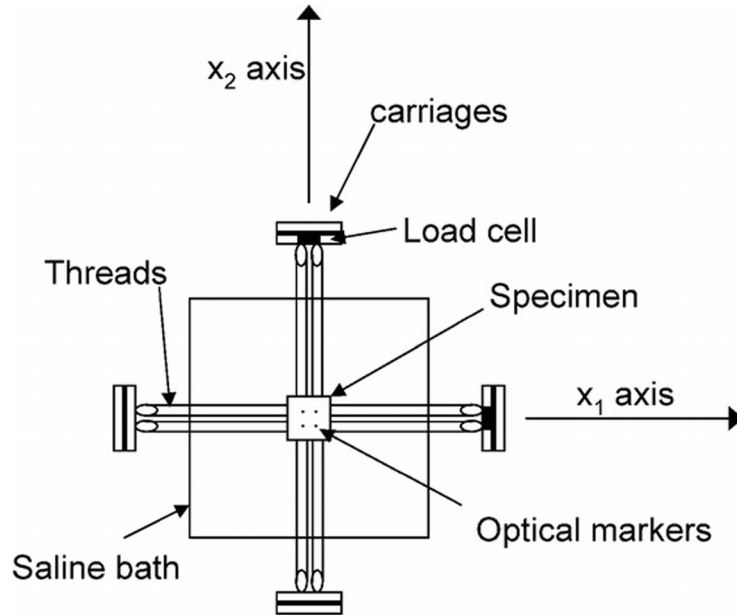


Figure 2-2: Biaxial tensile testing setup. Adapted from Sacks and Sun (2003)[58]

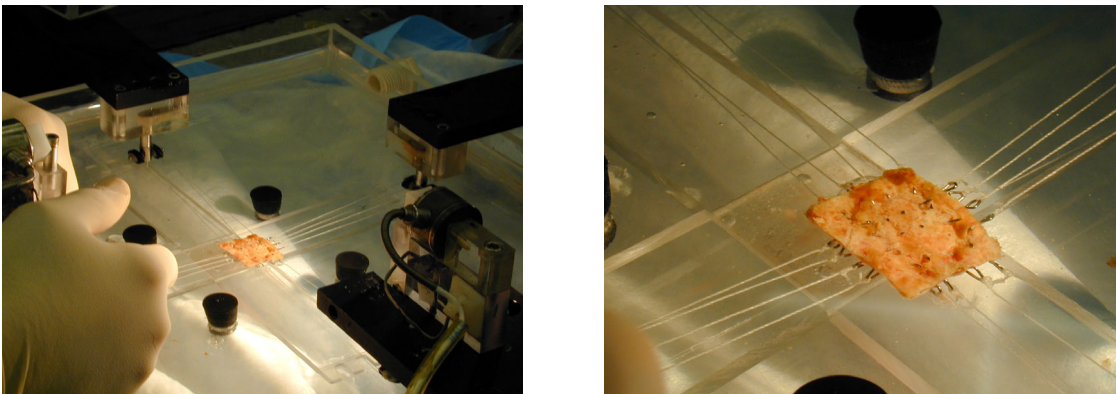


Figure 2-3: Typical AAA biaxial specimen

2.2.2 Specimen Procurement

2.2.2.1 Specimen Source

Nonaneurysmal Human Abdominal Aorta. A total of 18 human infrarenal nonaneurysmal abdominal aortic samples were harvested from either autopsy subjects (N=11) or organ donors (N=7) according to University of Pittsburgh Institutional Review Board guidelines. It should be noted that all of the organ donor specimens were retrieved from donors for recipients of kidney transplant, each of which was brain dead due to traumatic injury. The cause of death for each of the autopsy subjects is reported in [Tables 2-1, 2-2, 2-3](#). The ages of all subjects ranged from 19 to 75 years, with 5 subjects being less than 30 years (Group 1), 7 subjects between 30 and 60 years (Group 2), and 6 subjects over 60 years (Group 3).

Table 2-1: Age and source of death for Group 1 specimens

| Group 1 <30 yrs | | |
|-----------------|-----|---|
| Specimen | Age | Source/Cause of death |
| 1 | 19 | Organ donor for kidney transplant |
| 2 | 22 | Organ donor for kidney transplant |
| 3 | 23 | Organ donor for kidney transplant |
| 4 | 25 | Multi-organ system failure/sickle cell anemia |
| 5 | 26 | Heart transplant rejection |

Table 2-2: Age and source of death for Group 2 specimens

| Group 2 30<AGE<60 yrs | | |
|-----------------------|-----|-----------------------------------|
| Specimen | Age | Source/Cause of death |
| 6 | 35 | Organ donor for kidney transplant |
| 7 | 39 | Cryptococcal meningitis |
| 8 | 47 | Allergic reaction/sepsis |
| 9 | 47 | Organ donor for kidney transplant |
| 10 | 47 | Organ donor for kidney transplant |
| 11 | 50 | Heart transplant rejection |
| 12 | 50 | Organ donor for kidney transplant |

Table 2-3: Age and source of death for Group 3 specimens

| Group 3 >60 yrs | | |
|-----------------|-----|---|
| Specimen | Age | Source/Cause of death |
| 13 | 61 | Abdominal surgical complication/sepsis |
| 14 | 66 | Multi-organ system failure/cirrhosis |
| 15 | 69 | Acute respiratory distress syndrome/myocardial infarction |
| 16 | 71 | Multi-organ system failure/pneumonia |
| 17 | 75 | Cerebral aneurysm |
| 18 | 75 | Metastatic uterine carcinoma |

Human Descending Thoracic Aorta. Seven pairs of human descending thoracic (DTA) and abdominal aorta (AA) were harvested from autopsy within 24 hours of death, following NIH and IRB guidelines. The age range of all specimens tested was 25 to 66 years of age. The specimens were split into three groups according to age: Group 1 (<30 yrs old), Group 2 (>30 but <60 yrs old), and Group 3 (>60 yrs old).

Abdominal Aortic Aneurysm. All AA and AAA tissue specimens were retrieved according to University of Pittsburgh Institutional Review Board guidelines. AAA samples were obtained from open surgical aneurysm repair, primarily from the anterior portion of the aneurysm. Age-matched (> 60 yrs of age) AA tissue samples were harvested from autopsy within 24 hours of death.

Intra-luminal Thrombus. All ILT specimens were harvested from patients undergoing elective open AAA repair according to University of Pittsburgh Institutional Review Board guidelines. A previous study by our laboratory detailed three distinct layers present in the ILT (luminal, medial, and abluminal), highlighting the strong heterogeneity of this material as a whole [59]. The luminal layer of the ILT was isolated from the medial and abluminal layers by gentle peeling.

2.2.2.2 Specimen Storage

All samples were stored in 0.9% saline in a 4° C refrigerator [60] and tested within 48 hours from harvest. Square specimens approximately 2cm x 2cm in dimension were cut such that the longitudinal and circumferential orientations of the aorta were parallel with the square edges. It

should be noted that the aortic wall specimens were cut from a region of the infrarenal aorta where there was minimal atherosclerotic lesions and calcification. The loose connective tissue on the adventitial side of each aortic wall specimen was removed and the thickness of all specimen types were measured at six different locations with a dial caliper and averaged. The unloaded dimension of the specimen in the circumferential (X_{θ}) and longitudinal (X_L) directions were also measured and recorded.

2.2.3 Biaxial Protocol

Details of the methods for the biaxial tensile testing procedures and analyses used here have been reported previously [37, 56, 57, 61]. Briefly, the square specimens were mounted in a biaxial tensile testing device using four nylon sutures hooked to each side of the square specimen with surgical staples. The nylon sutures were connected to specially designed carriages that allow for self-equilibrated loads for each suture line. The specimen was mounted so that it was stretched along the circumferential (θ) and longitudinal (L) directions. Four markers were placed in a square fashion in the center of the testing specimen, and a CCD camera was used to capture marker displacement during loading. The specimen was tested using a tension-controlled protocol, where the ratio of axial tensions $T_{\theta\theta}:T_{LL}$ were kept constant during loading. The following protocols were used in the order listed: $T_{\theta\theta}:T_{LL}=1:1$, $0.75:1$, $1:0.75$, $0.5:1$, $1:1$, $1:0.5$, $1:1$, $0.1:1.0$, and $1.0:0.1$ ([Figure 2-4](#)). The multiple equibiaxial tension protocols (i.e. $T_{\theta\theta}:T_{LL}=1:1$) were performed throughout the test to ensure no structural damage occurred as a result of the mechanical testing.

The maximum tension value used for each nonaneurysmal and aneurysmal wall specimen was 120 N/m, which is the tension in a thin cylindrical tube, of a diameter (2 cm) and thickness

(2mm) consistent with that of the typical abdominal aorta, exposed to a physiological pressure (113 mmHg). The maximum tension value used for each ILT specimen was 40 N/m. This value was determined in preliminary experiments in our laboratory to be the maximum tension the luminal ILT can withstand in the biaxial tester without the surgical staples detaching from the tissue. It should also be noted here that each attempt to test the medial and abluminal layers of ILT resulted in the surgical staple pulling out from the biaxial specimen edges. This is consistent with our previous observation that these layers are significantly weaker than the luminal layer [59]. Prior to collecting data for subsequent analysis, each specimen was preconditioned through nine loading and unloading cycles to the same tension ratio. Data from the tenth loading cycle of each tension ratio protocol is used for analysis as described below.

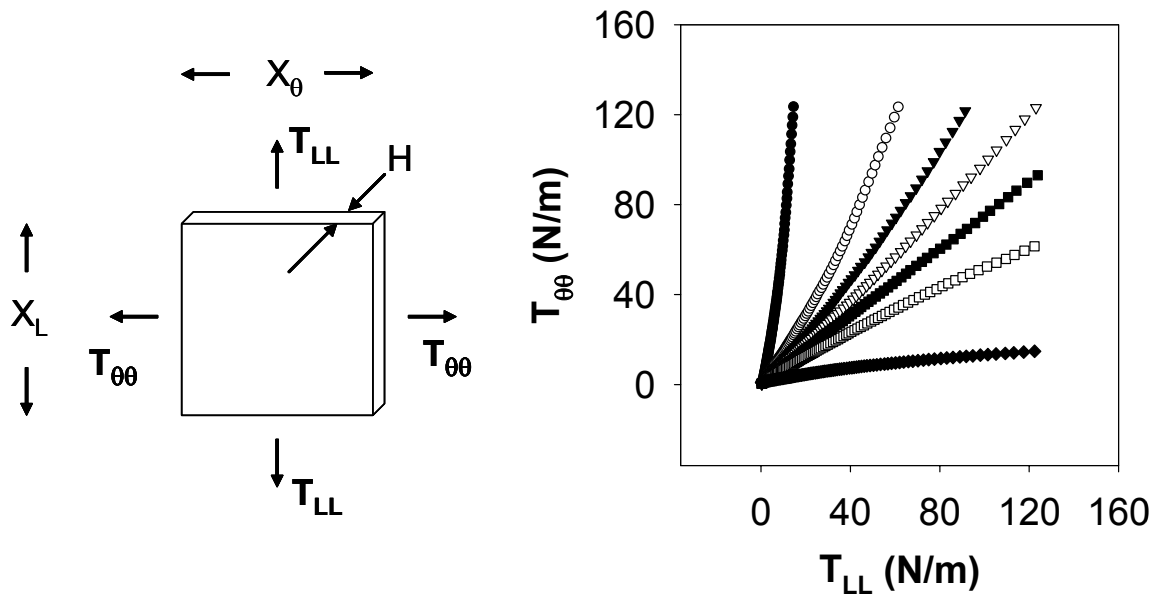


Figure 2-4: Biaxial specimen undeformed geometry (left) and tension-driven biaxial protocol (right)

2.2.4 Data Analysis

2.2.4.1 Stress

The 1st Piola-Kirchhoff stress tensor \mathbf{P} was calculated from the measured loads and the initial specimen dimensions, so that the non-zero components of \mathbf{P} were

$$P_{\theta\theta} = \frac{f_{\theta}}{HX_L}, \quad P_{LL} = \frac{f_L}{HX_{\theta}} \quad (2.1)$$

where f_{θ} and f_L are the measured loads in each direction and H is the averaged specimen thickness in the unloaded reference configuration. The 2nd Piola-Kirchhoff stress tensor \mathbf{S} was determined using $\mathbf{S} = \mathbf{P} \cdot \mathbf{F}^{-T}$, and the Cauchy stress tensor \mathbf{t} from $\mathbf{t} = \mathbf{P} \cdot \mathbf{F}/\mathbf{J}$, which for an incompressible material with negligible shear terms reduces to

$$t_{\theta\theta} = \lambda_{\theta} P_{\theta\theta} \quad t_{LL} = \lambda_L P_{LL}. \quad (2.2)$$

2.2.4.2 Strain

From the marker positions, the deformation gradient tensor \mathbf{F} was calculated at each data point (Sacks 2000). The components of the in-plane Green strain tensor \mathbf{E} were calculated using

$$\mathbf{E} = \frac{1}{2}(\mathbf{F}^T \mathbf{F} - \mathbf{1}). \quad (2.3)$$

The shear components of the deformation gradient tensor \mathbf{F} in all of the tested specimens were found to be negligible, so that the in-plane Green strain tensor components were determined using

$$E_{\theta\theta} = \frac{1}{2}(\lambda_{\theta}^2 - 1), \quad E_{LL} = \frac{1}{2}(\lambda_L^2 - 1). \quad (2.4)$$

The peak stretch values for each specimen in the circumferential and longitudinal directions for the equibiaxial protocol were recorded and compared. The overall extensibility of the tissue was quantified with the calculation of the areal strain:

$$e_A = \lambda_\theta \lambda_L - 1. \quad (2.5)$$

2.2.4.3 Stiffness

Unlike linearly elastic materials, the stiffness for nonlinear materials is a function of strain. Typically for soft biological materials, the stress-strain response is exponentially shaped, so that the incremental stiffness increases with strain. For all of the arterial tissues studied herein, the peak tension for the equibiaxial protocol was estimated to be in the physiological range of stresses and strains. For this reason, the stiffness of all biaxial specimens was assessed by calculating the maximum tangential modulus (MTM), defined as the peak slope of the equibiaxial stress-strain curves in each orthogonal testing direction.

2.2.5 Statistical Analyses

Student's t-tests were used to compare values across groups, while paired t-tests were used to compare values within groups. For data that was not normally-distributed, a Mann-Whitney rank sum test was performed. All statistical analyses were performed in SigmaStat v.2.03, with a p value less than 0.05 determining significance. All values are reported as mean \pm SEM.

2.3 RESULTS AND DISCUSSION

2.3.1 Nonaneurysmal Abdominal Aorta

2.3.1.1 Results

Biaxial Mechanical Response.

The mean percent error for the longitudinal and circumferential peak stretch for the multiple equitension protocols were $0.74\% \pm 0.3$ and $0.55\% \pm 0.4$, thus proving the response of each specimen was repeatable throughout the entire biaxial test and that no structural damage occurred to the tissue as a result of the experiment. Typical **S-E** plots for all biaxial protocols for all three age groups are shown in [Figure 2-5](#). The biaxial biomechanical response of those specimens in Group 1 (<30 yrs old) was markedly different as compared to those in Groups 2 and 3. The shapes of the response functions for Group 1 were, in general, nonlinear and sigmoidal in nature, while those from Groups 2 and 3 were nonlinear and displayed a single concavity. In addition, the specimens in the younger group displayed a much larger extensibility

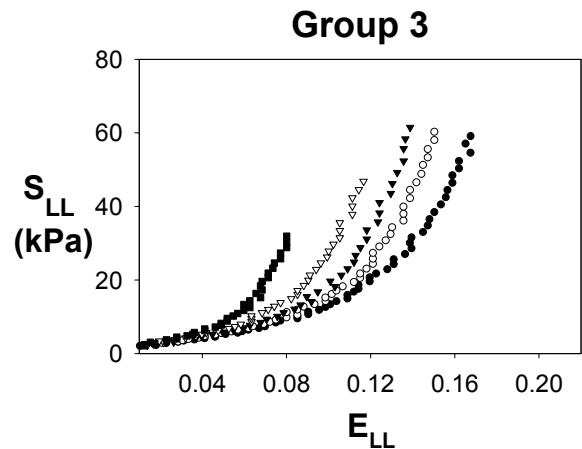
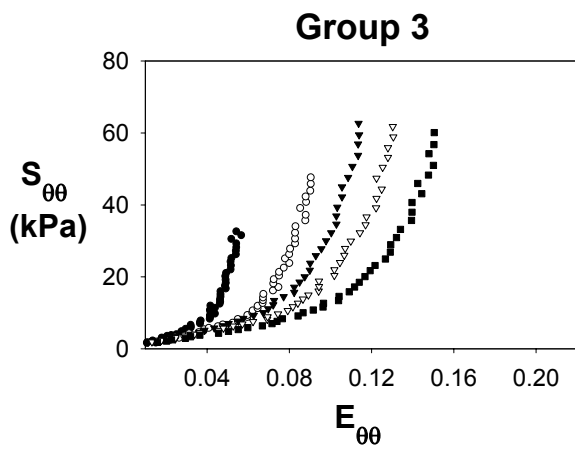
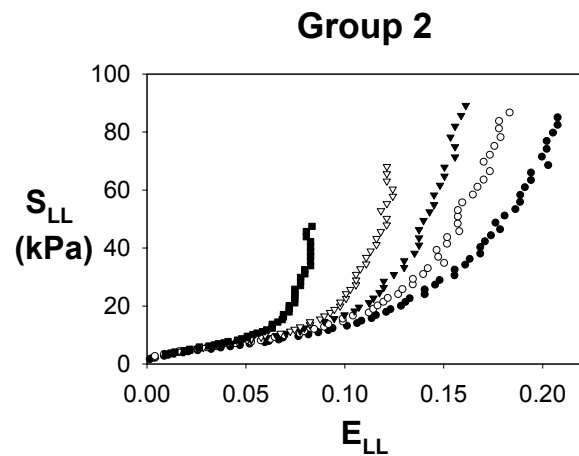
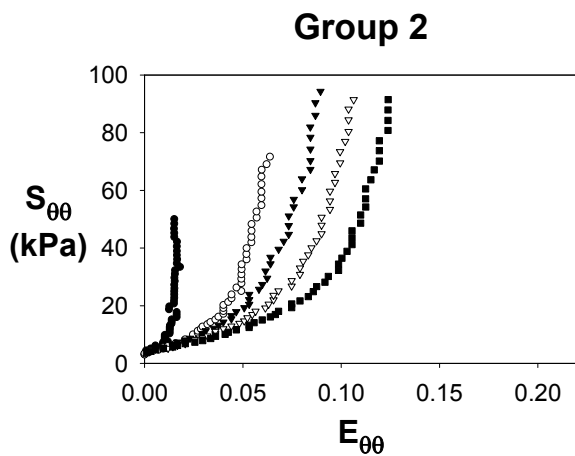
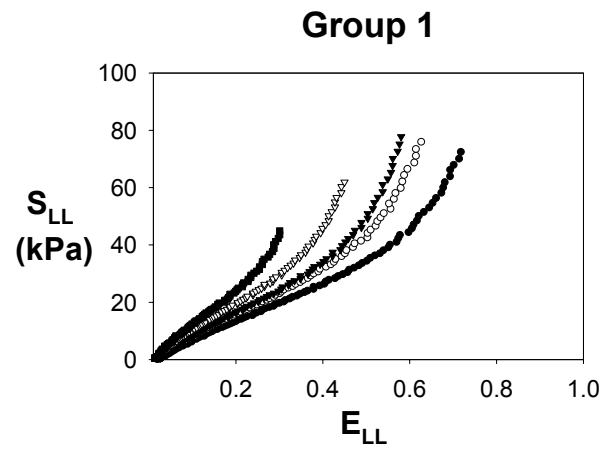
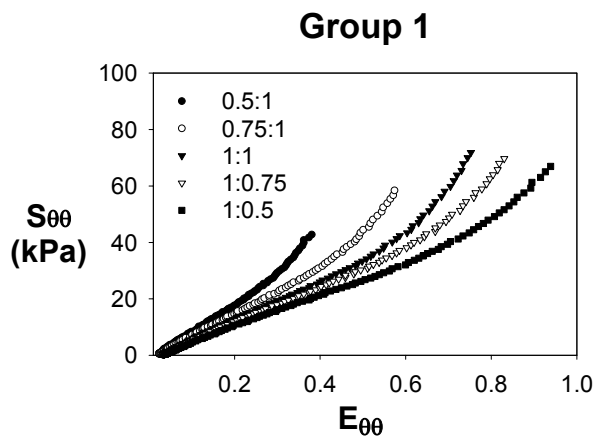


Figure 2-5: Typical stress-strain plots for all protocols and age groups

than either Groups 2 and 3. The peak stretch values in the circumferential and longitudinal directions are shown according to age group in [Figure 2-6](#). There were no statistical differences between circumferential and longitudinal peak stretch values for any age group. The corresponding longitudinal and circumferential peak stretches were significantly smaller for Groups 2 and 3 when compared to Group 1 ($p < 0.001$). The areal strain for each specimen can be seen versus age in [Figure 2-7](#). This plot displays the gradual decline in the gross extensibility of abdominal aortic tissue with age.

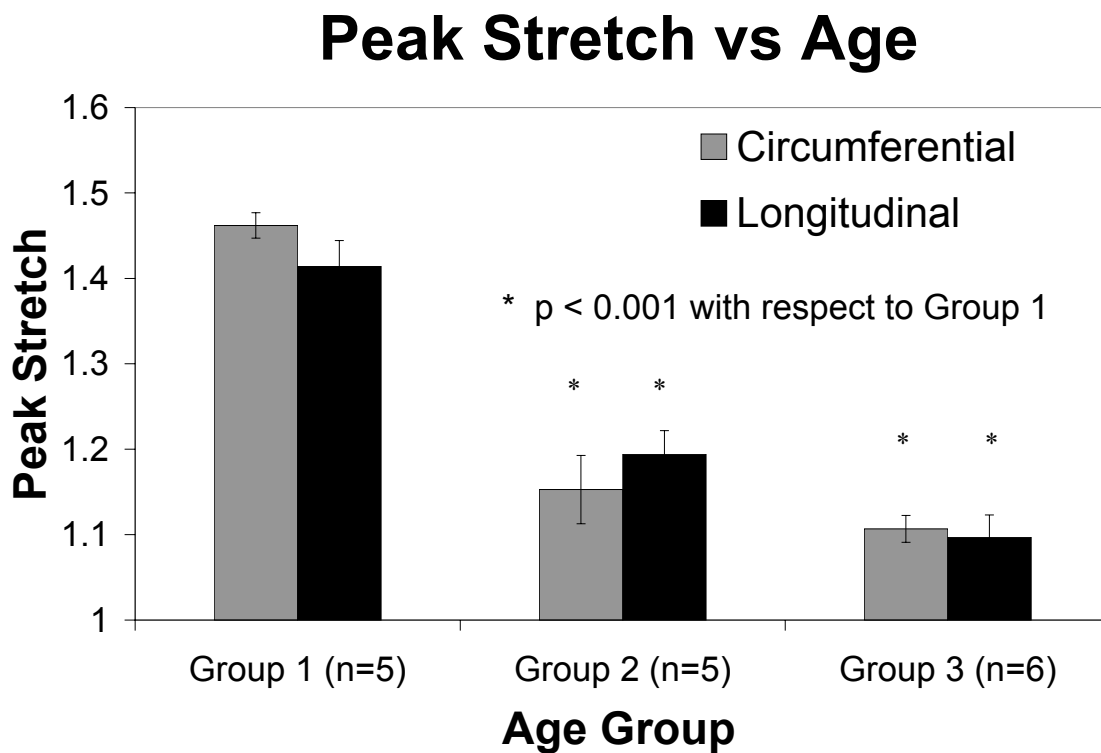


Figure 2-6: Peak stretch values in both directions according to age group. $p < 0.001$ for Group 2 and 3 peak stretch values compared to Group 1 values in both directions

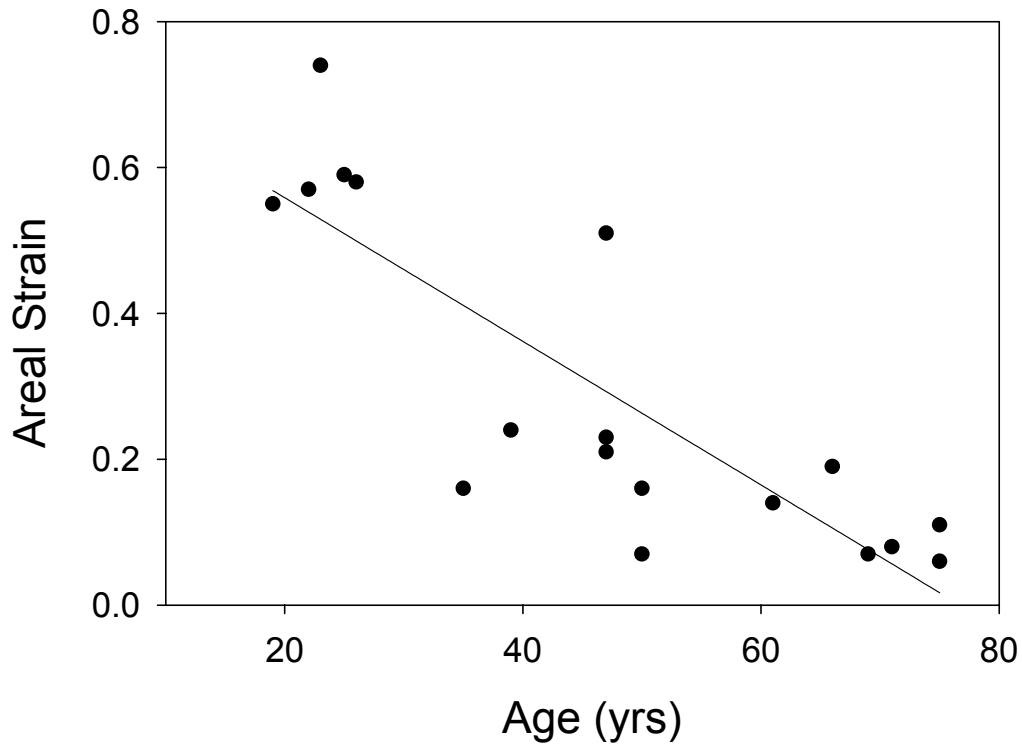


Figure 2-7: Areal strain as a function of age

2.3.1.2 Discussion

The biaxial biomechanical response of human nonaneurysmal abdominal aorta was evaluated in relation to age. It was found that this response changes from a sigmoidal shape of high extensibility for young tissue to a much stiffer exponential shape displaying a significantly lower areal strain for older tissue. The peak stretch values for equibiaxial protocols resulted in values that decreased with increasing age, but did not significantly differ when comparing longitudinal to circumferential directions within each age group.

Previous biomechanical studies on abdominal aorta have focused on pressure-diameter tests and uniaxial tensile tests. Our laboratory [32] previously reported the stiffening of the uniaxial biomechanical behavior of human aneurysmal aortic tissue in the longitudinal direction in comparison to nonaneurysmal tissue. Patel et al. [62] also studied the biomechanical behavior of canine aorta and determined this tissue to be anisotropic. The sigmoidal shaped biaxial biomechanical response of the Group 1 nonaneurysmal abdominal aorta reported here is similar to previous reports given by Ling et al. who also show a similar shaped stress-strain response for arterial biaxial loading [63]. The sigmoidal shape of the stress strain curves for this age group are also similar to the biconcavity known to be present in the mechanical response of polymer-like materials[64]. Nicosia et al. have also recently reported biaxial tensile testing results for the pig ascending thoracic aorta[65]. Their results suggest that the aortic root is stiffer in the circumferential direction than in the longitudinal direction. They also reported a stiffer response in the anterior portion of the aortic root than for the posterior region, with a relatively linear mechanical response up to 40% strain. Their results are in contrast to our reported data that showed no preferential increase in distensibility for either the longitudinal or circumferential directions in the human abdominal aorta.

The biaxial mechanical response of human nonaneurysmal abdominal aorta was quantified, taking note of changes that occur with advancing age. The biaxial tensile testing data here represent the only data in the literature for the multi-axial response of human abdominal aortic tissue. Such data can be used for the development of constitutive models for these tissues, which allows their implementation into finite element analyses. These results are important for any scientist interested in accurately predicting the stress environment within the nonaneurysmal abdominal aorta.

2.3.2 Descending Thoracic Aorta

2.3.2.1 Results

Seven matched pairs (from the same cadaver) of human descending thoracic (DTA) and abdominal aortas (AA) were harvested from autopsy within 24 hours of death, following NIH and IRB guidelines. Representative plots of the second Piola-Kirchhoff stress vs. the Green strain for the DTA and AA can be seen in [Figure 2-8](#). This figure suggests that the AA becomes stiffer after age 30, while the DTA becomes stiffer after age 60. By comparing the longitudinal (1) and circumferential (2) directions, one sees little evidence for anisotropy for either AA or DTA at any age. [Figure 2-9](#) shows the average MTM values for each group and for each location. Statistical analyses revealed a higher stiffness for the Group 3 DTA when compared to Groups 1 and 2 DTA after accounting for changes in direction ($p < 0.001$ in both cases). Group 2 AA specimens were also found to be stiffer than the Group 1 AA specimens after accounting for changes in direction ($p = 0.018$). AA specimens were found to be stiffer than DTA specimens after accounting for changes in age ($p = 0.03$). There were no other statistical differences when comparing MTM across age, direction, or location.

The average areal strain is shown for each group and location in [Figure 2-10](#). The average areal strain gradually decreased with age for both DTA and AA. The larger decrease in areal strain from Group 1 to Group 2 for AA correlates well with the large increase in MTM seen for the same age groups and location ([Figure 2-9](#)).

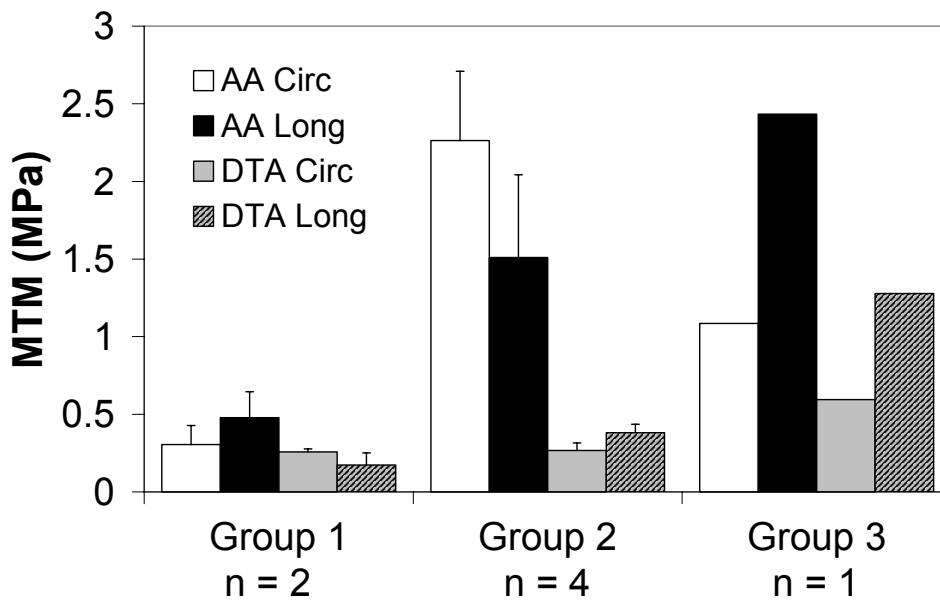
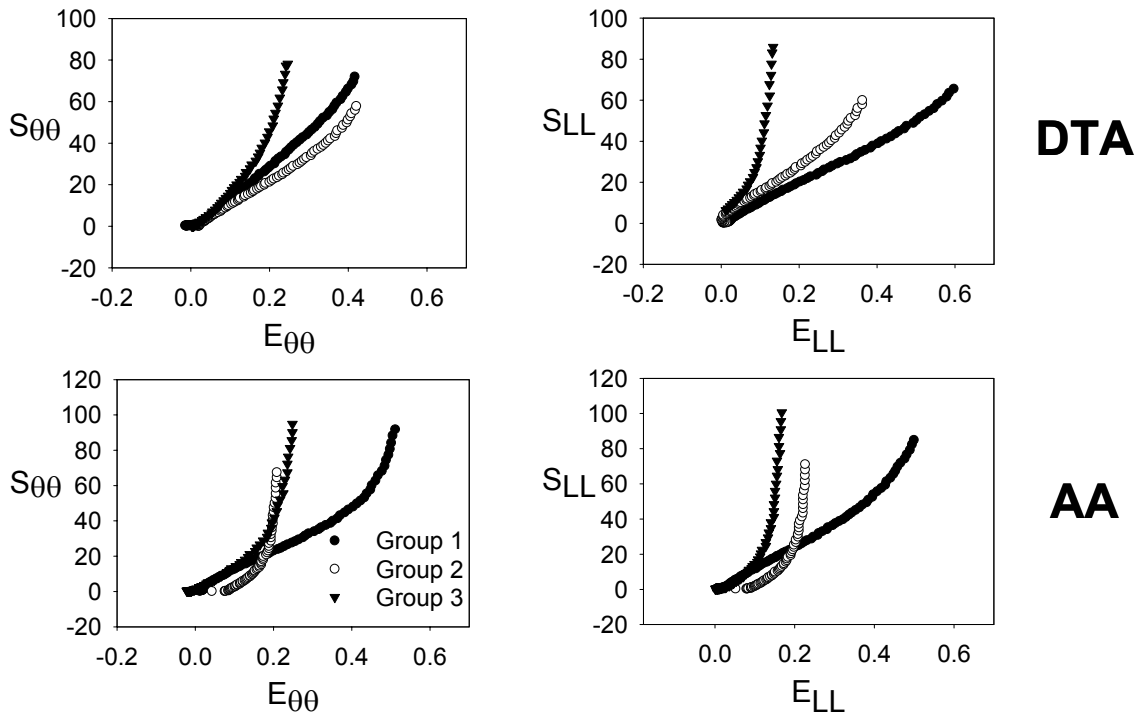


Figure 2-8: Representative stress-strain plots for DTA and AA specimens

Figure 2-9: Maximum tangential modulus (MTM) for each age group and location

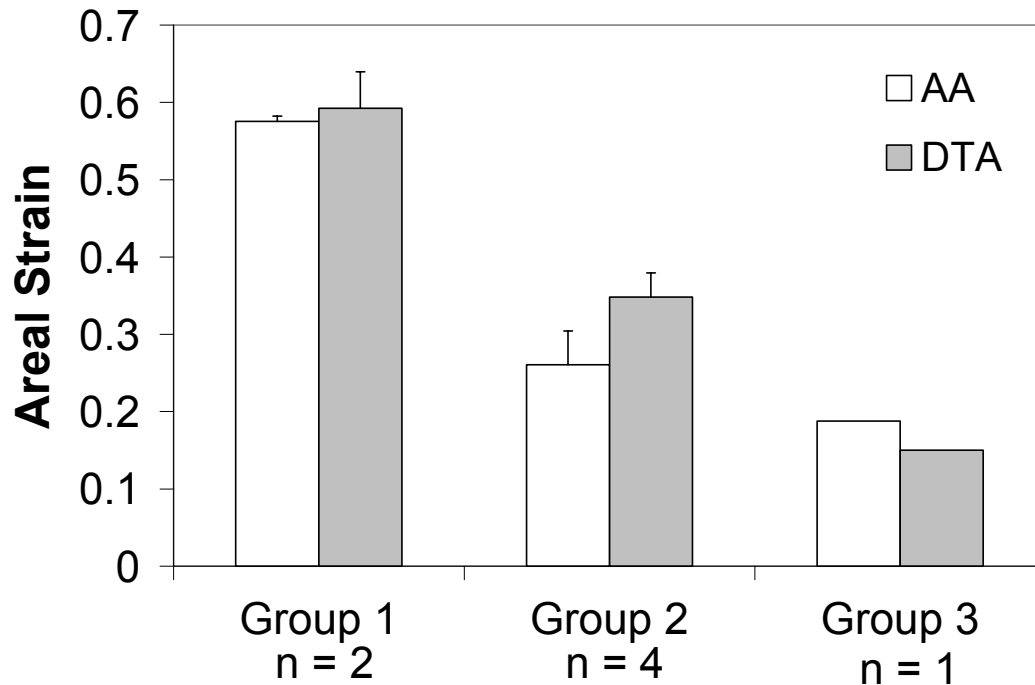


Figure 2-10: Areal strain for each age group and location

2.3.2.2 Discussion

The above results suggest that the biaxial response of AA and DTA are similar for the younger (< 30 yr) specimens. While AA demonstrated marked stiffening by middle age, DTA did not. The stiffness of AA did not change significantly after middle age whereas the DTA demonstrated marked stiffening. The only significant difference in stiffness between AA and DTA was at middle age, where the AA was as stiff as the older tissue, but DTA was as compliant as younger

tissue. There was no evidence for significant anisotropy for any tissue at any age. Our results suggest that the course of age-related stiffening of the aorta is location-dependent.

The data presented by Fung concerning the location-dependence of the uniaxial stiffness of dog aorta shows a gradual increase in the circumferential stiffness as one progresses along the aortic tree [66]. A similar result is found here, where the MTM was found to be significantly higher for AA than for DTA specimens of the same age group. The results reported here, however, suggest that the stiffening in the aorta gradually ‘works its way’ proximally towards the heart as one progresses in age. An in depth investigation which includes the age-dependency of the biaxial mechanical response of human ascending abdominal aorta along with the DTA and AA specimens may more clearly investigate this preliminary conclusion. Early uniaxial testing of human descending thoracic aorta was performed by Sherebrin et al[67]. They found the human descending thoracic aorta to be uniaxially more extensible in the circumferential direction, which is in agreement with the data presented here in which we found a stiffer response in the longitudinal direction for the Groups 2 and 3 DTA specimens ([Figure 2-9](#)). Other prior investigations into the mechanical properties of descending thoracic aorta has been limited to the uniaxial tensile testing of Landrace pigs[68, 69]. For example, Angouras et al. showed that at the same level of strain, inducing ischemia into the descending thoracic aorta of the pig resulted in a significantly stiffer uniaxial mechanical response at both low ($p=0.03$) and high strains ($p=0.003$) than the control aortas. Mohan and Melvin presented the biaxial mechanical response of human descending mid-thoracic aortic tissue via a bubble inflation technique. Their study was primarily focused on the failure mechanisms of this tissue, and concluded that under conditions of uniform biaxial stretch the tissue consistently failed in a direction perpendicular to the long axis of the aorta[50]. Other biaxial tensile tests of descending

thoracic aorta include the biaxial tensile tests of canine descending thoracic aorta reported by Zhou et al.[44]

While the bubble inflation technique used by Mohan and Melvin is capable of investigating the failure properties of the descending aorta, it is unable to subject the tissue specimen to a wide range of stresses and strains. Performing a test in which a wide range of stress/strain states are covered is advantageous for the development of a constitutive relation, as this offers the development of a relation that is comparably less sensitive to a specific loading condition. To the author's knowledge, the results reported here are the first for the planar biaxial tensile testing of human descending thoracic aorta and how this mechanical response varies with age.

2.3.3 Abdominal Aortic Aneurysmal Wall

2.3.3.1 Results

A total of twenty-six tissue specimens from the AAA (mean diameter 6.5 ± 0.2) of twenty-six patients (mean age = 72.3 ± 1.8) and eight AA specimens from eight subjects (mean age = 70.6 ± 1.9 , $p=0.64$ in comparison to AAA group) were tested and analyzed. The mean measured thickness values were 1.49 ± 0.11 mm and 1.32 ± 0.08 mm for the AA and AAA specimens, respectively ($p=0.29$). The mean measured thickness values within each specimen varied by 0.014 ± 0.01 mm and 0.019 ± 0.01 mm for the AA and AAA, respectively.

Results from the multiple equibiaxial protocols resulted in repeatable curves for all specimens, confirming that no structural damage of the tissue occurred as a result of the testing.

Representative **S-E** plots displayed a marked decrease in extensibility and increase in stiffness for AAA specimens as compared to age-matched AA specimens ([Figure 2-11](#)). There was also a decrease in initial slope and more abrupt change in stiffness for AAA specimens as compared to AA specimens ([Figure 2-11](#)). The peak shear stresses and strains ($S_{\theta L}$ and $E_{\theta L}$) were confirmed to be at least one order of magnitude smaller than normal stresses ($S_{\theta\theta}$, S_{LL}) and strains ($E_{\theta\theta}$, E_{LL}) for all AA and AAA specimens.

The mean peak Green strains $E_{\theta\theta,max}$ and $E_{LL,max}$ for the equibiaxial tension ($T_{\theta\theta}=T_{LL}=120$ N/m) protocol for the AA specimens were 1.12 ± 0.02 and 1.11 ± 0.02 , respectively. ($p=0.77$; [Figure 2-12A](#)) $E_{\theta\theta,max}$ and $E_{LL,max}$ under equibiaxial tension for the AAA specimens were 0.07 ± 0.01 and 0.091 ± 0.01 , respectively. ($p=0.047$; [Figure 2-12A](#)) There was no significant difference in $E_{LL,max}$ between the AA and AAA groups ($p=0.24$). However, $E_{\theta\theta,max}$ was found to be significantly smaller for AAA as compared to AA ($p=0.01$). The average values of $E_{LL,max}/E_{\theta\theta,max}$ for the AA and AAA groups were 0.96 ± 0.09 and 1.62 ± 0.01 , respectively ($p=0.1$). The mean areal strain for AA (0.25 ± 0.05) was significantly larger ($p=0.03$) than that of the AAA (0.16 ± 0.02), suggesting that AA tissue is more distensible than AAA tissue ([Figure 2-12B](#)). The average MTM in the circumferential direction was 11.7 ± 1.9 MPa and 3.9 ± 1.1 MPa for the AAA and AA, respectively ($p=0.03$). The average MTM in the longitudinal direction was 8.3 ± 1.2 MPa and 3.3 ± 0.6 MPa for the AAA and AA respectively ($p=0.03$). There were no significant differences between circumferential and longitudinal MTM in either group, although the MTM exhibited a trend towards higher values ($p=0.11$) in the circumferential versus longitudinal direction for AAA tissue ([Figure 2-13](#)).

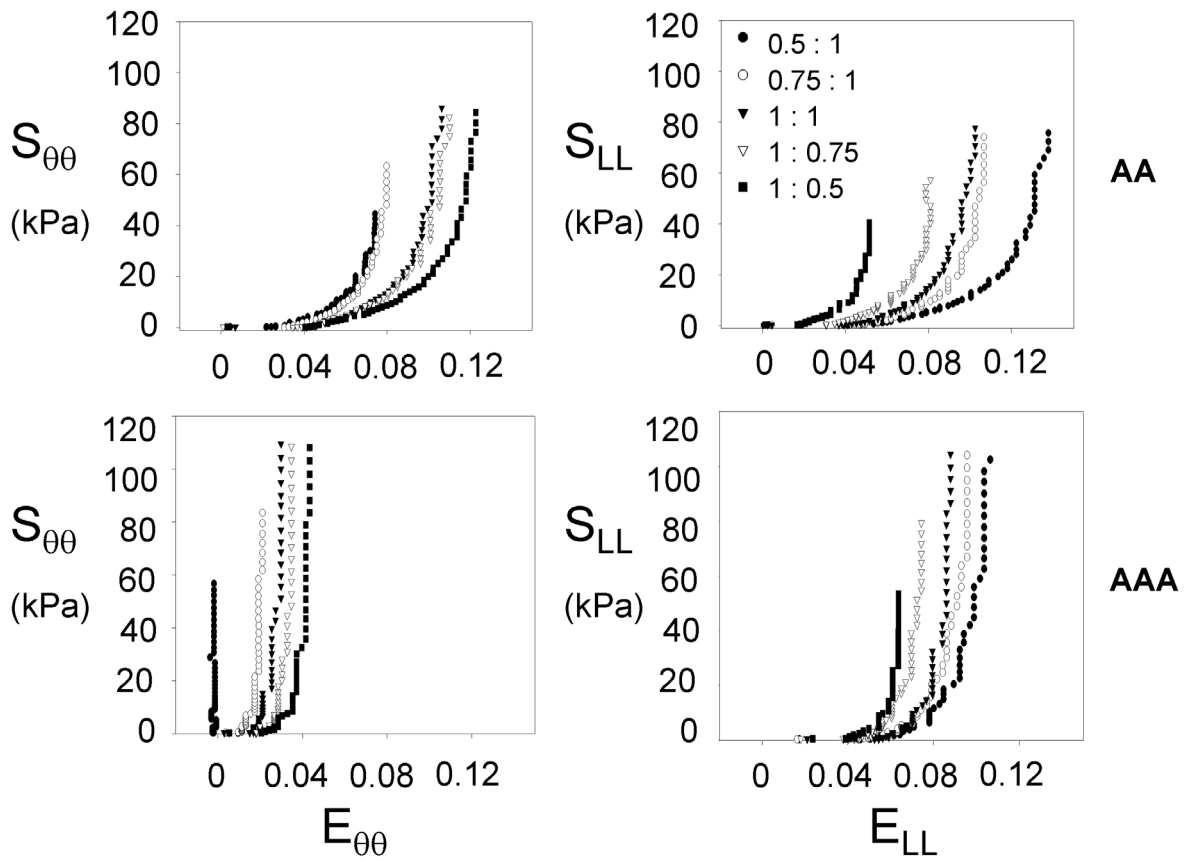


Figure 2-11: Stress-strain plots for a representative AAA and AA specimen

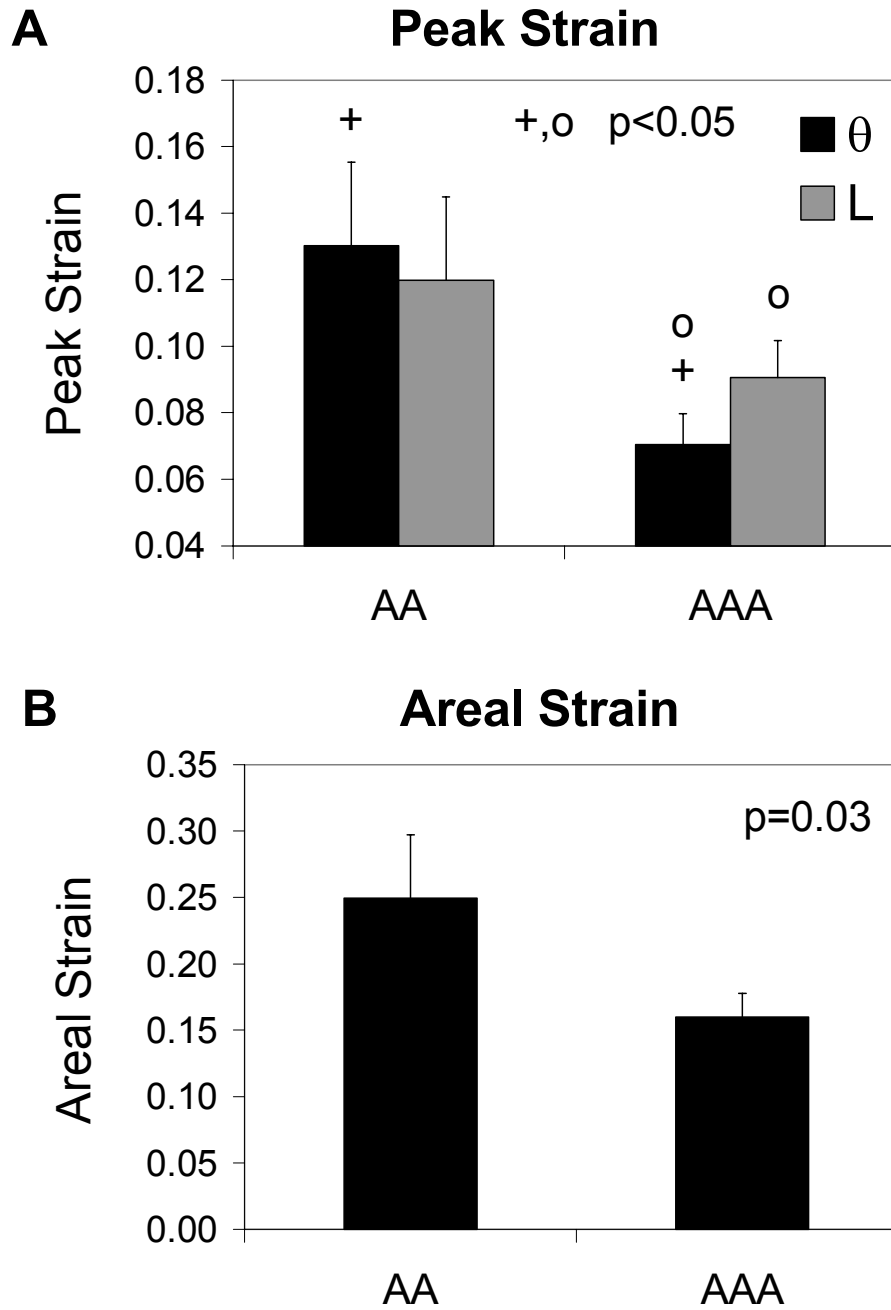


Figure 2-12: Peak strains (A) and areal strain (B) for AAA and AA tissue

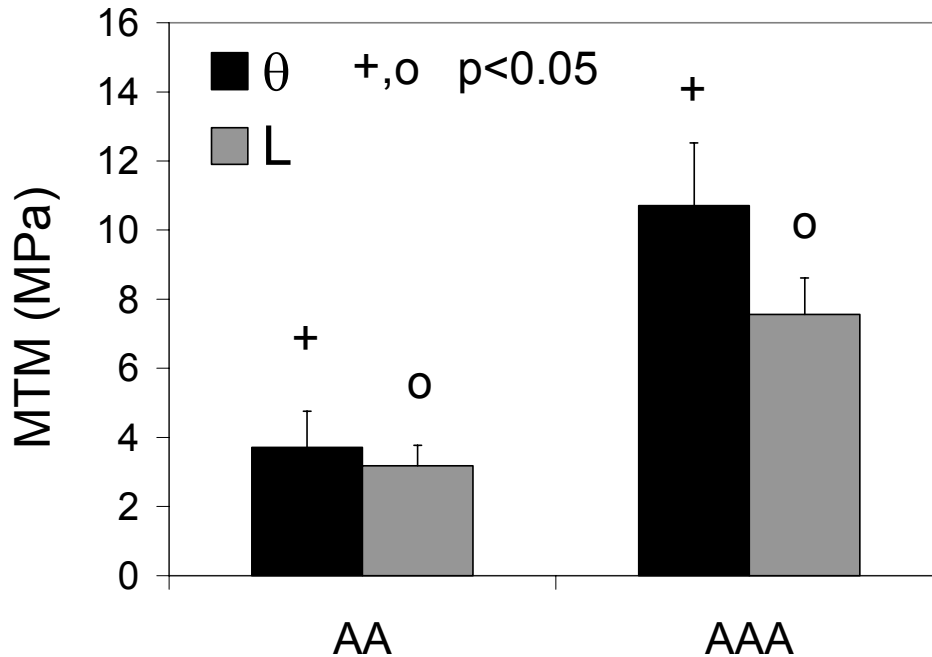


Figure 2-13: AAA and AA maximum tangential modulus for both experimental directions

2.3.3.2 Discussion

The biaxial testing of aneurysmal and non-aneurysmal aortic tissue allows for the investigation of anisotropy as well as the derivation of a more appropriate constitutive model for this tissue. The results herein suggest that aneurysmal degeneration of the human abdominal aorta is associated with a marked alteration in mechanical behavior. For example, AAA tissue is stiffer than AA ([Figures 2-11, 2-13](#)) as well as exhibiting a decrease in its extensibility under the same stress state ([Figure 2-12](#)). The decrease in circumferential peak stretch ([Figure 2-12A](#)), and the larger circumferential MTM in AAA ([Figure 2-13](#)) also suggest the presence of increased anisotropy in AAA as compared to age-matched AA. Although the differences between longitudinal and circumferential MTM within each group were not significant, there is a clear

trend of increased stiffness and decreased extensibility in the circumferential direction for AAA tissue. Since the stress-state imposed on the specimens for the present study lie within the range of stresses experienced by the AAA tissue in-vivo, the increase in anisotropy reported here should be considered physiologically significant.

To date there have been relatively few investigations of the mechanical response of abdominal aortic aneurysm tissue. He and Roach[53] reported the changes in composition of collagen and elastin within AAA and how this effects this tissues uniaxial mechanical response. Their results suggest a stiffening of AAA tissue with respect to nonaneurysmal tissue, similar to the results reported here. For modeling purposes, they applied a simplistic exponential equation to describe the uniaxial stress-strain relationship. While informative for quantifying gross changes in mechanical behavior, this type of equation is difficult to implement into the solution of both geometrically simple and complex boundary value problems. For such a purpose a continuum-based constitutive model must be derived. Such a model for the AAA wall was developed by Raghavan and Vorp in 2000 [38] in which they utilized uniaxial tensile testing results to develop a continuum-based isotropic constitutive relationship, which is easily implemented into commercial finite element codes.

The assumption of isotropy for the AAA wall was made in all of the investigations of AAA mechanical behavior to date. The biaxial tensile testing results reported here provide the appropriate mechanical dataset to investigate the anisotropy of AAA. The only other biaxial tensile testing of aneurysmal tissue in the literature is that given by Okamoto et al. in their study of the biaxial mechanical properties of dilated ascending thoracic aortic tissue[70]. In their study there was no set of control data for the aneurysmal tissue, so that the effects of aneurysmal dilation on the anisotropy of the ascending aorta could not truly be realized. The circumferential

stiffening of the AAA reported here represent the first investigation of this tissue's anisotropy. In addition, this dataset allows the development of an anisotropic constitutive relationship, which in turn may better estimate the stress and strain environment within patient-specific finite element analyses of AAA.

2.3.4 Intraluminal Thrombus

2.3.4.1 Results

Nine separate luminal ILT specimens were harvested from nine different patients (aged 71.0 ± 4.5 yrs) and used in this study. The AAAs were 5.9 ± 0.4 cm in diameter.

General Experimental Findings.

The multiple equibiaxial protocols resulted in repeatable curves for all specimens, suggesting that no structural damage of the tissue occurred as a result of the testing. The peak shear stresses and strains (S_{12} and E_{12}) remained one order of magnitude smaller than S_{11} , S_{22} , E_{11} and E_{22} for all specimens. Representative plots of the second Piola-Kirchhoff stress vs. Green strain displayed a near linear response in both directions for all specimens ([Figure 2-14](#)). ILT specimens fit the response functions well (average $R^2=0.988 \pm 0.003$ and $R^2=0.988 \pm 0.006$ for the circumferential and longitudinal directions, respectively).

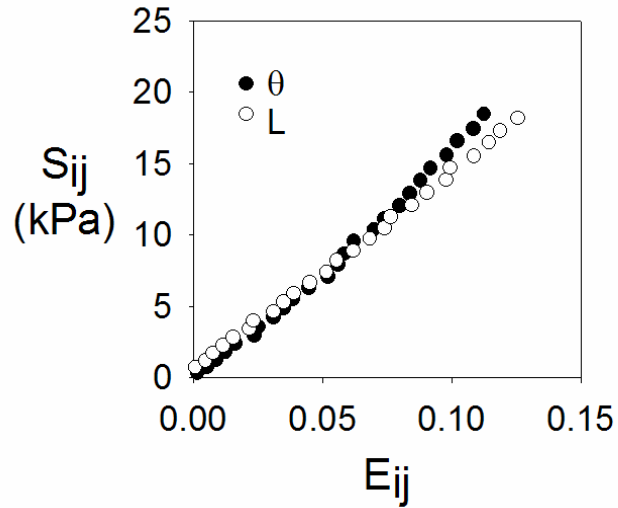


Figure 2-14: Representative stress-strain plot for the luminal layer of ILT

Mechanical Parameters.

The average peak stretches in the equibiaxial protocol for the ILT specimens were 1.18 ± 0.02 and 1.13 ± 0.02 in the circumferential and longitudinal directions, respectively ($p=0.14$; [Table 2-4](#)). The average areal strain for all specimens was 0.34 ± 0.03 . The average MTM for the equibiaxial protocol were $20.1 \pm 1.6 \text{ N/cm}^2$ and $23.1 \pm 2.9 \text{ N/cm}^2$ for the circumferential and longitudinal directions, respectively ($p = 0.37$; [Table 2-4](#)).

Table 2-4: Peak stretch, areal strain, and MTM for the luminal layer of ILT

| ILT MECHANICAL PARAMETERS | | | | | |
|---------------------------|-------------|-------------|-------|------------------|------------------|
| Specimen | λ_0 | λ_L | e_A | MTM ₀ | MTM _L |
| 1 | 1.19 | 1.14 | 0.36 | 16.0 | 20.1 |
| 2 | 1.13 | 1.07 | 0.21 | 25.8 | 32.8 |
| 3 | 1.11 | 1.13 | 0.25 | 26.0 | 23.0 |
| 4 | 1.24 | 1.09 | 0.36 | 16.0 | 21.8 |
| 5 | 1.27 | 1.19 | 0.51 | 15.3 | 15.7 |
| 6 | 1.12 | 1.16 | 0.31 | 19.9 | 14.9 |
| 7 | 1.10 | 1.20 | 0.32 | 26.9 | 18.5 |
| 8 | 1.23 | 1.13 | 0.39 | 17.0 | 19.2 |
| 9 | 1.25 | 1.08 | 0.35 | 18.0 | 42.1 |
| MEAN | 1.18 | 1.13 | 0.34 | 20.1 | 23.1 |
| SEM | 0.02 | 0.02 | 0.03 | 1.6 | 2.9 |

2.3.4.2 Discussion

The biaxial mechanical response of the luminal layer of freshly-harvested ILT from AAA was investigated and displayed a nearly linear response over the entire strain plane and across all biaxial protocols. The peak stretches and MTM values for the equibiaxial protocol in both the circumferential and longitudinal directions did not differ, providing evidence for this materials isotropic mechanical response.

Our results are in agreement with previous data reported by our laboratory [59], in which the uniaxial biomechanical response of the ILT was similar in the longitudinal and circumferential directions. While the MTM reported previously from uniaxial tensile tests

($MTM_0 = 54 \pm 7 \text{ N/cm}^2$ and $MTM_L = 57 \pm 7 \text{ N/cm}^2$) were larger than those reported here ($MTM_0 = 20.1 \pm 1.6 \text{ N/cm}^2$ and $MTM_L = 23.1 \pm 2.9 \text{ N/cm}^2$), both sets of data revealed no significant differences between the two directions, again supporting the idea that the ILT is an isotropic tissue. The differences in magnitude between the MTM values is due to the different testing methods used, and is likely due to two primary effects. First, it may be a result of a lack of a load free condition upon the start of the uniaxial test, as this error is minimized in the biaxial test. This pretension would result in the response being evaluated in a higher stress region of the stress-strain curve, resulting in a stiffer response for a given strain. Secondly, as the uniaxial specimen is deformed, all of the fibers within it are allowed to align themselves in the direction of loading, thus resulting in a stiffer response in this direction for this test. This would not be the case in equibiaxial testing, where the fibers are inhibited from rotating as the specimen is being deformed.

2.3.5 Limitations

Biaxial Testing

All aortic tissue samples were assumed to be pseudoelastic, so that the loading curves could be isolated and analyzed in the current work. The viscoelastic effects (e.g., hysteresis) of the tissue were dampened by using a 9 cycle preconditioning protocol which resulted in repeatable loading curves ([Figure 2-15](#)). In addition, each cycle of preconditioning was repeated immediately after the previous cycle, with each cycle lasting typically around 6 seconds long. The resolution of the CCD camera and image acquisition software used here was $\sim 0.021 \text{ mm/pixel}$.

Changes in Loading Curves Over Cycles

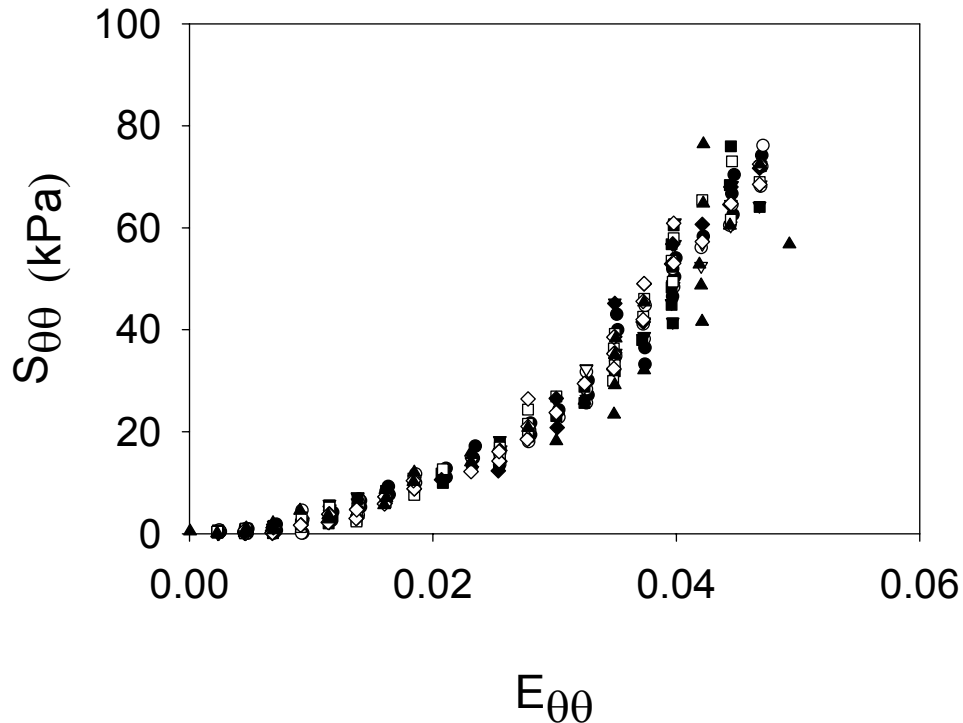


Figure 2-15: Stress versus strain in the circumferential direction for a representative specimen for all preconditioning cycles

Nonaneurysmal Abdominal Aorta

There are several limitations as pertain to the biaxial testing of nonaneurysmal aortic tissue. Those related to the experimental testing protocol itself have been discussed elsewhere [37, 61]. One important assumption that must be noted when analyzing the biaxial data reported here is that the stresses and strains are assumed to remain homogenous within the central region of the specimen (inside the four markers used for strain measurement). For an accurate assessment of this assumption, a large number of markers should be used in order to determine the strain

distribution. In addition, the stresses acting on the biaxial specimen are also assumed to be homogenous within the central region of the specimen, so that any St. Venant-like effects caused by hooking the specimen are minimized.

Although there were no statistically significant differences between the peak stretches of autopsy specimens as compared to organ donor specimens in any age group ($p > 0.2$), there may have been some error introduced when grouping these specimens together. Our results are in contrast to a recent report by Monson et al. which shows a slightly less extensible mechanical response for autopsy cerebral blood vessels as opposed to those retrieved from cadavers [71]. While there may have been bias as to the source of the nonaneurysmal specimens utilized in this study given the clinical history of each of the organ donors and autopsy subjects, this limitation was deemed acceptable given the lack of availability of human tissue.

Descending Thoracic Aorta

The most obvious limitation for the DTA mechanical investigations is the lack of sample size for the Group 1 and Group 3 specimens. This lack of power, however, is offset by the gain in statistical power achieved by utilizing matched DTA and AA samples from the same autopsy cadaver. Another limitation of the DTA specimens was the inconsistency in position from which these specimens were isolated from the subjects. For example, while the AA specimens were confined to a more local region of the aorta (between the renal arteries and the aortic bifurcation), the DTA samples were taken from various distances proximal to the renal arteries. Since it is known that the biomechanical properties of the aorta change as the aortic tree is traversed, this may have induced error in the data and subsequent conclusions. However, since

each subject had *paired* DTA and AA specimens, the general conclusions made here would be expected to hold for more repeatable excision of DTA specimens.

AAA Wall

There were no AA or AAA specimens taken from the same patient, thereby preventing any information to be gleaned on variability of the biaxial response as a function of location within an individual aorta. This may be especially important in AAAs, as preferential bulging of the aorta occurs on the anterior portion of the blood vessel. Another limitation of the current study was the grouping of both sexes into both experimental groups (AA and AAA), which may have resulted in greater variability in the data. This was felt to be acceptable due to the lack of an identifiable difference in any biomechanical endpoint (e.g., peak strains, material parameters) between the two sexes within either group. Although not an aim for the current study, the comparison of the gross fiber architecture between AA and AAA specimens and its effect on the macroscopic mechanical properties of these tissues would also be informative.

Intraluminal Thrombus

One obvious limitation to the biaxial tensile testing of the intra-luminal thrombus is the inability to test the medial and abluminal layers. This inability was likely a result of the decrease in structural organization present in these layers as compared to the luminal region [59]. More appropriate multi-axial testing methods are needed in order to investigate and identify the anisotropic response of these layers of ILT. Another limitation of the current study is that the biaxial testing of planar sheets of the luminal layer of ILT does not completely capture the in-vivo loading conditions, as this material also undergoes radial compression (thinning) over the

cardiac cycle [72]. However, although the full thickness of the ILT in-vivo is large in places (1-3cm) relative to its typical diameter (3-7cm), the thickness of the luminal layer is small in comparison (2.8 ± 0.08 mm, n=9). This suggests that the mechanical loading experienced by the *luminal* layer of ILT in-vivo may be predominantly 2D in nature.

3.0 ANISOTROPIC CONSTITUTIVE MODEL DEVELOPMENT

3.1 INTRODUCTION

The modeling of soft biological tissues has been done for many decades. Typically, these constitutive relations are classified according to the assumptions utilized in their development. For example, many researchers have assumed that biological tissues such as bone act in a linear fashion, assuming these tissues undergo small deformations in-vivo. For tissues undergoing large strains in-vivo, finite deformation theory must be applied in order to derive appropriate models relating stress and strain within a body. Another assumption typically utilized in the constitutive development of soft tissues is that of isotropy. Simply stated, mechanical isotropy assumes the material behaves in the same manner regardless of loading direction. Our laboratory has previously developed a finite deformation isotropic constitutive relation for the AAA wall as well as the ILT [38, 59]. As was displayed Chapter 2, the AAA wall displays an anisotropic mechanical response. The development of an anisotropic constitutive relation for the AAA wall may therefore be important in predicting the stresses acting on AAA in-vivo. Likewise, the derivation of an isotropic constitutive relation for the ILT based on multi-axial tensile testing experiments is also thought to be important in determining the stresses distributed to the wall via the ILT.

3.2 METHODS

3.2.1 Assumptions

3.2.1.1 Homogeneity

Soft tissues in general are primarily composed of water and have negligible permeability [47]. Stergiopoulos et al [73] studied the homogeneity of the medial layer of pig aorta. They concluded that the media has similar mechanical properties through the thickness of the wall as well as a uniform distribution of matrix protein and vascular smooth muscle cells. For this reason they concluded that the aortic media can be considered as an elastic, homogenous medium. The assumption of homogeneity for soft tissues has also been made our laboratory and by several other researchers[38, 41, 42, 48, 49, 59, 66, 70, 74-77]. Based on these previous investigations, the human abdominal aortic media and the intra-luminal thrombus will herein be assumed to act as a homogenous material.

3.2.1.2 Large Deformation

Blood vessels are also known to undergo finite deformations under normal physiologic conditions. For this reason, arterial tissue has been modeled as hyperelastic by many researchers [38, 74, 78-81]. A study by Vorp et al. also investigated the deformability of the ILT and revealed that it undergoes in-vivo deformations of approximately 8% over the cardiac cycle[72]. This suggests that a linear elastic constitutive relation for ILT may be inappropriate and may introduce large errors. A hyperelastic relation would therefore better suit the large deformations

observed by both the aortic media and ILT in-vivo. For these reasons, these tissues will be assumed to undergo large deformations and therefore will require the development of finite strain constitutive relations.

3.2.1.3 Incompressibility

Chuong and Fung studied the incompressibility of the arterial wall and determined that it acts as a nearly incompressible material in the range of stresses experienced in vivo [78]. Girerd et al. more recently studied the incompressibility assumption with the utilization of an ultrasound echo-tracking device. Their investigation studied the change in cross-sectional area of both the human internal mammary artery and radial artery and found there to be minimal changes in the cross-sectional area for various levels of strain. Since the artery length remained constant during their pressure increases, the lack of change in the cross-sectional area of the arterial wall suggests that the arterial wall of human arteries is essentially incompressible[82]. A similar study was performed by Vorp et al. in which ultrasound techniques were used to investigate the changes in cross-sectional area of ILT over the cardiac cycle. Similar results were reported in that there was found to be little change in area throughout the cardiac cycle for the ILT[72]. In addition, the ILT has also been previously modeled as an incompressible material by our laboratory[59]. Based on all of the afore-mentioned previous investigations, the aortic wall and intra-luminal thrombus tissue presented here will be modeled as an incompressible, homogenous, hyperelastic material undergoing finite deformations.

3.2.2 Assessment of Anisotropy

Simply stated, an anisotropic material is any material whose mechanical response is dependent on the direction of loading. For the purpose of constitutive model development, it is important to consider whether the assumption of isotropy creates significant errors in the prediction of stresses and strains within a soft tissue. In reality, most all soft tissues display some degree of anisotropy, due to the presence of a preferred direction of the collagen fiber network. The mechanical structure and function of a tissue will determine in great part whether its mechanical response is anisotropic. Planar biaxial testing provides a means for testing the degree of anisotropy present within a tissue as detailed below.

3.2.2.1 Peak Stretch

The biaxial protocols listed in [Figure 2-3](#) represent a wide range of stress and strain configurations within the biaxial specimen. The biaxial device utilized in the current study is able to control specimen deformation either with strain or load control. The tension (load) controlled protocol chosen herein suggests that the anisotropy of the specimens can be quantified by investigating the changes in peak strain for the equibiaxial ($T_{\theta\theta}:T_{LL}=1:1$) protocol. That is, for a given amount of equivalent loading in each orthogonal direction, the amount of anisotropy can be quantified by comparing the peak stretch values (or strains) throughout the equibiaxial protocol. Since the peak value of loading is assumed to be in a physiological range, the values of the stretches at this loading in the circumferential and longitudinal directions will be recorded and compared for each tissue.

3.2.2.2 Maximum Tangential Modulus

For similar reasons as stated above for the peak stretch values, the amount of anisotropy can also be quantified by the MTM in both of the orthogonal testing directions. Again, since the peak tension for the equibiaxial protocol was estimated to be in the physiological range of stresses and strains, any directional differences in MTM for a given tissue should be considered physiologically significant. For these reasons, the anisotropy of all biaxial specimens was also assessed by calculating and comparing the maximum tangential modulus (MTM) in both the circumferential and longitudinal directions.

3.2.2.3 Response Functions

Rather than speculate a-priori a potential form for the strain energy function W , the following method was employed to probe the pseudo-elastic response of arterial tissue in a protocol-independent manner. Details of this approach have been previously published [83]. Briefly, the **S-E** data for each axial component were *independently* fit to the following response functions

$$\begin{aligned} S_{\theta\theta} &= c_o \left(c_1 E_{\theta\theta} + c_3 E_{LL} + c_4 E_{\theta\theta} E_{LL} + \frac{1}{2} c_5 E_{LL}^2 + c_6 E_{\theta\theta} E_{LL}^2 + 2c_7 E_{\theta\theta}^3 \right) e^Q \\ S_{LL} &= c_o \left(c_2 E_{LL} + c_3 E_{\theta\theta} + \frac{1}{2} c_4 E_{\theta\theta}^2 + c_5 E_{LL} E_{\theta\theta} + c_6 E_{\theta\theta}^2 E_{LL} + 2c_8 E_{LL}^3 \right) e^Q \end{aligned} \quad (3.1)$$

where

$$Q = \left(c_1 E_{\theta\theta}^2 + c_2 E_{LL}^2 + 2c_3 E_{\theta\theta} E_{LL} + c_4 E_{\theta\theta}^2 E_{LL} + c_5 E_{LL}^2 E_{\theta\theta} + c_6 E_{\theta\theta}^2 E_{LL}^2 + c_7 E_{\theta\theta}^4 + c_8 E_{LL}^4 \right)$$

and c_i are constants. Note that equations (3.1) were not used as a constitutive model, but rather as a set of response functions that allow the interpolation of each stress component within the experimental strain range for $E_{\theta\theta}$ and E_{LL} . These response functions were *independently* fit to all

stress-strain data using the nonlinear regression software package SigmaStat (v. 2.03, SPSS, Chicago, IL) using a Marquart-Levenburg least-squares algorithm. The resulting response surfaces were used to guide the choice of W by plotting contours of constant stress for both $S_{\theta\theta}$ and S_{LL} . For a perfectly isotropic material such contours would display symmetry about the $y = x$ axis, while the degree of asymmetry would indicate the presence and amount of mechanical anisotropy present in the tissue (see [Figure 3-1](#)).

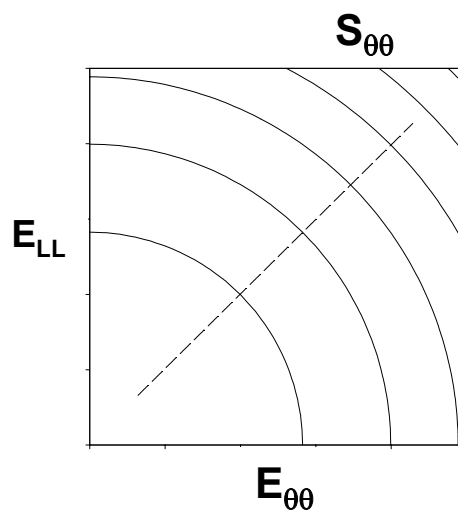


Figure 3-1: Circumferential stress contour plot for an idealized perfectly isotropic material

3.2.3 Population-wide Constitutive Modeling

The primary driving force for determining constitutive models for the current investigation is the implementation of such models into patient-specific finite element simulations of AAA. In particular, it is mandatory that constitutive models be developed that describe the averaged “population-wide” mechanical response, since these models are to be utilized in a noninvasive

manner for the prediction of and individual patient’s AAA wall stress. The manner in which an “averaged” constitutive relation will be derived for a given tissue will be based primarily on the form of the strain energy used to describe its mechanical response. For constitutive models which have material parameters that do not have any nonlinear interactions with each other, the “population-wide” set of parameters will be taken as the mean of each specimen’s individually-fitted material parameters. In the event that a model is developed which does contain material parameters which nonlinearly interact with one another, the following method to derive a “population-wide” set of material parameters will be utilized.

To determine the averaged response for a given arterial tissue, the individual tension vs. strain data for each component from each protocol were fit to the following equation

$$\mathbf{T} = a e^{b(\mathbf{E})} \quad (3.2)$$

where \mathbf{T} is the tension in N/m, \mathbf{E} is the Green strain, and a and b are parameters describing the tension-strain relationship for an individual biaxial testing protocol. The above equation was chosen to represent each individual protocol due to their exponential shape. This equation also allows the Green strains for a given protocol to be extrapolated for prescribed increments of tension spanning the entire tension range for each protocol (e.g., 0-120 N/m for the AAA wall). A custom-written Matlab (v6.0 R12) code (see Appendix A) was used to fit (3.2) to each set of T-E data, and extrapolate and average Green strain values for prescribed tension intervals of 2 N/m for each individual tension-protocol. Note that the response functions (3.1) could not be used to identify the averaged dataset since the specimens were tested under a tension (not a stress) controlled protocol from 0 to 120 N/m. The averaged tension values for each of the biaxial protocols were then converted to first-Piola Kirchhoff (\mathbf{P}) stress using the following equation

$$\mathbf{P} = \frac{\mathbf{T}}{n} \sum_{i=1}^n \frac{1}{t_i} \quad (3.3)$$

where \mathbf{T} is the averaged tension, n is the number of specimens in a given group, and t_i is the thickness for each individual specimen. The first-Piola Kirchhoff stresses calculated here were then converted to second-Piola Kirchhoff stresses ($\mathbf{S} = \mathbf{P} \cdot \mathbf{F}^{-T}$) for all five protocols and were used in the derivation of a single constitutive model for each tissue type. The material parameters from the nonlinear regression of the averaged datasets to the constitutive model were then taken to represent the average mechanical response of each tissue type. In order to provide information on both the spread of the averaged data as well as the material parameters, the upper and lower 95% confidence interval of \mathbf{E} at each level of tension and for each protocol was also calculated, providing upper and lower 95% confidence interval datasets from which material parameters were also derived by nonlinear regression to the constitutive model.

3.3 RESULTS AND DISCUSSION

3.3.1 Nonaneurysmal Abdominal Aorta

3.3.1.1 Results

Interpretation and Choice of W

All biaxial data fit the response functions (3.1) well with the smallest $R^2=0.92$ (range 0.92-0.96). Stress contour plots were constructed from the response functions for each specimen and used to graphically investigate the mechanical response. For a perfectly isotropic material, the stress

contours are symmetric about the $E_{11} = E_{22}$ axis. As shown in [Figure 3-2](#), the stress contours for Group 1 maintain a significant amount of symmetry, which suggests the use of an isotropic strain energy function for this group. The use of an isotropic W for Group 1 is further supported by our finding that the peak stretches in the longitudinal and circumferential directions for the equibiaxial protocol for this group did not significantly differ ([Figure 2-6](#)).

Although there were no significant differences in the equibiaxial longitudinal and circumferential peak stretches for Groups 2 and 3, the response functions for these groups consistently displayed an asymmetric response about the $E_{11} = E_{22}$ axis, suggesting a mechanically anisotropic response. Moreover, constant stress contours indicated a dramatic increase in stiffness with strain, compared with Group 1 ([Figure 3-2](#)). Thus, the response functions for Groups 2 and 3 suggested the use of a general anisotropic Fung-type strain energy function. Since the shear stresses and strains were negligible, the response of Groups 2 and 3 was adequately captured by:

$$\rho_0 W = \frac{c}{2} \left[\exp(A_1 E_{\theta\theta}^2 + A_2 E_{LL}^2 + 2A_3 E_{\theta\theta} E_{LL}) - 1 \right] \quad (3.4)$$

In preliminary studies, we noted that the biaxial data for Group 1 were not adequately fit to (3.4), as this function is unable to account for sigmoidal stress-strain data for this group. Based on the results in [Figures 2-5, 2-6, 3-2, and 3-3](#), we used a strain energy function of the form [84]

$$W = \sum_{i=0}^{\infty} \sum_{j=0}^{\infty} D_{ij} (I_1 - 3)^i (I_2 - 3)^j \quad (3.5)$$

where the D_{ij} are material constants and I_1 and I_2 are the first and second strain invariants of the left Cauchy strain tensor \mathbf{B} :

$$I_1 = \text{tr}\mathbf{B} \quad I_2 = \frac{1}{2} \left[(\text{tr}\mathbf{B})^2 - \text{tr}\mathbf{B}^2 \right] \quad (3.6)$$

The consecutive addition of terms in the infinite sum of (3.5) allows it to describe increasingly complex stress-strain behavior, including the sigmoidal response typical of rubber-like materials. Equation (3.5) was developed by Rivlin and Saunders [22], who utilized constant I_1 biaxial tests to determine the dependence of $\partial W/\partial I_1$ on each I_1 , from which the appropriate functional form of W was found. Since the current biaxial protocols were tension-driven, Rivlin's exact approach could not be duplicated. Instead, the following equations derived by Rivlin et al. were used to investigate the dependence of $\partial W/\partial I_1$ on I_1 .

$$\frac{\partial W}{\partial I_1} = \frac{\frac{\lambda_\theta^2 t_{\theta\theta}}{\lambda_\theta^2 - 1/\lambda_\theta^2 \lambda_L^2} - \frac{\lambda_L^2 t_{LL}}{\lambda_L^2 - 1/\lambda_\theta^2 \lambda_L^2}}{2(\lambda_\theta^2 - \lambda_L^2)}$$

$$\frac{\partial W}{\partial I_2} = \frac{\frac{t_{\theta\theta}}{\lambda_\theta^2 - 1/\lambda_\theta^2 \lambda_L^2} - \frac{t_{LL}}{\lambda_L^2 - 1/\lambda_\theta^2 \lambda_L^2}}{2(\lambda_L^2 - \lambda_\theta^2)} \quad (3.7)$$

This dependence can then be utilized in a manner similar to Rivlin and lead to the appropriate functional form of W .

Due to the sigmoidal nature of their response functions, the biaxial data for the Group 1 specimens were fit to the Rivlin-type strain energy function (3.5). In order to determine if this strain energy function requires the inclusion of both I_1 and I_2 , the relationship between the two invariants was inspected for each specimen (Figure 3-3). The observed linear dependence of I_1 and I_2 suggests that the inclusion of only one strain invariant is necessary. To determine what terms are necessary for W in equation 3.5, the relationship between $\partial W/\partial I_1$ and I_1 was investigated for each specimen (Figure 3-3). The observed relationship suggests that a quadratic expression for $\partial W/\partial I_1$ is sufficient for the characterization of this material, resulting in three

parameters in the expression for W given by (3.5). The final model that was fit to the biaxial data for Group 1 was then

$$\begin{aligned}
 W &= D_1(I_1 - 3) + D_2(I_1 - 3)^2 + D_3(I_1 - 3)^3 \\
 t_{\theta\theta} &= 2 \left(\lambda_\theta^2 - \frac{1}{\lambda_\theta^2 \lambda_2^2} \right) \left(\frac{\partial W}{\partial I_1} \right) \\
 t_{zz} &= 2 \left(\lambda_z^2 - \frac{1}{\lambda_\theta^2 \lambda_2^2} \right) \left(\frac{\partial W}{\partial I_1} \right)
 \end{aligned} \tag{3.8}$$

where D_1 , D_2 , and D_3 are material parameters.

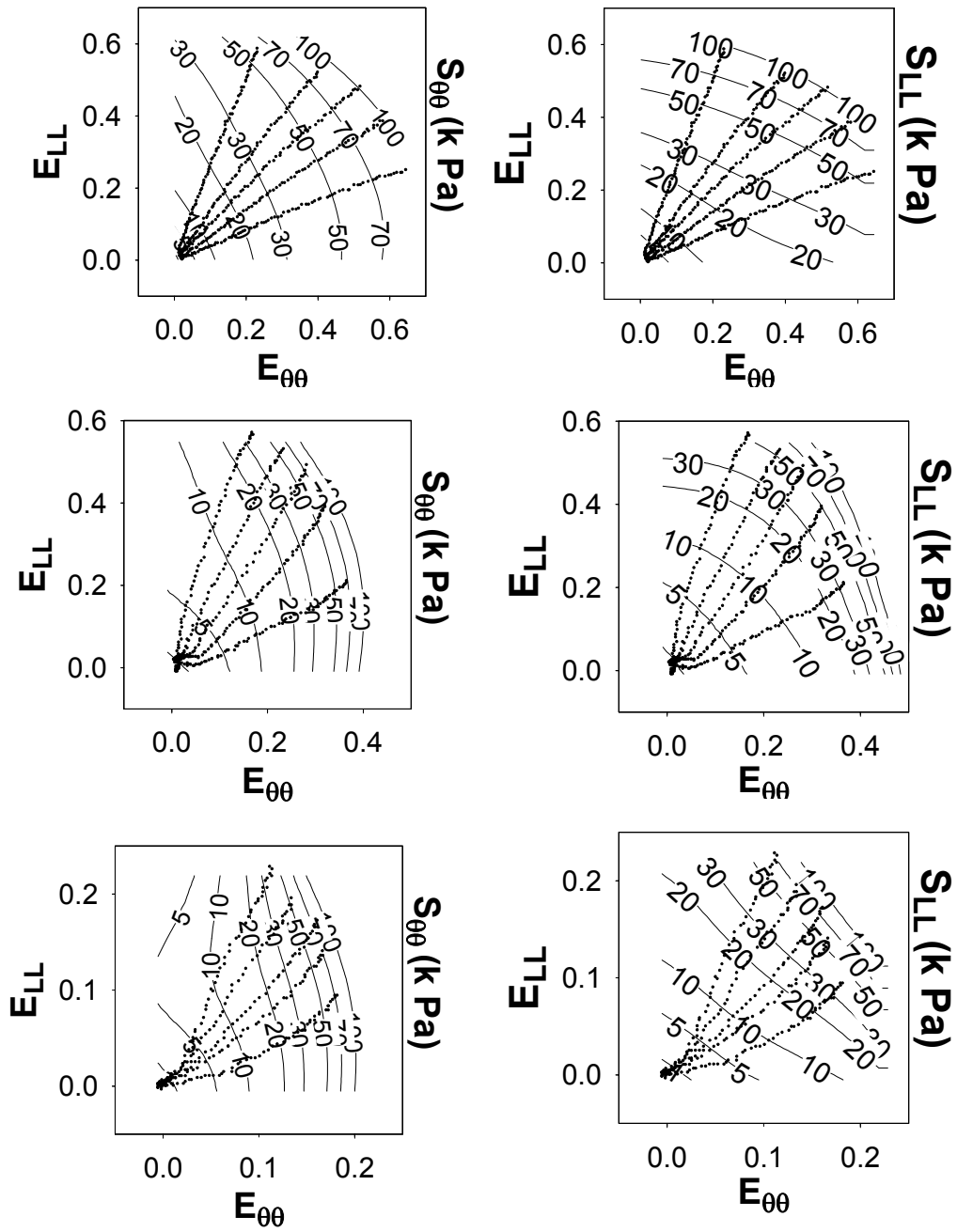


Figure 3-2: Circumferential and longitudinal stress contours for each age group

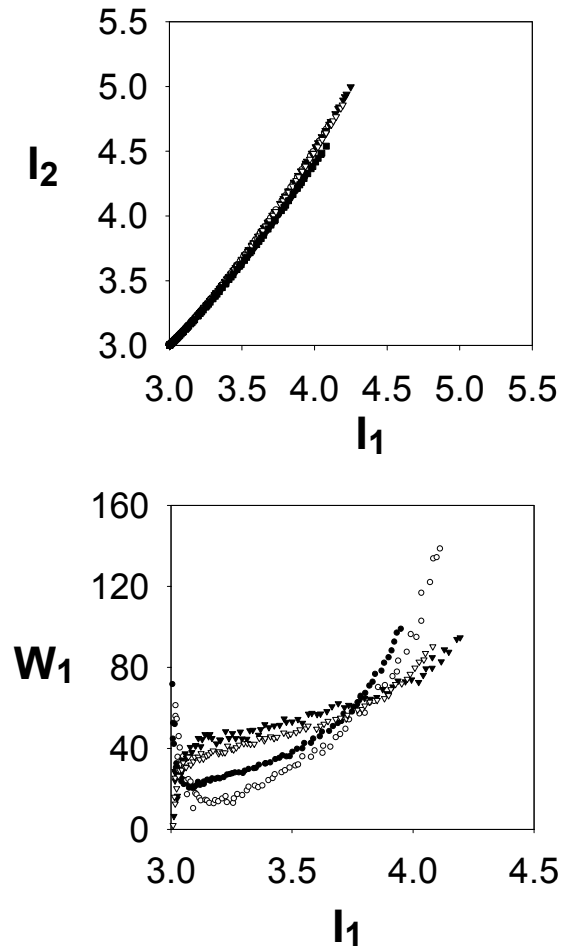


Figure 3-3: l_1 versus l_2 and $\partial W/\partial l_1$ versus l_1 for a representative AA specimen

Constitutive Modeling Results

The data for Group 1 fit equation (3.8) very well, with an average R^2 of 0.97 ± 0.01 . The best-fit model parameters are indicated in [Table 3-1](#). The data for Groups 2 and 3 fit equation (3.4) adequately with average R^2 values of 0.82 ± 0.10 and 0.90 ± 0.03 , respectively. The exception was one Group 2 specimen (specimen 10) which was from a 47 year old organ donor aorta that appeared (ie., minimal calcifications) and behaved as a Group 1 aorta. The best-fit model parameters for Groups 2 and 3 are indicated in [Tables 3-2](#) and [3-3](#), respectively. The experimental biaxial data as well as model fits using the best-fit material constants are shown for

representative specimens from Groups 1, 2 and 3 in [Figure 3-4](#). Note also in this figure the outer two biaxial protocols (not used in regression) are plotted along with their model fits and can be used to investigate the each models predictive capability. In general, all of the constitutive models were able to predict the stresses of aortic tissue for the strains typically experienced in vivo.

Table 3-1: Constitutive model parameters for the Group 1 specimens. OD=organ donor; MOSF=multisystem organ failure; HT TX REJ=heart transplant rejection.

| RIVLIN MODEL (3.8) – GROUP 1 | | | | | | |
|------------------------------|----------------------|----------------------|----------------------|----------------|-----|-----------|
| Specimen | D ₁ (kPa) | D ₂ (kPa) | D ₃ (kPa) | R ² | AGE | SOURCE |
| 1 | 9.95 | 1.55 | 0.82 | 0.99 | 19 | OD |
| 2 | 12.96 | 1.14 | 5.91 | 0.97 | 22 | OD |
| 3 | 7.87 | 2.17 | 1.86 | 0.97 | 23 | OD |
| 4 | 11.09 | 1.86 | 1.34 | 0.98 | 25 | MOSF/SCA |
| 5 | 17.12 | 1.00 | 0.42 | 0.98 | 26 | HT TX REJ |

Table 3-2: Constitutive model parameters for the Group 2 specimens. CREP MEN=creptycoccal meningitis; SEP=sepsis. X indicates the regression did not converge.

| FUNG MODEL (3.4) – GROUP 2 | | | | | | | | |
|----------------------------|--------|----------------|----------------|----------------|-------------------------------|----------------|-----|-----------|
| Specimen | c(kPa) | A ₁ | A ₂ | A ₃ | $\frac{(A_1+A_3)}{(A_2+A_3)}$ | R ² | AGE | SOURCE |
| 6 | 4.97 | 8.92 | 14.54 | 2.89 | 0.68 | 0.93 | 35 | OD |
| 7 | 0.75 | 26.89 | 20.39 | 2.93 | 1.28 | 0.93 | 39 | CREP MEN |
| 8 | 1.58 | 30.45 | 19.11 | 3.14 | 1.51 | 0.94 | 47 | SEP |
| 9 | 6.53 | 12.94 | 11.75 | 3.75 | 1.08 | 0.98 | 47 | OD |
| 10 | X | X | X | X | X | X | 47 | OD |
| 11 | 0.42 | 628.29 | 168.81 | 89.13 | 2.8 | 0.66 | 50 | HT TX REJ |
| 12 | 2.29 | 57.43 | 34.31 | 14.26 | 1.48 | 0.99 | 50 | OD |

Table 3-3: Constitutive model parameters for the Group 3 specimens. MI=myocardial infarction; CEREB AN=cerebral aneurysm; MET CARC=Metastatic uterine carcinoma

| FUNG MODEL (3.4) – GROUP 3 | | | | | | | | |
|----------------------------|--------|----------------|----------------|----------------|-------------------------------|----------------|-----|----------|
| Specimen | c(kPa) | A ₁ | A ₂ | A ₃ | $\frac{(A_1+A_3)}{(A_2+A_3)}$ | R ² | AGE | SOURCE |
| 13 | 0.46 | 58.24 | 66.30 | 5.00 | 0.89 | 0.99 | 61 | SEP |
| 14 | 4.3 | 12.21 | 16.23 | 4.10 | 0.80 | 0.96 | 66 | MOSF |
| 15 | 0.88 | 221.58 | 197.45 | 7.81 | 1.12 | 0.97 | 69 | MI |
| 16 | 0.47 | 148.48 | 101.68 | 21.06 | 1.38 | 0.82 | 71 | MOSF |
| 17 | 0.39 | 124.97 | 90.51 | 14.14 | 1.33 | 0.84 | 75 | CEREB AN |
| 18 | 4.59 | 132.10 | 111.90 | 26.20 | 1.15 | 0.96 | 75 | MET CARC |

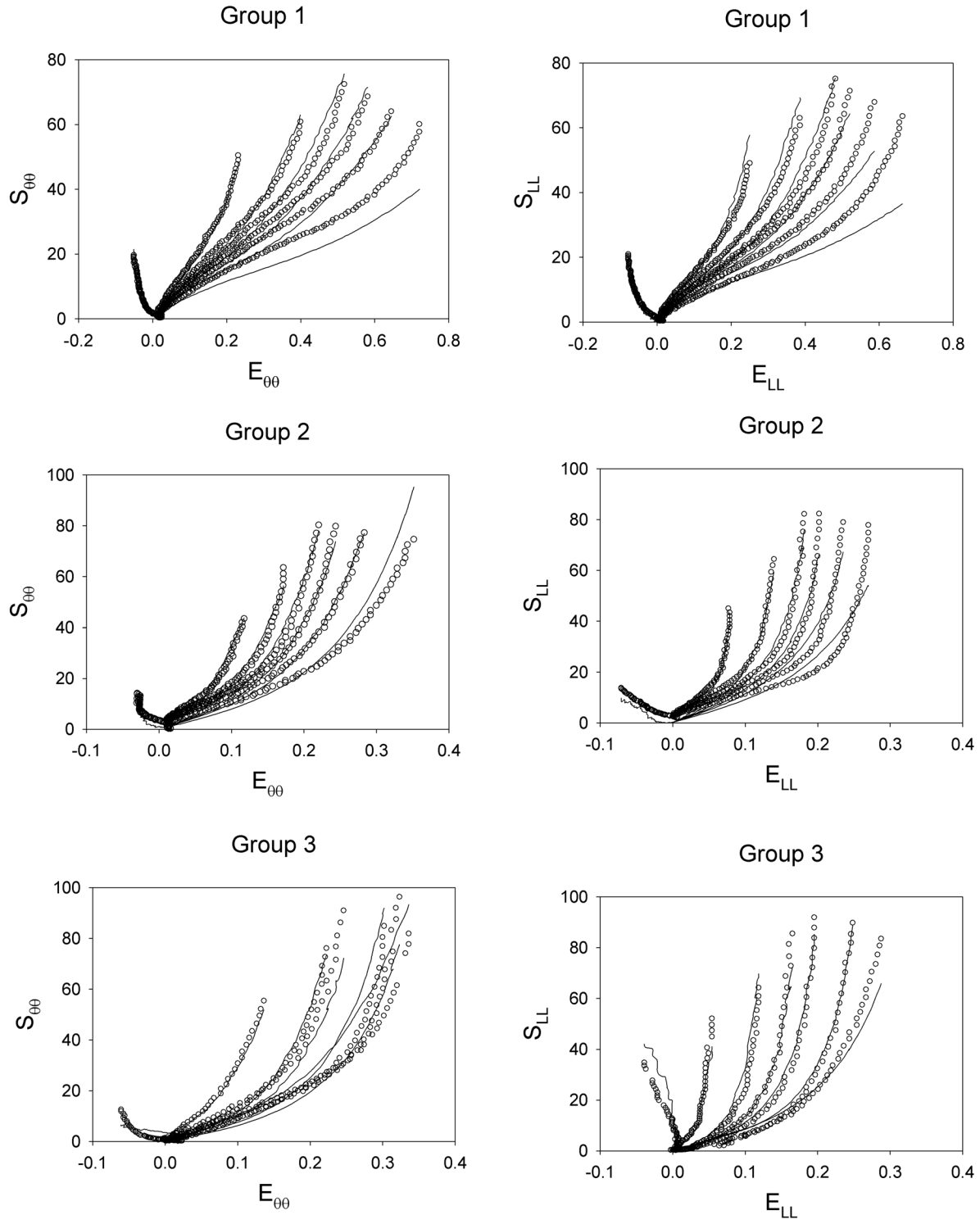


Figure 3-4: Experimental data and model fits for representative Group 1-3 specimens

3.3.1.2 Discussion

The pseudoelastic response of human abdominal aorta was modeled as a homogenous incompressible hyperelastic material using two different strain energy functions. Based on the experimental response of this tissue, the specimens younger than age 30 were modeled using a Rivlin-type polynomial strain energy function, while all of the older specimens were modeled using the exponential Fung-elastic form of W . The use of the Fung model for the specimens in Groups 2 and 3 was chosen based on the anisotropic, exponential form of their response functions. When the Fung model was fit to the specimens in Group 1, it was unable to capture the sigmoidal or biconcavity nature of the response of this tissue. As a result, all specimens in Group 1 failed to converge when fit to the Fung strain energy function. Likewise, the data for the specimens in Groups 2 and 3 fit the Rivlin form of W poorly. Therefore, our data suggests a shift in the mechanical response of human abdominal aortic tissue past the age of 30.

Zhou et al. [44] reported the biaxial anisotropy of canine aortic tissue as measured by the differences in material parameters A_1 and A_2 in an equation similar to (3.4). In particular, they noted that the longitudinal stress-strain curve became nonlinear at smaller strains and had a steeper nonlinear region than did the circumferential curves. This resulted in a value for A_2 that was consistently twice as large as that for A_1 . This was in contrast to our data, which showed values for A_1 larger than those for A_2 in all but three specimens. These differences may be due to the fact that Zhou et al. used a segment of thoracic aorta from mongrel dogs, as opposed to the human infrarenal aortic tissue used here. Yin et al. [85] investigated the age-associated changes in viscoelastic behavior of canine aorta both in the activated and inactivated state. Although they did not find a large dependence of the stiffness on frequency, they did find a marked increase in stiffness with age for both the ascending and descending canine thoracic aorta in both the

activated and inactivated states. These results are consistent with our results in which there was a large increase in stiffness in abdominal aorta after a given age.

The degree of anisotropy of human ascending thoracic aorta reported by Okamoto et al. [52] was measured using a dimensionless ratio of material parameters from (3.4):

$$t_{\theta\theta}/t_{LL} = (A_1 + A_3)/(A_2 + A_3) \quad (3.9)$$

where $t_{\theta\theta}$ and t_{LL} are the Cauchy stresses in the circumferential and longitudinal directions, respectively. They found that this ratio did not consistently suggest a preferred direction for this tissue as the value for this ratio ranged from 0.64 to 2.00. The same analysis using the results of Groups 2 and 3 resulted in an average value for this parameter of 1.42 ± 0.3 (range 0.68 to 2.8) and 1.11 ± 0.1 (range 0.80 to 1.38), respectively. The parameter values for all specimens are listed in [Tables 3-1](#), [3-2](#), and [3-3](#). Consistent with the results reported by Okamoto et al., the value of this parameter for human abdominal aorta did not suggest a universal preferred material direction, but the fact that this ratio was greater than one for a majority of our specimens gave evidence for a stiffer biomechanical response in the circumferential direction as compared to the longitudinal direction. This anisotropic behavior can better be illustrated by noting the non-symmetry of the circumferential contour plots of Groups 2 and 3 in [Figure 3-2](#).

3.3.2 Descending Thoracic Aorta

As seen from [Tables 3-4](#) and [3-5](#), equation (3.4) fit the older DTA data and the Groups 2 and 3 AA data well with all $R^2 > 0.95$. The above model did not converge when fitting the Groups 1 and 2 DTA or the Group 1 AA. This was primarily due to the nearly linear and sometimes sigmoidal response of these specimens, leading to erroneously high and or low values of the material parameter c . This result suggests that the DTA becomes increasingly nonlinear after

middle age, while the AA becomes nonlinear at a much younger age. This trend is again similar to that found for the changes in MTM for DTA and AA as a function of age.

Table 3-4: Constitutive model parameters for nonaneurysmal aorta fit to equation (3.4)

| Abdominal Aorta | | | | | |
|------------------------|------------|----------|-----------|-----------|-----------|
| Specimen | Age | c | A1 | A2 | A3 |
| 1 | 25 | | | DNC | |
| 2 | 26 | | | DNC | |
| 3 | 32 | 4.874 | 12.015 | 6.461 | 1.182 |
| 4 | 39 | 0.752 | 26.893 | 20.388 | 2.929 |
| 5 | 44 | 42.719 | 4.499 | 4.359 | 2.108 |
| 6 | 47 | 1.583 | 30.448 | 19.107 | 3.138 |
| 7 | 66 | 3.47 | 13.01 | 19.189 | 3.972 |

Table 3-5: Constitutive model parameters for nonaneurysmal descending thoracic aorta fit to equation (3.4)

| Descending Thoracic Aorta | | | | | |
|----------------------------------|------------|----------|-----------|-----------|-----------|
| Specimen | Age | c | A1 | A2 | A3 |
| 1 | 25 | | | DNC | |
| 2 | 26 | | | DNC | |
| 3 | 32 | | | DNC | |
| 4 | 39 | | | DNC | |
| 5 | 44 | | | DNC | |
| 6 | 47 | 0.573 | 10.956 | 27.526 | 3.576 |
| 7 | 66 | 13.48 | 8.585 | 14.702 | 1.23 |

3.3.3 Abdominal Aortic Aneurysmal Wall

3.3.3.1 Results

AA and AAA specimens fit the response functions well, with average R^2 values of 0.94 ± 0.02 and 0.87 ± 0.03 , respectively. Typical AA and AAA response function plots display a significant amount of anisotropy, with preferential stiffening in the circumferential direction for the AAA tissue as compared to age-matched AA tissue ([Figure 3-5](#)). [Figures 3-5](#), [3-6](#), and [3-7](#) also display the exponential mechanical response that was present in all AA and AAA specimens. Moreover, the contour plots revealed a significant degree of asymmetry, which clearly indicates the presence of mechanical anisotropy. We also observed negligible shear stresses in our experimental data. These results suggested the use of an anisotropic strain energy function. While a four parameter Fung elastic model was initially utilized, it was found unable to fit the experimental data with physically realistic parameter values (see Discussion).

Based on the above considerations, we assumed AA and AAA tissue could be modeled using the following strain energy function developed by Choi and Vito [86] for canine pericardium and used for native and chemically modified bovine pericardium [77]

$$W = b_0 \left(e^{\frac{1}{2}b_1 E_{\theta\theta}^2} + e^{\frac{1}{2}b_2 E_{LL}^2} + e^{b_3 E_{\theta\theta} E_{LL}} - 3 \right) \quad (3.10)$$

One advantage of equation (3.10) is the explicit separation of contributions from each Green-strain tensor component, reducing the degree of parameter covariance. In order to derive physically reasonable bounds for the constitutive parameters in (3.10), the following analytical biaxial analyses were performed [76]. First, consider a biaxial specimen being stretched in the circumferential direction ($\lambda_\theta > 1$) while being held to the same stretch in the longitudinal direction ($\lambda_L = 1$). We must apply a positive stress in the θ direction ($S_{\theta\theta} > 0$) in order to achieve the desired

stretch, while also applying a positive stress in the L direction ($S_{LL}>0$) to keep $\lambda_L=1$. Similarly, if we apply a positive stretch in the L direction ($\lambda_L>1$) while maintaining the circumferential stretch ($\lambda_\theta=1$), we require both $S_{LL}>0$ and $S_{\theta\theta}>0$, respectively. The second Piola Kirchhoff stresses derived from (3.10) are

$$S_{\theta\theta} = b_0 \left(b_1 E_{\theta\theta} e^{\frac{1}{2} b_1 E_{\theta\theta}^2} + b_3 E_{LL} e^{b_3 E_{\theta\theta} E_{LL}} \right) \quad (3.11)$$

and

$$S_{LL} = b_0 \left(b_2 E_{LL} e^{\frac{1}{2} b_2 E_{LL}^2} + b_3 E_{\theta\theta} e^{b_3 E_{\theta\theta} E_{LL}} \right). \quad (3.12)$$

Noting that $b_0>0$ for all deformations, cases 1 and 2 require, respectively,

$$\begin{aligned} b_1 E_{\theta\theta} > 0, & \quad b_3 E_{\theta\theta} > 0 & \quad \forall & \quad \lambda_\theta > 1, \quad \lambda_L = 1, \\ b_3 E_{LL} > 0, & \quad b_2 E_{LL} > 0 & \quad \forall & \quad \lambda_L > 1, \quad \lambda_\theta = 1. \end{aligned} \quad (3.13)$$

Therefore, $b_1 > 0$, $b_2 > 0$, and $b_3 > 0$ must remain positive in order for these parameters to remain physically reasonable.

When applying these constraints, equation (3.10) fit all of the individual specimens well with an average R^2 of $0.95 \pm .02$ and $0.90 \pm .02$ (mean \pm SEM) for the AA (Table 3-6) and AAA (Table 3-7) groups, respectively. Average stress vs. strain plots for the AA and AAA display the increase in stiffness and decrease in extensibility of the biaxial response of AAA tissue as compared to AA tissue (Figure 3-6). The material parameters for the constitutive model (3.10) fit to the averaged dataset and the \pm 95% C.I. datasets are given in Table 3-8.

Table 3-6: Constitutive model parameters for the nonaneurysmal abdominal aorta

| Abdominal Aorta | | | | | | | | |
|-----------------|-------------|-------|-------|-------|------------------------|-----------------------------------|-----------------|-------|
| Specimen | b_0 (kPa) | b_1 | b_2 | b_3 | $\text{sqrt}(b_1/b_2)$ | $E_{LL,max}/E_{\theta\theta,max}$ | W_{120} (kPa) | R^2 |
| 1 | 0.13 | 391.6 | 302.6 | 309.8 | 1.14 | 1.00 | 1.3 | 0.90 |
| 2 | 0.09 | 370.4 | 269.3 | 276.2 | 1.17 | 0.71 | 2.9 | 0.86 |
| 3 | 0.20 | 194.7 | 361.4 | 206.3 | 0.73 | 0.85 | 4.1 | 0.99 |
| 4 | 0.39 | 70.4 | 53.2 | 40.4 | 1.15 | 1.15 | 8.6 | 0.99 |
| 5 | 0.18 | 698.5 | 607.2 | 498.3 | 1.07 | 1.00 | 2.4 | 0.97 |
| 6 | 0.87 | 522.1 | 410.8 | 332.0 | 1.13 | 1.21 | 5.7 | 0.96 |
| 7 | 0.88 | 39.1 | 53.6 | 45.2 | 0.85 | 0.55 | 10.6 | 0.96 |
| 8 | 0.11 | 166.9 | 185.8 | 150.1 | 0.95 | 1.26 | 3.3 | 0.99 |
| MEAN | 0.36 | 306.7 | 280.5 | 232.3 | 1.02 | 0.96 | 4.87 | 0.95 |
| SEM | 0.12 | 81.4 | 65.9 | 54.7 | 0.06 | 0.09 | 1.14 | 0.02 |

Table 3-7. Constitutive model parameters for the AAA wall specimens

| Abdominal Aortic Aneurysm | | | | | | | | |
|---------------------------|-------------|--------|--------|--------|------------------------|-----------------------------------|-----------------|-------|
| Specimen | b_0 (kPa) | b_1 | b_2 | b_3 | $\text{sqrt}(b_1/b_2)$ | $E_{LL,max}/E_{\theta\theta,max}$ | W_{120} (kPa) | R^2 |
| 1 | 0.01 | 4791.3 | 5756.4 | 3624.0 | 0.9 | 3.70 | 3.4 | 0.87 |
| 2 | 0.08 | 313.2 | 356.4 | 256.3 | 0.9 | 1.74 | 3.6 | 0.92 |
| 3 | 0.49 | 488.9 | 305.0 | 113.2 | 1.3 | 1.71 | 4.1 | 0.93 |
| 4 | 0.37 | 222.2 | 239.1 | 208.0 | 1.0 | 0.74 | 4.9 | 0.98 |
| 5 | 0.61 | 733.9 | 1318.5 | 671.6 | 0.7 | 2.11 | 2.8 | 0.97 |
| 6 | 0.07 | 1146.3 | 949.2 | 960.8 | 1.1 | 2.89 | 1.9 | 0.98 |

Table 3-7 (continued)

| | | | | | | | | |
|------|------|--------|--------|--------|------|------|------|------|
| 7 | 0.65 | 570.2 | 293.8 | 357.8 | 1.4 | 1.06 | 9.5 | 0.83 |
| 8 | 1.14 | 308.1 | 284.3 | 245.2 | 1.0 | 0.43 | 4.8 | 0.76 |
| 9 | 0.15 | 657.7 | 346.8 | 435.8 | 1.4 | 0.98 | 1.1 | 0.92 |
| 10 | 0.10 | 289.5 | 152.4 | 179.2 | 1.4 | 0.80 | 4.3 | 0.98 |
| 11 | 0.18 | 261.3 | 249.4 | 208.7 | 1.0 | 1.98 | 7.2 | 0.97 |
| 12 | 0.04 | 2107.5 | 971.4 | 1569.5 | 1.5 | 1.11 | 4.3 | 0.81 |
| 13 | 1.51 | 298.1 | 308.3 | 282.5 | 1.0 | 1.08 | 8.4 | 0.96 |
| 14 | 0.07 | 769.2 | 1407.0 | 724.9 | 0.7 | 1.03 | 2.3 | 0.98 |
| 15 | 0.32 | 1048.3 | 2042.7 | 1115.6 | 0.7 | 1.51 | 3.0 | 0.94 |
| 16 | 0.05 | 300.6 | 135.7 | 153.6 | 1.5 | 0.30 | 2.6 | 0.97 |
| 17 | 0.46 | 914.4 | 440.5 | 795.4 | 1.4 | 2.37 | 6.0 | 0.90 |
| 18 | 0.11 | 549.1 | 217.5 | 205.3 | 1.6 | 1.31 | 3.6 | 0.94 |
| 19 | 0.20 | 274.6 | 408.5 | 244.2 | 0.8 | 0.65 | 4.9 | 0.98 |
| 20 | 0.68 | 1125.3 | 908.1 | 1091.0 | 1.1 | 1.86 | 3.0 | 0.95 |
| 21 | 0.31 | 4996.9 | 3784.3 | 4645.1 | 1.1 | 0.64 | 1.4 | 0.82 |
| 22 | 0.36 | 194.3 | 184.4 | 184.4 | 1.0 | 4.60 | 2.6 | 0.62 |
| 23 | 0.19 | 172.7 | 73.0 | 110.4 | 1.5 | 1.81 | 1.9 | 0.90 |
| 24 | 0.02 | 580.5 | 640.6 | 416.2 | 1.0 | 0.76 | 1.0 | 0.71 |
| 25 | 0.35 | 275.0 | 194.5 | 325.9 | 1.2 | 3.59 | 3.7 | 0.82 |
| 26 | 0.11 | 3008.8 | 2160.8 | 2300.1 | 1.2 | 1.21 | 1.1 | 0.95 |
| MEAN | 0.33 | 1015.3 | 928.0 | 824.0 | 1.14 | 1.62 | 3.75 | 0.90 |
| SEM | 0.07 | 256.3 | 254.1 | 218.0 | 0.05 | 0.21 | 0.42 | 0.02 |

Table 3-8: Constitutive model parameters for the averaged AA and AAA datasets

| Averaged Data Fit | | | | | | | | | |
|--------------------------|-------|-------------|-------|-------|-------|------------------|-----------------------------------|-----------------|-------|
| | Group | b_0 (kPa) | b_1 | b_2 | b_3 | $\sqrt{b_1/b_2}$ | $E_{LL,max}/E_{\theta\theta,max}$ | W_{120} (kPa) | R^2 |
| Upper 95% | AAA | 0.13 | 613.7 | 537.1 | 522.9 | 1.07 | 1.290 | 5.6 | 0.97 |
| C.I. | AA | 0.27 | 214.6 | 210.6 | 187.8 | 1.01 | 0.963 | 11.8 | 0.99 |
| Averaged | AAA | 0.14 | 477.0 | 416.4 | 408.3 | 1.07 | 1.300 | 3.2 | 0.97 |
| Dataset | AA | 0.32 | 141.1 | 143.3 | 127.9 | 0.99 | 0.965 | 5.6 | 0.99 |
| Lower 95% | AAA | 0.15 | 379.6 | 331.3 | 327.8 | 1.07 | 1.314 | 2.2 | 0.98 |
| C.I. | AA | 0.38 | 99.2 | 103.5 | 92.5 | 0.98 | 0.964 | 3.9 | 0.99 |

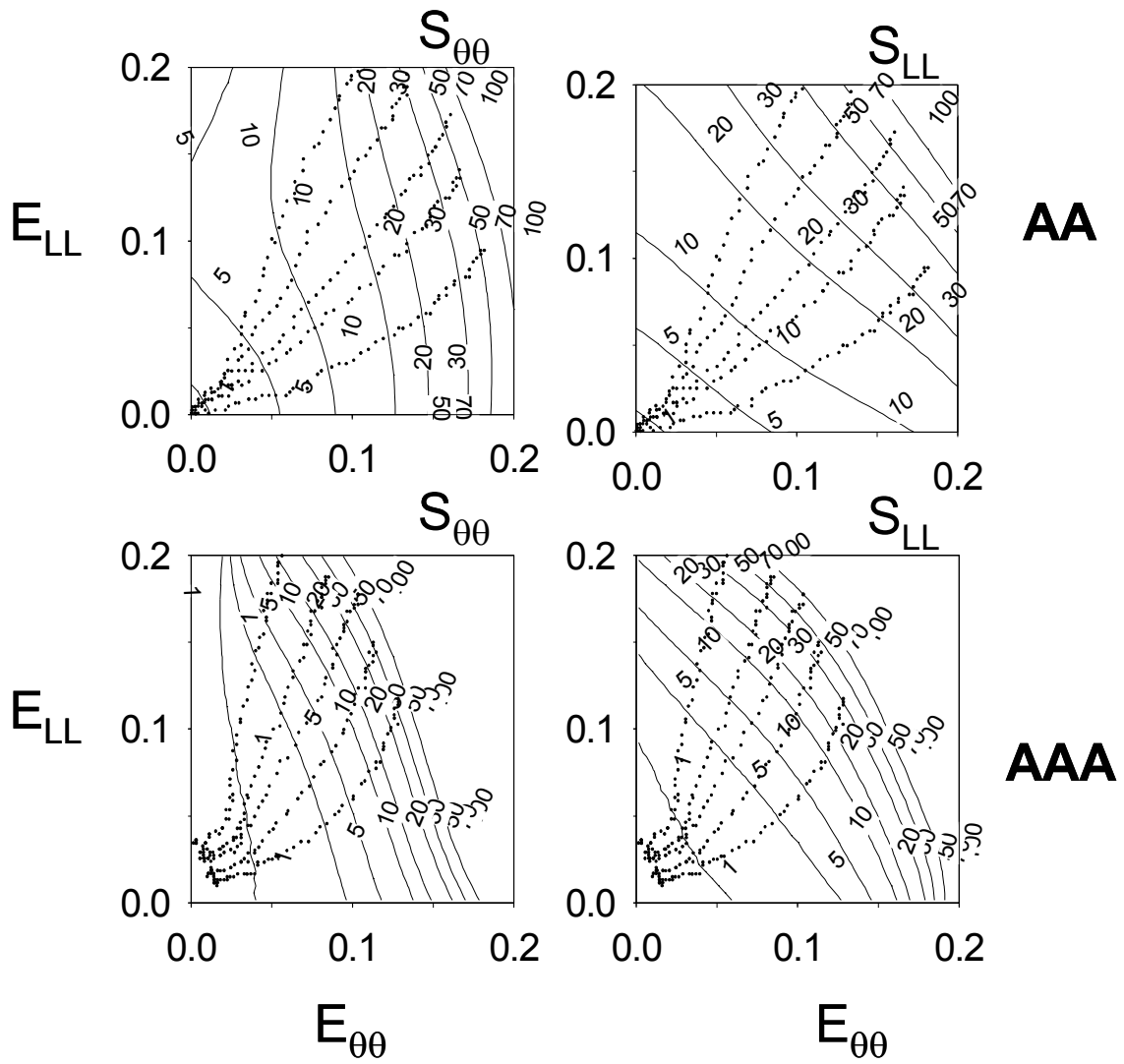


Figure 3-5: Representative AA and AAA stress contour plots

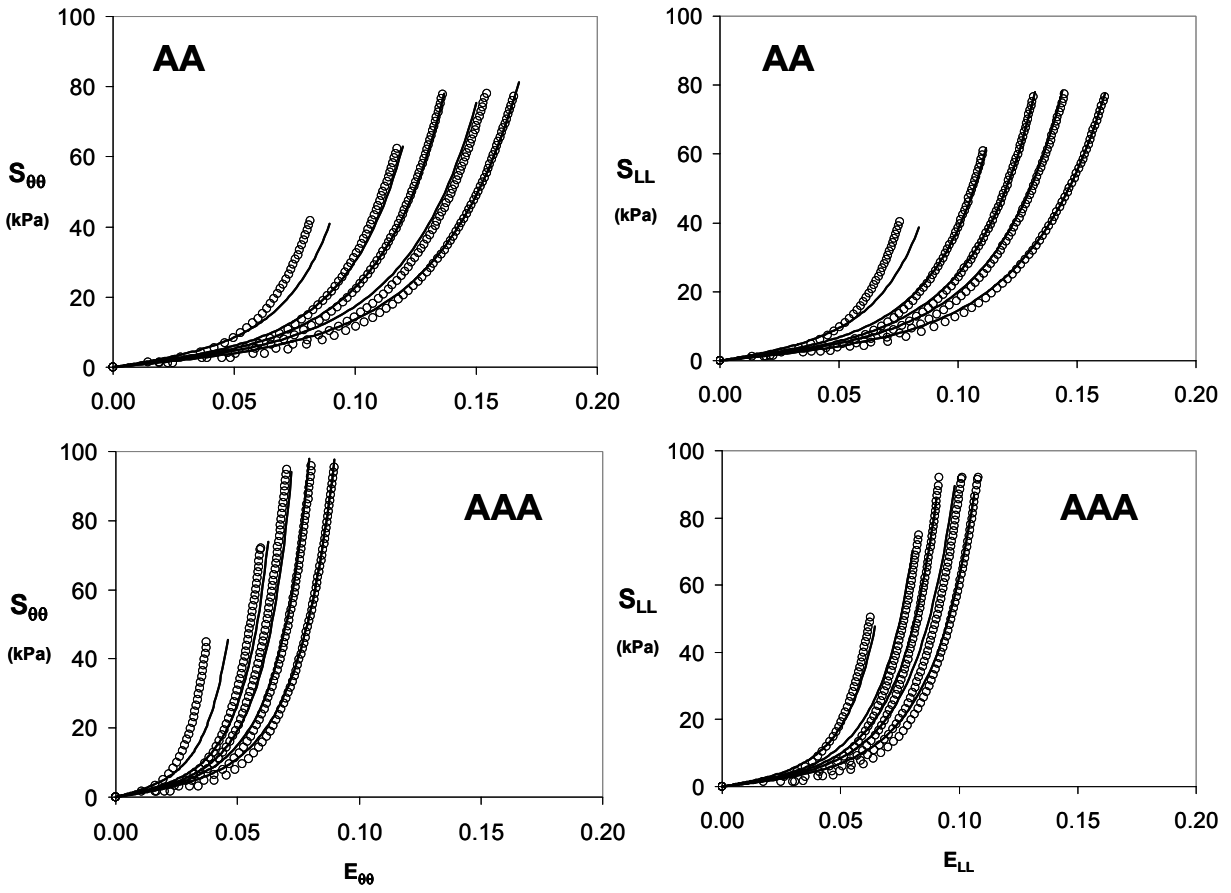


Figure 3-6: Averaged datasets and model fits for AA and AAA tissue

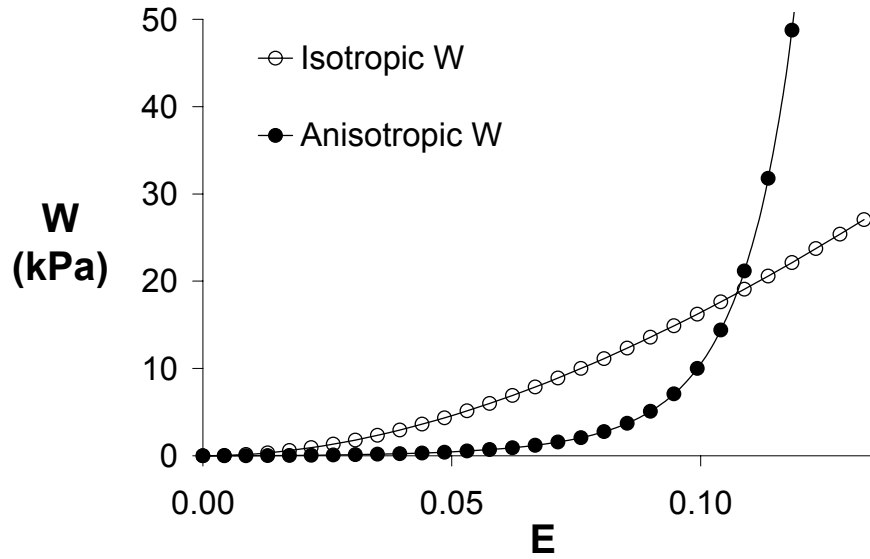


Figure 3-7: Strain energy as a function of equibiaxial strain for the isotropic [38] and anisotropic (equation 3.10) constitutive models

It can be seen from [Table 3-6](#), [3-7](#), and [3-8](#) that the average magnitudes of the constitutive model parameters $b_{1,3}$ for the AAA specimens remain larger than that for the AA specimen fits. In addition to the ratio of peak strains in equibiaxial tension, the following anisotropy parameter [86]

$$\text{sqrt}\left(\frac{b_1}{b_2}\right) \tag{3.14}$$

was calculated and compared across groups. It should be noted that although this parameter is a measure of the overall relative contribution of b_1 and b_2 to the strain energy, it does not account for the changes in the degree of anisotropy as a function of strain. The average values of this parameter were 1.02 ± 0.06 and 1.14 ± 0.05 for the AA and AAA groups, respectively ($p=0.27$). In addition, as a measure of overall stiffness, the strain energy at an equibiaxial tension of 120

N/m (W_{120}) was calculated for each specimen and compared across groups. The average values for this parameter were 4.87 ± 1.14 and 3.75 ± 0.42 for the AA and AAA groups, respectively ($p=0.26$). As can be seen from [Tables 3-6](#) and [3-7](#), W_{120} was lower for those specimens that displayed higher b_1 - b_3 values. This was primarily due to there being lower strain components at an equibiaxial tension of 120 N/m for these “stiffer” specimens.

3.3.3.2 Discussion

The primary microstructure of the abdominal aortic media consists of layers of collagen and elastin arranged in a fibrous network, with the fibers primarily running in organized and orthogonal directions of the blood vessel. Because AAA is associated with the degradation of these fibers [53, 87, 88], one might expect to see differences in both the content and structure of these fibers in AAA as compared to AA. Comparing the anisotropic behavior of human abdominal aorta between diseased states may provide evidence for structural changes as a result of aneurysm formation.

The average value of $E_{\theta\theta\max}$ was significantly lower for AAA as compared to AA tissue ([Figure 2-12A](#)), suggesting a decrease in circumferential distensibility for AAA as compared to AA. This result was supported by the decrease in the ratio of peak strains ($E_{LL,\max} / E_{\theta\theta\max}$) ([Tables 3-6](#) and [3-7](#)) and e_A ([Figure 2-12B](#)) for AAA than for AA. These results are consistent with the reported loss of elastin in this tissue [53, 87, 88]. The larger values of the anisotropy index (3.14) for most of the individual ([Tables 3-6](#) and [3-7](#)) as well as averaged ([Table 3-8](#)) AAA specimens gives further evidence of an increase in the circumferential stiffening of this tissue as compared to nonaneurysmal tissue. This result is confirmed by the preferential circumferential stiffening seen in most of the AAA stress contour plots ([Figure 3-5](#)). This

increase in circumferential stiffness is in agreement with our previous uniaxial tensile testing results, which demonstrated that circumferentially oriented specimens are stiffer than corresponding longitudinal specimens [89]. The fact that the anisotropic index (3.14) did not consistently suggest a preferred direction for the current study (Tables 3-6 and 3-7) is similar to previous reports on the biaxial mechanical response of human ascending thoracic aneurysmal tissue in which this tissue also did not suggest a consistent preferred material direction [70].

In preliminary investigations, our first approach for the choice of W was the popular Fung-type exponential constitutive relation of the form

$$W = \frac{1}{2} c(e^Q - 1) \quad (3.15)$$

where

$$Q = A_{ijkl} E_{ij} E_{kl} \quad (3.16)$$

and c and the A_{ijkl} are material parameters, with $i, j = \theta, L, R$. Neglecting all shear terms ($S_{\theta R} = S_{LR} = S_{RR} = 0$, $E_{\theta R} = E_{LR} = 0$), equation 3.16 becomes

$$Q = A_1 E_{\theta\theta}^2 + A_2 E_{LL}^2 + 2A_3 E_{\theta\theta} E_{LL} \quad (3.17)$$

While the constitutive relation given by (3.15, 3.17) fit our biaxial data well, the resulting constitutive parameters were not physically reasonable. Using a similar theoretical formulation of a strip biaxial test as previously described by Humphrey [76], it can be shown that all of the constitutive parameters in (3.15, 3.17) must remain positive in order to be physically reasonable. For 1/8 of our AA and 10/26 of our AAA specimens, the A_3 parameter resulted in a negative number when using these equations. When constraining this parameter to be positive in the nonlinear regression, this value approached zero and resulted in an insignificant fit.

The negative A_3 was thought to be due to the intrinsic model covariance resulting from the e^Q term in (3.15). It is interesting to note that the constitutive relation given by (3.10) avoids

this covariance by separating out each of the individual exponential terms and allowing each strain tensor component (e.g., $\exp(1/2 E_{LL}^2)$) to *independently* contribute to the total strain energy. Constitutive model parameter covariance has recently been identified as a major source of modeling error [90, 91]. Our results are similar to that reported by Choi and Vito [86], who also noted negative A_3 parameter values when fitting their canine pericardial data to the Fung-elastic model. These results underscore the need for further research into this important area for phenomenological constitutive model approaches in organ-level biomechanical studies.

Prior research in our laboratory has involved the derivation of a population-wide stress-strain relation from the uniaxial tensile testing of AAA tissue [38]. In order to compare the differences in the previous isotropic relation derived from uniaxial testing [38] with the anisotropic relation derived here from biaxial testing, the strain energies for both models were plotted for an equibiaxial strain state up to 12% strain ([Figure 3-7](#)). Note that the isotropic strain energy displays significantly larger strain energy at lower strains as compared to that for the anisotropic model ([Figure 3-7](#)). Note also that the mechanical response predicted from the biaxially derived constitutive model exhibits a marked increase in slope compared to that predicted from the uniaxially derived model at a strain value of 12% (325 MPa vs. 31 MPa, respectively; [Figure 3-7](#)).

One possible explanation for this difference may be the predominant reorientation of collagen fibers in uniaxial tension. Collagen fiber recruitment is primarily a function of two components: the successive recruitment of crimped collagen fibers and the reorientation of these fibers into the primary loading axis. For a uniaxial test, all fibers are free to align themselves in the direction of loading, while in biaxial tension these fibers are not available to rotate as a result of the orthogonally applied load. The earlier recruitment and preferential alignment of collagen

fibers for AAA in uniaxial tension would result in the stiffening effect observed here ([Figure 3-7](#)). Another potential explanation for the shorter toe region in the uniaxial response is possible presence of a substantial preload in uniaxial tensile tests. Our results therefore demonstrate that the uniaxial response of AAA tissue is much stiffer in the lower strain regions (less than about 10%) and is less stiff in the higher strain regions as compared to the biaxial response of this tissue.

3.3.4 Intraluminal Thrombus

3.3.4.1 Results

Stress contour plots from the ILT response functions displayed symmetry about the axis of unity ([Figure 3-8](#)), suggesting isotropy for this material. Note also the contours remain nearly equidistant from one another in the low and high strain regions, suggesting a lack of a sharp increase in stress with increasing strain ([Figure 3-8](#)).

Due to the isotropic form of the response function plots, an isotropic formulation of W was considered:

$$W = \sum_{i=0}^{\infty} \sum_{j=0}^{\infty} F_{ij} (I_1 - 3)^i (I_2 - 3)^j \quad (3.18)$$

where F_{ij} are material constants and I_1 and I_2 are the first and second invariants of the Left Cauchy-Green strain tensor. W_1 ($W_1 = \partial W / \partial I_1$) vs I_1 plots were investigated in order to determine how many and which terms should be included in the infinite sum of (3.18). The linear relationship between I_1 and I_2 for all ILT specimens ([Figure 3-9](#)) warrants the exclusion of

I_2 from the strain energy function. The linearly increasing relationship between W_1 and I_1 ([Figure 3-9](#)) suggests a quadratic term at most is needed to fully capture the mechanical response of the luminal layer of ILT. The constitutive relation fit to the ILT biaxial data was then

$$\begin{aligned}
 W &= F_1(I_1 - 3) + F_2(I_1 - 3)^2 \\
 t_{\theta\theta} &= 2 \left(\lambda_\theta^2 - \frac{1}{\lambda_\theta^2 \lambda_L^2} \right) \left(\frac{\partial W}{\partial I_1} \right) \\
 t_{LL} &= 2 \left(\lambda_L^2 - \frac{1}{\lambda_\theta^2 \lambda_L^2} \right) \left(\frac{\partial W}{\partial I_1} \right)
 \end{aligned} \tag{3.19}$$

The results for the nonlinear regression of biaxial data to ([3.19](#)) are given in [Table 3-9](#). The averaged parameters here can be used as a population-wide constitutive relation for the luminal ILT, since there exists no nonlinear interactions between these parameter values.

Table 3-9: Constitutive model parameters for the luminal layer of ILT

| ILT CONSTITUTIVE RELATION | | | |
|---------------------------|----------------|----------------|----------------|
| Specimen | F ₁ | F ₂ | R ² |
| 1 | 4.43 | 11.81 | 0.96 |
| 2 | 18.59 | 1.71 | 0.92 |
| 3 | 12.07 | 14.05 | 0.98 |
| 4 | 6.36 | 5.06 | 0.80 |
| 5 | 3.40 | 5.55 | 0.97 |
| 6 | 10.20 | 4.55 | 0.95 |
| 7 | 3.86 | 17.27 | 0.99 |
| 8 | 5.46 | 7.90 | 0.85 |
| 9 | 7.47 | 10.48 | 0.83 |
| MEAN | 7.98 | 8.71 | 0.92 |
| SEM | 1.64 | 1.69 | 0.02 |

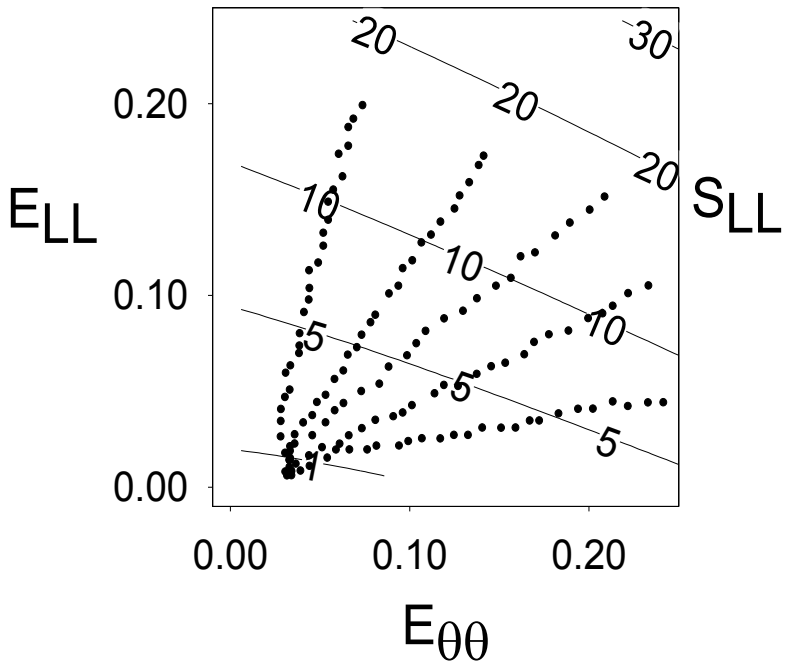
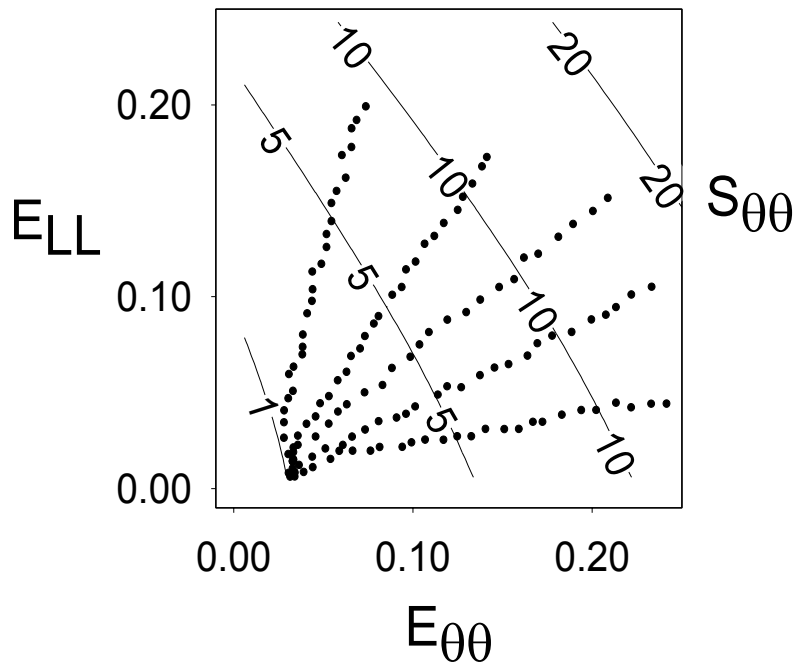


Figure 3-8: Representative stress contour plot for the luminal layer of ILT

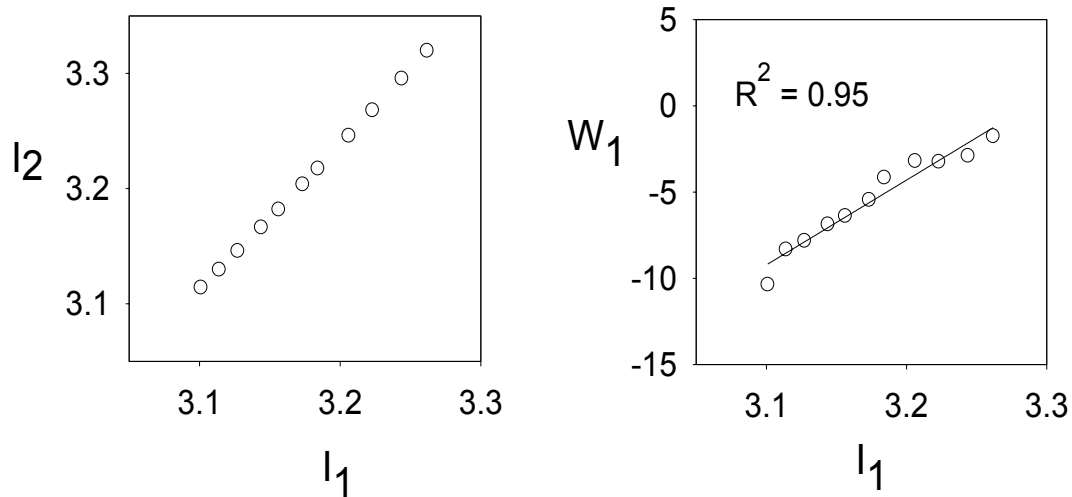


Figure 3-9: l_1 versus l_2 and $\partial W/\partial l_1$ versus l_1 for a representative ILT specimen

3.3.4.2 Discussion

Stress contours indicated the presence of mechanical isotropy, which was further supported by similar peak stretch and MTM values in the circumferential and longitudinal directions for the equibiaxial protocols. The isotropic mechanical response of the ILT was successfully captured using a second order polynomial strain energy function.

The effect of the ILT on AAA wall stresses has been described previously by our laboratory and others [55, 92-96]. For example, Mower et al. [95] reported a 30% reduction in peak wall stress in the presence of ILT in large axisymmetric AAAs. We showed that including the ILT in patient-specific stress analyses of AAA markedly influences both the magnitude and distribution of wall stress [55]. All of the studies to date, however, have made the assumption that the ILT is an isotropic homogenous material. The gross appearance of three distinct layers

of ILT [59] suggests this may be an inappropriate assumption. The present work investigated the anisotropy of the luminal layer of ILT by isolating and testing it in a multi-axial loading condition.

Likewise, the constitutive relations derived for an isotropic material tested uniaxially versus biaxially will be different. To illustrate this for ILT, the strain energy for the constitutive relation derived by Wang et al. [59] for the luminal layer is compared to that derived here for the equibiaxial strain case ([Figure 3-10](#)). We noted similar findings when comparing the uniaxial vs. biaxial constitutive relations for the AAA wall [57]. These comparisons underscore the importance of using appropriate experimental methods when deriving constitutive relations for soft biological materials.

Our results show that the biaxial mechanical behavior of the luminal layer of ILT displays an isotropic response. This mechanical response can be modeled using a strain energy function that is a second-order polynomial of the first strain invariant. Although the derivation of an isotropic relation for ILT has been reported previously, the derivation of an isotropic material from uniaxial testing may lead to large errors in the mechanical response ([Figure 3-10](#)). The utilization of the biaxially-derived constitutive relation for the luminal layer of ILT into patient-specific AAAs may lead to improved wall stress estimates, and therefore a better indication of those AAAs at high risk of rupture.

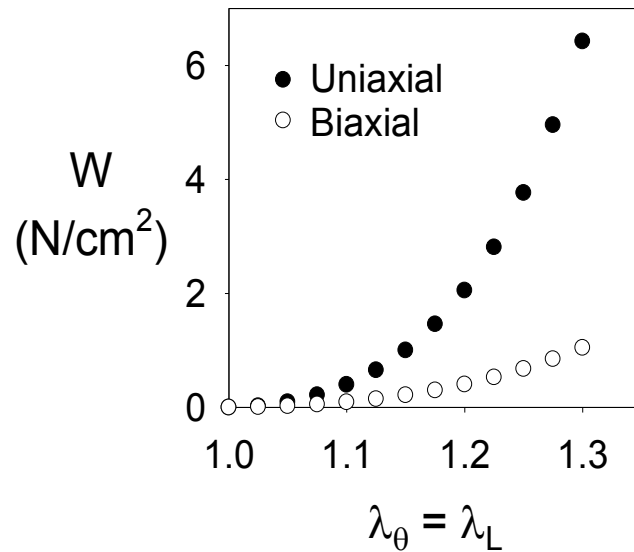


Figure 3-10: Strain energy as a function of equibiaxial strain for the uniaxially[59] and biaxially-derived constitutive models of the luminal layer of ILT

3.3.5 Limitations

Nonaneurysmal Abdominal Aorta

One discrepancy of our data is the lack of ability of the organ donor specimen 10 to be appropriately modeled by the Fung-type strain energy function (see [Table 3-2](#)). The reason for this is most likely due to the “young” appearance of this tissue as well as its biomechanical response. That is, the specimen had minimal calcifications and displayed a more sigmoidal response as compared to all other specimens of the same age group. This shape resulted in nonconvergence when fitting the Fung-elastic model due to its lack of ability to capture multiple convexities. This possibility should be kept in mind whenever applying a Fung-type exponential strain energy function. That is, one cannot simply use age to determine the appropriate form of W , but must include other considerations. The presence and amount of atherosclerotic plaque

present, for example, should also be taken into account when developing an appropriate constitutive model for aortic tissue.

Another limitation of the study looking at the age-dependency of the nonaneurysmal aorta is the use of two separate strain energy functions to model the same tissue. This could have been avoided by using a sum of the Rivlin and Fung-type strain energy functions, but this would have resulted in cumbersome models with a large number of material parameters. For the present study it was thought to be more important to describe the large change in biomechanical response with age than to develop a single form of W for abdominal aorta across all ages. Finally, in the long-term structurally-based approaches for constitutive modeling would offer a means for improved understanding of the underlying mechanisms responsible for the observed changes. As previously demonstrated [97], this will require incorporation of quantitative morphological on tissue structure data not yet available for the aortic wall.

Descending Thoracic Aorta

Similar to the biaxial tensile testing data, the constitutive model data reported here for the DTA is limited by the lack of sample size for the Group 1 and Group 3 specimens. Another limitation in modeling the DTA specimens was the inability of the proposed constitutive model to adequately describe the Group 1 AA and Groups 1 and 2 DTA specimens. Similar to the Group 1 specimens for the nonaneurysmal abdominal aorta ([Section 3.3.1](#)), these specimens displayed a biconcavity that was unable to be captured by the proposed Fung-elastic constitutive model. This result reinforces the conclusion that the DTA becomes stiffer and displays a more abrupt change in slope at a later age than the AA. Since the primary purpose of this portion of the present work was to investigate the changes in biaxial mechanical behavior for DTA versus AA

specimens and not to derive constitutive models for these tissues, no attempt was made to fit the DNC specimens in [Table 3-4](#) and [3-5](#) to a polynomial constitutive relation similar to equation 3.8.

AAA Wall

A primary limitation of the current work is the assumption that the aortic tissue is assumed to be a homogenous material. This assumption may lead to even more pronounced errors in the case of AAA given the atherosclerotic plaque formations typical in this disease. The reason that this assumption is necessary stems from the lack of experimental data/evidence of the material inhomogeneity present in AAA. Of course, the presence of calcifications within the AAA wall is known to exist and has recently been included in recent finite element simulations of AAA in our laboratory [98]. The inhomogeneity of the structural components in the AAA wall in directions tangent to the surface have yet to be quantified. Such information may be beneficial in identifying local sites of weakness or high stress within the AAA.

While the constitutive model ([3.10](#)) fit all of the AAA and age-matched AA specimens well, there are some disadvantages associated with this phenomenological approach to modeling. While the model parameters in b_1 and b_2 represent the contribution of the strain energy in the circumferential and longitudinal directions, respectively, and the parameter b_3 represents the coupling between the material axes, no more information can be gleaned from these parameters concerning the structural organization of the soft tissue which may have been responsible for the changes in biomechanical behavior of the abdominal aorta in the presence of aneurysm. One possible method for determining such information would be to approach the modeling of these tissues from a microstructural approach. That is, in contrast to the phenomenological approach

to soft tissue constitutive modeling, the structural method utilizes the structural organization of the tissue and relates it to the macroscopic mechanical behavior. Changes in the parameters of such a model between AAA and AA tissue would more likely quantify additional information regarding the microstructural changes that occur in the development of aneurysmal disease.

Intraluminal Thrombus

There are several limitations to the biaxial testing of the ILT. Each ILT specimen was taken from the luminal layer of ILT from patients undergoing elective repair of their AAA. There was only one ILT specimen procured from each AAA patient, and as such no specific information regarding the heterogeneity of the luminal layer of ILT can be gleaned. The consistency of the results as noted by the small errors in constitutive parameters ([Table 3-9](#)), however, suggests that the mechanical response of the luminal layer does not vary largely from patient to patient. In addition to those limitations described above, it should also be noted that the ILT has a high water content. The constitutive modeling developed here, however, neglects the presence and effects of the water within this tissue. Further studies that investigate the contribution of fluid movement and pressure dissipation within the ILT will help to answer the validity of this assumption.

Parameter Estimation

A primary concern in the constitutive modeling of soft biological tissues is the issue of parameter uniqueness and parameter variability. This becomes even more of an issue when dealing with constitutive models that contain parameters that are covariant as in equation (). It is interesting to note that in early trials the Fung-elastic model was unable to adequately capture the biaxial

mechanical response of AAA tissue. This was thought to be primarily due to the extreme covariance existing between the parameters in this model. When applying the model used by Choi and Vito to the AAA wall data, these issues did not arise. The separation of the exponential terms in this equation as compared to the Fung-elastic equation was thought to decrease the amount of covariance between the parameters in this model.

In order to test whether the constitutive model parameters reported for the averaged AA and AAA models were global and not local minima, the following analysis was performed. The initial guesses for the parameters utilized in the regressions reported in this chapter were varied by one order of magnitude below and two orders of magnitude above those used in the current analysis (all $b_i=1$). In other words, the initial guesses for the parameters b_0 , b_1 , b_2 , and b_3 were each individually and sequentially changed from 1 to 0.1 and 100, respectively. The results from these regressions were then compared to the values reported for the averaged AA and AAA data fits in [Table 3-8](#). Six of the eight regressions in the AAA group resulted in the exact parameters shown for that group in [Table 3-8](#). The remaining two regressions resulted in a maximum difference of 0.7% for all of the parameter values. Seven of the eight regressions in the AA group resulted in the exact parameters shown for that group in [Table 3-8](#). The remaining regression resulted in a maximum difference less than 0.1% as compared to the average parameters in [Table 3-8](#).

In addition to the above analysis, the averaged AAA wall dataset and its parameter values were investigated further. Since the residuals were not found to be normal in the regression analysis, no 95% confidence intervals on the model parameters can be directly constructed from the regression analysis. In order to quantify the variability in these parameters (in addition to the analysis involving the fitting of the 95% CI dataset), a bootstrapping analysis was

performed. Simply stated, bootstrapping involves the creation of several data sets that each mimics the statistical properties of the original dataset. Each of these generated data sets is analyzed like the original one and the variability among the resulting coefficients is taken to represent the uncertainty in the actual estimates. The methods used here are those used previously by Yin et al. [99]. For a detailed description of these methods the reader is referred elsewhere [99, 100]. For this analysis, the stress is assumed to consist of the sum of the actual stress, smooth errors representing deviations of the model with reality, and rough errors representing experimental noise. A pool of smooth curves was created in Matlab by fitting each of the residual plots for the averaged AAA model fits. These smooth curves were meant to represent the systematic deviations of the model from reality. A pool of rough errors was also created by subtracting the smooth curves from the residual values. These rough errors were meant to represent the presence of experimental noise. Each bootstrapped data set was then constructed as the sum of the model (averaged AAA in [Table 3-8](#)) with randomly selected smooth error curve and randomly selected rough errors. For the current investigation, 50 replicate or ‘bootstrapped’ data sets were constructed and fit to the averaged constitutive model (equation 3.10). A plot of each of these bootstrapped parameter sets along with the parameters from [Table 3-8](#) is shown in [Figure 3-11](#). From this figure a qualitative estimate of the parameter variability can be constructed.

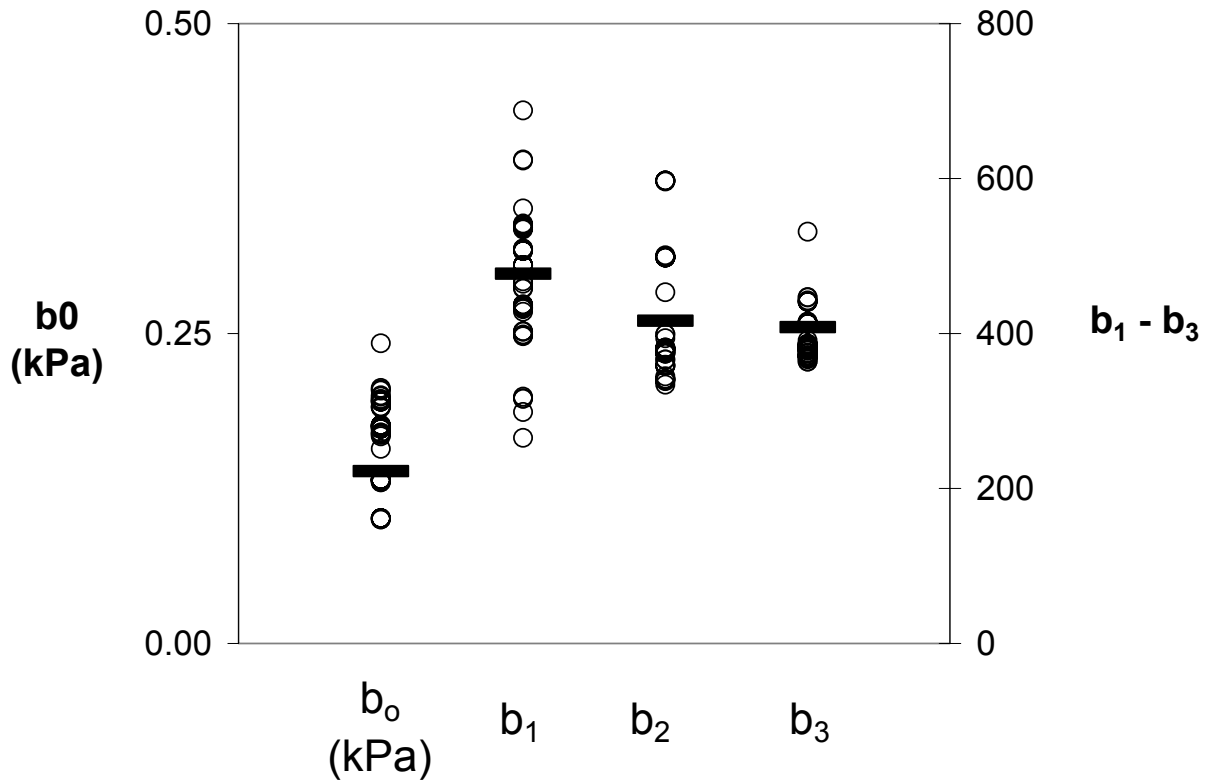


Figure 3-11: Model parameter variability of the averaged AAA constitutive model using bootstrapping methods. Open circles are the bootstrapped parameter sets, while dashes correspond to the averaged AAA model in Table 3-8

4.0 3D RECONSTRUCTION AND MESHING OF AAA

4.1 INTRODUCTION

4.1.1 Reconstruction of Biological Tissues

The reconstruction of biological tissues from medical imaging data has been performed by engineers and scientists for decades in order to investigate the stresses acting on these tissues in vivo. With recent advances in medical imaging and computational power, the reconstruction of tissues within the body has extended to virtually every organ, bone, soft tissue, and blood vessel within the human body. Several different imaging modalities have been used for the reconstruction of biological tissues, including sonography [101], intravascular ultrasound [102], biplane angiography [103], magnetic resonance imaging (MRI) [104], and computed tomography imaging (CT) [28, 33-35, 105]. For the purposes of reconstructing the precise 3D geometry of AAAs, the use of CT has been used by our laboratory and others [28, 33-35, 55]. Due to the complex geometry present in the aneurysmal abdominal aorta, the use of a biquintic finite element interpolation technique has recently been utilized in our laboratory to smooth the CT data in 3D [106]. Wang et al. has also more recently included the presence of the ILT into patient-specific 3D reconstructions of AAA from CT [55].

4.1.2 Current Reconstruction Protocol

The 3D reconstruction of patient specific AAA with ILT reported by Wang et al. [55] acted as a starting point for the 3D reconstruction of AAA utilized in the current work. The current reconstruction protocol used in our laboratory is an updated version of this protocol (see [Section 4.2.8](#)). A custom-written program in IDL (v. 5.6, Research Systems, Inc) was used to digitize the luminal surface of the AAA wall and ILT when present utilizing splines constructed from seven control points. The output of this program was then input into a C program which smoothes the point cloud in 3D using biquintic finite element interpolation [107]. A custom-written Matlab (v. 6.5.0 Release 13, The MathWorks, Inc.) program then took this point cloud and created 2D vertex files, one for each constant longitudinal slice of the AAA point cloud. These vertex files were read into a commercially available executable program, which created a surface IGES file readable by the surface CAD Rhinoceros (v. 2.0, Robert McNeel and Associates). The solid portion of the ILT was then created in Rhinoceros using Boolean operations on the corresponding AAA and ILT solids. Once the 3D solid AAA model (STL file) was created in Rhinoceros, it was meshed into quadrilateral (AAA wall) and hexahedral elements (ILT) using the meshing program True Grid (v. 2.1, XYZ Scientific Applications, Inc.). The mesh files for the wall and ILT were then read into a custom-written Matlab program which compiled and printed out an input file readable by the commercially-available finite element solver ABAQUS (v. 6.3, Hibbitt and Karleson, 2003). [Figure 4-1](#) summarizes the steps currently used to prepare a finite element model of a patient specific AAA readable by the finite element solver ABAQUS. All of the above steps for the patient-specific reconstruction of AAA used in the current study are detailed in the following sections.

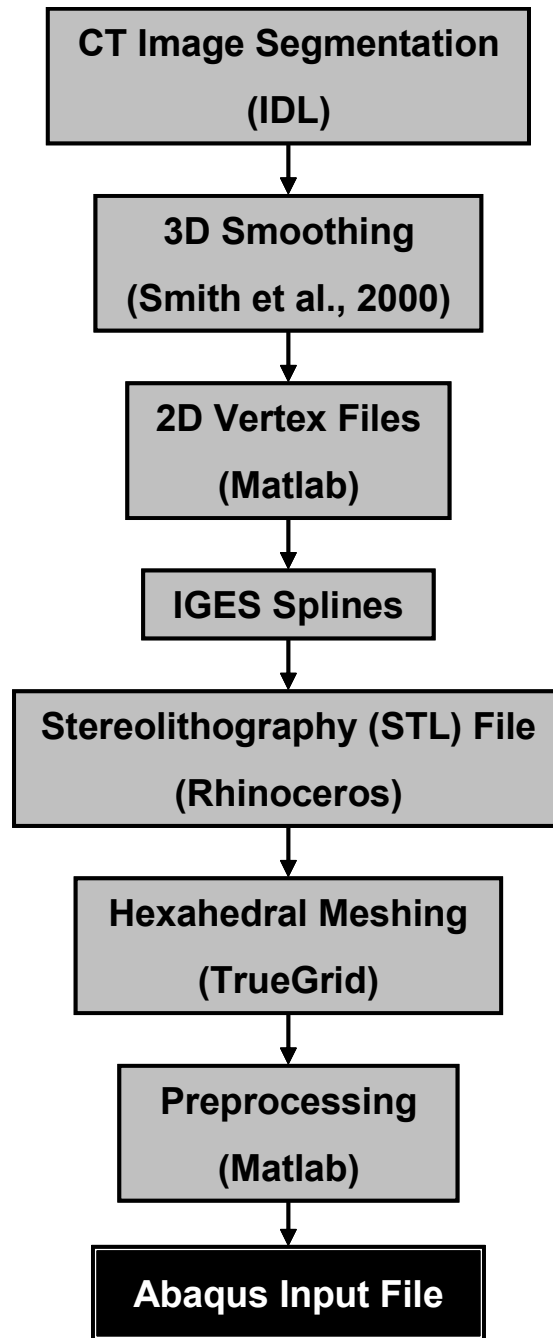


Figure 4-1: Summary of current AAA reconstruction protocol

4.2 Methods

4.2.1 Computed Tomography of AAA

A computed tomography (CT) scan uses X-rays to produce detailed pictures of structures inside the body. A CT scanner directs a series of X-ray pulses through the body. Each X-ray pulse lasts only a fraction of a second and represents a “slice” of the organ or area being studied. The end result of a CT scan is a grayscale image, with white areas typically corresponding to dense tissues such as bone, gray areas indicating brain tissue, muscles and other soft tissues, and black areas corresponding to air-filled spaces as in the lung. For properly-timed contrast enhanced CT scans, free flowing blood also displays in pure white. A typical slice from an abdominal CT scan showing the cross section of a AAA can be seen in [Figure 4-2](#). For the more interested reader, a detailed description of the CT scan process and why it is used clinically is presented in the following website (http://my.webmd.com/hw/health_guide_atoz/hw233596.asp).

All of the patients analyzed in the present work underwent CT imaging for the general purpose of diagnosis and treatment of their aneurysm. Each patient’s CT scan was based on an imaging protocol that has previously been developed for the visualization of the wall and ILT within their AAA [55]. Typically, this involved the injection of an iodine-based contrast agent (120 ml at 3ml/sec) prior to scanning. After reconstruction of the raw CT data, the dataset was sliced into longitudinal slices of 2.5mm, which typically resulted in ~48 single images for an approximately 12 cm long AAA.

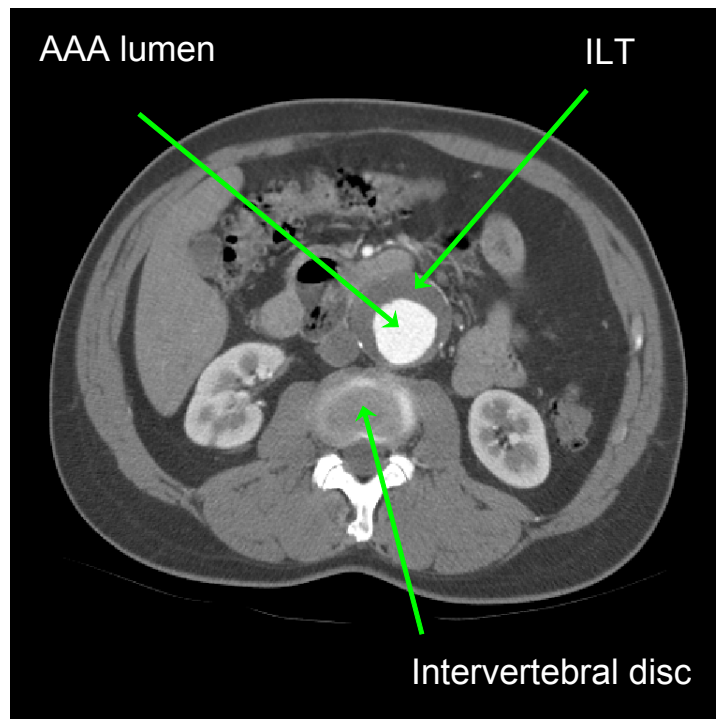


Figure 4-2: Typical image slice from an abdominal CT scan

4.2.2 Segmentation

The term “segmentation” is used in image processing to describe the isolation of a particular body within a medical image. For the purposes of this work, segmentation will refer to the isolation and identification of the AAA vessel wall, the lumen containing free floating blood, and the ILT that typically exists between these two. Due to the location of the abdominal aorta, the region of interest (ROI) within each CT image will consist of the region anterior to the intervertebral disc (or vertebrae). In addition, the longitudinal ROI will be defined as that portion of the aorta distal to the renal artery bifurcation yet proximal to the aortic bifurcation. A custom-written program in IDL (v. 5.5.2, Research Systems Incorporated) was used to segment

the AAA wall and ILT. In this program, 2D splines with seven control points were used to outline the contour of the AAA wall as well as the border of the AAA lumen ([Figure 4-3A](#)). In cases where the ILT is crescent shaped, the spline representing the luminal contour is extended outside the AAA wall in regions where there is no ILT thickness ([Figure 4-3B](#)). This created surfaces (and the subsequent solids) that allowed the Boolean creation of the solid ILT (see [Section 4.2.5](#)). The outputs of the IDL program are a set of files, one file for each slice of the AAA wall and ILT. The filenames for these are 'Draw&.%%%', where %%% represents the image slice of interest, ranging from the first slice ('000') to the last slice (e.g., '047') and & is either 0 or 1 for the AAA wall or luminal contour, respectively. Each of these files consists of two columns corresponding to the X Y pixel locations of the contour within each image. For a CT image file, the entire image is divided into a 512 x 512 array of pixels. These slice files provide the necessary data set for the next step in the reconstruction process – preprocessing for 3D smoothing.

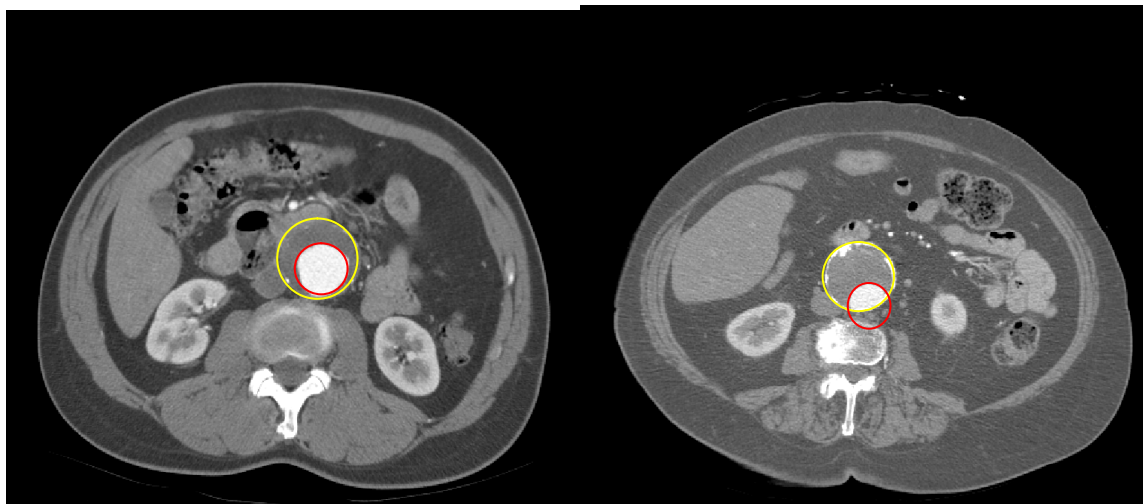


Figure 4-3: Segmentation of AAA wall (yellow) and concentric (A) and crescent-shaped (B) ILT (red)

4.2.3 Preprocessing for 3D Smoothing

The purpose of this step in the reconstruction process is two fold – to combine all of the data from the slice files (e.g., Draw0.012) into a single file that is readable by the 3D smoothing program, and to perform any necessary 2D smoothing. The preprocessing program is called ‘recon3D.txt’ and was written for the user-interface programming language Mathematica (v. 5.0 Wolfram Research) by Dr. David Wang, a recent graduate of our laboratory. A print out of this file can be seen in **Appendix B**. The details of this program can be found in Dr. Wang’s PhD thesis [40]. The input required for this program, in addition to each of the slice files, is another file (named ‘input.dat’) containing a list of the slice files, the slice thickness for the CT images (typically 2.5mm), as well as the pixel dimensions (e.g., 0.76:0.76 means each pixel is 0.76 mm by 0.76 mm wide). The output of ‘recon3D.txt’ is a text file named ‘Draw&XYZ.txt’ where & is again 0 or 1 for the AAA wall or luminal contour, respectively. This file contains three columns corresponding to the (X, Y, Z) spatial coordinates of a 3D point cloud with 72 points for each longitudinal location (in increments of 5 degrees, 0:5:360). Therefore, for a contour containing 52 slice files, this 3D point cloud will consist of $52 \times 72 = 3744$ data points. Saving the Draw&XYZ.txt as a .dat file (e.g., ‘wall.dat’) and inserting the following code at the beginning of this file

```
1      #      1  
1      1
```

where # corresponds to the number of data points (e.g., 3744), finalizes this portion of the reconstruction protocol, as this .dat file can then be read into the 3D smoothing program detailed below. A Matlab script (idl2dsmith.m, **Appendix C**) was created that automatically creates the input.dat file as well as launching Mathematica for the execution of the recon3d.txt program.

4.2.4 3D Smoothing

The 3D point cloud, while derived from smooth 2D splines, is still not smoothed in three dimensions, as errors originating from the differences in location of the AAA wall and lumen from slice to slice in the longitudinal direction still exist. In order to smooth the data point cloud in three dimensions, a biquintic finite element interpolation technique previously developed was utilized [107]. This method generates a contiguous surface of C2 continuity, allowing computation of the finite strain and curvature tensors over the entire surface with respect to a single in-surface coordinate system. The Sobolev norm is used in this technique to stabilize the interpolating polynomial at boundaries and in regions of sparse data. A major advantage of this program is its ability to smooth a set of unstructured grid of data points in 3D using a single interpolation scheme. The output of this program is a '.plt' file of a 3D triangular mesh directly importable into the post-processing program Tecplot (v. 9.0, Dundas Software Limited). In addition to the 3D smoothed triangular mesh, this output file also contains the first and second principle curvatures at each node. Another Matlab script was created (dsmith2iges, **Appendix D**) which takes the .plt file created by the 3D smoothing program and creates an IGES file containing curves corresponding to constant longitudinal slices from the smoothed .plt mesh. An IGES file (extension .igs) is created for both the AAA wall contour as well as the luminal contour.

4.2.5 Surface and Solid Modeling

Once the IGES files are created for both contours of interest, these files are imported into the NURBS (Non-Uniform Rational B-Spline) software Rhinoceros (v. 2.0 SR2, Robert McNeel & Associates). Using this software, both sets of IGES curves are lofted into smoothed 3D surfaces ([Figure 4-4](#)). The AAA wall IGES surface is then saved and is ready for meshing. These surfaces files can easily be ‘capped’ on both ends to create two solid surfaces, one corresponding to everything within the AAA wall and one corresponding to the free flowing blood (or, if the ILT is crescent shaped this will include areas outside of the AAA wall). In order to create the solid volume of ILT, a Boolean operation is performed in which the solid representing the free flowing blood (corresponding to red contours in [Figure 4-5A](#)) is subtracted from the ‘solid’ AAA wall (corresponding to black contours in [Figure 4-5A](#)), thus creating a solid corresponding to the ILT volume within the AAA ([Figure 4-5C](#)). Therefore, at the end of this step of the reconstruction protocol, there are two IGES files, one surface IGES for the AAA wall and one solid IGES file representing the ILT.

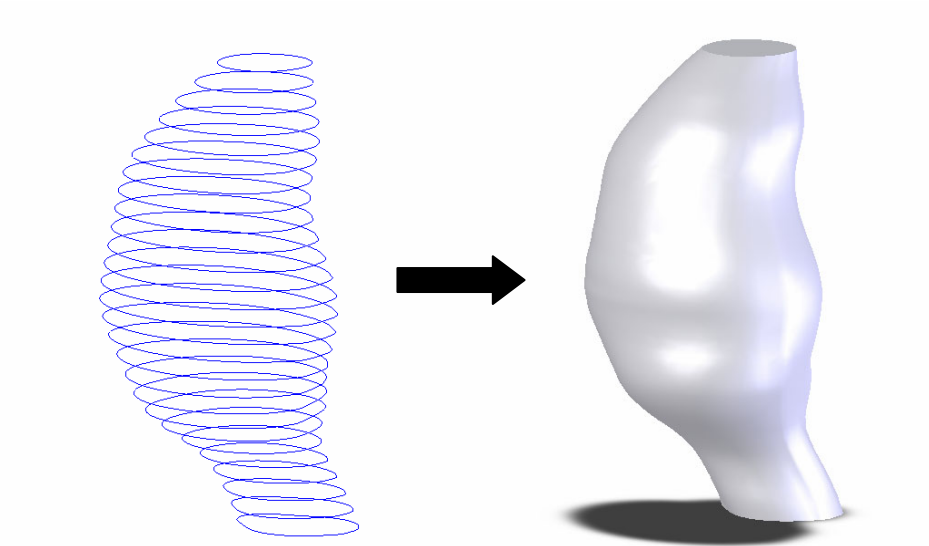


Figure 4-4: Lofting of IGES splines to create a smoothed 3D surface

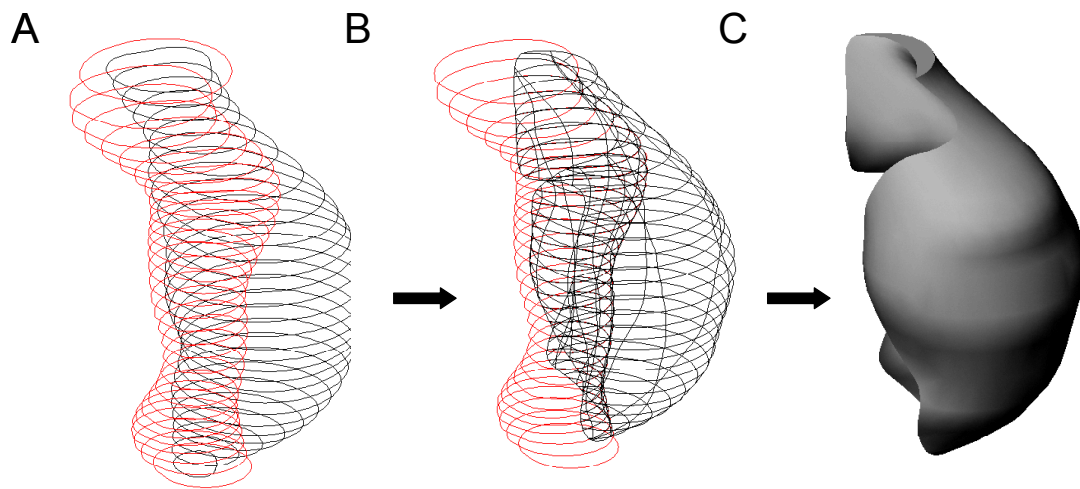


Figure 4-5: Boolean operation on the AAA in order to create the solid ILT

4.2.6 Hexahedral Meshing

4.2.6.1 Wall

As detailed in [Section 4.2.4](#), the 3D smoothing program resulted in a .plt file containing a smoothed triangular mesh. Unfortunately, triangular elements must be smaller than quadrilateral elements in order to gain the same amount of geometrical accuracy. This means that implementing the triangular mesh for the AAA wall would result in a greater computational cost than would a larger (area per element) quadrilateral element. In addition, the AAA wall, despite its tortuosity, can easily be meshed with quadrilateral elements due to its cylindrically-based geometry. For all of the above reasons, the AAA wall was meshed in the hexahedral/quadrilateral meshing program TrueGrid (v. 2.2.0.b, XYZ Scientific Applications). In brief, for the meshing of the AAA wall surface, the following steps were performed in TrueGrid.

1. Create TrueGrid (TG) curves corresponding to the top and bottom of the AAA
2. Create a TG surface corresponding to the AAA wall
3. Create a TG surface block to be used as the AAA wall mesh
4. Attach the top and bottom of the TG block to the curves created in 1.
5. Project the entire TG block onto the TG surface created in 2.
6. Add elements in the longitudinal and circumferential direction within each section of the block
7. Redistribute and smooth the entire TG block using the “unifm” command in TG
8. Export a .txt file containing the quadrilateral mesh

Once the output mesh file was created, this file is used as an input into the ABAQUS preprocessing as detailed in [Section 4.2.7](#).

For the solution of boundary value problems using the finite element method, the accuracy of a finite element approximation is known to approach the exact solution as the number of nodes (and elements) increases. Since the computational cost (CPU time) of a simulation also increases with increasing mesh density, it is necessary to determine the appropriate mesh density required to guarantee an accurate finite element result. Thus, a mesh independency study was performed on the AAA wall in order to determine the minimum number of nodes (and corresponding elements) needed to guarantee computational accuracy. For this purpose, the mean stress acting on a representative AAA defined as

$$\sigma_{ave} = \frac{\sum_{i=1}^N \sigma_i}{N} \quad (4.1)$$

where σ_i is the stress acting on a given node and N is the total number of nodes was calculated for increasing mesh densities. The total number of nodes is not an accurate measure of mesh density, since the surface area of one AAA may differ largely from that of another. For this reason, the total number of nodes within a AAA was normalized to its surface area:

$$f = \frac{\text{Total Number of Nodes of AAA Wall}}{\text{AAA Wall Surface Area}} \quad (4.2)$$

and used as a quantitative measure of mesh density. An asymptotic value for σ_{ave} as $f \rightarrow \infty$ was chosen based on the plot of σ_{ave} versus f and the percent change in σ_{ave} was analyzed with increasing values of f . A cutoff value for f was determined and used as a lower limit of mesh density for all AAAs meshed in the current study.

4.2.6.2 Intra-luminal Thrombus

The solid ILT was meshed in TrueGrid with the use of first-order hexahedral elements, typically with 2-4 elements through the thickness of the ILT. The use of hexahedral elements for the ILT is warranted given recent results which show the extreme number of tetrahedral elements which would be required in order to gain an equivalent level of computational accuracy [108]. The TrueGrid meshing protocol for the ILT is a modified version of that for the AAA wall. For the ILT, curves must be created for both the luminal and wall contours of the ILT at the proximal and distal ends of the ILT solid surface. In addition, a surface corresponding to both the luminal surface as well as the ILT ‘attached to the AAA wall’ must be created. Similar attachments and projections as described in [Section 4.2.6.1](#) are then made from a solid TG block onto the appropriate ILT curves and surfaces. Another .txt file is then exported from TrueGrid containing the hexahedral mesh representing the ILT within each AAA. A similar mesh independency study was performed for the solid elements of the ILT as described for the AAA wall in the previous section. For these simulations, the mesh of the AAA wall remained constant, while the mean stresses acting on the ILT was analyzed for increasing mesh densities. In addition, the value of the mesh density parameter f was redefined as the number of nodes in the ILT normalized to ILT volume instead of AAA wall surface area. Similar to the AAA wall mesh independency study, a cutoff value for ILT mesh density (f) was determined based on the results of these simulations.

4.2.7 Preprocessing for ABAQUS Input File Creation

For this portion of the reconstruction protocol, a Matlab script (TruGrid_2_ABAQUS_with_ILT.m, , **Appendix E**) was created that reads in the mesh files

(wall and ILT if present) and creates an input file that is ready for execution in the finite element solver ABAQUS. As detailed in [Section 5.2.2.3](#), this involved the definition of a mesh independent local material coordinate system that varied longitudinally along the AAA centerline. In addition to these local material coordinate systems, the user-defined constitutive relation derived in [Section 3.3.3](#) was also printed out in the input file created by these Matlab scripts. Overall, the most important function of this portion of the reconstruction protocol was being able to 1) create a repeatable method for defining the local material coordinates of a AAA and 2) streamline the preprocessing and input file creation such that an ABAQUS formatted input file can easily be created once the AAA wall and ILT are meshed. For a sample input file created from this portion of the reconstruction protocol, please see **Appendix F**.

4.2.8 Summary of New Protocol Changes

For the accurate creation of AAA geometry, the reconstruction protocol previously developed by Wang [40] was updated in several ways. The segmentation process was improved with a custom-written program in IDL utilizing seven-control point splines. Previously the segmentation was performed in the image processing software Scion Image (v. 4.0.1, 1998 Scion Corporation, Frederick, Maryland), which required the manual tracing of luminal and AAA wall contours. Such a method not only was time-consuming and extremely user-dependent, but also resulted in a 2D point cloud with considerable amounts of noise. The previous laborious process of manually tracing an entire AAA typically required 8 hours, while the new segmentation process required less than 3 hours for both the AAA wall and the ILT. There were also several additions to the new reconstruction protocol aimed at providing a computationally more efficient finite element solution. Chief amongst these were the addition of hexahedral and quadrilateral

meshing in the program TrueGrid. The previous reconstruction protocol included the meshing of the wall and ILT as solid meshes. In particular, the use of first-order elements in the wall (quadrilateral shells) and ILT (8-noded hexahedral elements) has provided a decrease in computational time while not sacrificing solution accuracy. Finally, the current reconstruction protocol was streamlined with the automation of data transfer between portions of the reconstruction protocol. For example, the Matlab script 'idl2dsmith.m' was created in order to automate the transfer of data from the segmentation program (IDL) into the 3D smoothing algorithm [106]. A similar result was achieved with the implementation of the script 'dsmith2iges.m'. Finally, the laborious process of creating an ABAQUS input file was also streamlined with the Matlab script 'TruGrid_2_ABAQUS_with_ILT.m'. The updates implemented in the current reconstruction protocol as well as their advantages are listed in [Table 4-1](#).

Table 4-1: Summary of changes to the AAA reconstruction protocol

| Reconstruction Method | Old Protocol | New Protocol | Advantage |
|--------------------------------------|---|--|---|
| Segmentation | Manual (Scion Image) | Semi-automated (2D splines in IDL) | Smoother 2D dataset as well as ↓ in user-dependence and segmentation time |
| Meshing | Wall and ILT (2 nd order tetrahedral elements, meshed in Patran) | Wall (1 st order quadrilateral shells, TrueGrid) ILT (1 st order hexahedral solid elements, meshed in TrueGrid) | ↓ computational cost for equivalent accuracy |
| Data transfer between protocol steps | Manual data file creation/manipulation | Automated data transfer | Streamlines and simplifies reconstruction protocol |

4.3 RESULTS AND DISCUSSION

4.3.1 Meshing Results

4.3.1.1 AAA Wall

The mesh independency study resulted in less than a 1% change in stress for a wide range of mesh densities ([Figure 4-6](#)). The average stress in the AAA (σ_{ave}) increased slightly with increasing values of f . A plot of the absolute value of the percent change in σ_{ave} versus f shows less than 0.2% change in σ_{ave} for values of f greater than 9 cm^{-2} ([Figure 4-6](#)). For this reason, all AAA walls analyzed in the current work were meshed with a value of f greater than or equal to 9 cm^{-2} . The average number of nodes for all AAA walls ($n=35$) meshed in the current work

was 3267 ± 40 with an average surface area of $182.5 \pm 1.5 \text{ cm}^2$. [Table 4-2](#) lists the number of nodes, surface area, and mesh density factor f for all AAAs meshed in the current study.

Table 4-2: Mesh densities for all AAA wall meshes. ‘N’=non-ruptured; ‘R’=ruptured

| AAA | AAA Surface Area (cm ²) | Number of Wall Nodes | f (cm ⁻²) |
|-------|-------------------------------------|----------------------|-----------------------|
| AAA1 | 133.3 | 1936 | 14.52 |
| AAA2 | 242.3 | 2726 | 11.25 |
| AAA3 | 186.6 | 2544 | 13.63 |
| AAA4 | 208.1 | 2014 | 9.68 |
| AAA5 | 157.7 | 2150 | 13.64 |
| AAA6 | 177.2 | 4248 | 23.98 |
| AAA7 | 145.2 | 3200 | 22.04 |
| AAA8 | 255.6 | 2655 | 10.39 |
| AAA9 | 115.1 | 2340 | 20.32 |
| AAA10 | 202.9 | 2538 | 12.51 |
| AAA11 | 134.0 | 1924 | 14.35 |
| AAA12 | 108.3 | 2520 | 23.27 |
| AAA13 | 149.3 | 3328 | 22.29 |
| AAA14 | 171.9 | 2279 | 13.26 |
| AAA15 | 159.9 | 2585 | 16.17 |
| AAA16 | 196.2 | 2805 | 14.30 |
| AAA17 | 172.1 | 5376 | 31.24 |
| AAA18 | 206.8 | 2600 | 12.57 |
| AAA19 | 185.3 | 2736 | 14.77 |
| AAA20 | 217.5 | 2332 | 10.72 |
| AAA21 | 262.1 | 3132 | 11.95 |
| N1 | 217.6 | 2244 | 10.31 |
| N2 | 129.3 | 6586 | 50.94 |
| N3 | 130.5 | 2596 | 19.89 |
| N4 | 157.8 | 5376 | 34.07 |
| N5 | 309.3 | 7140 | 23.08 |
| R1 | 214.8 | 2176 | 10.13 |
| R2 | 110.4 | 2021 | 18.31 |
| R3 | 155.7 | 3953 | 25.39 |
| R4 | 259.5 | 3564 | 13.73 |
| R5 | 114.8 | 6016 | 52.42 |
| R6 | 253.0 | 4080 | 16.13 |
| R7 | 181.8 | 1938 | 10.66 |
| R8 | 125.6 | 4094 | 32.59 |
| R9 | 241.1 | 4608 | 19.12 |
| MEAN | 182.5 | 3267.4 | 19.2 |
| SEM | 1.5 | 39.8 | 0.3 |

The wall mesh for AAA4 is shown in [Figure 4-7](#). For this AAA, the surface area (208.1 cm²) of the AAA was meshed with 1961 first order quadrilateral shell elements (2014 nodes), resulting in a mesh density factor of 9.68 cm⁻².

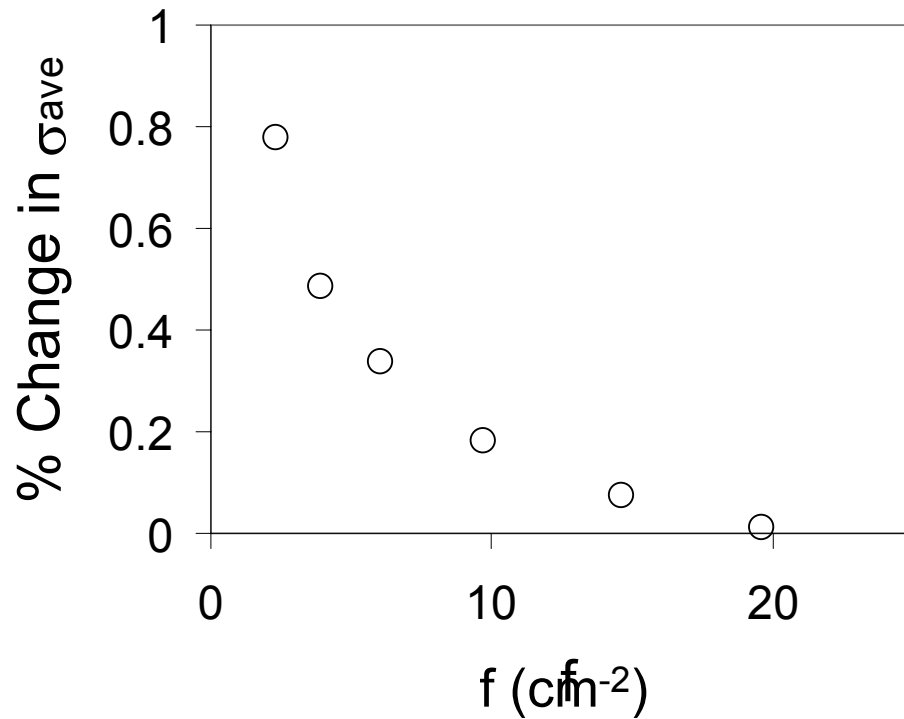


Figure 4-6: Percent change in mean AAA wall stress with increasing mesh density

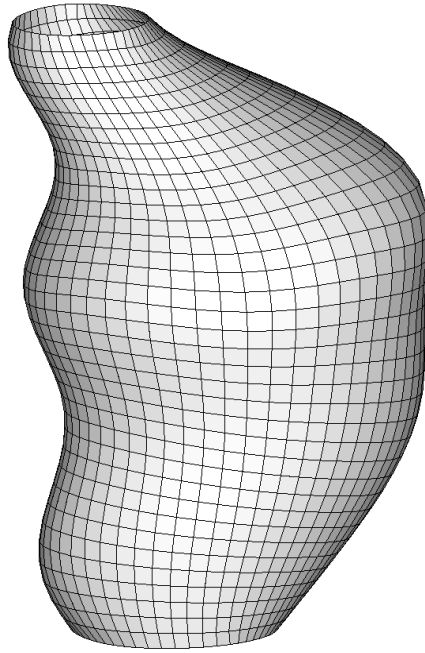


Figure 4-7: Representative mesh for AAA4, $f = 9.68$

4.3.1.2 Intra-luminal Thrombus

The mesh independency study for the ILT resulted in less than a 1% change in stress for mesh densities greater than $f=22 \text{ cm}^{-3}$ ([Figure 4-8](#)). In contrast to the mesh independency study performed for the AAA wall, σ_{ave} decreased slightly with increasing values of f . A plot of the absolute value of the percent change in σ_{ave} versus f shows less than 0.8% change in σ_{ave} for values of f greater than 20 cm^{-3} ([Figure 4-8](#)). For this reason, all ILTs analyzed in the current work were meshed with a value of f greater than or equal to 22 cm^{-3} .

The average number of nodes for all ILTs ($n=35$) meshed in the current work was 8223 ± 176 with an average volume of $106.6 \pm 1.8 \text{ cm}^3$. [Table 4-3](#) lists the number of nodes, volume of ILT, and mesh density factor (f) for all ILTs meshed in the current study.

Table 4-3: Mesh densities for all ILT meshes. NA denotes the AAA had no ILT

| AAA | Volume of ILT (cm³) | Number of ILT Nodes | f (cm⁻³) |
|------------|---------------------------------------|----------------------------|----------------------------|
| AAA1 | 45.8 | 5148 | 112.40 |
| AAA2 | 183.1 | 5250 | 28.68 |
| AAA3 | 35.0 | 6324 | 180.89 |
| AAA4 | 17.3 | 1224 | 70.79 |
| AAA5 | 86.0 | 4300 | 50.03 |
| AAA6 | NA | NA | NA |
| AAA7 | 91.3 | 6528 | 71.48 |
| AAA8 | 229.5 | 5104 | 22.24 |
| AAA9 | 104.0 | 4000 | 38.48 |
| AAA10 | 45.6 | 1248 | 27.37 |
| AAA11 | 89.7 | 3276 | 36.54 |
| AAA12 | 54.8 | 3696 | 67.40 |
| AAA13 | 121.8 | 4800 | 39.41 |
| AAA14 | 162.5 | 4884 | 30.06 |
| AAA15 | 94.8 | 3600 | 37.97 |
| AAA16 | 105.9 | 4416 | 41.70 |
| AAA17 | 104.3 | 27470 | 263.40 |
| AAA18 | 171.1 | 7040 | 41.15 |
| AAA19 | 99.0 | 7788 | 78.67 |
| AAA20 | 140.2 | 7920 | 56.48 |
| AAA21 | 64.1 | 17510 | 273.17 |
| N1 | 170.5 | 13250 | 77.71 |
| N2 | NA | NA | NA |
| N3 | 4.8 | 9660 | 2029.41 |
| N4 | 48.4 | 20160 | 416.36 |
| N5 | 209.0 | 15750 | 75.36 |
| R1 | 148.2 | 3960 | 26.72 |
| R2 | 219.6 | 14500 | 66.03 |
| R3 | 89.1 | 8892 | 99.81 |
| R4 | 26.3 | 2090 | 79.47 |
| R5 | 34.7 | 12885 | 371.75 |
| R6 | 129.5 | 5484 | 42.35 |
| R7 | 190.9 | 6840 | 35.83 |
| R8 | NA | NA | NA |
| R9 | 94.4 | 18135 | 192.11 |
| MEAN | 106.6 | 8222.9 | 158.8 |
| SEM | 1.8 | 176.2 | 10.2 |

The ILT mesh for AAA8 is shown in [Figure 4-9](#). For this AAA, the ILT volume (208.1 cm²) was meshed with 3696 first order hexahedral solid elements (5104 nodes), resulting in a mesh density factor of 22.24.

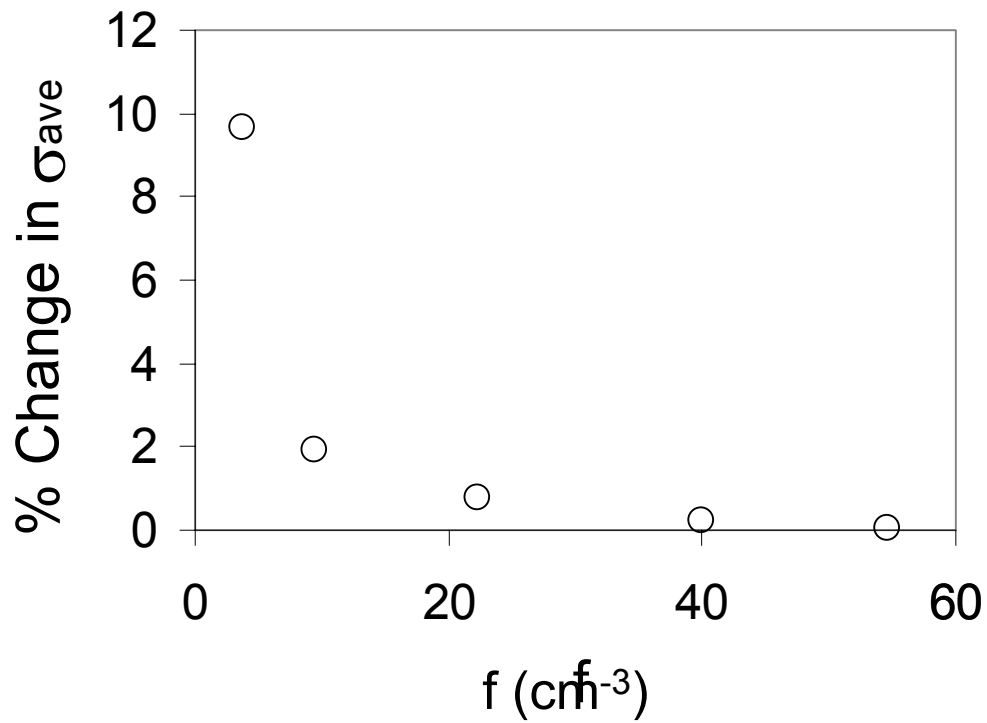


Figure 4-8: Percent change in mean ILT stress with increasing mesh density

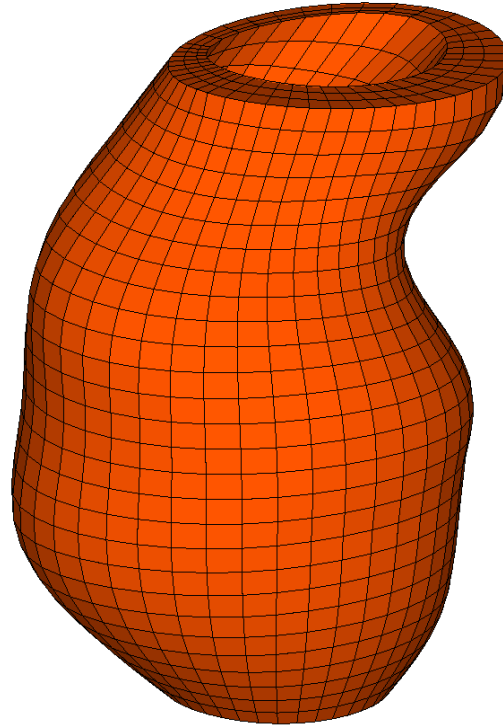


Figure 4-9. Representative mesh for the ILT of AAA8, $f = 22.24$

4.3.2 Visual Inspection of Smoothed 3D Mesh

For the purposes of qualitatively assuring the accuracy of the reconstruction protocol, the final smoothed AAA wall mesh was plotted for each AAA along with its respective 3D point cloud from the segmentation portion of the protocol (the file resulting from [Section 4.2.3](#)). Comparing these datasets provides a qualitative check that the 3D smoothing, surface construction, and meshing of the AAA wall did not result in any unwanted geometrical modifications. In other words, any geometrical differences present between these datasets should be a direct result of the 3D smoothing. A representative comparison plot is shown in [Figure 4-10](#). The smoothed wall mesh for AAA7 displays minimal deviation from the original segmented 3D point cloud,

suggesting that the 3D smoothing and mesh creation did not largely alter the ‘true’ geometry present in the CT scan.

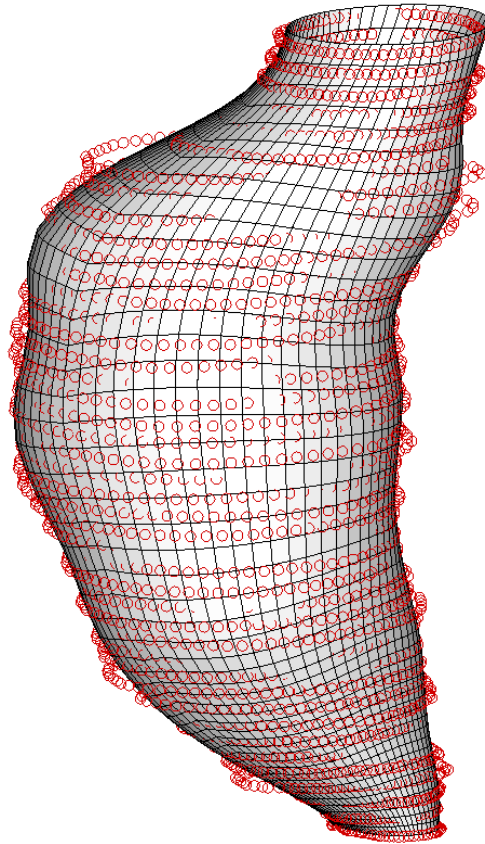


Figure 4-10: Smoothed AAA7 wall mesh (black) and 3D point cloud resulting from the segmentation process (red)

4.3.3 Discussion

In the current work we have extended the reconstruction of AAA from previous work. Specifically, we have improved the segmentation process with the implementation of smooth 2D

splines instead of the manually tracing previously required [40]. Improvements in the meshing algorithm have also resulted in a decrease in the computational time required in solving a patient-specific AAA finite element simulation. While these improvements represent a significant effort in the patient-specific reconstruction of AAA, future studies should address some of the limitations in the reconstruction process as detailed later in this section.

Previous work on the stress analysis of AAA has shown that the inclusion of patient-specific geometry is mandatory for the correct estimation of AAA wall stress [28, 33-35, 38, 40, 55, 106, 109-111]. Recent work by Wang et al. has shown that the inclusion of the ILT into patient-specific finite element simulations of AAA changes both the magnitude and distribution of stress within a AAA [40, 55]. For this reason, the ILT was reconstructed in all of AAAs in the current study, except when there was no ILT present. Since the reconstruction process involves both patient-specific geometrical modeling as well as the inclusion of the solid ILT, the time required to segment the AAA is substantial. The 2D splines that have been utilized in the current work serve in part to address this limitation. There are, however, several other examples in the literature where the reconstruction of soft tissues and organs have been automated with the use of other segmentation tools. For example, the use of “snake” algorithms have been utilized in the reconstruction of many organs and tissues within the body [112-118]. These algorithms use 2D splines that either grow or shrink in order to wrap themselves around the soft tissue/organ of interest. For a detailed description and review of this and other segmentation tools for the segmentation of biological tissues the reader is referred elsewhere [119].

As previously described, a CT scan directs a series of X-ray pulses through the body. Each X-ray pulse lasts only a fraction of a second and represents a “slice” of the organ or area being studied. After placing the patient in the proper position on the scanning table, the first

slice is initiated. Once the X-Ray tube rotates around your body 360 degrees to take one cross-sectional image, the table will be slightly moved in order to get the next plane. While the patient's body is being scanned the patient is asked to hold their breath in order that the movement of the abdomen during breathing does not add to the error in 3D position of organs and tissues. Since a CT scan does not take an *instantaneous* snapshot of the *entire* AAA but instead calculates a time-averaged geometry, errors in the 3D position of the AAA arise from 1) the blood vessel wall displacement due to the time-varying luminal pressure and 2) any differences in 3D position due to the breathing cycle unable to be accounted for by the patient holding their breath. These factors are responsible for the error present in the rough segmented 3D point cloud shown in [Figure 4-10](#) (in red).

There are several other limitations associated with the current reconstruction protocol itself. As can be seen from [Figure 4-1](#), the process of creating a smoothed finite element mesh from CT images requires several steps utilizing several different software packages. While recent efforts have been successful in making the reconstruction process more streamlined, less user-dependent, and more automated, these aspects of the protocol can still be improved. For example, utilizing one program for the segmentation, 2D smoothing, 3D smoothing, and mesh creation would significantly simplify the reconstruction protocol since a large effort is currently made in transferring data between sequential programs in the protocol.

All of the AAA wall reconstructions in the current work were meshed with first order quadrilateral shell elements. Since in a CT scan it is often times impossible to measure the blood vessel wall thickness, a 3D distribution of thickness on the AAA wall was not able to be detected. Therefore, all of the AAA wall shell elements analyzed in the current work were assigned a constant wall thickness of 1.3 mm. This value was the average thickness of all of the

biaxial AAA specimens tested in [Section 2.3.3](#). Recent work by Raghavan et al. [109] suggests that wall thickness may be an important factor in determining an individual aneurysms risk of rupture. The investigation of new imaging techniques for AAA such as magnetic resonance imaging (MRI) may provide the detail required to noninvasively predict the 3D distribution of wall thickness within a AAA.

The atherosclerotic nature of AAA formation often results in the calcification of the AAA wall. The reconstruction protocol described here has ignored the presence of any calcified plaques. The calcifications present in the AAA wall may result in a significant change in the constitutive properties of this material, resulting in changes in the predicted stress using finite element analysis. In fact, the presence of the calcifications has recently been included in AAAs and has been shown to increase the stress on the AAA wall in areas of highly calcified tissue [98]. While the presence of calcification has not been included in the present work, the results and conclusions regarding the effects of anisotropy on AAA wall stress would be expected to hold even with the inclusion of localized plaques.

As shown in [Figure 4-1](#), the process of creating an input file for ABAQUS from a set of CT scan images requires the use of several software programs, each with its own purpose. The inter- and intra-user variability in using the developed protocol is another source of error present in the reconstruction process. Both of these sources of error are most likely to have the largest effect in the first portion of the protocol – the segmentation. The remaining portions of the protocol involve the manipulation of data files via computer programs, which were automated and therefore resulted in no intra- or inter-user variability. The use of the two-dimensional control point splines in the segmentation program (written in IDL) is thought to minimize the inter- and intra-user variability in the segmentation of the AAA wall and ILT. The current image

segmentation methodology is thought to provide an improvement in repeatability as compared to previous methods of segmentation (typically in a software similar to NIH Image), which involved pointing and clicking on the desired boundary of interest for the entire 360° circumference. The currently utilized IDL program provided for a repeatable number of data points around the circumference of the boundary for each longitudinal slice, which is not possible using a point-and-click method. For the current work, the amount of inter- and intra-user variability was not quantified. This should be addressed in future work and also kept in mind whenever implementing the current methodology in further studies involving the 3D reconstruction of AAA.

The reconstruction protocol for AAA in the current work has been improved in several ways. The segmentation of the AAA wall and ILT from CT images has been improved with the use of two dimensional control point splines. The computational cost of running a AAA finite element simulation has also been decreased with the use of the hexahedral meshing program TrueGrid. The time required to create a smooth finite element mesh from a set of CT images has also been accelerated with the use of Matlab scripts designed to ease the transfer of data between protocol steps and software programs. While the current reconstruction protocol represents a significant improvement on previous work, there still remain areas where the entire process could be made even more automated.

5.0 ANISOTROPIC FINITE ELEMENT SIMULATIONS

5.1 INTRODUCTION

Rupture of abdominal aortic aneurysms occurs when the continuous and cyclic pressure acting on the lumen of the AAA creates a wall stress which eventually overcomes the ability of the wall to withstand those forces (the wall strength). Thus, the biomechanical point of view of AAA rupture states that there are two primary factors influencing AAA rupture – AAA wall stress and wall strength. By taking this point of view, it is easy to recognize that the risk of AAA rupture will increase with increasing wall stress as well as decreasing wall strength. It is not surprising then, that the prediction of stress in aneurysms has been reported by several researchers in the literature [33, 34, 55, 95, 111, 120-126]. Some of these studies utilize the finite element method, which is able to model aneurysms with varying degrees of complexity. Early finite element models of aneurysms in the literature utilized simplistic geometries (e.g., spherical) and small deformation constitutive relations [95, 123, 127]. Later work demonstrated that the complex shape (e.g., local curvatures) are an important factor in determining the peak stress acting on an individual AAA [28, 128]. The isotropic constitutive model developed by Raghavan and Vorp represented the first large strain relation for the AAA wall [38]. Several other researchers have since utilized this relation when estimating the stresses acting on patient-specific AAA finite element simulations [33-35, 55]. One of the more recent advances in the finite element analyses

of AAA was the inclusion of the intra-luminal thrombus by Wang et al. [55], whose simulations demonstrated that the presence of the ILT can significantly effect both the magnitude and distribution of stress within a AAA. More recently Raghavan et al. investigated the effect of variable wall thickness on AAA stresses and demonstrated that this may be a very important factor in predicting the rupture risk using finite element analyses [109]. The effect of localized calcification on peak AAA wall stress was also investigated recently by Speelman et al. who reveal a unique dependence of AAA wall stress on the location and stiffness of mineralized plaques in patient-specific AAA simulations [98].

The present work addresses the assumption of isotropy for the AAA wall. Nearly all biological materials display some amount of anisotropy due to their non-uniform composition and structure. Recent work by Nicosia et al. demonstrated the anisotropy present in the porcine ascending aorta [65]. They conclude that the utilization of an isotropic constitutive relation for the ascending aorta is insufficient in providing a physiologically realistic prediction of stress. Kyriacou and Humphrey also recently underscored the importance of including multiaxial constitutive relations into finite element stress analyses of intracranial saccular aneurysms, especially given their unique three-dimensional shape [129]. The anterior bulging present in the aneurysmal formation of the abdominal aorta also suggests that this region may indeed be in a state of multiaxial stress.

Appropriate stress approximation has been proposed as an important component in AAA rupture prediction. The results in Chapter 3 of this work display the anisotropy present in the aneurysmal abdominal aorta in the multiaxial stress state. In addition, the general strain energy ([Figures 3-7, 3-10](#)) was also shown to be different for uniaxially versus biaxially tested specimens. The implementation of the anisotropic constitutive relation for the AAA wall and the

isotropic biaxially-derived relation for the luminal layer of the ILT may lead to a more appropriate estimation of stress within patient-specific AAAs. This improvement may also be important in noninvasively identifying those AAAs which have a high risk of rupture.

5.2 METHODS

5.2.1 Boundary Conditions

The estimation of stress via the finite element method requires three primary inputs. First, the geometry must be adequately discretized into finite elements. The discretization (meshing) of the AAA and ILT is detailed in [Section 4.2.6](#). Second, appropriate constitutive relations for each of the materials in the finite element analysis must be derived. These relations have been derived for both the AAA and ILT in [Sections 3.3.3](#) and [3.3.4](#), respectively. Finally, the forces and displacements acting at the boundaries of the finite element mesh must also be prescribed. The adequacy and validity of the assumptions utilized in each of these three inputs in the finite element method determines the accuracy of the finite element approximated solution. Once all three of the above inputs have been provided, the boundary value problem being considered can be solved with the finite element method. In the finite element method there are two types of boundary conditions: essential (sometimes called Dirichlet) boundary conditions and natural (sometimes called Neumann) boundary conditions. Essential boundary conditions prescribe the value of the state variable (e.g., displacement) at the boundary nodes. Natural boundary conditions prescribe either the value of flux (e.g., force) or a combination of the values of the flux and state variable at the boundary nodes. As will become apparent, the finite element simulation of AAA requires the application of both of these types of boundary conditions. The

following sections describe these boundary conditions in detail as well as detailing other assumptions made in the finite element analysis of patient-specific AAAs.

5.2.1.1 Blood Pressure

An increase in the blood pressure acting on the interior of a AAA would obviously cause an increase in the stress acting on the AAA wall. It is therefore not surprising that hypertension has been identified as a major risk factor for AAA rupture [130]. Since the interest here is to noninvasively predict the risk of rupture for patient-specific AAAs under *normal physiologic conditions*, the blood pressure occurring in the patients' medical charts was not utilized as a natural boundary condition in the finite element analyses of AAA in this work. This was avoided for several reasons. First, it may be that a patient's blood pressure measured in a hospital setting does not accurately represent his or her daily blood pressure. Secondly, a AAA patient that has been admitted into a hospital for coexisting conditions will more often than not have their blood pressure pharmacologically controlled. Lastly, the inability to suitably represent a AAA patient's blood pressure due to its fluctuation over time was thought to add unwanted variability to the current work. Because we were interested in predicting the changes in AAA wall stress as a result of such variables as the diameter, curvature, tortuosity, amount and presence of ILT and not the highly variable value of a patient's blood pressure, each of the AAA simulations in the current work were performed with the application of a systolic 120 mmHg. This pressure was applied to either the luminal contour of the ILT or to the AAA wall when the ILT was not present.

5.2.1.2 Longitudinal Tethering

The abdominal aorta is in a unique and complex physical environment, especially in the presence of an aneurysm. Several studies have investigated the longitudinal stretch present in blood vessels and shown them to be under a state of longitudinal tethering in-vivo [66, 131-133]. For the current work, the nodes comprising the proximal and distal ends of each AAA were constrained in all three displacement degrees of freedom. This was done to mimic the in-vivo longitudinal tethering thought to be present in the abdominal aorta. It was found in the current study that constraining the radial displacement of nodes on the ends of the AAA did not result in localized stress concentrations, but did result in faster convergence of the finite element solution. The boundary conditions utilized here have also been used by several other researchers in the patient-specific finite element simulation of AAA [28, 33-35, 40, 55, 109]. The effects of the spine and the pressure due to other organs present in the abdominal aorta were neglected in this study. Future work should include the forces put on the abdominal aortic wall by these surrounding structures.

5.2.1.3 Reference Configuration

Arteries are known to be in a state of residual stress in-vivo. Fung quantified the amount of residual stress in the canine aorta and its relation to location along the aortic tree [66]. Several other researchers have investigated the presence and effects of residual stresses in arteries [134-138]. The presence of residual stresses requires the definition of three states of stress for blood vessels: the unstressed state, the unloaded state, and the loaded state. The unstressed state refers

to the configuration of the aorta in which there are no residual stresses. Often times this state is attained with a radial cut of a ring of aortic tissue resulting in the relief of residual stresses and the ‘opening’ of the ring. The unloaded state is the configuration of the blood vessel in which there exists no longitudinal force or luminal pressure acting on the aorta. This state is not stress free due to the presence of residual stresses. Finally, the loaded state represents the deformed configuration of the blood vessel caused by both longitudinal tethering and luminal pressure in.

For the purposes of the finite element simulation of AAA, the systolic pressure should be applied to the unloaded state with longitudinally tethering force already present. For the current work, the longitudinal tethering of the aorta was mimicked with the constraint of the distal and proximal ends. Since the geometry in a CT scan represents a time-averaged loaded state configuration (see [Section 4.2.1](#)), the geometry of a AAA in the completely unloaded state was not available. Therefore the systolic pressure was applied to the loaded state configuration in the current work. The error associated with using the loaded configuration as the unloaded state has been investigated previously by Wang et al. [40]. Their results indicate the maximum error in peak stress within an AAA is 8% (from 17.96 to 19.52 N/cm²) when utilizing a loaded configuration instead of an unloaded one. A similar error would be expected herein since for the current work the loaded ‘CT’ geometry was also treated as the unloaded geometry for which the systolic 120 mmHg was applied. Once again, this increase in stress would most likely not change the results of the current work regarding the differences in stress due to the presence of anisotropy.

5.2.1.4 Shear Stresses

Predicting the stresses acting on the AAA wall is the primary reason for simulating patient-specific AAAs. The stresses present in the wall due to the luminal pressure, however, are not the only stresses present. The time-varying flow of blood past the luminal surface of the AAA also creates a state of shear stress on the endothelial layer of the wall. Recent studies have indicated that the maximum shear stress acting on the luminal layer of a AAA due to pulsatile flow is on the order of 3 Pa [139-143]. Since the peak value of this shear stress is an order of magnitude lower than that reported for solid finite element simulations, the effect of shear on the state of stress within the AAA wall was neglected in the current study.

5.2.2 Implementation of the Anisotropic Constitutive Relation into ABAQUS

As stated in [Section 5.2.1](#), one of the inputs into a finite element simulation is the constitutive model. Simply stated, a constitutive model relates the stresses and strains within a deformable body. There are several different types of constitutive models, and each subclass is typically classified according to the assumptions used in its derivation. Some tissues in the body such as bone can be modeled as linear elastic homogenous isotropic (LEHI) materials, in which the small deformation of the material allows a linear relation between stress and strain. For soft tissues, however, the deformations are typically large (>1% strain) and therefore require a finite-strain constitutive model. In fact, the circumferential strain of a AAA due to the pressure pulse alone (~40 mmHg) has been reported to be greater than 2% [72]. Despite the increases in stress resulting from the inhomogeneities known to be present in AAAs due to localized calcification [98], many researchers assume a homogenous mechanical response for the AAA wall [33-35, 38,

55]. The AAA wall will be assumed to act as a nonlinearly elastic homogenous material for the simulations in the present work. The anisotropic constitutive relation derived in the current work ([Section 3.3.3](#)) was implemented into the commercially available finite element code ABAQUS as detailed in the following sections.

5.2.2.1 Solving a Nonlinear Problem Using Newton's Method

There are several sources of nonlinearity in a boundary value problem including geometrical nonlinearity, material nonlinearity, and boundary nonlinearity. In the pressurization of a AAA there exists material and geometrical nonlinearities. For this reason the solution to the finite element analysis cannot be performed in one large step as is the case in a linear analysis. Instead, the solution is found by specifying the loading as a function of time and incrementing time to obtain the nonlinear response. Therefore, the simulation is broken up into a number of *time increments* and an approximate equilibrium configuration is found at the end of each time increment. Within each time increment, Newton's method uses multiple *iterations* to find the equilibrium solution in an increment [144].

For a body to be in equilibrium, the net force acting at every node must be zero. Therefore, the basic statement of equilibrium is that the external loads acting on a body, P , and the internal forces, I , must balance one another, $P - I = 0$. [Figure 5-1](#) displays the nonlinear response of a structure to a small load increment, ΔP . ABAQUS uses the tangent stiffness, K_0 , which is based on its configuration at time u_0 , and ΔP to calculate a displacement correction, c_a , for the structure. The structures configuration is then updated to u_a using c_a . The structures internal forces I_a are then compared to the total applied load P using the *force residual* defined as

$R_a = P - I_a$. If R_a is zero at every degree of freedom within a model, point **a** in [Figure 5-1](#) would lie on the load-displacement curve and the structure would be in perfect equilibrium. For a nonlinear problem R_a will never be perfectly zero so it is compared to a tolerance value, below which ABAQUS accepts the configuration as an equilibrium configuration. If the tolerance value is not met, then ABAQUS forms a new stiffness, K_a , based on the updated configuration u_a . The new stiffness along with the residual R_a determine a new displacement configuration c_b , which lies closer to the systems equilibrium state. A new force residual can then be calculated as $R_b = P - I_b$. This iteration process is repeated within each increment of Newton's method until the force residual meets the force residual tolerance value, after which the system is assumed to be in equilibrium [144].

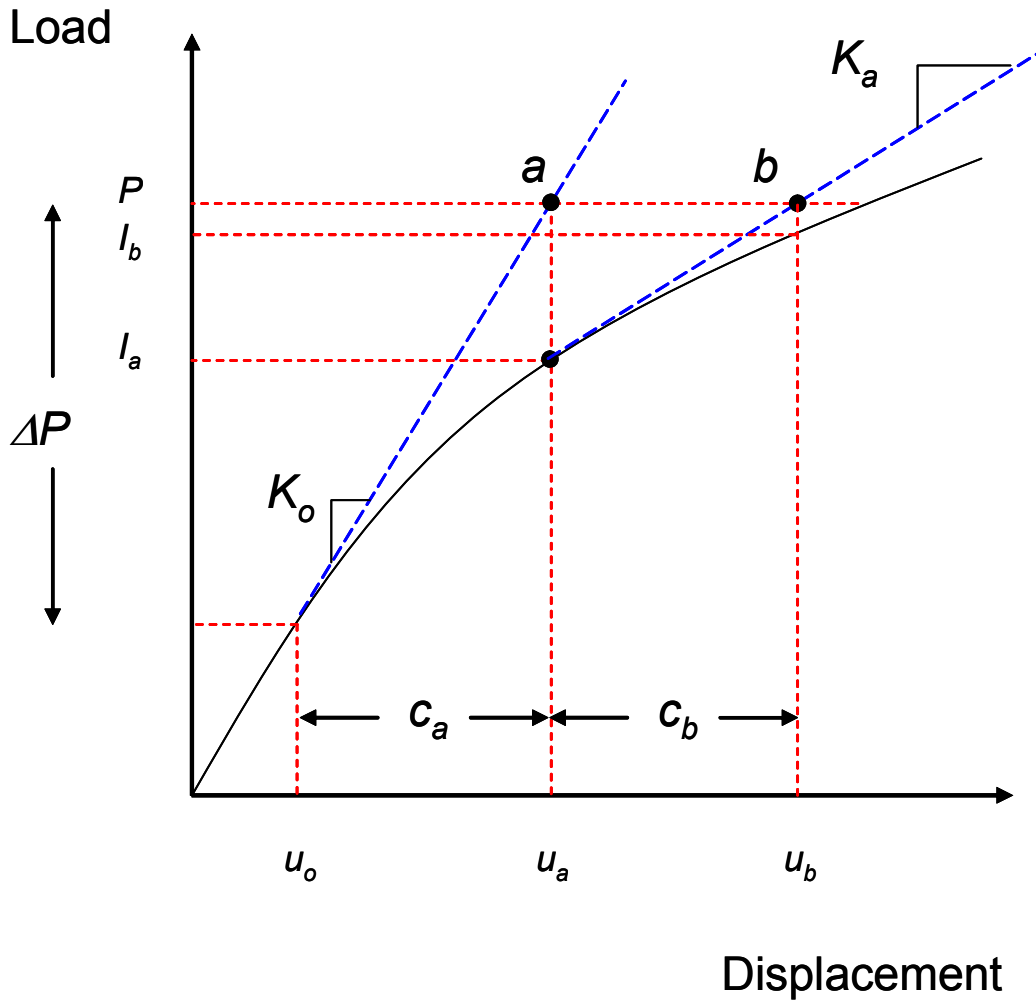


Figure 5-1: Pictorial view of Newton's method for solving nonlinear problems

Newton's method works well for load displacement curves that are convex as is the case in [Figure 5-1](#). Such convex load-displacement curves would be the situation for isotropic polymeric materials such as rubber. For concave load displacement curves, however, the Newton's method has problems in predicting reasonable values for the displacement corrections c_a , c_b , etc. This is especially true in the case where the load displacement curve is nearly horizontal with the displacement axis. The low stress and strain region of the constitutive model for the AAA wall described in [Section 3.3.3](#) would create a load-displacement curve that is

nearly horizontal to the displacement axis. This situation creates a stiffness K_i and a corresponding displacement correction C_{i+1} that attempt a displacement iteration that is far outside any reasonable equilibrium deformation state. This problem is exacerbated by the extremely sharp increase in stress present in the anisotropic constitutive relation ([Section 3.3.3](#)), which creates a rather thin range of reasonable displacement configurations for large changes in load (see gray box in [Figure 5-2](#)). In preliminary studies using the UMAT for the anisotropic relation for AAA wall, it was found that the above issue resulted in simulations which were either unable to complete the initial increment, or required so small of an initial increment (0.01 % of final load) that the solution of the analysis became cumbersome and computationally inefficient. In order to circumvent this problem, an initial increase in slope was implemented into the UMAT so that at low strains the simulation easily found an intermediate equilibrium state ([Figure 5-3](#)). The strain energy was augmented in the following way

$$W = \frac{1}{2}u_{11}E_{\theta\theta} + \frac{1}{2}u_{22}E_{LL} + \frac{1}{2}u_{12}E_{\theta L} + b_0 \left(e^{\frac{1}{2}b_1 E_{\theta\theta}^2} + e^{\frac{1}{2}b_2 E_{LL}^2} + e^{b_3 E_{\theta\theta} E_{LL}} \right) \quad (5.1)$$

where $u_{11} = u_{22} = u_{12} = 40$. Note that equation ([5.1](#)) does not represent an attempt at improving the constitutive model derived in [Section 3.3.3](#), but is simply a tool used to jump start and accelerate the convergence of the finite element simulation. Implementing this computational tool allowed each simulation to start with a reasonable initial incremental step (~5% of final load) and correspondingly resulted in a decreased CPU time when running the anisotropic AAA finite element simulations. As one can see from [Figure 5-3](#), there is minimal error (< 1.5 %) in the large stress-strain region when utilizing this computational tool, since at extremely low strains the u_i terms dominate but at higher strains the exponential terms on the right side of equation ([5.1](#)) control the strain energy.

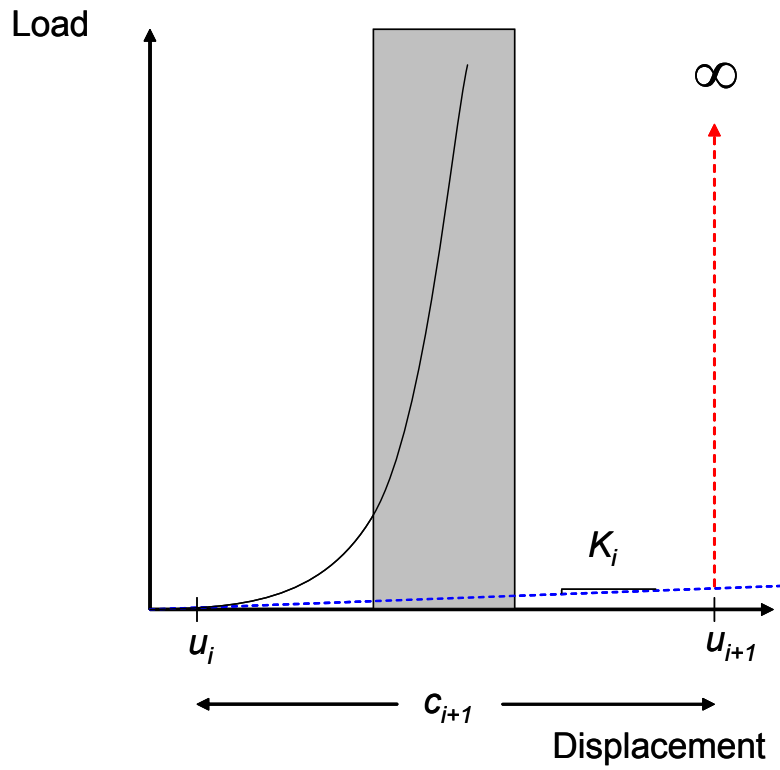


Figure 5-2: Problems associated with low initial slopes when using Newton's method

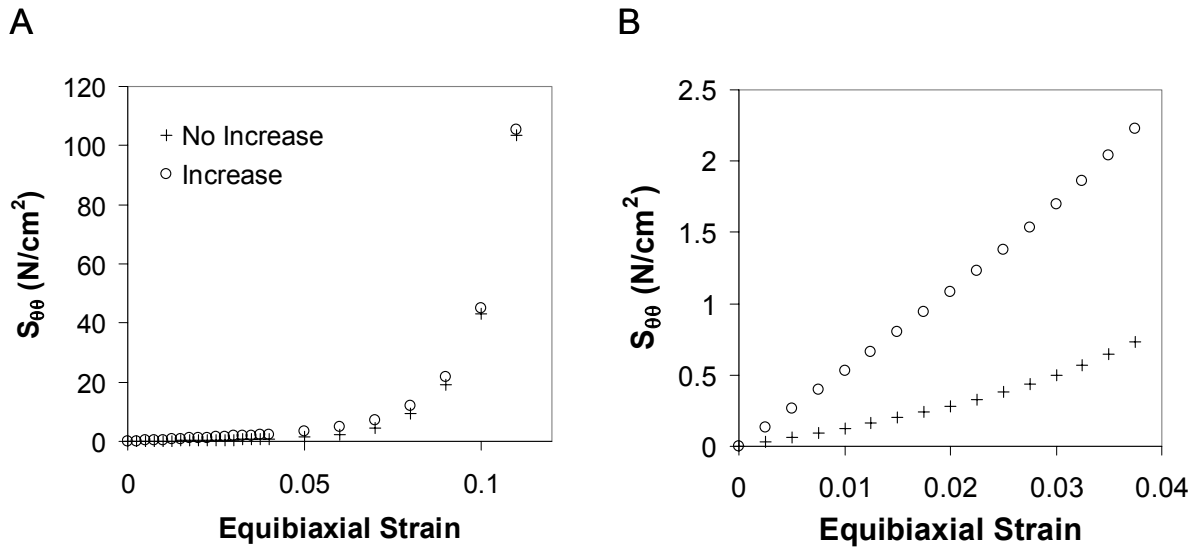


Figure 5-3: A) Differences in stress with the implementation of equation 5.1. B) Blown up view of A)

5.2.2.2 User-Defined Material Properties

The anisotropic constitutive relation detailed in [Section 3.3.3](#) was implemented into the finite element software with the use of the user defined material function (UMAT) available in ABAQUS. The purpose of the Fortran UMAT subroutine within the ABAQUS solver is primarily two-fold. First the function must determine the stresses using both the constitutive relation and the incremental displacements (arguments in the subroutine). Secondly, the function must also calculate and output the material Jacobian matrix ($\partial\Delta\sigma/\partial\Delta\epsilon$) which will aid in the calculation of the new incremental displacement used in the next increment. The location and purpose of the UMAT subroutine within an ABAQUS increment is summarized in [Figure 5-4](#).

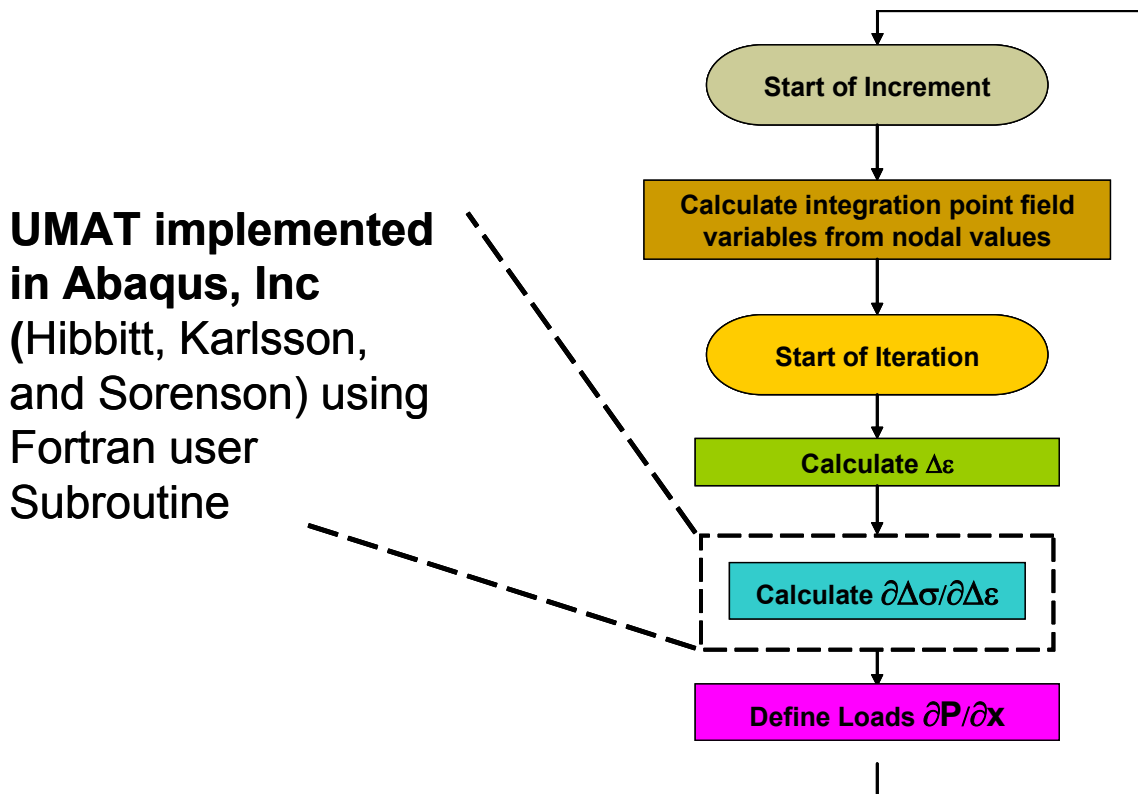


Figure 5-4: Outline of the purpose of UMAT subroutine within ABAQUS

An Excerpt from the UMAT subroutine is shown below.

```

...
C  CALCULATE THE STRAIN
C
E11=0.5*(DFGRD1(1, 1)**2+DFGRD1(2, 1)**2-1)
E22=0.5*(DFGRD1(1, 2)**2+DFGRD1(2, 2)**2-1)
E12=0.5*(DFGRD1(1, 1)*DFGRD1(1, 2)+DFGRD1(2, 2)*DFGRD1(2, 1))
E21=0.5*(DFGRD1(1, 2)*DFGRD1(1, 1)+DFGRD1(2, 2)*DFGRD1(2, 1))
E33=ZERO
....
C  CALCULATE THE STRESS
C
S11= 2*u11*E11 +C*(b1*E11*EXP(0.5*b1*E11**2)+A3*E22*EXP(b3*E11*E22))
S22= 2*u22*E22 +C*(b2*E22*EXP(0.5*b2*E22**2)+A3*E11*EXP(b3*E11*E22))
S12= 2*u12*E12 + C*(b4*E12*EXP(0.5*b4*E12**2))
S33= ZERO
...
C  CALCULATE THE STIFFNESS MATRIX
C
DDSDDE(1,1)= 2*F1*S11+F1*F1*J1+K1*S12+F1*K1*J8+K1*S12+F1*K1*J8+K1*K1*J7
DDSDDE(2,2)= K2*K2*J4+K2*S12+F2*K2*J9+K2*S12+F2*K2*J9+2*F2*S22+F2*F2*J2
DDSDDE(3,3)= F1*S11+F1*K2*J5+F1*F2*J3+2*K1*S12+K1*K2*J3+F2*S22+K1*F2*J6
DDSDDE(1, 2)= F1*F1*J4+F1*K1*J9+K1*F1*J9+K1*K1*J2
DDSDDE(1,3)= F1*F1*J5+F1*S12+K1*F1*J3+F1*S12+K1*F1*J3+2*K1*S22+K1*K1*J6
DDSDDE(2,3)= 2*K2*S11+K2*K2*J5+F2*S12+K2*F2*J3+F2*S12+K2*F2*J3+F2*F2*J6
DDSDDE(2, 1)= DDSDDE(1, 2)
DDSDDE(3, 1)= K2*S11+F1*K2*J1+F2*S12+F1*F2*J8+K1*K2*J8+K1*F2*J7
DDSDDE(3, 2)= F1*K2*J4+F1*S12+F1*F2*J9+K1*K2*J9+K1*S22+K1*F2*J2
...

```

The entire UMAT subroutine is also shown in **Appendix G**. Note here that the stress S33 is defined as zero. This is done simply due to our choice of elements for the AAA wall. The AAA wall was meshed with first order reduced-integration quadrilateral shell elements (S4R), for which the stress in the direction orthogonal to the plane of the shell is zero.

5.2.2.3 Definition of Local Material Coordinates

The material coordinates of a given shell element will determine the direction to which S_{11} , S_{22} , E_{11} , and E_{22} act. By default, ABAQUS assigns the local 1 direction as the projection of the global X axis onto the surface of the shell. For a AAA, this would not result in an adequate definition of local material coordinates, since the local longitudinal direction of an element on the AAA wall changes with the centerline of the AAA. As a first trial, the entire AAA was positioned in 3D space such that the open ends of the AAA point in the positive and negative global X-directions. In this case the projection of the global X-axis onto each element resulted in an adequate definition of the local longitudinal direction for those AAAs displaying a large amount of symmetry about the X-Y plane. For the majority of AAAs, however, the presence of the ILT and the tortuous path of blood flow within an AAA results in a nonsymmetrical geometry. The 3D path of the centerline of AAAs is in general a more reliable indication of the local longitudinal direction of the AAA wall. For this reason, each AAA wall mesh was divided up into several (e.g., 40) longitudinal z-sections, and the center of each slice was found ([Figure 5-5](#)). 3D spline tools were then utilized in Matlab to create a spline through the centerline points along the AAA ([Figure 5-5](#)). The projection of this 3D spline onto the surface of each AAA wall element was then used to define the local longitudinal direction of the shell. The normal direction of the shell is automatically defined in ABAQUS using the ordering of nodes within an element. Once the local longitudinal and normal directions of the shell element are defined, the final local circumferential direction of the shell is computed using the right hand rule. The above formulation provided an accurate, repeatable and mesh-independent definition of the local material directions ([Figure 5-6](#)).

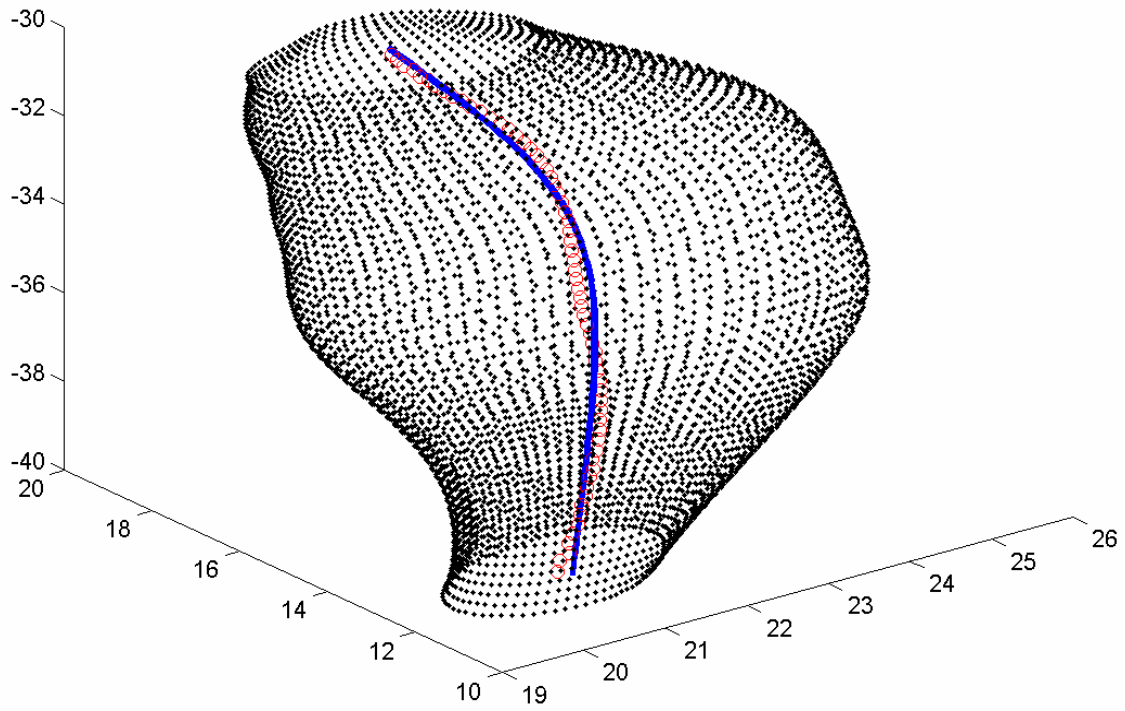


Figure 5-5: Longitudinal center points and resulting 3D spline used to define local material coordinates

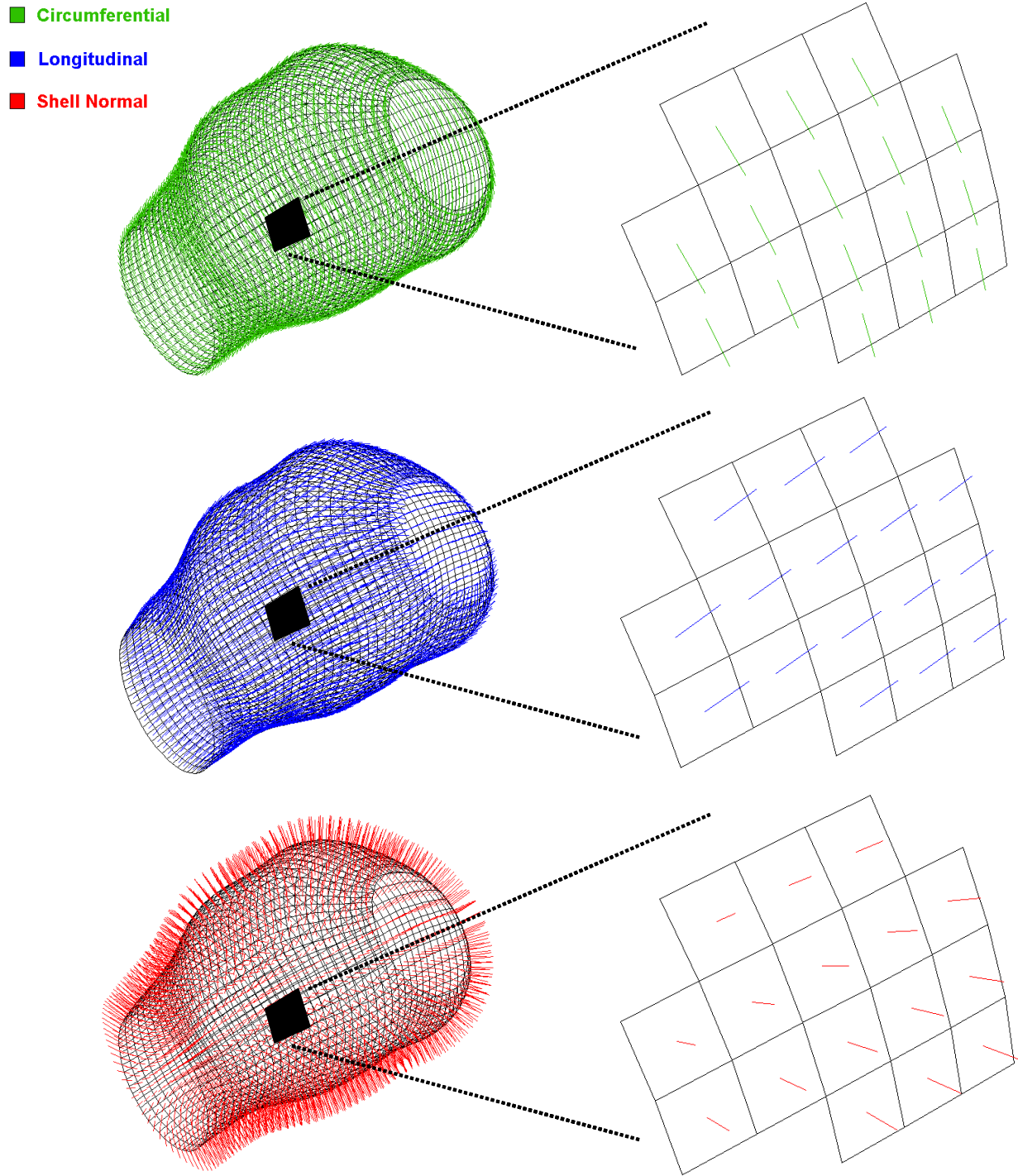


Figure 5-6: A representative AAA showing the definition of local material coordinates

Implementing this information into the ABAQUS input file required the creation of a coordinate system for each longitudinal z-section of the AAA wall with the *ORIENTATION command as well as the referencing of this coordinates system in the *Shell Section command for the elements comprising that longitudinal z-section of the wall. An excerpt of one of these longitudinal z-sections is shown below.

```
...  
*Shell Section, elset=wall1, material=wall, orientation=cylcoord1  
0.130000, 5  
...  
*Orientation, name=cylcoord1, definition=coordinates, system=cylindrical  
18.860296, 16.828611, -1.633000, 18.925944, 17.154957, -1.930759  
1, 0  
....
```

The isolation of an element set comprising a given longitudinal z-section, the creation of a coordinate system for that longitudinal z-section, as well as the assignment of this coordinate system to the appropriate element set was all created in the input file created by the Matlab scripts `TruGrid_2_ABAQUS_with_ILT.m` and `TruGrid_2_ABAQUS_without_ILT.m` (**Appendix E**).

5.2.3 Biaxial Simulations

In order to test the accuracy of the UMAT subroutine, the equibiaxial protocol several AAA wall biaxial tensile tests were simulated. The computational results of the anisotropic simulations

were compared with the biaxial experimental data as well as simulations utilizing the isotropic constitutive relation

$$W = \alpha(I_B - 3) + \beta(I_B - 3)^2 \quad (5.2)$$

$$t = 2\left(\alpha + 2\beta\left[\lambda^2 + \frac{2}{\lambda}\right]\right)\left(\lambda^2 - \frac{1}{\lambda}\right) \quad (5.3)$$

which has previously been used in the literature to model the AAA wall [38]. Patient specific data from a uniaxial tested specimen were fit to equations (5.2) and (5.3), which gave the parameters for the patient specific isotropic, or PT ISO, simulation. Constitutive model parameters for the average isotropic, or AVE ISO, simulation were previously derived by fitting data from 69 uniaxial tested specimens to equations (5.2) and (5.3) [29].

A subset of AAA wall biaxial specimen (n=14) were constructed in ABAQUS CAE using their respective dimensions from the experimental biaxial test. A Matlab (v. 6.5) code was written to select nodes along the four outer edges of the specimen (**Appendix H**). Each node was assigned a force boundary condition so that the specimen experienced 120 N/m tension per side. Patient specific data from one biaxially tested specimen were fit to the constitutive model developed in [Section 3.3.3](#) which yielded parameters for the patient specific anisotropic, or PT ANI, simulation. The constitutive model parameters derived for the average data set in [Section 3.3.3](#) were used for the average anisotropic, or AVE ANI, simulations. It should be noted that the uniaxial and biaxial specimens used to derive the constitutive relations used in the PT ANI and PT ISO simulations were taken from the same location within the same AAA patient.

The stress-strain relationships for the biaxial experiments were compared to the computational results of the PT ISO and PT ANI simulations. The strain at 60kPa for the biaxial

data was compared with the strain at 60kPa for both the isotropic and anisotropic simulations ([Figure 5-7](#)). The modulus at ~3% strain was calculated by

$$m = \frac{t_2 - t_1}{\varepsilon_2 - \varepsilon_1} \quad (5.4)$$

where t_1 and t_2 are the Cauchy stresses occurring 5 data points above and below 3% strain, respectively and ε_1 and ε_2 are the strains occurring 5 data points above and below 3% strain, respectively ([Figure 5-7](#)). All statistical comparisons were performed using a one-way ANOVA (Sigma Stat, v. 3.0) with a significance of $p < 0.05$.

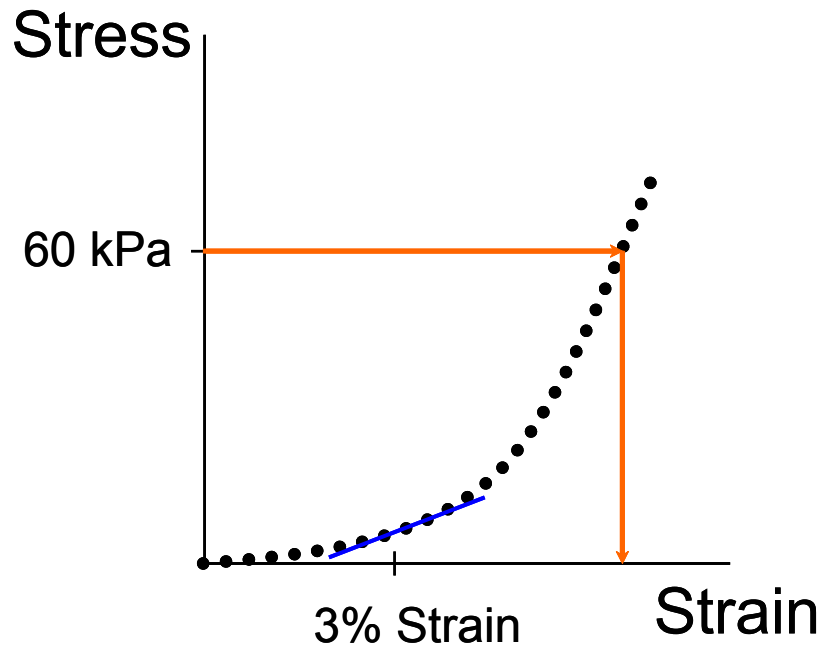


Figure 5-7: Definition of the strain and modulus used in comparing biaxial simulations

5.2.4 Cylindrical Simulation

As a first step to three dimensional simulations, the anisotropic constitutive model for the AAA wall developed in [Section 3.3.3](#) was used in the simulation of a pressurized cylinder. For this simulation, a 9 cm long cylinder of 3.0 cm diameter and 2 mm thickness was pressurized to 120 mmHg, with each end of the cylinder being constrained in all degrees of freedom. The analytical solution for the hoop stress due to the pressurization of a thick walled cylinder (thickness/radius = 0.13 > 0.05) takes the form

$$\sigma_{\theta}(r) = \frac{a^2 P_i - b^2 P_o}{b^2 - a^2} + \frac{(P_i - P_o) a^2 b^2}{(b^2 - a^2) r} \quad (5.5)$$

where $\sigma_{\theta}(r)$ is the hoop stress as a function of the radial coordinate (r), P_i is the internal pressure (120 mmHg), P_o is the external pressure (0 mmHg), a is the internal radius (1.4 cm), and b is the external radius (1.6 cm). The hoop stress at the luminal, mid-wall, and adventitial integration points of the shell element were compared to the analytical solution for the pressurization of a thick-walled cylinder.

5.2.5 Anisotropic AAA Finite Element Simulations

There were 35 AAAs simulated in the current work which were broken up into three groups: elective repairs (n=21, AAA1 – AAA21), non-ruptured repairs (n=5, N1 – N5), and ruptured repairs (n=9, R1 – R9). Elective repair simulations were derived from CT scans from AAA patients who underwent scheduled elective open repair of their AAA. Non-ruptured simulations consisted of AAA simulations for which there existed a set of CT scans at least 1 year apart, with the latter scan providing evidence the AAA remained quiescent. For these simulations, the images from the earlier CT scan were used to reconstruct the AAAs. Ruptured repair

simulations were derived from CT scans taking place no more than one year prior to AAA rupture.

The electively repaired AAAs (n=21) were utilized to investigate the differences in stress due to the implementation of the anisotropic constitutive relation for the AAA wall ([Section 3.3.3](#)) and biaxially-derived isotropic constitutive relation for the ILT ([Section 3.3.4](#)). For this purpose, the input file automatically created by the Matlab script described in [Section 4.2.7](#) was modified using several different combinations of constitutive models for the AAA wall and ILT. AAA simulations including the anisotropic relation for the AAA wall and isotropic relation for the ILT were denoted as ANI ISO. Simulations which used the anisotropic relation for the AAA wall ([Section 3.3.3](#)) and the biaxially-derived model for luminal layer of the ILT ([Section 3.3.4](#)) were denoted ANI ANI. For these simulations, the medial and abluminal regions of the ILT were modeled using the isotropic constitutive relation derived *for these layers* previously [59]. Simulations utilizing the previously developed isotropic constitutive relations for the AAA wall [38] and ILT [59] were labeled ISO ISO. Finally, the influence of anisotropy in the absence of the ILT was investigated with simulations utilizing the anisotropic (ANI NOILT) and isotropic (ISO NOILT) relations for the AAA wall with no ILT present. It is important to note that for each of the electively repaired AAA, the only difference present between these simulations is the changes in mechanical behavior of the AAA wall and ILT. For each individual simulation, the peak stress and strain within the AAA was recorded and compared across groups. In addition, the mean stresses acting on each AAA were also recorded and compared.

The ruptured and non-ruptured AAAs (n=9, n=5, respectively) were used to investigate whether or not the peak and average stresses within a AAA are different between these two groups. The presence of a statistically larger stress for the ruptured group would indicate that

stress may be an important factor in determining a given AAAs risk of rupture. The fact that the non-ruptured AAAs remained quiescent for an entire year would suggest this group of AAAs may have a decreased stresses acting on the AAA wall. Of course, since rupture is mechanically dependent on stress *and* strength, the lack of a statistical difference between these groups may be due to large differences in the strength of each of these AAAs. For all of the ruptured (R1-R9) and non-ruptured AAAs (N1-N5), the peak and mean stresses and strains acting on the AAA wall were recorded and compared.

5.2.6 Stress Concentration Quantification

In addition to the average and peak stresses acting on a given AAA, the concentration of stress was also quantified and compared for both the anisotropic vs. isotropic simulations as well as the ruptured vs. electively repaired AAAs. The AAA stress distribution was quantified with the use of another Matlab function (**Appendix I**) which calculated the maximum stress gradient within a given spherical region of interest. More specifically, a given AAA was traversed one node at a time calculating the gradients between the node of interest and all other nodes within a prescribed spherical distance ([Figure 5-8](#)). The maximum value of this gradient was chosen for each node of interest so that a value of stress distribution was calculated for each node on the entire AAA wall mesh. The magnitude of the peak stress gradient (which node had the highest stress gradient) located remotely from the models edges was compared to its experimental counterpart (e.g., maximum stress gradient for AAA1 ANI ISO versus AAA1 ISO ISO). These quantities were also compared in the ruptured versus non-ruptured groups.

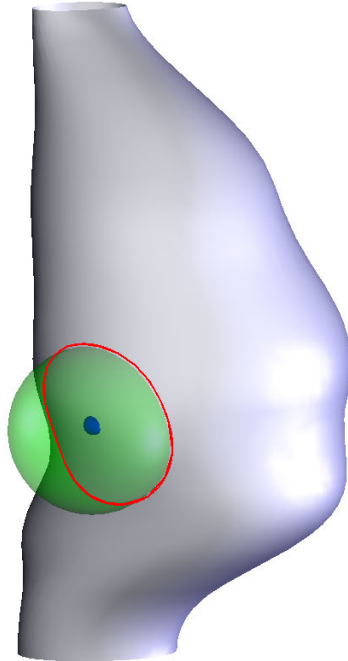


Figure 5-8: Determination of stress gradients within a spherical region of interest (large red sphere) around a finite element node (small blue sphere)

5.3 RESULTS AND DISCUSSION

5.3.1 Biaxial Simulations

Plots of the experimental and computational Cauchy stress versus stretch ratio for a representative biaxial specimen are shown in [Figure 5-9](#). Note the stiffer response for the PT ISO as compared to the PT ANI simulation. Note also that the similarity between the PT ANI computational data and the experimental biaxial data. Since both of the constitutive relations utilized in the PT ANI and PT ISO simulations were derived from tissue from the same location

and AAA patient, this plot displays the differences in stress prediction resulting from constitutive relations derived from uniaxial and biaxial testing. The biaxial data and average anisotropic simulations yielded significantly greater strain values compared to the average isotropic simulations at a given stress of 60kPa ([Figure 5-10](#)). At a given strain of $\sim 3\%$, the moduli of the average isotropic simulations were significantly greater than those of the biaxial data and average anisotropic simulations ([Figure 5-11](#)).

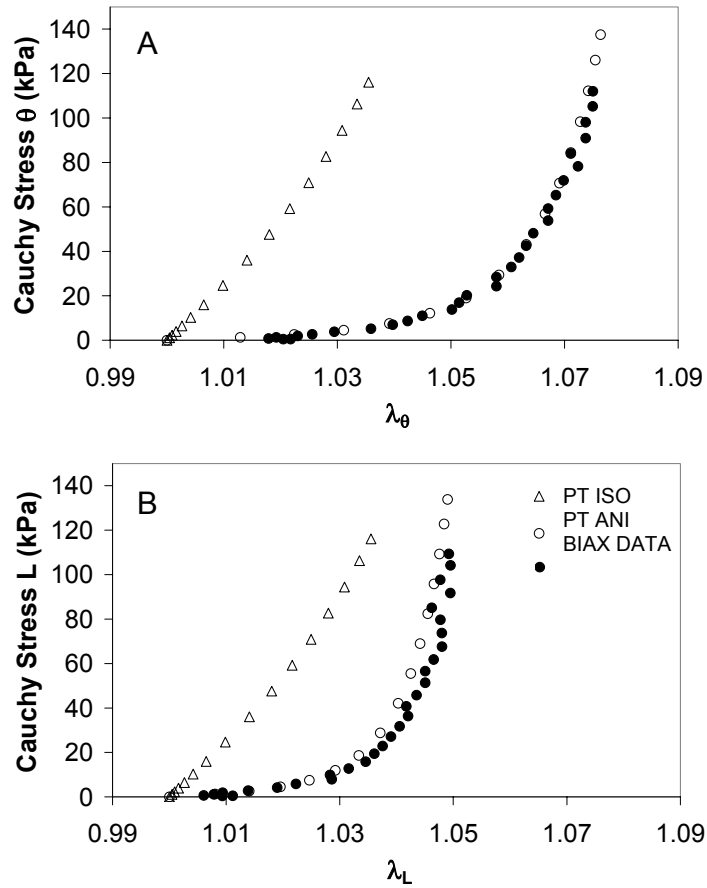


Figure 5-9: Circumferential (A) and longitudinal (B) Cauchy stress versus stretch ratio for the PT ISO and PT ANI simulations and the corresponding biaxial experimental data

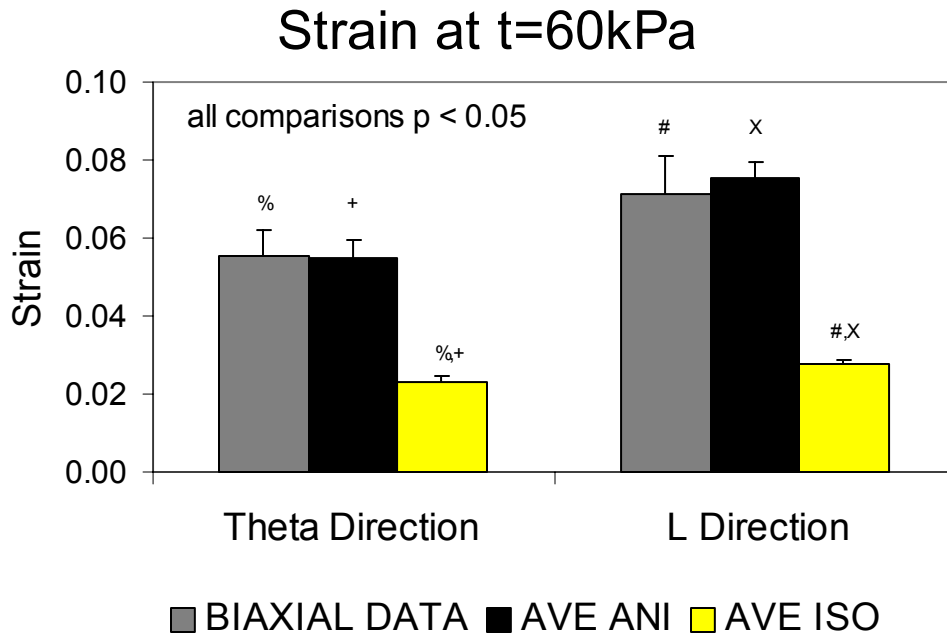


Figure 5-10: The strain values at t = 60 kPa for 14 biaxial simulations

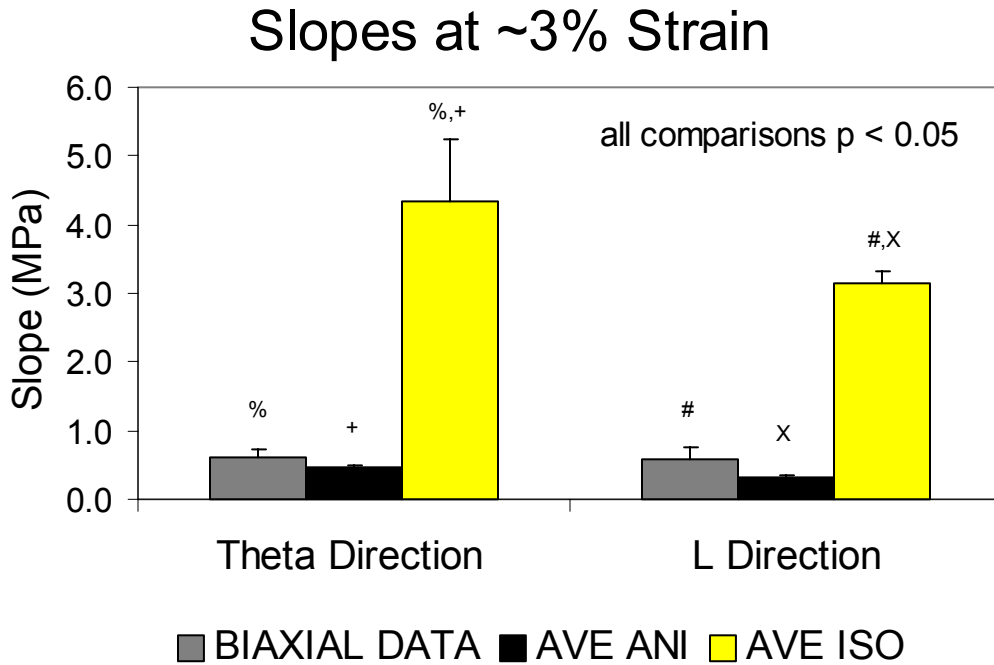


Figure 5-11: The moduli at a strain of 3% for 14 biaxial simulations

5.3.2 Cylindrical Simulation

The results of the cylindrical simulation utilizing the anisotropic UMAT and the analytical stresses using equation (5.5) are summarized in [Table 5-1](#). The percent error in the hoop stress at the luminal ($r=1.4\text{cm}$), mid-wall ($r=1.5\text{cm}$), and adventitial (1.6cm) integration points were 0.41%, 1.96%, and 5.30%, respectively. The hoop stress distribution for the finite element solution is shown in [Figure 5-12](#).

Table 5-1: Hoop stress for the analytical and computational solution of the pressurization of a thick walled cylinder

| | Stress (N/cm ²) | | |
|---------------|-----------------------------|----------------------|----------------------|
| | $r = 1.4 \text{ cm}$ | $r = 1.5 \text{ cm}$ | $r = 1.6 \text{ cm}$ |
| Analytical | 12.05 | 11.17 | 10.45 |
| Computational | 12.00 | 10.95 | 9.90 |
| % Error | 0.41 | 1.96 | 5.30 |

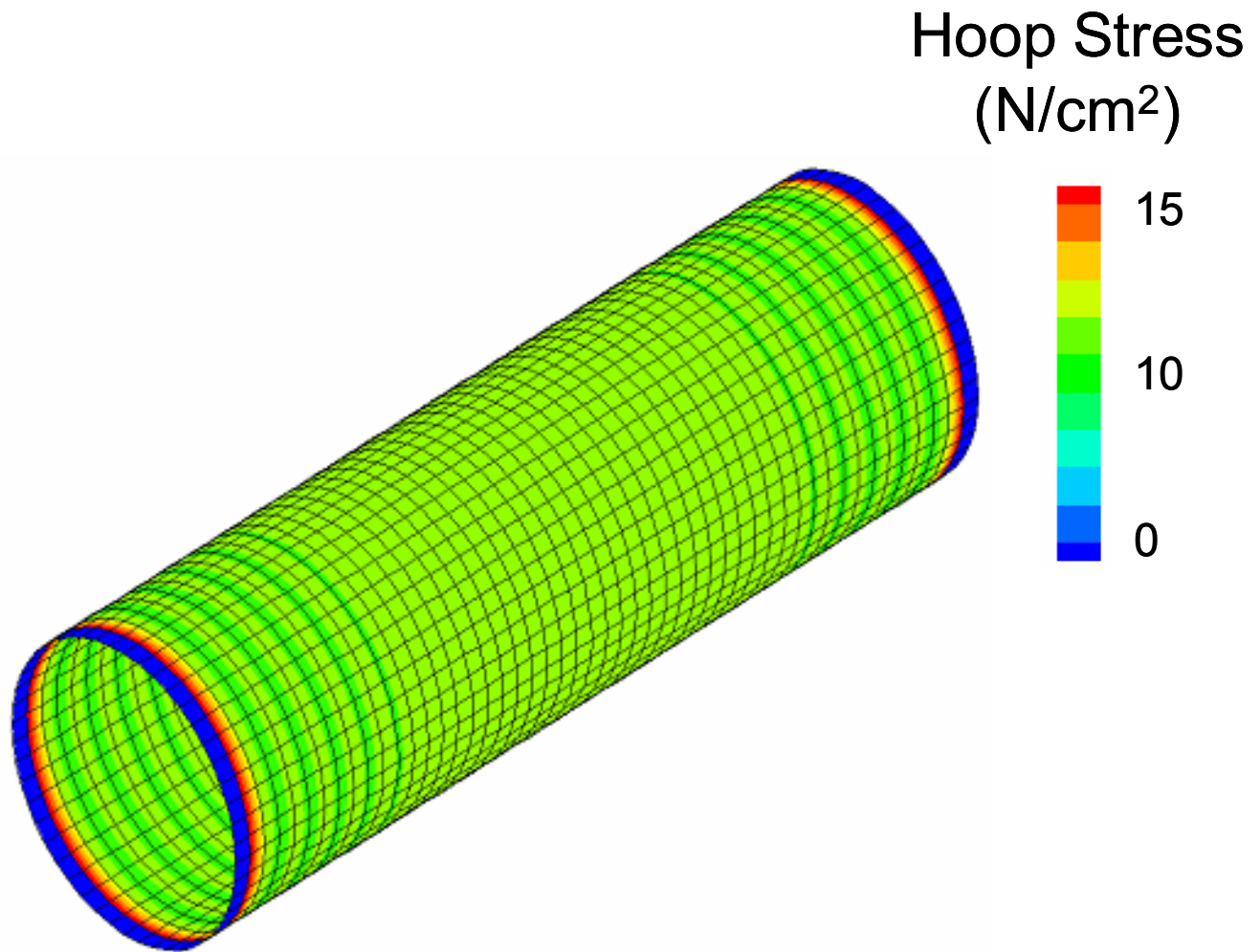


Figure 5-12: Maximum principal stress distribution for the computational solution of the cylindrical simulation

5.3.3 Anisotropic Versus Isotropic AAA Simulations

The peak maximum principal stresses for each of the electively repaired simulations are shown in [Table 5-2](#). In this table the different columns represent the different combinations of constitutive relations utilized for the AAA wall and ILT as described in [Section 5.2.5](#). Note that

AAA6 and AAA14 did not have any ILT, so only the ANI NOILT and ISO NOILT simulations were run for these AAAs. As detailed in this table, the mean peak stresses for the electively repaired simulations were 38.30 ± 3.04 , 36.06 ± 2.73 , 38.83 ± 3.31 , 54.70 ± 2.44 , and 51.27 ± 2.09 N/cm² for the ANI ISO, ISO ISO, ANI ANI, ANI NOILT, and ISO NOILT simulations, respectively. Using a paired t-test, there were significant differences between the ANI ISO and ISO ISO average peak stresses ($p < 0.001$) as well as between the ANI NOILT and ISO NOILT peak stresses ($p = 0.014$). Using a Wilcoxon Signed Rank test, there were no statistically differences between the average peak stresses of the ANI ISO and ANI ANI simulations. Whether the anisotropic or isotropic relation was used for the AAA wall, the peak stresses were statistically larger for simulations neglecting the presence of the ILT ($p < 0.001$ for ANI ISO vs ANI NOILT and ISO ISO vs ISO NOILT). In general, the presence of the anisotropic constitutive relation elevated the peak stress within a given AAA. It is interesting to note, however, that this was not true for all of the electively repaired AAA simulations as 3 out of the 21 simulations had an elevated peak stress for simulations utilizing the isotropic relation for the AAA wall (AAA9, AAA13, and AAA16). This was even more pronounced in the absence of the ILT, as 5 out of the 21 isotropic simulations had higher peak stresses than their anisotropic counterparts (AAA2, AAA8, AAA12, AAA14, and AAA18). The maximum principal stress distribution for a representative electively repaired AAA is shown in [Figure 5-13](#).

Table 5-2: Peak maximum principal stresses for the electively repaired AAA simulations. ANI ISO = anisotropic AAA wall + isotropic ILT; ISO ISO = isotropic AAA wall + isotropic ILT; ANI ANI = anisotropic AAA wall + biaxial derived luminal ILT; ANI NOILT = equivalent to ANI ISO excluding presence of ILT; ISO NOILT = equivalent to ISO ISO excluding presence of ILT

| Simulation | Peak Stress (N/cm ²) | | | | |
|------------|----------------------------------|---------|---------|-----------|-----------|
| | ANI ISO | ISO ISO | ANI ANI | ANI NOILT | ISO NOILT |
| AAA1 | 39.64 | 37.86 | 39.76 | 49.80 | 44.77 |
| AAA2 | 36.35 | 35.00 | 36.18 | 49.92 | 53.70 |
| AAA3 | 58.83 | 50.42 | 59.19 | 58.76 | 51.94 |
| AAA4 | 68.26 | 65.91 | 68.19 | 69.30 | 66.48 |
| AAA5 | 37.56 | 34.94 | 37.73 | 50.44 | 46.08 |
| AAA6 | | | | 68.70 | 54.68 |
| AAA7 | 32.08 | 31.22 | 32.46 | 49.54 | 48.34 |
| AAA8 | 37.72 | 36.43 | 37.81 | 73.50 | 76.37 |
| AAA9 | 14.51 | 16.10 | 14.08 | 43.74 | 38.01 |
| AAA10 | 66.10 | 60.81 | 75.65 | 82.96 | 63.83 |
| AAA11 | 42.59 | 39.20 | 42.79 | 55.46 | 51.68 |
| AAA12 | 33.10 | 29.63 | 32.83 | 39.38 | 44.56 |
| AAA13 | 19.07 | 19.68 | 19.14 | 59.61 | 50.59 |
| AAA14 | | | | 51.03 | 51.50 |
| AAA15 | 39.27 | 35.99 | 39.39 | 49.00 | 45.97 |
| AAA16 | 40.80 | 41.39 | 40.68 | 55.35 | 51.11 |
| AAA17 | 41.07 | 37.73 | 40.97 | 51.35 | 47.85 |
| AAA18 | 28.76 | 27.62 | 28.63 | 58.73 | 63.67 |
| AAA19 | 35.89 | 32.95 | 35.96 | 47.10 | 45.64 |
| AAA20 | 22.78 | 21.56 | 22.76 | 39.30 | 36.84 |
| AAA21 | 33.39 | 30.78 | 33.51 | 45.68 | 43.07 |
| MEAN | 38.30 | 36.06 | 38.83 | 54.70 | 51.27 |
| SEM | 3.04 | 2.73 | 3.31 | 2.44 | 2.09 |

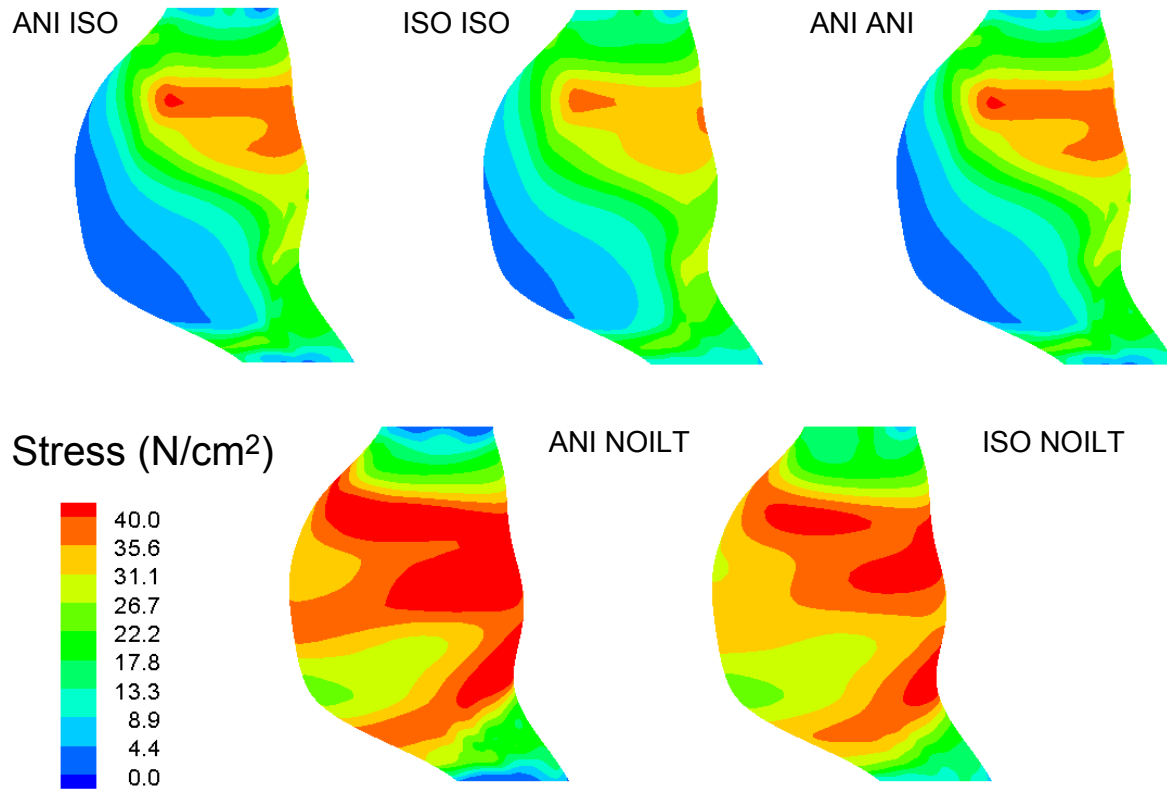


Figure 5-13: Maximum principal stress distributions for AAA17. ANI ISO = anisotropic AAA wall + isotropic ILT; ISO ISO = isotropic AAA wall + isotropic ILT; ANI ANI = anisotropic AAA wall + biaxial derived luminal ILT; ANI NOILT = equivalent to ANI ISO excluding presence of ILT; ISO NOILT = equivalent to ISO ISO excluding presence of ILT

The mean maximum principal stresses for each of the electively repaired simulations are shown in [Table 5-3](#). Again, the different columns in this table represent the different combinations of constitutive relations utilized for the AAA wall and ILT. As detailed in this table, the mean maximum principal stresses for the electively repaired simulations were 16.50 ± 1.88 , 17.67 ± 1.82 , 15.53 ± 1.7 , 30.29 ± 0.72 , and 29.83 ± 0.73 N/cm² for the ANI ISO, ISO ISO, ANI ANI, ANI NOILT, and ISO NOILT simulations, respectively. Using a paired t-test, there were significant differences between the ANI ISO and ISO ISO mean maximum principal

stresses ($p < 0.001$) as well as between the ANI NOILT and ISO NOILT mean maximum principal stresses ($p < 0.001$). Using a Wilcoxon Signed Rank test, there was a statistical difference between the mean maximum principal stresses of the ANI ISO and ANI ANI simulations ($p < 0.001$). Unlike the average peak stresses, the presence of the anisotropic constitutive relation generally reduced the mean maximum principal stress within a AAA that has ILT. When there was no ILT present, however, the mean maximum principal stresses were elevated in the anisotropic simulations. Again, these conclusions were not universal as there were simulations not following this trend.

Table 5-3: Mean maximum principal stresses for the electively repaired AAA simulations

| Simulation | Mean Stress (N/cm ²) | | | | |
|------------|----------------------------------|---------|---------|-----------|-----------|
| | ANI ISO | ISO ISO | ANI ANI | ANI NOILT | ISO NOILT |
| AAA1 | 19.30 | 20.76 | 19.96 | 28.93 | 28.33 |
| AAA2 | 12.72 | 15.31 | 13.35 | 35.38 | 35.17 |
| AAA3 | 23.46 | 23.84 | 23.71 | 26.09 | 25.92 |
| AAA4 | 33.72 | 33.45 | 33.96 | 35.40 | 34.86 |
| AAA5 | 16.59 | 17.28 | 16.97 | 29.04 | 28.38 |
| AAA6 | | | | 29.80 | 29.37 |
| AAA7 | 11.32 | 12.02 | 11.68 | 24.28 | 24.24 |
| AAA8 | 10.01 | 11.45 | 10.44 | 35.96 | 35.62 |
| AAA9 | 3.05 | 3.97 | 3.15 | 27.51 | 26.59 |
| AAA10 | 28.61 | 32.53 | 31.73 | 34.94 | 34.96 |
| AAA11 | 12.41 | 14.24 | 13.36 | 33.18 | 32.17 |
| AAA12 | 13.54 | 14.80 | 14.03 | 28.16 | 27.10 |
| AAA13 | 7.20 | 8.93 | 7.66 | 30.45 | 29.85 |
| AAA14 | | | | 32.37 | 32.19 |
| AAA15 | 15.35 | 16.46 | 15.90 | 30.79 | 29.80 |
| AAA16 | 16.00 | 17.42 | 16.51 | 29.06 | 29.06 |
| AAA17 | 15.00 | 16.02 | 15.45 | 30.35 | 30.26 |
| AAA18 | 7.30 | 8.42 | 7.53 | 31.88 | 31.64 |
| AAA19 | 12.94 | 14.10 | 13.15 | 27.31 | 27.02 |
| AAA20 | 7.84 | 9.43 | 8.18 | 26.90 | 26.42 |
| AAA21 | 17.93 | 19.14 | 18.39 | 28.28 | 27.60 |
| MEAN | 14.96 | 16.29 | 15.53 | 30.29 | 29.83 |
| SEM | 1.63 | 1.64 | 1.70 | 0.72 | 0.73 |

In addition to the peak and mean maximum principal stress acting within a given AAA, the peak and mean maximum principal strain was also quantified for each electively repaired AAA. The peak maximum principal strains in the ANI ISO simulations were statistically larger than for the ISO ISO simulations (0.139 ± 0.005 vs. 0.127 ± 0.005 , $p = 0.012$). There was also a slight increase in the peak maximum principal strains when comparing ANI ISO to ANI ANI simulations (0.139 ± 0.005 vs. 0.142 ± 0.005 , $p = 0.012$). There was no significant change in the peak maximum strain when neglecting the presence of the ILT (ANI NOILT vs. ISO NOILT, 0.142 ± 0.005 vs. 0.150 ± 0.003 , $p = 0.152$). The peak maximum principal strains for all of the electively repaired AAAs are shown in [Table 5-4](#).

The mean maximum principal strains in the ANI ISO simulations were also statistically larger than for the ISO ISO simulations (0.074 ± 0.004 vs. 0.069 ± 0.004 , $p = 0.001$). There was a slight decrease in the mean maximum principal strains when comparing ANI ISO to ANI ANI simulations (0.074 ± 0.004 vs. 0.076 ± 0.004 , $p < 0.001$). There was no significant change in the mean maximum strain when neglecting the presence of the ILT (ANI NOILT vs. ISO NOILT, 0.100 ± 0.001 vs. 0.101 ± 0.001 , $p = 0.538$). The peak maximum principal strains for all of the electively repaired AAAs are shown in [Table 5-5](#). The maximum principal strain distribution for a representative electively repaired AAA is shown in [Figure 5-14](#).

Table 5-4: Peak maximum principal strain for the electively repaired AAA simulations

| Simulation | Peak Maximum Principal Strain | | | | |
|------------|-------------------------------|---------|---------|-----------|-----------|
| | ANI ISO | ISO ISO | ANI ANI | ANI NOILT | ISO NOILT |
| AAA1 | 0.190 | 0.139 | 0.190 | 0.135 | 0.145 |
| AAA2 | 0.174 | 0.130 | 0.176 | 0.177 | 0.147 |
| AAA3 | 0.157 | 0.154 | 0.156 | 0.142 | 0.156 |
| AAA4 | 0.150 | 0.166 | 0.150 | 0.158 | 0.166 |
| AAA5 | 0.146 | 0.128 | 0.147 | 0.152 | 0.143 |
| AAA6 | | | | 0.208 | 0.154 |
| AAA7 | 0.133 | 0.121 | 0.132 | 0.112 | 0.147 |
| AAA8 | 0.159 | 0.139 | 0.159 | 0.136 | 0.180 |
| AAA9 | 0.088 | 0.087 | 0.087 | 0.114 | 0.129 |
| AAA10 | 0.148 | 0.163 | 0.150 | 0.146 | 0.166 |
| AAA11 | 0.124 | 0.143 | 0.123 | 0.130 | 0.157 |
| AAA12 | 0.120 | 0.116 | 0.120 | 0.131 | 0.144 |
| AAA13 | 0.111 | 0.092 | 0.113 | 0.135 | 0.149 |
| AAA14 | | | | 0.159 | 0.154 |
| AAA15 | 0.142 | 0.116 | 0.143 | 0.129 | 0.142 |
| AAA16 | 0.134 | 0.137 | 0.135 | 0.131 | 0.150 |
| AAA17 | 0.136 | 0.125 | 0.137 | 0.129 | 0.144 |
| AAA18 | 0.145 | 0.118 | 0.146 | 0.170 | 0.166 |
| AAA19 | 0.136 | 0.125 | 0.136 | 0.125 | 0.147 |
| AAA20 | 0.114 | 0.101 | 0.115 | 0.124 | 0.123 |
| AAA21 | 0.140 | 0.120 | 0.140 | 0.149 | 0.131 |
| MEAN | 0.139 | 0.127 | 0.140 | 0.142 | 0.150 |
| SEM | 0.005 | 0.005 | 0.005 | 0.005 | 0.003 |

Table 5-5: Mean maximum principal strain for the electively repaired AAA simulations

| Simulation | Mean Maximum Principal Strain | | | | |
|------------|-------------------------------|---------|---------|-----------|-----------|
| | ANI ISO | ISO ISO | ANI ANI | ANI NOILT | ISO NOILT |
| AAA1 | 0.099 | 0.084 | 0.101 | 0.099 | 0.100 |
| AAA2 | 0.078 | 0.068 | 0.081 | 0.106 | 0.112 |
| AAA3 | 0.099 | 0.095 | 0.099 | 0.099 | 0.096 |
| AAA4 | 0.102 | 0.104 | 0.102 | 0.103 | 0.106 |
| AAA5 | 0.079 | 0.075 | 0.081 | 0.101 | 0.098 |
| AAA6 | | | | 0.112 | 0.103 |
| AAA7 | 0.066 | 0.066 | 0.068 | 0.086 | 0.091 |
| AAA8 | 0.057 | 0.052 | 0.060 | 0.102 | 0.108 |
| AAA9 | 0.028 | 0.025 | 0.029 | 0.095 | 0.094 |
| AAA10 | 0.097 | 0.107 | 0.099 | 0.101 | 0.108 |
| AAA11 | 0.072 | 0.066 | 0.076 | 0.101 | 0.104 |
| AAA12 | 0.076 | 0.068 | 0.078 | 0.097 | 0.096 |
| AAA13 | 0.054 | 0.047 | 0.057 | 0.102 | 0.100 |
| AAA14 | | | | 0.103 | 0.106 |
| AAA15 | 0.078 | 0.071 | 0.081 | 0.101 | 0.099 |
| AAA16 | 0.079 | 0.075 | 0.081 | 0.096 | 0.097 |
| AAA17 | 0.075 | 0.067 | 0.078 | 0.098 | 0.100 |
| AAA18 | 0.048 | 0.044 | 0.050 | 0.106 | 0.106 |
| AAA19 | 0.071 | 0.066 | 0.072 | 0.098 | 0.096 |
| AAA20 | 0.054 | 0.048 | 0.056 | 0.097 | 0.096 |
| AAA21 | 0.088 | 0.082 | 0.089 | 0.101 | 0.099 |
| MEAN | 0.074 | 0.069 | 0.076 | 0.100 | 0.101 |
| SEM | 0.004 | 0.004 | 0.004 | 0.001 | 0.001 |

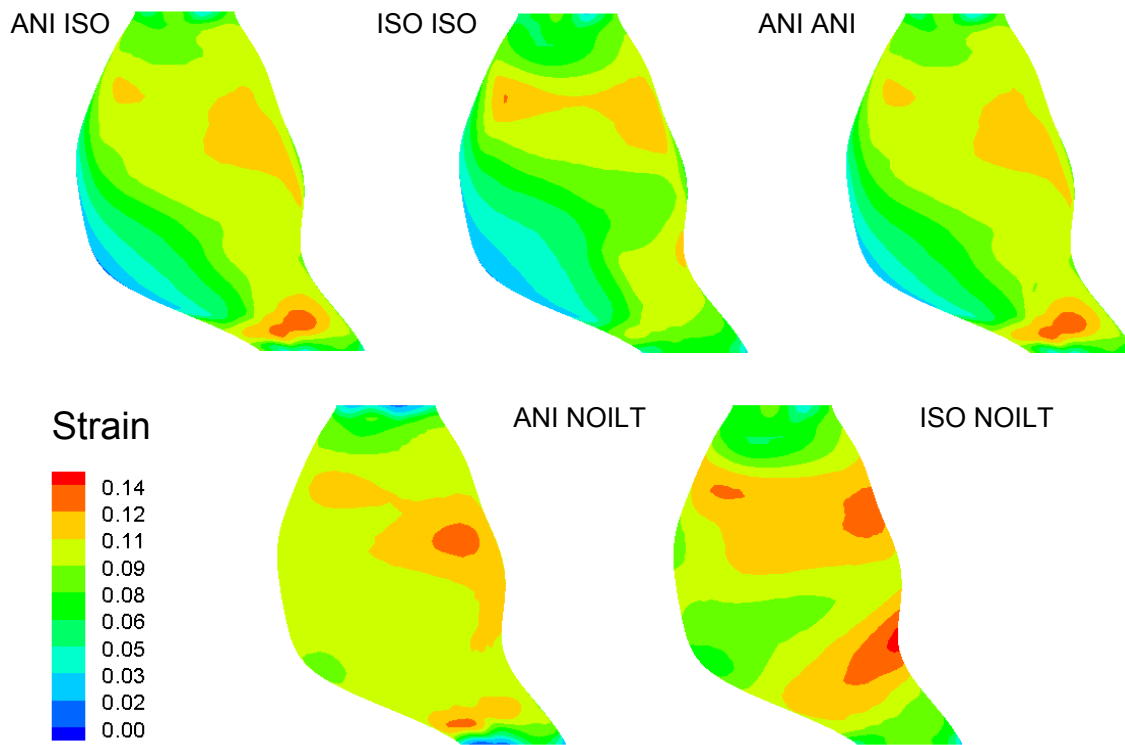


Figure 5-14: Maximum principal strain distributions for AAA17

The peak gradients of the maximum principal stress for each of the electively repaired simulations are shown in [Table 5-6](#). As detailed in this table, the mean maximum principal stresses for the electively repaired simulations were 27.06 ± 2.04 , 23.15 ± 2.02 , 27.52 ± 2.16 , 32.44 ± 1.39 , and 23.60 ± 1.36 N/cm³ for the ANI ISO, ISO ISO, ANI ANI, ANI NOILT, and ISO NOILT simulations, respectively. Using a paired t-test, there was a significant increase in the peak stress gradient for the ANI ISO versus ISO ISO simulations ($p=0.01$) as well as for the ANI NOILT versus ISO NOILT simulations ($p<0.001$). Using a Wilcoxon Signed Rank test, there was no statistical difference between the peak stress gradients of the ANI ISO versus ANI

ANI simulations ($p=0.113$). The utilization of the anisotropic constitutive relation for the AAA wall resulted in an increase in peak wall stress gradient, with these differences being amplified in simulations neglecting the presence of the ILT. The maximum principal stress gradient distribution for a representative electively repaired AAA is shown in [Figure 5-15](#).

Table 5-6: Peak maximum principal stress gradient for the electively repaired AAA simulations

| | Peak Stress Gradients | | | | |
|------|-----------------------|---------|---------|-----------|-----------|
| | ANI ISO | ISO ISO | ANI ANI | ANI NOILT | ISO NOILT |
| S1 | 34.87 | 26.24 | 34.54 | 34.04 | 27.94 |
| S2 | 32.68 | 28.10 | 32.51 | 34.57 | 24.41 |
| S3 | 46.84 | 28.23 | 47.67 | 41.16 | 26.51 |
| S4 | 30.30 | 18.60 | 30.40 | 28.45 | 18.75 |
| S5 | 25.40 | 23.60 | 25.53 | 27.67 | 23.85 |
| S6 | | | | 32.25 | 26.47 |
| S7 | 24.33 | 20.99 | 24.25 | 31.67 | 24.71 |
| S8 | 28.88 | 23.99 | 28.79 | 38.23 | 26.96 |
| S9 | 8.04 | 8.80 | 7.97 | 24.49 | 13.87 |
| S10 | 36.84 | 38.17 | 43.02 | 44.96 | 27.91 |
| S11 | 26.29 | 17.08 | 27.00 | 35.08 | 23.17 |
| S12 | 28.58 | 18.96 | 29.12 | 37.56 | 22.44 |
| S13 | 10.86 | 11.31 | 10.59 | 30.48 | 23.68 |
| S14 | | | | 37.97 | 19.69 |
| S15 | 19.48 | 19.23 | 19.50 | 24.72 | 19.80 |
| S16 | 29.91 | 31.10 | 30.48 | 28.43 | 25.97 |
| S17 | 19.67 | 16.11 | 20.12 | 26.30 | 16.72 |
| S18 | 23.67 | 22.11 | 23.64 | 26.37 | 24.58 |
| S20 | 40.63 | 48.89 | 40.60 | 44.18 | 44.12 |
| S21 | 22.58 | 17.39 | 22.80 | 26.76 | 16.65 |
| S25 | 24.22 | 21.03 | 24.38 | 25.91 | 17.45 |
| MEAN | 27.06 | 23.15 | 27.52 | 32.44 | 23.60 |
| SEM | 2.04 | 2.02 | 2.16 | 1.39 | 1.36 |

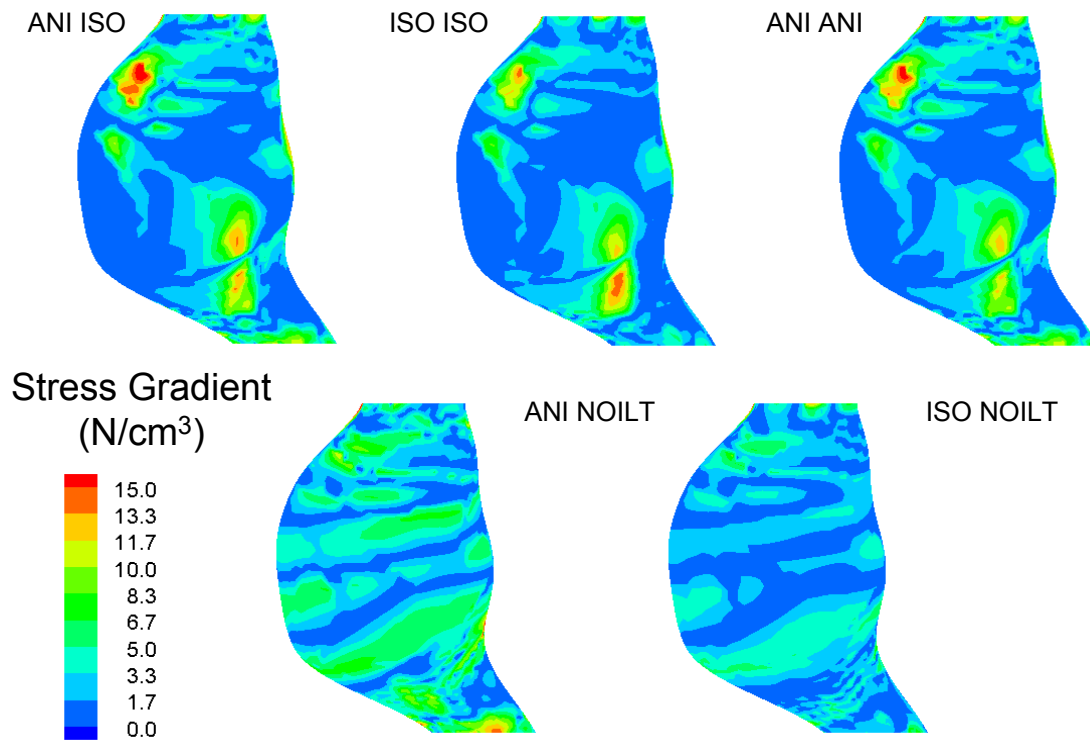


Figure 5-15: Maximum principal stress gradient distribution for AAA17

5.3.4 Ruptured Versus Electively-Repaired AAA Simulations

The peak maximum principal stresses for each of the non-ruptured and ruptured simulations are shown in [Table 5-7](#) and [Table 5-8](#), respectively. The ruptured simulations are from patients whose AAA ruptured, while the non-ruptured simulations are derived from CT scans from patients whose AAA remained quiescent for at least 1 year. In this dataset, there were two AAAs which did not have any ILT (N2 and R2). As detailed in this table, the mean peak stresses for the non-ruptured and ruptured AAAs were 45.98 ± 4.26 and 49.89 ± 4.02 N/cm², respectively ($p = 0.55$). There was no significant difference between the mean stresses for the non-ruptured

and ruptured AAAs (20.39 ± 1.66 vs. 20.65 ± 2.61 , $p = 0.95$). There were also no statistical differences in the peak and mean maximum principal strains between each of the groups (0.143 ± 0.008 vs. 0.161 ± 0.009 , $p = 0.20$ and 0.088 ± 0.005 vs. 0.085 ± 0.007 , $p = 0.75$, respectively). Maximum principal stress and strain distributions for a pair of representative AAAs are shown in [Figures 5-16](#) and [5-17](#), respectively.

Table 5-7: Peak and mean maximum principal stresses and strains for the non-ruptured AAA simulations

| Simulation | Peak Stress (N/cm ²) | Non Ruptured | | |
|------------|----------------------------------|----------------------------------|-------------|-------------|
| | | Mean Stress (N/cm ²) | Peak Strain | Mean Strain |
| N1 | 53.02 | 15.83 | 0.129 | 0.075 |
| N2 | 41.40 | 23.67 | 0.156 | 0.099 |
| N3 | 58.93 | 24.04 | 0.144 | 0.097 |
| N4 | 36.49 | 21.13 | 0.166 | 0.093 |
| N5 | 40.06 | 17.28 | 0.121 | 0.078 |
| MEAN | 45.98 | 20.39 | 0.143 | 0.088 |
| SEM | 4.26 | 1.66 | 0.008 | 0.005 |

Table 5-8: Peak and mean maximum principal stresses and strains for the ruptured AAA simulations

| Simulation | Peak Stress (N/cm ²) | Ruptured | | |
|------------|----------------------------------|----------------------------------|-------------|-------------|
| | | Mean Stress (N/cm ²) | Peak Strain | Mean Strain |
| R1 | 33.50 | 7.42 | 0.124 | 0.049 |
| R2 | 54.47 | 31.76 | 0.189 | 0.123 |
| R3 | 63.99 | 24.87 | 0.158 | 0.078 |
| R4 | 53.72 | 18.17 | 0.195 | 0.085 |
| R5 | 55.05 | 22.46 | 0.164 | 0.090 |
| R6 | 44.40 | 16.65 | 0.169 | 0.085 |
| R7 | 67.30 | 31.05 | 0.186 | 0.105 |
| R8 | 42.25 | 18.84 | 0.137 | 0.073 |
| R9 | 34.32 | 14.57 | 0.130 | 0.078 |
| MEAN | 49.89 | 20.65 | 0.161 | 0.085 |
| SEM | 4.02 | 2.61 | 0.009 | 0.007 |

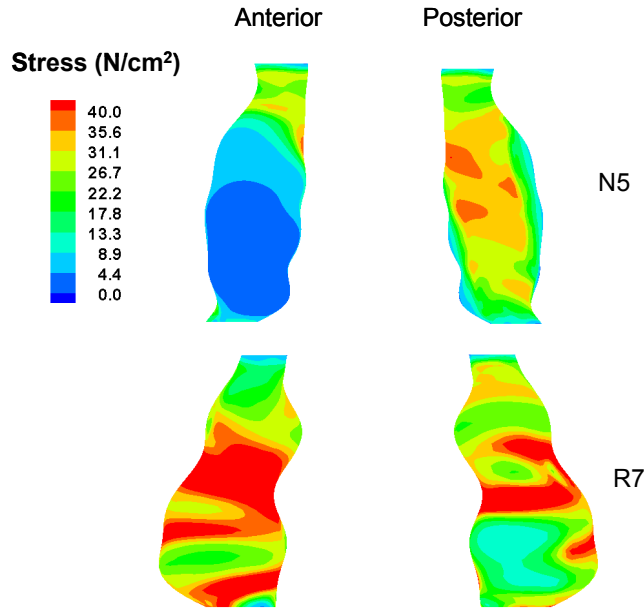


Figure 5-16: Maximum principal stress distributions for N5 and R7

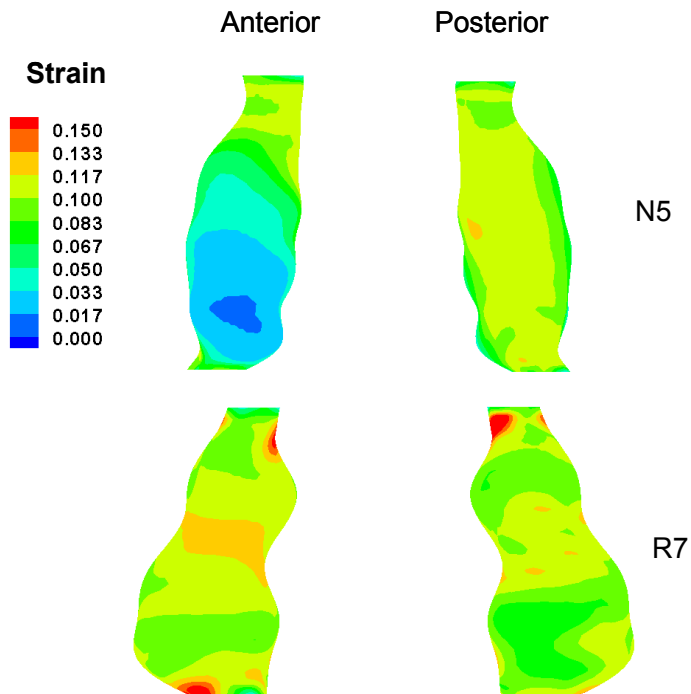


Figure 5-17: Maximum principal strain distributions for N5 and R7

The peak gradients of the maximum principal stress for each of the non-ruptured and ruptured AAAs are shown in [Table 5-9](#). As detailed in this table, the mean peak stress gradients for the non-ruptured and ruptured AAAs were 20.77 ± 3.74 and 30.96 ± 3.10 N/cm³, respectively ($p = 0.049$). Maximum principal stress gradient distributions for representative ruptured and non-ruptured AAAs are shown in [Figure 5-18](#).

Table 5-9: Peak maximum principal stress gradients for the non-ruptured and ruptured AAA simulations (* $p = 0.049$)

| Simulation | Peak Stress Gradients (N/cm ³) | | | |
|------------|--|----|----------|--|
| | Non Ruptured | | Ruptured | |
| N1 | 27.86 | R1 | 17.43 | |
| N2 | 19.13 | R2 | 40.30 | |
| N3 | 29.23 | R3 | 38.79 | |
| N4 | 8.40 | R4 | 27.27 | |
| N5 | 19.20 | R5 | 31.03 | |
| | | R6 | 27.91 | |
| | | R7 | 27.07 | |
| | | R8 | 26.97 | |
| | | R9 | 31.17 | |
| MEAN | 20.77* | | 30.96* | |
| SEM | 3.74 | | 3.10 | |

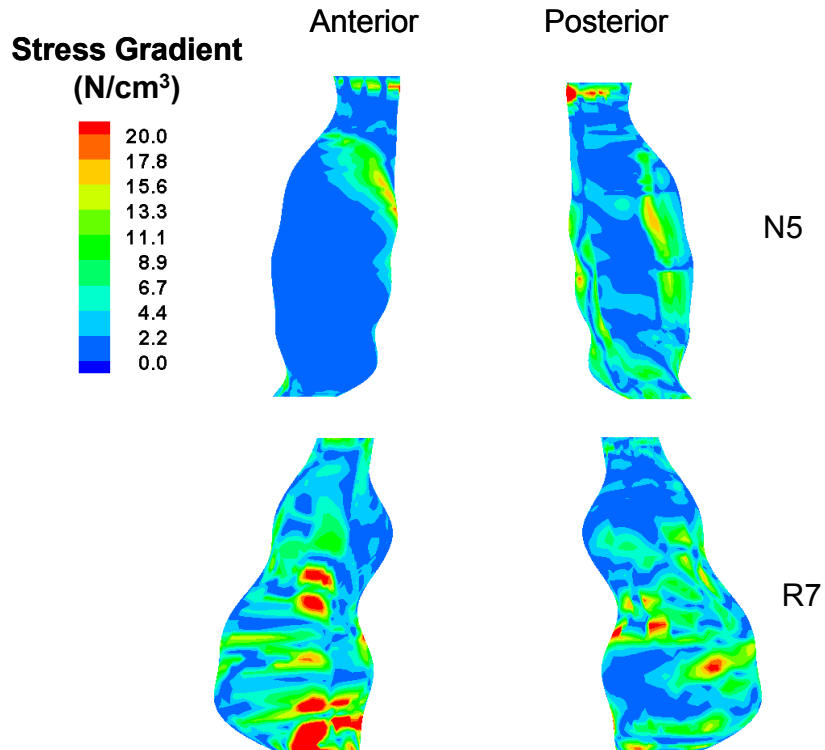


Figure 5-18. Maximum principal stress gradient distributions for N5 and R7

5.3.5 Discussion

An anisotropic constitutive relation was successfully implemented into the commercially available finite element package ABAQUS. The user-defined FORTRAN subroutine (UMAT) was tested and validated using biaxial tensile simulations and a simulation of the pressurization of a 3D cylinder. The user-defined anisotropic relation was then applied to patient-specific AAA simulations. The results for maximum principal stress, strain, and stress gradient for the anisotropic simulations were compared to simulations utilizing a previously derived isotropic constitutive relation (n=21, AAA1-AAA21). These results suggest that the peak wall stress is, in

general, significantly increased when using the anisotropic constitutive relation. This was not the case for all simulations, as for some simulations the isotropic relation resulted in a higher peak stress. The presence of the biaxially-derived constitutive relation for the luminal ILT did not largely alter the stresses acting on the AAA wall. The utilization of the anisotropic constitutive relation for the AAA wall resulted in an increase in peak wall stress gradient, with these differences being amplified in simulations neglecting the presence of the ILT. When comparing the ruptured to non-ruptured AAAs, there were no significant differences between the peak stress, mean stress, peak strain, and mean strain. The peak stress gradient, however, was significantly increased in the ruptured group of AAAs.

AAA simulations using axisymmetric hypothetical geometries have previously been created and analyzed in the literature [95, 123, 127, 128, 145, 146]. Such analyses fail to take into account the unique and patient-specific geometry known to be present in AAAs [107, 110, 147]. Several studies have since investigated the stresses acting on realistic patient-specific AAAs reconstructed from noninvasive imaging techniques [28, 33-35, 55, 94]. These studies revealed that the mechanical stress acting on the AAA wall cannot be estimated using simplistic hypothetical geometries or other crude analyses such as the Law of LaPlace. Raghavan et al. were the first to estimate the stresses acting on patient-specific AAAs using a geometry derived from CT scan images. Wang et al. improved upon this reconstruction technique with the inclusion of the ILT into the patient-specific modeling of AAAs [55]. The reconstruction technique utilized herein is an updated version of this reconstruction protocol, with decreases in reconstruction time and user to user variability as well as improvements in computational efficiency via a more automated reconstruction protocol.

The estimation of stress using the finite element method requires the identification of an accurate constitutive relation for the AAA wall and ILT. Early finite element simulations of AAA assumed the wall and ILT to act as linear isotropic materials, such that these materials could be modeled with the definition of a Young's modulus and Poisson's ratio [95, 111, 123, 127, 145, 146]. Such engineering analyses are appropriate for materials undergoing small strains (e.g., steel), while for materials undergoing large strains a more rigorous finite strain constitutive model must be derived. The AAA wall has been shown to undergo large strains in-vivo [72, 148], rendering significant error in the application of a small strain relation into finite element analyses of AAA. Raghavan et al. were the first to develop a large strain constitutive relation for the AAA wall [38], while Wang et al. did the same for the ILT [59]. The constitutive relations for both of these investigations can easily be implemented into most commercially available finite element packages. However, both of these relations are also isotropic relations derived from the uniaxial tensile testing of excised aneurysm contents.

A recent investigation has shown that the aneurysmal wall displays an anisotropic mechanical response [57] ([Sections 2.3.3 and 3.3.3](#)). The implementation of this anisotropic constitutive relation ([Section 5.3.3](#)) results in a significant increase in peak stress in most AAAs ([Table 5-2, Figure 5-13](#)). The use of an anisotropic relation did not, however, result in an increased peak stress level for *all* AAAs, suggesting that the effect of anisotropy on the peak stress within a given AAA is patient-specific. The differences in the stress distributions within a given AAA were also more amplified in cases where the ILT is neglected ([Figures 5-13, 14, 15](#)). It is interesting to note that the presence of an anisotropic relation for the AAA wall resulted in larger strains in the presence of ILT, while the anisotropic simulations had lower peak strains when neglecting the presence of the ILT ([Figure 5-14](#)). This figure also shows that in addition

to the magnitude of peak strain, the location of peak strain may also be different with the implementation of an anisotropic constitutive relation. This result was not true, however, for all AAA simulations. This result further confirms the idea that the stresses and strains within an individual AAA are largely a function of the locally varying geometrical parameters such as ILT thickness and local curvature.

The effect of the intra-luminal thrombus on the stresses acting on finite element simulations of AAA has been investigated previously [55, 93, 95, 149]. Mower et al. showed that the presence of the ILT can reduce the stresses acting on an AAA up to 51% [95]. Wang et al. were the first to implement a large strain constitutive relation into patient specific AAA simulations. Their results agree with Mower et al., showing the ILT acts as a stress cushion and can reduce wall stress up to 38% [55]. In contrast, work by Thubrikar et al. has shown that the pressures acting at the AAA wall are 91% of those in the lumen [149]. Similar findings were recently reported by Takagi et al [150]. Results reported here corroborate the work done by Mower et al. and Wang et al., in that the presence of the ILT (ANI ISO vs. ANI NOILT and ISO ISO vs. ISO NOILT) significantly decreased the peak stress acting on the AAA wall. It was also interesting to note that the inclusion of the biaxially-derived constitutive relation for the luminal layer of the ILT did not largely alter the stresses and strains within the AAA wall ([Tables 5-2, 4, and 5](#); [Figures 5-13, 14](#)). This is similar to results reported by Di Martino et al. who showed that the variation of mechanical properties of the ILT within physiological limits results in a variation of AAA wall stresses of only 5% [93].

When comparing the ruptured versus non-ruptured AAA simulations, it was found there was no significant difference in the peak stress, strain between these two groups. [Figure 5-19](#) shows the mean peak stress acting on all ruptured and non-ruptured AAAs for simulations

utilizing both of the anisotropic and isotropic constitutive relations for the AAA wall. The previously derived isotropic constitutive model for the ILT was used in all of these simulations [59]. While both constitutive relations showed a trend towards increased peak stress in the ruptured group, neither group reached significance. The smaller decrease in the p-value for the anisotropic comparison may be evidence for an improvement in stress prediction for this relation. These results are in contrast to work done by Fillinger et al., who showed a significant increase peak wall stress for ruptured and symptomatic AAAs compared to non-symptomatic AAAs who were electively repaired [33]. In their simulations the ILT was neglected, which may have provided for the differences not found in the current study.

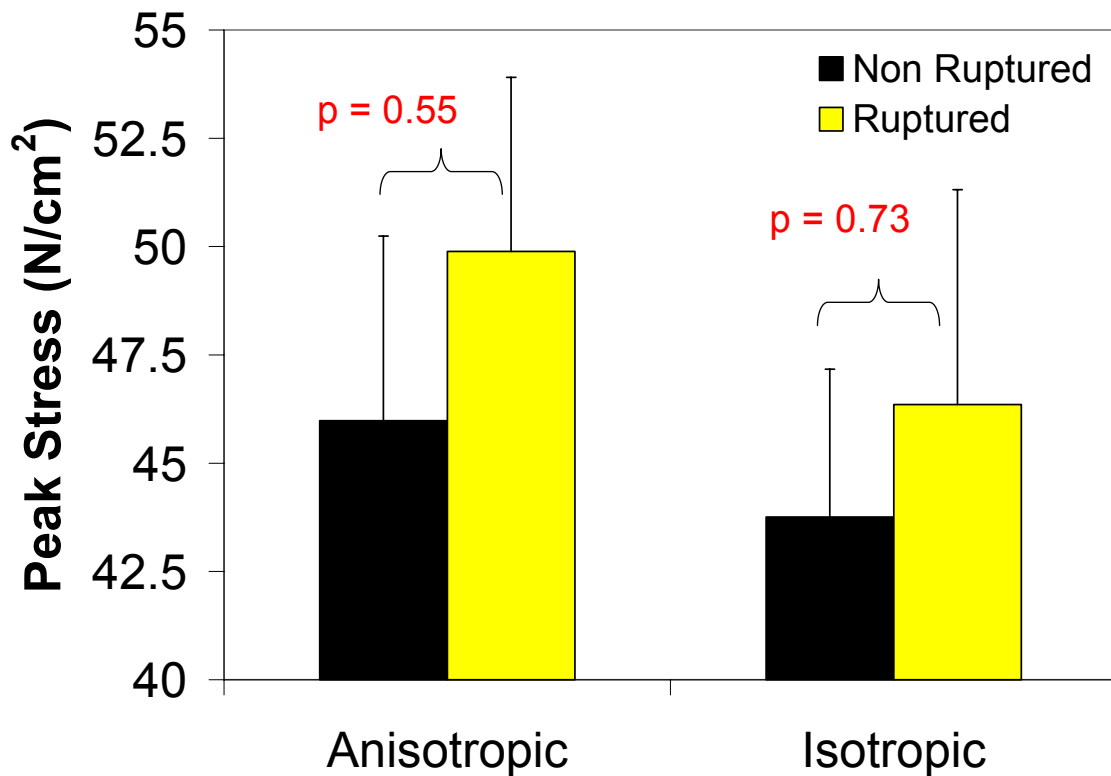


Figure 5-19: Comparison of anisotropic and isotropic simulations for ruptured and non-ruptured groups

Some of the limitations in the current work result from the assumptions applied in deriving a noninvasive estimation of AAA wall stress. One of these assumptions is that the material properties for all AAA patients can be modeled using one constitutive relation. This assumption stems from the inability to noninvasively derive a constitutive relation on a patient specific basis. While such a relation would be ideal, the error arising from using a population-wide anisotropic constitutive model can be assessed by analyzing the stresses on AAA simulations in which the upper and lower 95% confidence interval constitutive models (see [Section 3.3.3](#), [Table 3-8](#)) are utilized. Using a representative AAA, the error in peak wall stress was found to be 2.4% for the upper and 1.8% for the lower 95% confidence interval. These results are similar to results reported previously in which the upper and lower 95% confidence interval variations in isotropic AAA wall constitutive parameters resulted in less than 4% change in peak wall stress [38]. The same type of analysis was performed by Di Martino et al. on the ILT which resulted in a maximum variation of 10% on the AAA wall stress due to large yet physically reasonable variations in mean ILT model parameters. These results suggest that the peak stress acting on an individual AAA are relatively insensitive to the errors introduced using a set of mean or population-wide model parameters.

Another limitation of the current work is the assumption that the CT configuration (Ω_{CT}) from which the AAA models are derived is the “stress free” configuration (Ω_0). This assumption may lead to significant error in wall stress estimation as the state of stress within a blood vessel has previously been shown to be in a state of stress even in the unloaded configuration (due to residual stresses/strains) [66, 134, 135, 137]. There currently exists no experimental information on the residual stresses and strains present in the aneurysmal abdominal aorta. Such information would provide for a better understanding of the location on

the stress-strain curve the AAA acts in-vivo. In order to quantify the error associated with using the CT geometry as the “stress free” configuration ($\Omega_{CT}=\Omega_0$) the following analysis was performed. An asymmetrical hypothetical AAA was used to mimic the stress free configuration (Ω_0 , upper left of [Figure 5-20](#)). This AAA was pressurized to 100 mmHg in ABAQUS, from which the deformed geometry was extracted and assumed to correspond to the configuration of the AAA during a CT scan (Ω_{CT} , upper right of [Figure 5-20](#)). A 120 mmHg was then applied to this deformed geometry to mimic the boundary conditions utilized in the current work ($\Omega_0=\Omega_{CT}$, lower right of [Figure 5-20](#)). Of course, the “true stress” acting on the AAA can be modeled with the the pressurization (0 to 120 mmHg) of the zero stress state configuration. Comparing the nodal stresses between the “true stress” simulations and the simulation assuming $\Omega_{CT}=\Omega_0$ revealed a maximum and mean difference in stress of 1.0% and 0.7%, respectively ([Figure 5-20](#)). All of the above simulations were run with the anisotropic constitutive relation derived and implemented in the current work. The results reported here are in contrast to a similar investigation reported previously in our laboratory for the isotropic constitutive relation which showed a maximum error in peak stress of 8% (range 2% to 10%) [40]. Recent work by Marra et al. estimated the zero-stress state geometry of a patient-specific AAA using dynamic magnetic resonance imaging [151]. Their results indicate an error of 8.2% in peak wall stress when comparing the pressurization of the zero-pressure geometry to the diastolic dynamic magnetic resonance geometry pressurized to the systolic blood pressure [151]. While the results reported above indicate the assumption of $\Omega_{CT}=\Omega_0$ seems to introduce little error in the stress estimation of a hypothetical AAA, the effect of this assumption on stress estimations of patient-specific AAA requires further investigation.

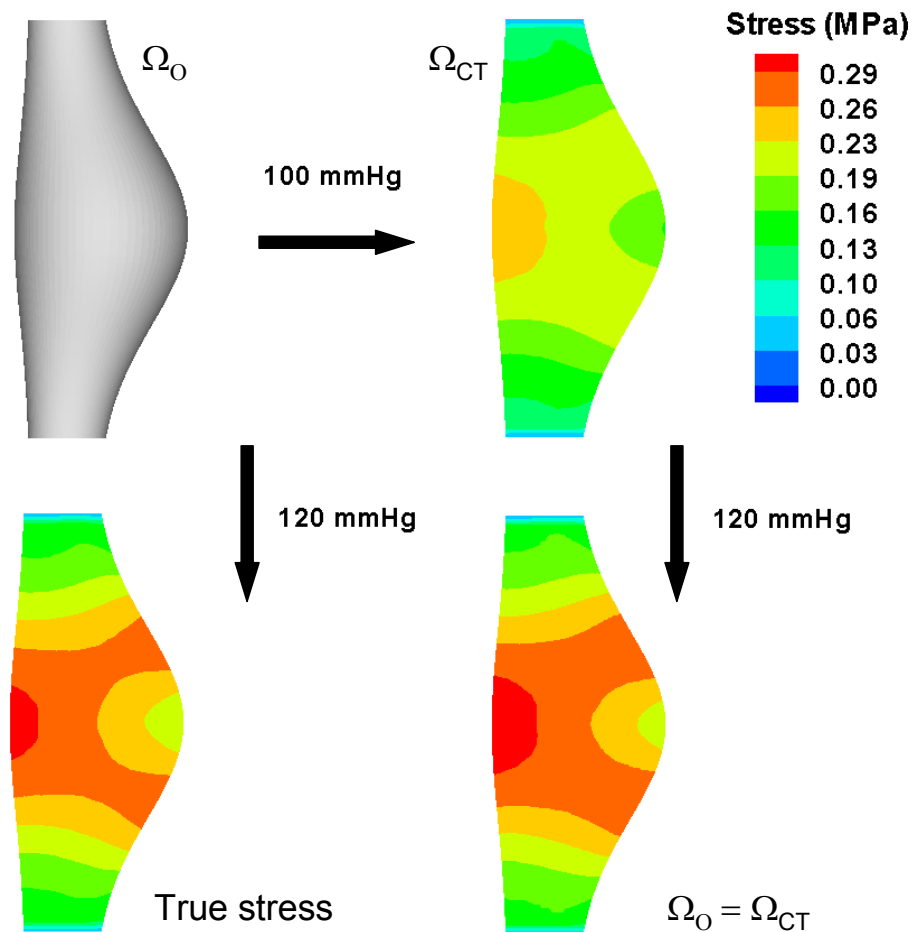


Figure 5-20: Differences in stress values using the assumption that the CT configuration is the zero stress configuration

Other limitations for the current finite element simulations include the assumptions used along the boundaries of the AAA. AAA are in a unique physical environment in-vivo, as they are bounded in the posterior by the spine and held in place by surrounding tissues and the tethering due to branching vessels. Once again, the lack of experimental data on the forces experienced by the AAA due to these physical boundary conditions precludes its inclusion in the finite element simulations investigated here.

Another key limitation in the present work stems from the constitutive modeling of the ILT. Herein we assume the ILT to act as a purely solid continuous material. The ILT, however, is known to be primarily composed of water [152]. The fluid phase present in the ILT may be important in not only the transmission of pressure and stress, but may also be important in governing the oxygen and nutrient transport to the AAA wall. To this end, Vorp et al. has previously shown with hypothetically shaped computational simulations that the presence of the ILT limits the transport of oxygen to the AAA wall [153]. Further work in this area should be aimed at how the fluid phase in the ILT (and its different layers [154]) effects the stresses acting on the AAA wall as well as how the fluid and nutrient flow within the ILT changes on a patient-specific basis.

On average, the presence of an anisotropic constitutive relation in patient-specific finite element simulations of AAA increased the peak stress acting on most AAAs. The lack of a consistent increase in peak stress in anisotropic vs. isotropic AAA simulations suggests that its effect may be patient-specific. While peak stress in simulations using both relations was not found to be a significant predictor of AAA rupture, the anisotropic relation utilized here may provide a better estimate of stress as evidenced by the larger difference in peak stress when comparing ruptured to non ruptured AAAs. The anisotropy present in the AAA wall ([Section 3.3.3](#)) was successfully implemented into patient-specific finite element simulations of AAA. The presence of a multiaxial stress-state for the AAA wall in-vivo suggests that this implementation provides a more accurate state of stress for the AAA wall.

6.0 NONINVASIVE ESTIMATION OF AAA WALL STRENGTH

6.1 INTRODUCTION

From a biomechanical point of view, AAA rupture occurs when the stress in a region of the aneurysm wall exceeds the local strength of the tissue. It is therefore believed that a patient-specific biomechanics-based approach that utilizes estimates of both wall stress and wall strength distributions would provide the most reliable assessment of the propensity for rupture of a particular AAA.

As described in earlier, several researchers propose the use of finite element analysis for the noninvasive prediction of patient-specific AAA wall stress distribution [28, 32, 34, 35, 55, 92, 93, 95, 111, 123, 146]. The peak stress acting on a AAA was recently utilized to demonstrate that peak wall stresses for ruptured AAA are significantly higher than electively repaired aneurysms, even when controlled for size. [35, 155] This study suggested that using peak wall stress to assess AAA rupture risk is an improvement over using AAA diameter. However, since local wall stress is only one of the two factors dictating mechanical failure of the AAA wall, the most accurate estimation of the rupture potential of individual AAA requires that the wall strength distribution be taken into account as well. That is, a certain value of peak wall stress

may cause rupture for one AAA but not for another depending on that individual AAA's wall strength distribution.

Despite this, AAA wall strength distribution has not been given the same amount of investigative attention as the wall stress distribution. Vorp et al. first documented the failure strength of AAA wall as measured by ex vivo tensile testing of freshly obtained AAA samples. [32] Subsequent work has shown that AAA wall strength differs from location to location within a given aneurysm, and is generally weaker in regions of increased thickness of adjacent intraluminal thrombus (ILT). [31] However, for the purpose of clinically assessing rupture potential of AAA, a noninvasive means to calculate in vivo wall strength distribution is necessary. There is currently no technique available in the literature to accomplish this.

The goal is therefore to develop and validate a noninvasive method to evaluate AAA wall strength distribution in vivo. To accomplish this, statistical methods will be used to construct a model relating the local strength of the AAA wall to certain carefully chosen noninvasively measurable variables.

6.2 SUMMARY OF SHORTCOMINGS OF PREVIOUS APPROACH

Previous work performed by David H. J. Wang was aimed at developing a method for noninvasively predicting AAA wall strength [40]. The work described herein utilizes similar techniques to that used previously, with several notable improvements. First, the method used previously used to measure locally varying predictors of AAA wall strength (e.g., local ILT thickness, local AAA diameter) was user-dependent and possibly biased. This method involved

the isolation of a small rectangular piece of AAA wall with the entire thickness of ILT attached. This wedge of ILT and wall was taken to the laboratory bench top and used in the measurement of the local value of ILT thickness. The remaining ILT (that remaining after the wedge of ILT and wall was removed) was also required in order to determine local values for transverse diameter ([Figure 6-1](#)).

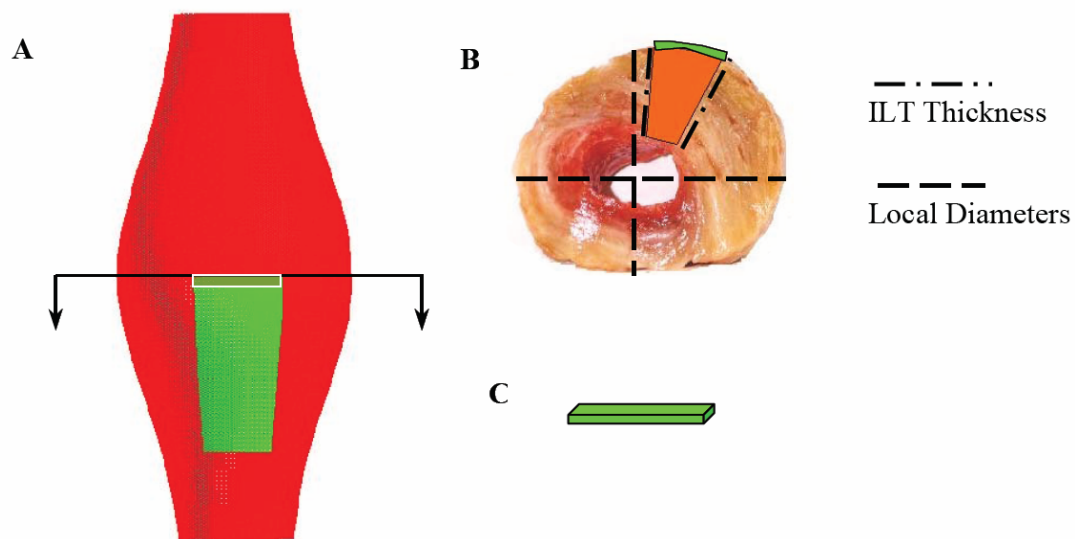


Figure 6-1: Schematic of AAA wall sample preparation and local parameter measurement using the previous method. A wedge-shaped sample of ILT was cut and removed with a piece of wall attached (A). Then the whole thrombus was removed from the aneurysm as is routine in open surgical repair. The wedge-shaped ILT was put back in the whole thrombus and sliced longitudinally, as shown in (B). The local ILT thickness and local diameter was then measured on the cross-section. A slice of circumferentially-oriented wall specimen was harvested from the wedge-shaped sample edge (C). Taken from [40].

This technique may have been biased as to the type of ILT isolated from electively repaired AAAs since it stands to reason that any ILT which was not highly structured (of liquid consistency) would not be able to be isolated as a wedge attached to the AAA wall. In addition, this method for measuring ILT thickness and local diameter does not easily translate into the clinical arena, since imaging modalities such as CT scan are typically used to measure such variables as transverse diameter. Given these limitations to the earlier approach, a new method which uses CT scan images to measure locally varying values of ILT thickness and local diameter was developed. This method is described in detail later in this chapter.

Secondly, the prior method used to calculate the thickness of an individual uniaxial tensile testing specimen was also thought to be suspect. In earlier tests, the value of thickness was measured physically with a contacting digital caliper. Since this method is not non-contacting, it most likely compressed the tissue and resulted in an artificially small value of true AAA wall thickness. This resulted in a statistical model predicting wall strength above the range of AAA wall strength reported in the literature previously. For the specimens tested since the prior work, a laser micrometer was used as a non-contacting method for measuring the thickness of AAA uniaxial tensile testing specimens. A equation was also developed in order to convert the earlier measured values of wall thickness to more those measured via the laser micrometer. This process is also described in detail later in this chapter.

Thirdly, and probably the most concerning of all of the limitations of the earlier approach was the assumption of independence between uniaxial specimens. While the earlier methodology checked for (and provided evidence for) independence using appropriate statistical techniques, this assumption would not be expected to hold given a large enough dataset. Simply stated, in linear regression each sample used in the derivation of the statistical model should be

completely independent and uncorrelated with every other sample. The fact that there were some AAA patients used in the model construction for which there was more than one uniaxially derived value of strength suggests that this assumption is inappropriate, even if appropriate statistical checks suggest otherwise. In order to correct for the inherent autocorrelation in the data used in the model construction, the method of linear mixed-effects modeling was utilized. This method is still linear regression and therefore must meet all of its assumptions except for the autocorrelation, or independence assumption.

Fourthly, the previous method used in defining the variable NORD was the local transverse diameter divided by the maximum transverse diameter. The variable NORD was included in the model as a measure of the longitudinally varying value of transverse diameter. Its normalization allows the comparison of this variable across AAA patients. Normalizing the local transverse diameter by its maximum value within a AAA results in a variable whose maximum is 1. Since the variable NORD was meant to be a measure of the extent of dilation within a AAA, using a value of non-dilated diameter to normalize the local transverse diameter provides a more appropriate measure of dilation since its upper limit is in theory not bounded. Therefore, the variable NORD in the current work was defined as the local value of transverse diameter normalized to a value of non-dilated aortic diameter based on the patient's age and sex.

Finally, the statistical model for AAA wall strength was further improved by increasing the number of specimen's used in the model construction. In the prior methodology, the entire dataset was divided into two groups – one for model construction and one for model validation. Here, we combine these two datasets and add additional data for the construction of the statistical model, thereby increasing the power of the statistical regression analysis. [Table 6-1](#) summarizes all of the improvements made to the statistical model derived previously.

Table 6-1: Improvements in model used to noninvasively estimate AAA wall strength

| | Old | New |
|--|----------------------------|--------------------------------|
| ILT thickness and local diameter measurement | Bench top | CT scan |
| NORD Definition | Local / maximum diameter | Local / nonaneurysmal diameter |
| Autocorrelation assumption | Yes | No |
| N (construction) | 34 specimens (11 patients) | 81 specimens (39 patients) |
| Tensile testing thickness | Caliper | Laser micrometer |

6.3 METHODS

6.3.1 Initial Selection of Variables Predicting AAA Wall Strength

In order to develop a noninvasive estimate of AAA wall strength we will use a statistical approach. Linear regression techniques will be used to relate local values of wall strength to other noninvasively measurable predictor variables (sometimes called covariates). The lack of attention given to variables directly influencing AAA wall strength in the literature requires we utilize a different approach to identify potential predictors to be used in the regression analysis. We will introduce several variables that have been associated with AAA enlargement and

rupture in the literature and include these as initial predictors of AAA wall strength. Backwards step-wise linear regression will then be used to identify those variables that are required to predict AAA wall strength. All statistical analyses were carried out in the statistical program NCSS 2004, except the mixed-effects regression which was carried out in the statistical package R, v. 1.9.1. The following sections describe the rationale for choosing this subset of potential predictor variables.

6.3.1.1 Smoking

A recent retrospective study by Lindblad et al. found that men who smoked, among other factors, were at significantly higher risk for developing large AAAs [156]. Wanheinen et al. also provided evidence that current smoking affects the later development of AAA [157]. Other ultrasound screening surveys and case-control studies have demonstrated a strong association between cigarette smoking and AAA [158, 159]. Smoking has also been associated with rapid AAA enlargement and rupture [160, 161], as it was reported that there is a 5-fold increase in AAA rupture risk for cigarette smokers versus non-smokers [161]. While the strength of the association and the presence of a dose response suggest a causal relation between smoking and AAA development, specific mechanisms are unclear [162]. One possible mechanism is the continued absorption of chemicals from smoking may have effects on the proteolytic and fibrinolytic activities of the AAA wall, and also on smooth muscle cell metabolism [160], each of which could have a direct affect on AAA wall strength.

Cohen et al. investigated the effect of cigarette exposure on rabbit aortic elastase activity. Their results showed an increase in elastase activity in rabbits exposed to cigarette smoke compared to control animals [163]. Cannon et al. studied the correlation between smoking and

the amount of circulating serum proteolytic activity and found this to be increased in patients with AAA. Nordskog et al. also studied the effects of cigarette smoke condensate on cultured human aortic endothelial cells and found there to be increase expression of genes involved in the release of extracellular matrix degradation proteases (MMP-1, MMP-8, MMP-9) [164]. Since several researchers have suggested that the development and rupture of AAA is associated with a disruption in the balance of collagen and elastin turnover [53, 165-167], these studies provide evidence that smoking may be an important factor in the development of AAA. For these reasons smoking (SMK) was included as a possible covariate in the construction of the statistical wall strength model.

6.3.1.2 Family History

Familial tendency of AAA has been demonstrated by several investigators, including our laboratory [168, 169]. In a large case-control study by Darling et al. [170], 15 percent of AAA patients reported an AAA in at least one first degree relative as compared with 1.8 percent of controls (odds ratio = 9.7). Other studies have reported similar findings [168, 171, 172]. To our knowledge, no studies exist that examine the influence of family history on AAA wall microstructure or biomechanical properties. However, because of the strong familial tendencies in AAA disease, we chose to include family history (HIST) as a potential predictor of AAA wall strength.

6.3.1.3 Gender

Although the frequency of AAA among men is between two to four times higher than among women in the same age group [173, 174], epidemiologic studies have shown a higher risk of rupture of AAA in women than in men. [173, 174] A recent study by Wilson et al. showed that women have a shorter time to AAA rupture from initial diagnosis compared with men [175]. Solberg et al. recently investigated the association of gender with the growth rate of AAAs and found a significant increase in the growth rate of AAAs in women than in men [176]. These differences may be a result of the estrogen mediated reduction in macrophage (MMP-9) production found in women [177]. These studies, as well as preliminary data from our laboratory [178], suggest that there may be a difference in AAA wall integrity between males and females. In addition, other work in our laboratory has shown a trend towards a decrease in strength for specimens taken from women versus men undergoing elective repair of their AAA ([Figure 6-2](#)). These results suggest possible gender differences in AAA development and rupture. For this reason, gender was included as a potential covariate in the construction of the statistical wall strength model.

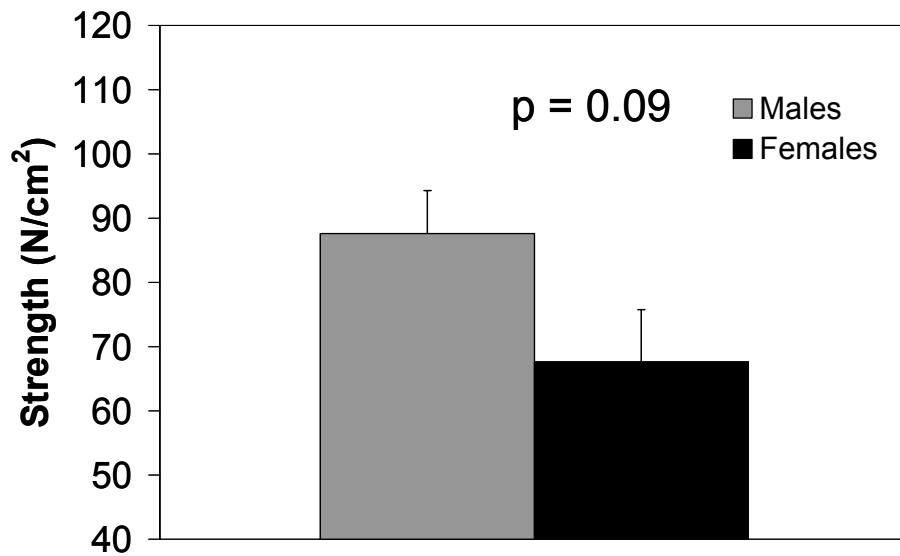


Figure 6-2: Mean wall strength values for men (n=24) versus women (n=10)

6.3.1.4 Age

In healthy arteries, the synthesis and degradation of collagen and elastin are carefully regulated by a balance between the activation and inhibition of proteases and their antagonists [179]. In the process of aging, this balance is temporally destroyed through the induction of matrix metalloproteinase gene expression or the secretion of enzymes by inflammatory cells. [179] This imbalance may in fact be responsible for the large changes observed in the biaxial mechanical behavior of the abdominal aorta as a function of age ([Section 2.3.1](#)) [56]. It is also known that the prevalence of AAA increases with increasing age [173, 174]. Since the development and progression of aneurysmal disease is thought to be concomitant with decreases in extracellular matrix strength, this observation suggests that the aorta as a whole may become weaker with advancing age [162]. The changes in the extracellular matrix as a function of age has been

quantified previously in the literature [179-181]. These studies show that the amount of collagen present in the aorta increases with age, while the amount of elastin decreases with age. These changes may be a result of the recent report of increases in MMP-2 activity in the aging aorta [182] ([Figure 6-3](#)). The age of a AAA patient was therefore considered important in predicting the strength and therefore included as a potential covariate in the statistical wall strength model.

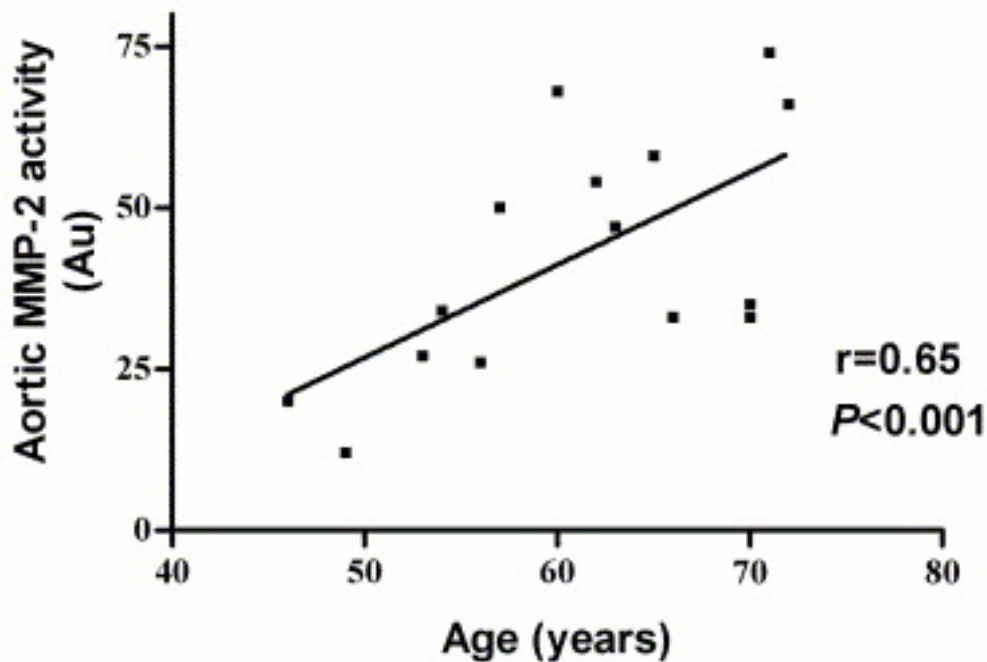


Figure 6-3: Correlation between age (in years) and aortic matrix metalloproteinase-2 (MMP-2) activity. Taken from McNulty et al. [182]

6.3.1.5 Intraluminal Thrombus Thickness

The intima and subintimal media in the infrarenal aorta are not nourished by the vasa vasorum, but instead by luminal blood flow [183]. Computational and experimental studies by Vorp et al.

have shown data supporting the hypothesis that the ILT commonly found in AAA serves as a barrier to the oxygen supply from the lumen, possibly causing hypoxia of the aortic wall. [31, 153] Kazi et al. also reported that aneurysm wall covered with ILT displayed more frequent signs of inflammation, apoptosis, and degraded extracellular matrix than AAA wall in which there was no ILT [184]. A more recent report by this group showed the differences in protease expression between thrombus-free and thrombus covered wall [185]. Work in our laboratory has also shown a strong inverse correlation between the ILT thickness and adjacent wall strength within the same AAA [135] ([Figure 6-4](#)). Given these previous studies showing the alterations in the mechanical integrity of ILT-covered aneurysmal wall, the local ILT thickness was taken as a potential predictor of AAA wall strength.

Association of wall strength with ILT thickness

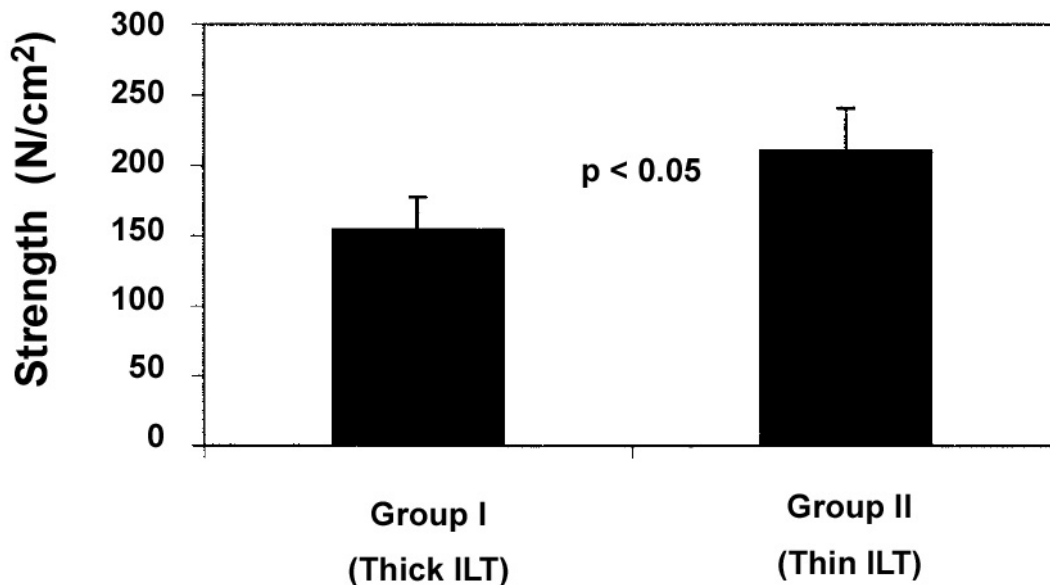


Figure 6-4: Comparison of tensile strength for group I versus group II specimens. Significant difference was noted by means of the paired t test. Taken from Vorp et al. [31]

6.3.1.6 Maximum and Local Transverse Diameter

As a AAA develops and enlarges, medial lamellar units are destroyed, and the main structural proteins responsible for providing structural integrity to the aorta (namely elastin and collagen) are degraded. [88, 186] Our laboratory has shown that there is also a significant decrease in the tensile strength of the AAA compared to nonaneurysmal tissue [30]. This observation along with evidence that larger AAAs have a higher risk of rupture [187, 188] might also suggest that the failure strength of AAA wall reduces progressively as a AAA enlarges. Evidence of a possible decrease in structural integrity of the AAA wall with increasing AAA diameter has also been given by Papalambros et al. who showed an increase in MMP-9 activity in large (>6 cm) AAAs [189]. Given these previous investigations displaying the connection between AAA wall structure and size, both the maximum transverse diameter and normalized local transverse diameter (NORD) were taken as potential predictors of wall strength.

In summary, the variables that were included as potential predictors of AAA wall strength were gender (SEX), age (AGE), family history (HIST), smoking (SMK), local ILT thickness (ILT), maximum transverse diameter (SIZE), and normalized local transverse diameter (NORD).

6.3.2 Specimen Procurement and Variable Recording

Consenting patients undergoing traditional AAA repair surgery at the University of Pittsburgh Medical Center provided tissue samples and predictor variable information. All procedures were carried out in accordance with guidelines established by the NIH and the University of Pittsburgh biomedical Institutional Review Board. The entire dataset was randomly separated into the following groups: group A, which consisted of 43 uniaxial specimens from 21 patients, group B,

which consisted of 40 uniaxial specimens from 18 patients, and group C, which consisted of a union of groups A and B minus any statistical outliers as described in [Section 6.3.4.3](#). Group A was used in the choice of independent variables via backwards stepwise linear regression. Group B could then be used as a means of assessing the variability in model parameters. Finally, since Group C was composed of a union of Groups A and B (and therefore provided the largest amount of statistical power), it was used in the derivation of a final statistical model of AAA wall strength. Comparing the 95% confidence intervals for the model coefficients derived from regressing each of these groups to the final statistical model provides a means of analyzing the variability of these coefficients as well as validating the statistical model.

6.3.2.1 Demographical Data Collection

Values of “global” predictor variables (i.e., these that do not vary spatially within a given AAA) were obtained in the following way. A patient’s age (in years), sex (1/2 = male, -1/2 = female), smoking status (1/2 = smoker, -1/2 = nonsmoker), and family history (1/2 = with, -1/2 = without) were obtained from the patient’s hospital chart. The values of 1/2 and -1/2 were chosen for all of the binary variables in order to center these variables about zero, which decreases the chances of making an incorrect statistical inferences on the model parameters [190, 191]. The AAA maximum transverse diameter (in cm) was measured directly on CT or recorded from the patient’s chart when CT scans were unavailable.

6.3.2.2 Local Variable Measurement

There were two methods for measuring the local ILT thickness and local diameter for a given AAA wall specimen. The first method was that utilized previously in our laboratory ([Figure 6-1](#)) [40]. In this method, a wedge of ILT with AAA wall attached (typical dimensions were 1.5 cm wide by 4 cm long) was cut and removed from the intact aneurysm. The aneurysm was then cut open and the remaining ILT was removed. The whole ILT specimen with a piece of the wall attached was then sliced perpendicular to its longitudinal axis. This resulted in circumferentially oriented uniaxial specimens (of typical dimensions 0.2 cm wide by 1.5 cm long) attached as small angular segments on the periphery of roughly circular ILT cross-sections. Measurements of two randomly chosen ILT cross sectional diameters at 90° of each other were taken and averaged to provide the local AAA wall diameter for each circumferentially-oriented wall sample. ILT thickness measurements were taken at each end of each circumferentially-oriented wall sample, and the average was taken as local ILT thickness for that specimen. These benchtop measurements of ILT thickness and local diameter were confirmed by measuring the ranges of these variables on CT scan when available.

In the second method, a prolene stitch was placed on the AAA wall specimen to mark the longitudinal level of the inferior mesenteric artery (IMA), which was then used as a marker to link the location of a particular uniaxial specimen (of typical dimensions 0.2 cm wide by 1.5 cm long) with the appropriate longitudinal slice on CT images. The local diameter and ILT thickness were then measured directly on the appropriate slice of the patient's CT scan.

For both of the above methods for measuring local diameter, NORD was calculated by normalizing the local diameter by the diameter of the infrarenal aorta as predicted from the patients' age and sex using a relationship derived from the literature [192].

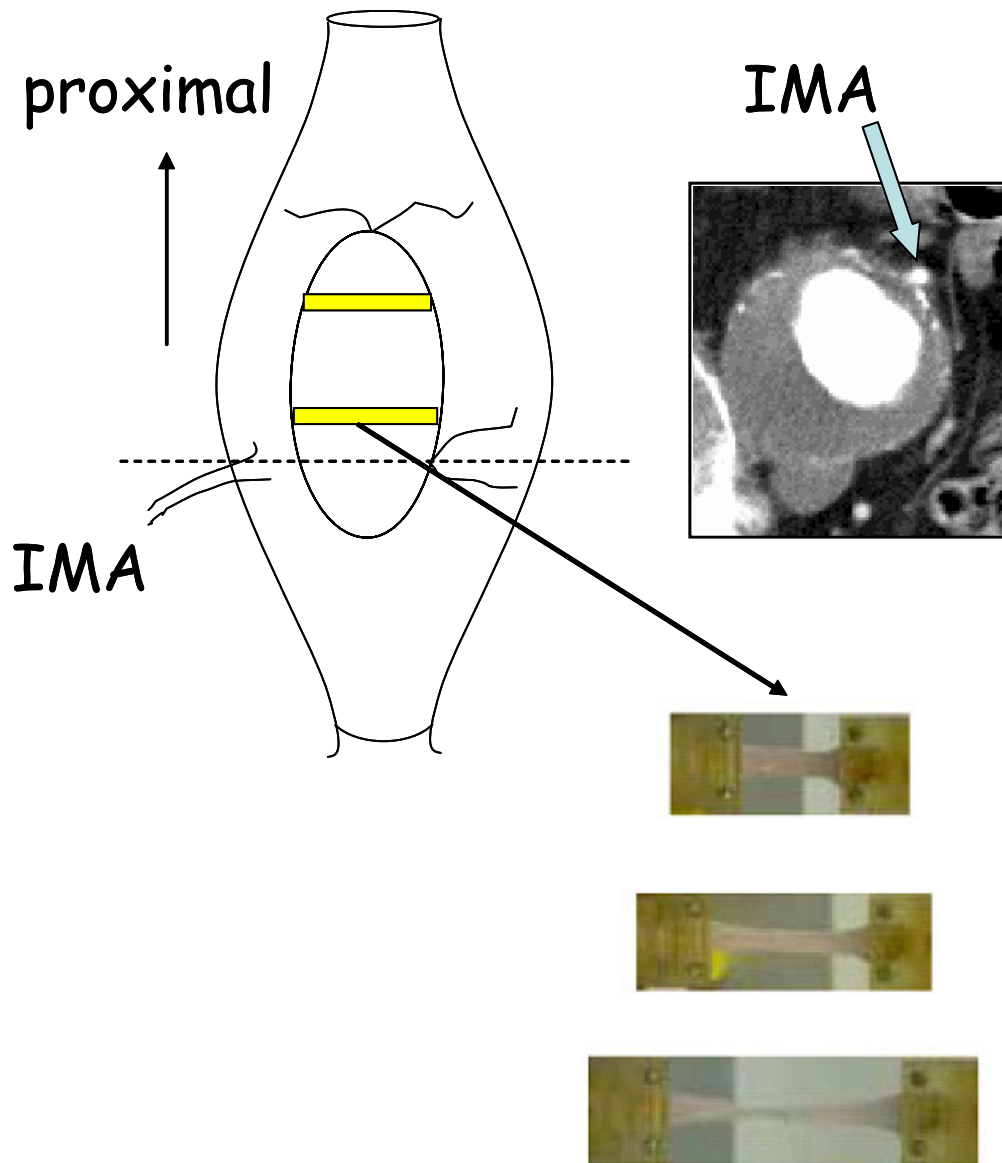


Figure 6-5: Depiction of improved method for determining local transverse diameter and IMA thickness for a uniaxial specimen. The longitudinal level of the IMA was used as a landmark on the excised specimen for determining the appropriate CT slice on which local IMA and diameter were measured.

6.3.3 Uniaxial Tensile Testing

After the measurement of these local parameters, the circumferentially oriented wall samples were removed from the ILT and tested to failure in our uniaxial tensile testing device as described elsewhere [30]. Briefly, the rectangular specimens were pulled at a strain rate of 8.5%/min until failure while simultaneously recording tensile load at a sampling rate of 5 Hz. The stretch (λ) on the sample was defined as the current change in specimen length normalized to original specimen length. The Cauchy stress (σ) acting on the specimen was then computed as

$$\sigma = (f/A_0)*\lambda \quad (6.1)$$

where f is the current load, A_0 is the initial undeformed cross sectional area ($A_0 = \text{width} * \text{specimen thickness}$), and λ is the stretch ratio. For more details on using this device for uniaxial tensile testing of soft tissues the reader is referred elsewhere [30, 38, 59, 178].

It is worth noting that the thickness of each specimen was measured using either digital calipers ($n=55$) or a laser micrometer ($n=28$). All thickness measurements were adjusted for differences between these measurement techniques. Specifically, the thickness values for the caliper-measured specimens ($n=55$) were adjusted using a derived linear relationship between the average caliper and laser-measured values. All specimens were immersed in a container of PBS and tested immediately or stored at 4°C and tested within 24 hours. The peak value of Cauchy stress attainable by each specimen (i.e., its failure strength) was recorded. Only specimens that failed at points remote from the clamps were considered in the present study.

6.3.4 Statistical Modeling of AAA Wall Strength

6.3.4.1 The Initial Wall Strength Model

Based on the evidence provided in Section 6.3.1, the initial generalized statistical model for predicting AAA wall strength was:

$$\begin{aligned} \text{STRENGTH} = & \beta_0 + \beta_1 * \text{ILT} + \beta_2 * \text{AGE} + \beta_3 * \text{SIZE} + \beta_4 * \text{DIA} + \beta_5 * \text{HIST} + \beta_6 * \text{SMK} \\ & + \beta_7 * \text{SEX} + \varepsilon \end{aligned} \quad (6.2)$$

where $\beta_0, \beta_1, \dots, \beta_7$ are regression coefficients. STRENGTH is the predicted strength of a point on the AAA wall in N/cm^2 , ILT is local attached ILT thickness in cm, AGE is patient's age in years, SIZE is the maximum cross-sectional diameter of the AAA in cm, DIA is the local transverse diameter, HIST is family history (1/2 = with, -1/2 = without), SMK is patient's smoking status (1/2 = smoker, -1/2 = nonsmoker), SEX is patient's gender (1/2 = male, -1/2 = female), and ε is the residual, i.e., the difference between the model predicted local wall strength and the measured local wall strength. The choice of 1/2 and -1/2 for the binary variables in the model were chosen in order to "center" these covariates, which reduces the chance of making incorrect statistical inference regarding the estimates of model coefficients. [190, 193] Any continuous variables were also centered by subtracting each measurement by the mean of that variable in group C.

6.3.4.2 Assumptions for Linear Regression

In order to utilize linear multiple regression techniques to derive a statistical model for AAA wall strength, the data must be meet several assumptions. Specifically, the assumptions that must be met in this type of regression are linearity, constant variance, normality, multicollinearity, and autocorrelation [194, 195]. It should be noted that in the present work all of these assumptions must be met except that for autocorrelation, which is accounted for using linear mixed-effects modeling (detailed in [Section 6.3.4.3](#)). Each of the regression assumptions is briefly detailed in the following sections. For a more complete description of each of these assumptions, the reader is referred elsewhere [39, 40, 190, 191, 194, 196].

Linearity

The assumption of linearity simply states that the dependent variable, in our case strength, can be modeled as a linear combination of a set of independent variables (e.g., NORD, ILT). One way to ascertain if this is an appropriate assumption for a given dataset is to visually inspect the residuals of the regression. Simply stated, the i th residual of a regression analysis (ε_i) is the difference between the i th observed value (y_i) of strength and its model-predicted value of strength (\hat{y}_i), or

$$\varepsilon_i = y_i - \hat{y}_i \quad (6.3)$$

Plotting the residuals versus each of the independent variables is an easy way to detect any nonlinear relationships. If the residuals of a regression display any nonlinear patterns, then the dependent variable cannot be predicted from the set of chosen linear independent variables. In this case a nonlinear model or a transformation of the independent variables may be required [39, 40, 194, 196].

Constant Variance

One of the most important assumptions in linear regression is that concerning the variance of the residuals. In order for the regression technique to work appropriately, the residuals (equation [6.3](#)) must be randomly distributed about zero. Similarly to the assumption of linearity, the presence of non-constant variance of the residuals can be detected using a plot of the residuals versus each of the independent variables. Here, the residuals must be randomly be distributed about a mean Y (strength) value. Any deviation from such a plot (e.g., increasing bow-tie appearance) is evidence of non-constant variance and therefore must be corrected with appropriate statistical techniques. Typically, taking the square root or the natural logarithm of the independent variable displaying the non-constant variance will correct the problem [39, 40, 194, 196]. Examples of hypothetical residual plots in which the assumptions of linearity and constant variance can be tested are shown in [Figure 6-6](#).

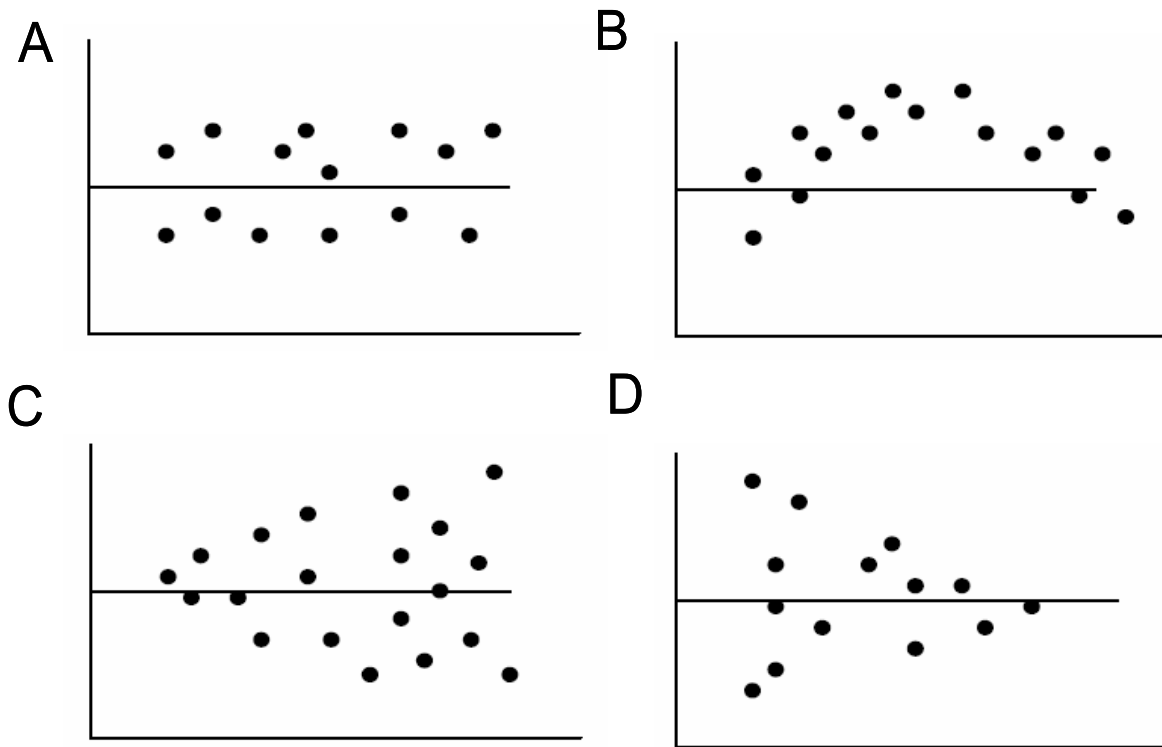


Figure 6-6: Residuals (on all y-axes) versus individual independent variables (X_i 's) for a set of hypothetical data. A) Data satisfy both the linearity and constant variance assumptions. B) Data depart from linearity. C) Residual variance increases with Y. D) Residual variance increases with Y. Adapted from [40, 194].

Normality

In addition to the requirement that the residuals not display any nonlinear or non-constant trends on plots of residuals versus the independent variables, the assumption of normality requires that the residuals be normally distributed. A linear plot of the residuals of strength versus the expected normals (normal probability plot) gives evidence for normality. Normality is required

in linear regression in order to guarantee the results of t-tests on the model parameters as well as the F-test on the entire regression. A more formal way of testing for normality is to run the omnibus test, which checks the skewness and kurtosis of the data. Skewness measures the direction and degree of asymmetry in a frequency histogram of the data. Positive skewness results when data is shifted to the left of a normal distribution, while negative skewness occurs when the data is shifted to the right. The skewness statistic for a perfectly normal distribution is exactly zero, however values of +3 to -3 are typically accepted values for normal or near-normal distributions. Kurtosis measures the ‘flatness’ of the frequency histogram of the data, or the ‘heaviness’ of the tails of a distribution. The kurtosis statistic for a perfectly normal distribution is equal to 3, however generally values between 2 and 4 are evidence of normality [39, 40, 194, 196]. Graphical illustrations of skewness and kurtosis for hypothetical data sets can be seen in [Figure 6-7](#).

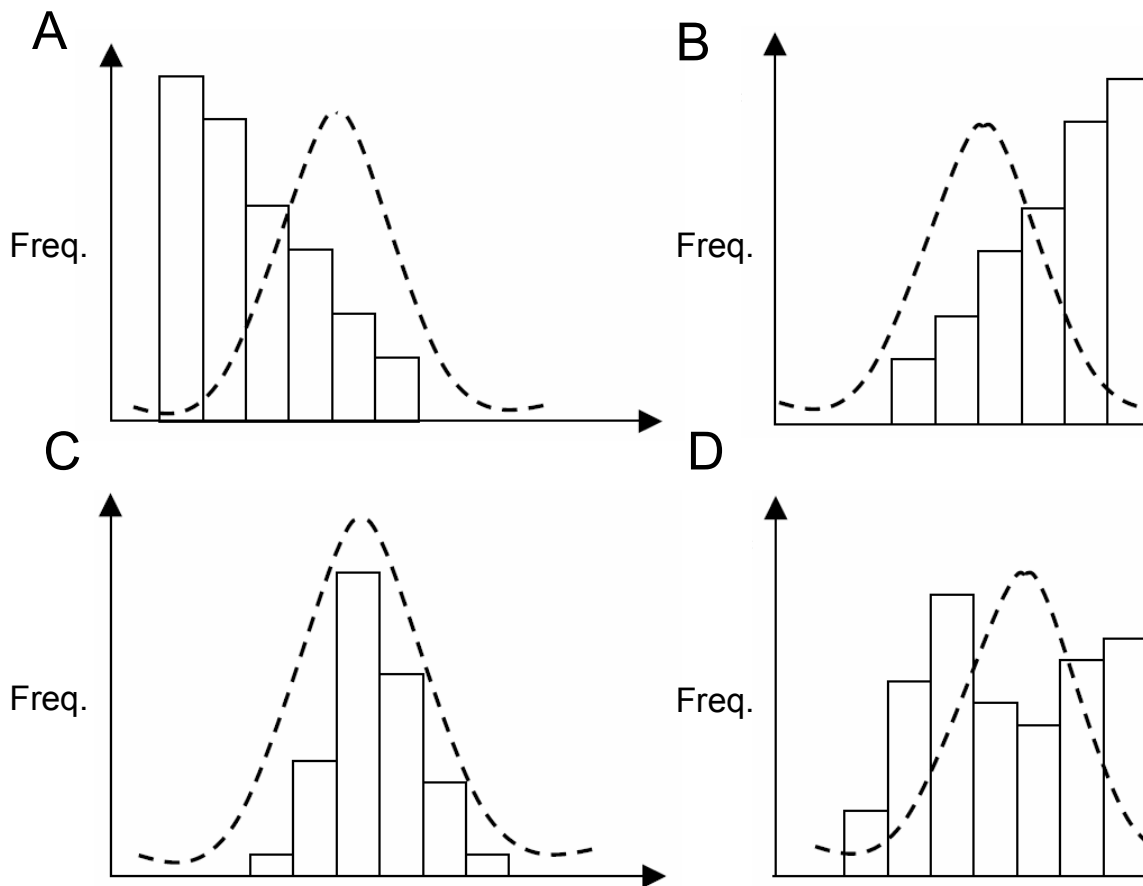


Figure 6-7: Histograms of hypothetical data illustrating the meaning of skewness and kurtosis. A) Positive skewed distribution; B) Negative skewed distribution. C) Distribution with kurtosis = 4.25; D) Distribution with kurtosis = 1.75. C) and D) have approximately the same skewness. The dotted lines represent the normal distribution curve. Adapted from [40, 194].

Multicollinearity

Multicollinearity occurs when one or more independent variables are related. This problem is likely to be a problem when there are redundant independent variables in the regression model.

The correlation matrix for a regression model can often provide evidence for multicollinearity between independent variables. Independent variable displaying correlations greater than 0.5 between one another are typically candidates for removal or further transformation [39, 40, 194, 196]. A more formal test to detect the presence of multicollinearity in a regression model is the variance inflation factor (VIF) method. VIF is defined as

$$VIF_i = 1 / (1 - R_i^2) \quad (6.4)$$

where R_i^2 is the R^2 when the i th independent variable is regressed on the remaining independent variables. Typically, values of $VIF > 10$ for large datasets (>100) are evidence of multicollinearity, since the dependence of the i th independent variable on the remaining independent variables is at least 90%. For smaller datasets however (<50), a VIF greater than 4 is evidence of multicollinearity between one or more of the independent variables [39, 40, 194, 196]. The most efficient way of dealing with multicollinearity is to either drop one of the highly correlated independent variables or combine these into a single independent variable.

6.3.4.3 Outliers and High Influential Points

In order to use multiple linear regression techniques for variable selection (i.e., to determine which parameters are significant in predicting local AAA wall strength), care was taken to ensure that no outliers were present in the collected data. The Hat diagonal and Studentized residual were used to detect outliers in X-space and Y-space, respectively. Any Studentized residual values $> t_{n-p-1,0.025}$ (n =number of observations, p =number of parameters in the model) and any Hat diagonal $> 2 * p/n$ were identified as outliers [40, 194, 195].

Once any candidate X and Y-space outliers are identified, these points were also investigated to see if they are highly influential points in the linear regression. The Cook's Distance measure, D_i was used for this purpose and is defined as:

$$D_i = \left(\frac{r_i^2}{p} \right) \left(\frac{1 - H_{ii}}{H_{ii}} \right) \quad (6.5)$$

where r_i^2 is the studentized residual, p is the number of independent variables, and H_{ii} is the i th hat diagonal for the linear regression [39, 40, 194, 196]. D_i is an overall measure of how an observation impacts the regression coefficients. Hutcheson and Sofroniou [197] suggest that any values of D_i greater than $4/(n-p)$ where n is the number of data points and p is the number of independent variables denotes a highly influential data point.

6.3.4.4 Variable Selection Technique – Backwards Stepwise Regression

Backwards stepwise linear regression techniques were utilized to determine if individual predictor variables were significant [40, 194, 195]. Briefly, if the associated p value for a certain variable was found to be greater than 0.10, that parameter was considered statistically insignificant and removed from the model [40, 194, 195]. If more than one p value was greater than 0.10, the parameter with the highest p value was removed and regression analysis was repeated using the updated model until all remaining individual p values were less than or equal to 0.10 [40, 194, 195].

6.3.4.5 Linear Mixed-Effects Modeling

In order to build the final statistical model for AAA wall strength, linear mixed-effects modeling will be utilized. The use of mixed-effects modeling allows the relaxation of the assumption of autocorrelation required in multiple linear regression. Mixed-effects models are primarily used to describe relationships between a response variable (strength) and some covariates in data that are grouped according to one or more classification factors [198, 199]. Since for the current study there are multiple specimens from an individual patient, the patient is considered to be one level of grouping. A more detailed discussion of mixed-effects modeling the reader is referred elsewhere. [198, 199] Briefly, a mixed-effects model that is comprised of one level of grouping takes the form

$$\mathbf{y}_i = \mathbf{X}_i \boldsymbol{\beta} + \mathbf{Z}_i \mathbf{b}_i + \varepsilon_i, \quad i=1, \dots, M \quad (6.6)$$

where $\boldsymbol{\beta}$ is the p -dimensional vector of fixed effects, \mathbf{b}_i is the q -dimensional vector of random effects, \mathbf{X}_i and \mathbf{Z}_i are the known fixed-effects and random-effects regressor matrices, ε_i is the within-group error vector with a Gaussian distribution, and M is the number of groups [198, 199]. For the current statistical model of strength, we will have one random-effect that is the intercept term (β_0 in equation [6-2](#)), while the covariates (ILT, NORD, HIST, SEX, etc.) will be considered as fixed-effects. Therefore in our model p will be equal to the number of remaining significant predictor (independent) variables, q will be one since we have one level of grouping (the patient), and M will equal the number of patients in whichever group (A, B, or C) we are considering. It is important to note that although the β_i may behave like parameters, formally they are just another level of random variation in the model so we do not “estimate” them as such. The mixed-effects modeling was performed in the statistical software R, v. 1.9.1, which is freeware available on the world wide web (<http://www.r-project.org>).

6.4 RESULTS AND DISCUSSION

6.4.1 Assumptions for Linear Regression

Linearity

In order to investigate whether AAA wall strength can be predicted from a linear regression analysis, the residuals of the regression were plotted versus each of the independent variables. Residual plots displaying any nonlinear trends would suggest the use of a higher order or other nonlinear regression model. All of the residuals displayed random variation versus each independent variable, suggesting multiple linear regression can be used in predicting AAA wall strength (**Appendix J**).

Constant Variance

Similar to the check for the assumption for linearity, the residual plots versus each independent variable can be used to check for departures from constant variance. These plots resulted in a random array of data points for all independent variables (**Appendix K**) except for the independent variable ILT which displayed a decreasing bow-tie appearance (**Figure 6-8**). This non-constant variance was corrected by transforming the variable ILT to its square root, $ILT^{1/2}$, which resulted in a more random variance for all values of this independent variable (**Figure 6-9**). Equation (6.2) was therefore updated to

$$\begin{aligned} \text{STRENGTH} = & \beta_0 + \beta_1 * ILT^{1/2} + \beta_2 * \text{AGE} + \beta_3 * \text{SIZE} + \beta_4 * \text{DIA} + \beta_5 * \text{HIST} + \beta_6 * \text{SMK} \\ & + \beta_7 * \text{SEX} + \varepsilon \end{aligned} \quad (6.7)$$

where the independent variable $ILT^{1/2}$ now has units of $cm^{1/2}$, and all other independent variables in the regression equation remain unchanged.

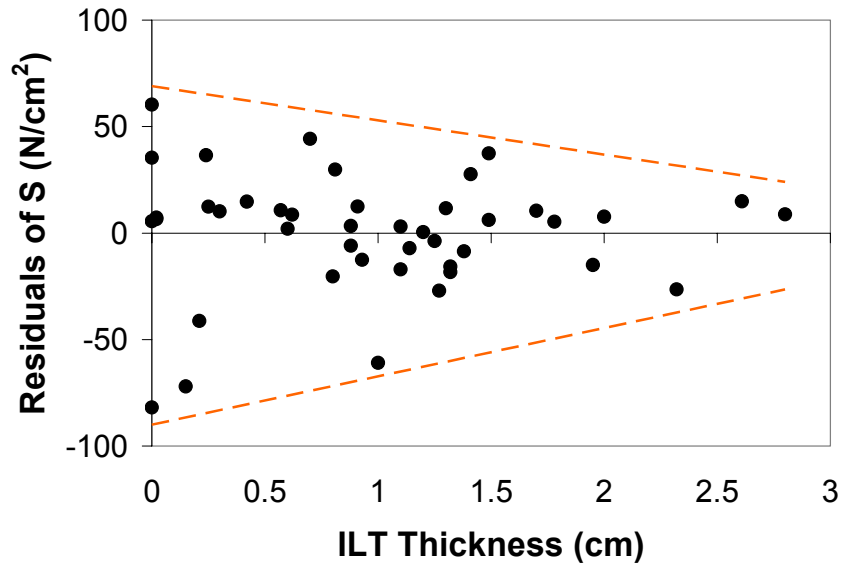


Figure 6-8: Residuals of S versus ILT displaying decreasing bow-tie appearance (red dotted lines)

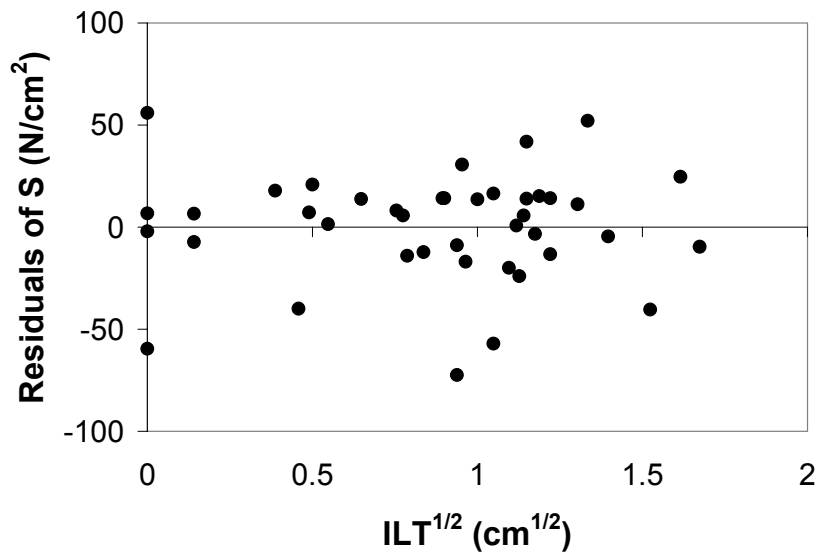


Figure 6-9: Residuals of S versus corrected variable $ILT^{1/2}$

Normality

The normal probability plot for the regression of Group A data to equation (6.6) displayed a nearly linear relationship ([Figure 6-10](#)). In order to more quantitatively test for normality, an omnibus test was run on this regression which resulted in a skewness value of -1.82 and a kurtosis value of 2.09. Both of these values lie within the typical bounds set for identifying non-normal distributions. A histogram of the data with these values of skewness and kurtosis is displayed in [Figure 6-11](#).

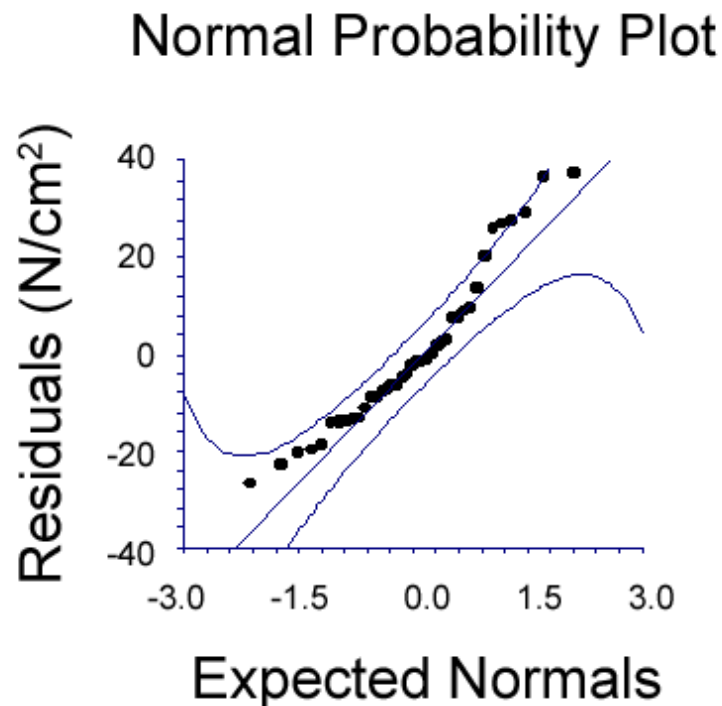


Figure 6-10: Normal probability plot when regressing Group A data to equation 6.7

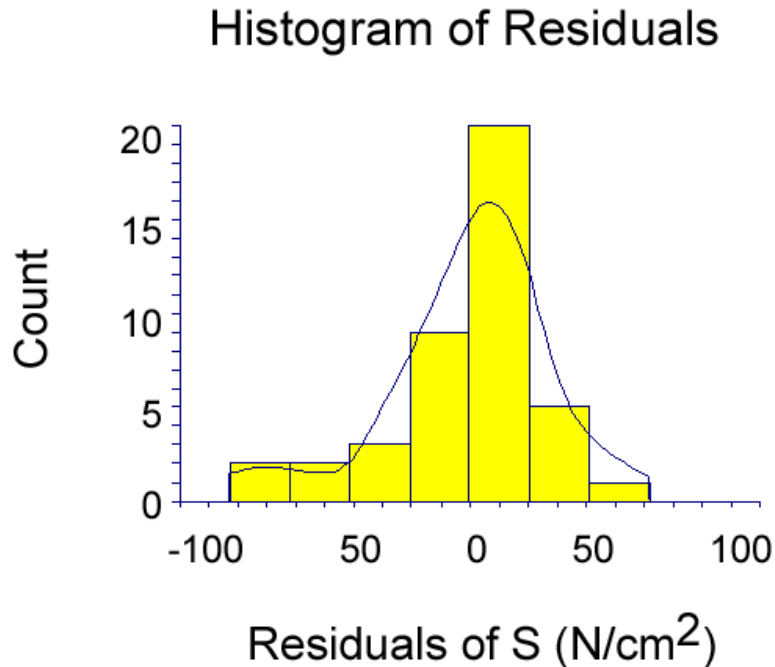


Figure 6-11: Histogram of residuals when regressing Group A data to equation 6.7

Multicollinearity

As stated in [Section 6.3.4.2](#), multicollinearity can be detected by investigating the correlation matrix between independent variables used in regression analysis. The correlation matrix resulting from the multiple linear regression of equation (6.6) to the data from Group A resulted in a correlation of 0.52 between the variables DIA and SIZE ([Table 6-2](#)). The correlations between all remaining variables were less than 0.39. This regression also resulted in a large value of VIF (4.19) for the independent variable DIA in comparison to all other variables ([Table 6-3](#)).

Table 6-2: Correlations between independent variables after regression of equation 6.7. Shaded cells represent high (>0.5) correlations.

| | AGE | HIS | DIA | SEX | SIZE | SMK | ILT^{1/2} | S |
|--------------------------|------------|------------|------------|------------|-------------|------------|--------------------------|----------|
| AGE | 1.00 | 0.01 | -0.03 | -0.06 | -0.19 | -0.16 | -0.02 | 0.00 |
| HIS | 0.01 | 1.00 | 0.06 | -0.39 | -0.16 | -0.14 | -0.08 | -0.41 |
| DIA | -0.03 | 0.06 | 1.00 | -0.28 | 0.52 | -0.25 | 0.23 | -0.47 |
| SEX | -0.06 | -0.39 | -0.28 | 1.00 | -0.15 | 0.08 | 0.16 | 0.34 |
| SIZE | -0.19 | -0.16 | 0.52 | -0.15 | 1.00 | 0.13 | -0.05 | 0.09 |
| SMK | -0.16 | -0.14 | -0.25 | 0.08 | 0.13 | 1.00 | 0.12 | 0.07 |
| ILT^{1/2} | -0.02 | -0.08 | 0.23 | 0.16 | -0.05 | 0.12 | 1.00 | -0.42 |
| S | 0.00 | -0.41 | -0.47 | 0.34 | 0.09 | 0.07 | -0.42 | 1.00 |

Table 6-3: Variance inflation factors (VIF) after regression of equation 6.7

| Independent Variable | Multicollinearity | |
|-----------------------------|--------------------------|---|
| | VIF | R² vs other variables |
| AGE | 1.08 | 0.07 |
| HIS | 1.38 | 0.28 |
| DIA | 4.19 | 0.76 |
| SEX | 1.56 | 0.36 |
| SIZE | 1.62 | 0.38 |
| SMK | 1.36 | 0.26 |
| ILT ^{1/2} | 1.68 | 0.41 |

In order to correct for this multicollinearity, the independent variable SIZE was dropped from the regression analysis. This choice was made primarily due to the fact that DIA is capable of detecting changes in strength *within* any given AAA, while SIZE is not. In order to be able to compare changes in dilation from patient to patient (DIA may vary simply due to changes in the size of a person’s nonaneurysmal aorta), the variable DIA was replaced by the variable NORD, which is defined as the variable DIA normalized to a value of nonaneurysmal infrarenal diameter

based on the patients sex and age [192]. Therefore, the resulting regression equation for AAA wall strength was given by:

$$\text{STRENGTH} = \beta_0 + \beta_1 * \text{ILT}^{1/2} + \beta_2 * \text{AGE} + \beta_3 * \text{NORD} + \beta_4 * \text{HIST} + \beta_5 * \text{SMK} + \beta_6 * \text{SEX} + \varepsilon \quad (6.8)$$

where NORD is a dimensionless independent variable. The above equation was further analyzed to determine which independent variables are required in noninvasively predicting AAA wall strength.

6.4.2 Outliers and Highly Influential Points

The Hat diagonal values as well as the Studentized residuals for Group A data are shown in [Table 6-4](#). As is shown in this table, there were 2 data values that were outliers in X space since they displayed Hat diagonal values greater than $2 * p/n = 0.279$. There were also 3 values that were Y-space outliers based on the studentized residual value of $t_{n-p-1, 0.025} = t_{36, 0.025} = 2.04$. Of these 5 X and Y-space outliers, two were considered highly influential points as their Cook's distance value was greater than $4/(n-p) = 0.108$. These two data points were removed from the Group A dataset. A similar analysis was performed on the Group B data, which resulted in no X-space or Y-space outliers.

In summary, there were originally 43 specimens from 21 patients in Group A, of which 2 were removed as highly influential outliers. There were no X-space or Y-space outliers detected in group B, which consisted of 40 specimens from 18 patients. This left 81 specimens from 38 patients in group C from which the final statistical model for AAA wall strength was derived.

Table 6-4: Hat diagonal and studentized residuals for regressing Group A data to equation 6.8. Shaded cells represent outliers or highly influential points. Data points 6 and 35 were removed as highly influential outliers.

| Data Point | Studentized Residual | Hat Diagonal | Cook's D |
|------------|----------------------|---------------|---------------|
| 1 | -0.9946 | 0.1837 | 0.0318 |
| 2 | 0.2978 | 0.1822 | 0.0028 |
| 3 | 1.986 | 0.2142 | 0.9527 |
| 4 | -1.555 | 0.1343 | 0.0536 |
| 5 | -0.3879 | 0.2549 | 0.0074 |
| 6 | -3.1161 | 0.1769 | 0.2981 |
| 7 | -0.2286 | 0.249 | 0.0025 |
| 8 | 0.4251 | 0.1511 | 0.0046 |
| 10 | 0.0397 | 0.1445 | 0 |
| 11 | 0.4799 | 0.2788 | 0.0127 |
| 12 | 0.6777 | 0.2185 | 0.0183 |
| 13 | 0.1785 | 0.2269 | 0.0013 |
| 14 | 0.8793 | 0.2605 | 0.0389 |
| 15 | 0.3233 | 0.2289 | 0.0044 |
| 16 | -0.3215 | 0.1687 | 0.003 |
| 17 | -0.4935 | 0.1666 | 0.007 |
| 18 | 0.7306 | 0.2086 | 0.0201 |
| 19 | -0.197 | 0.159 | 0.001 |
| 20 | -0.6482 | 0.1658 | 0.0119 |
| 21 | -0.2249 | 0.1891 | 0.0017 |
| 22 | -0.8185 | 0.1847 | 0.0217 |
| 23 | 1.445 | 0.1443 | 0.0503 |
| 24 | 0.0924 | 0.0767 | 0.0001 |
| 25 | 0.5302 | 0.1044 | 0.0047 |
| 26 | 0.5708 | 0.1363 | 0.0073 |
| 27 | 2.3211 | 0.1229 | 0.1079 |
| 28 | 0.0276 | 0.1044 | 0 |
| 29 | 0.6682 | 0.2064 | 0.0166 |
| 30 | 0.5954 | 0.2066 | 0.0132 |
| 31 | 0.5769 | 0.2099 | 0.0126 |
| 32 | -0.4332 | 0.1947 | 0.0065 |
| 33 | -0.1887 | 0.1746 | 0.0011 |
| 34 | -0.4366 | 0.1939 | 0.0066 |
| 35 | -2.1812 | 0.2732 | 0.2554 |
| 36 | 0.6372 | 0.1939 | 0.0139 |
| 37 | 0.6958 | 0.0908 | 0.0069 |
| 38 | 0.3411 | 0.0663 | 0.0012 |
| 39 | -0.7275 | 0.0913 | 0.0076 |
| 40 | -1.9643 | 0.082 | 0.0492 |
| 41 | 0.325 | 0.0798 | 0.0013 |
| 42 | 0.0694 | 0.1006 | 0.0001 |
| 43 | 0.5273 | 0.2123 | 0.0145 |

6.4.3 Backwards Stepwise Regression – Variable Selection

A backwards stepwise linear regression technique was utilized on the Group A data set to determine which of the independent variables in equation 6.8 are necessary in noninvasively predicting AAA wall strength. This analysis sequentially revealed that SMK ($p = 0.93$) and AGE ($p = 0.14$) were statistically insignificant predictors. Therefore the final model used in deriving a model of AAA wall strength was

$$\text{STRENGTH} = \beta_0 + \beta_1 * \text{ILT}^{1/2} + \beta_2 * \text{NORD} + \beta_3 * \text{HIST} + \beta_4 * \text{SEX} + \varepsilon \quad (6.9).$$

This model was used in the derivation of a final statistical model for AAA wall strength using the linear mixed-effects modeling described in the following section.

6.4.4 Mixed-Effects Modeling

The 95% confidence intervals for the mixed-effect model parameters for groups A, B and C are displayed in [Figure 6.12](#). The mixed-effect model parameter values and their associated p-values for the fit to group C data are summarized in [Table 6-5](#). The final model derived from group C is then

$$\begin{aligned} \text{STRENGTH} = & 72.9 - 33.5 * (\text{ILT}^{1/2} - 0.79) - 12.3 * (\text{NORD} - 2.31) - \\ & 24 * \text{HIST} + 15 * \text{SEX} \end{aligned} \quad (6.10)$$

We find that this model (equation [6.10](#)) corresponds to the experimental data from group C moderately well ($R^2 = 0.60$, [Figure 6-13](#)).

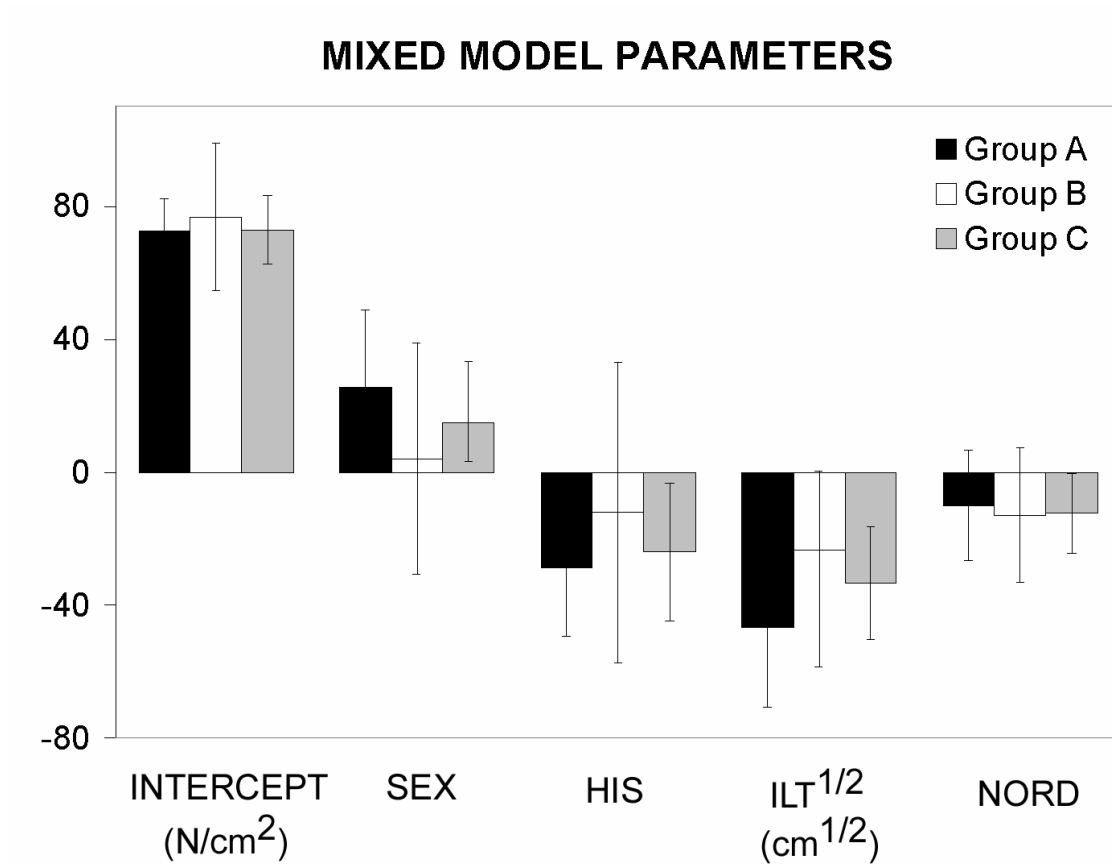


Figure 6-12: 95% CI's intervals for the mixed-effects model parameters for all Groups

Table 6-5: Parameter values for Group C linear mixed-effects regression

| Independent Variable | Lower 95% CI | Coefficient | Upper 95% CI | p value |
|----------------------|--------------|-------------|--------------|---------|
| Intercept | 62.7 | 72.9 | 83.1 | < 0.001 |
| ILT ^{1/2} | -50.6 | -33.5 | -16.4 | < 0.001 |
| NORD | -24.5 | -12.4 | -0.2 | 0.04 |
| HIST | -44.7 | -24 | -3.5 | 0.09 |
| SEX | 3.4 | 15 | 33.3 | 0.004 |

Inspection of equation 6.10 provides several insights as to its physical meaning:

- For two patients with the same gender and identical AAAs, the one with family history has a AAA that is globally weaker by 24 N/cm^2 compared to the one without family history.
- For two patients with the same family history and identical AAAs, a female will have a AAA that is globally weaker by 15 N/cm^2 compared to a male.
- For any two points within any given AAA with the same NORD, an increase in $\text{ILT}^{1/2}$ of 1.0 results in a corresponding decrease in strength of 33.5 N/cm^2
- For any two points within any given AAA with the same $\text{ILT}^{1/2}$, an increase in NORD of 1.0 results in a corresponding decrease in strength of 12.3 N/cm^2

6.4.5 Model Application

[Figure 6-12](#) displays the relatively large span of the 95% confidence intervals for the Group B data set. It should be noted that the application of this model can only be used within the range of covariates used in its construction. For our final model (group C), the ranges of NORD and $\text{ILT}^{1/2}$ are (1.06, 3.92) and (0, 1.9), respectively. The fact that the confidence intervals for group C in [Figure 6-12](#) do not include zero confirms that each respective variable is positively or negatively correlated with AAA wall strength. In addition, one can see that the model predicted experimentally measured wall strength reasonably well for group C ([Figure 6-13](#)).

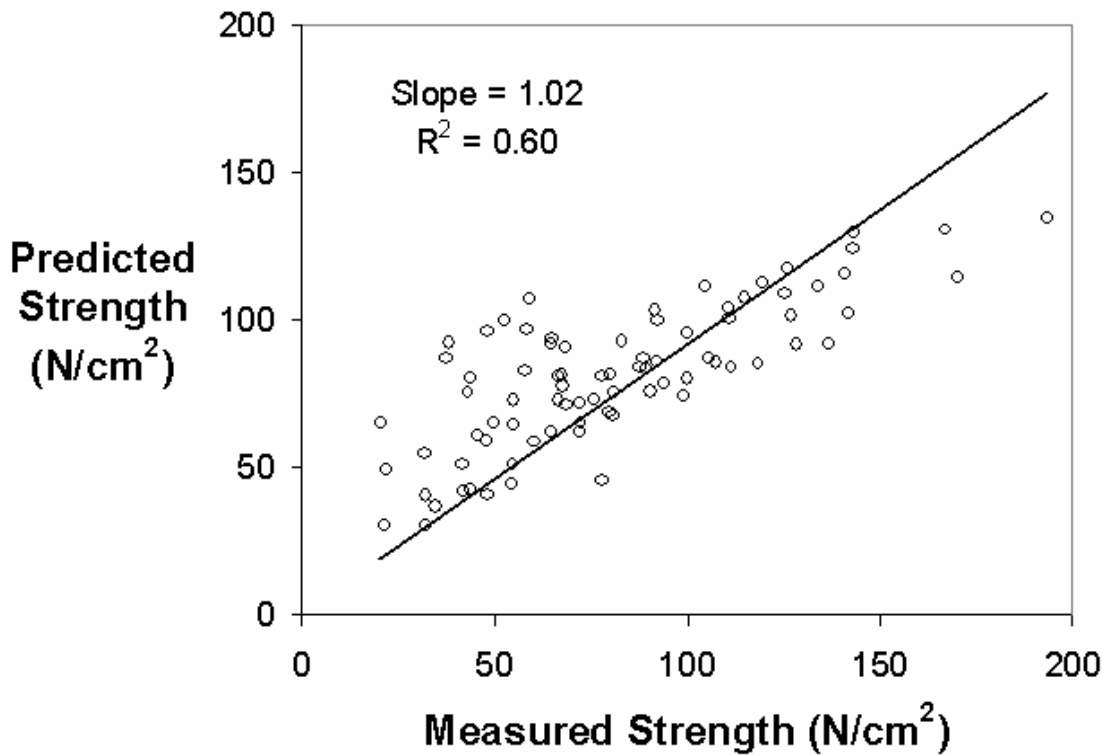


Figure 6-13: Predicted versus measured wall strength for Group C

The characteristics of the four patients whose AAA wall strength distributions were evaluated for demonstration purposes are shown in [Table 6-6](#). A custom written Matlab script was created which calculates the strength using equation [6.10](#) for each node of a AAAs finite element mesh ([Appendix L](#)). The 3D distribution of wall strength for each AAA reveals a unique, complex pattern ([Figure 6-14](#)). In general, wall strength values are higher at both neck regions and lower in the bulge region. Note that AAA 3 did not include any ILT, which resulted in strength variations dependent only on the local diameter of the AAA. Local wall strength values predicted for the four AAA studied ranged from 56.3 N/cm² to 132.9 N/cm².

Table 6-6: Characteristics of four AAA patients used in the demonstration of AAA wall strength

| Patient | Max. Calculated Strength (N/cm²) | Min. Calculated Strength (N/cm²) | Max. ILT Thickness (cm) | Gender | Size (cm) | Hist |
|----------------|--|--|--|---------------|----------------------|-------------|
| 1 | 133 | 62 | 2.3 | M | 6.0 | No |
| 2 | 118 | 56 | 3.0 | M | 6.1 | No |
| 3 | 111 | 83 | 0.7 | F | 6.4 | No |
| 4 | 125 | 77 | 1.8 | M | 6.4 | No |

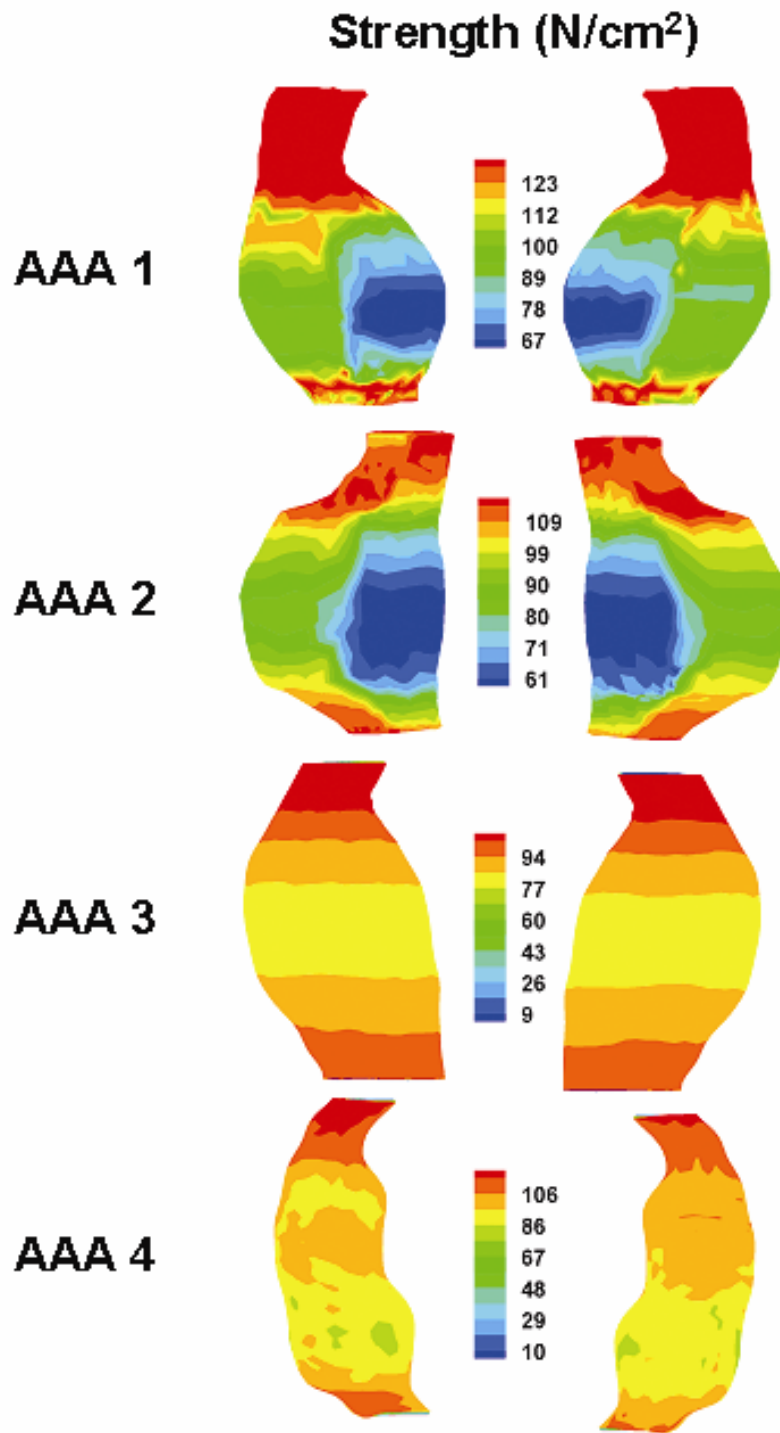


Figure 6-14: Anterior (left) and posterior (right) view of the 3D distribution of AAA wall strength for four AAA patients using equation 6.10.

6.4.6 Electively Repaired AAAs

In order to investigate the differences in AAA wall strength using the previously derived model [39, 40] compared to model derived in the current work, the wall strength was calculated for each of the 21 AAA models described in [Section 5.2.5 \(Table 6-7\)](#). A representative comparison between these methods is shown in [Figure 6-15](#) for AAA8. The mean peak wall strength for these AAAs was 126 ± 2.15 and 229.34 ± 16.21 N/cm² for the current and previous AAA strength models, respectively ($p < 0.001$). The mean minimum wall strength for these AAAs was 93.88 ± 3.79 and 152.25 ± 14.85 N/cm² for the current and previous AAA strength models, respectively ($p < 0.001$). The mean of the average strength acting on each of these AAAs was 112.39 ± 2.80 and 205.76 ± 13.97 N/cm² for the current and previous AAA strength models, respectively ($p < 0.001$). The primary reason that the new strength method resulted in smaller peak, minimum, and mean strength values was due to the use of a laser micrometer measured thickness value in the uniaxial tensile tests, as opposed to the contacting method used previously which likely underestimated the thickness in these tests.

Table 6-7: Strength values using the old and new methods for AAA strength prediction

| Aneurysm | New Strength (N/cm ²) | | | Old Strength (N/cm ²) | | |
|----------|-----------------------------------|-------|-------|-----------------------------------|-------|-------|
| | Peak | Min | Mean | Peak | Min | Mean |
| AAA1 | 113.4 | 84.2 | 103.9 | 185.8 | 72.2 | 123.4 |
| AAA2 | 113.3 | 75.4 | 94.8 | 233.7 | 118.2 | 155.4 |
| AAA3 | 137.1 | 119.3 | 133.8 | 259.2 | 173.0 | 237.4 |
| AAA4 | 120.8 | 98.7 | 111.8 | 298.6 | 169.4 | 224.2 |
| AAA5 | 139.3 | 98.7 | 127.5 | 397.2 | 360.6 | 384.2 |
| AAA6 | 138.1 | 130.5 | 133.8 | 252.3 | 139.9 | 188.4 |
| AAA7 | 122.0 | 80.8 | 104.0 | 314.4 | 158.4 | 233.9 |
| AAA8 | 137.9 | 88.6 | 116.2 | 372.3 | 315.8 | 349.4 |
| AAA9 | 129.8 | 106.3 | 118.8 | 232.9 | 122.0 | 170.3 |
| AAA10 | 136.2 | 112.7 | 128.8 | 281.4 | 161.7 | 213.3 |

Table 6-7 (continued)

| | | | | | | |
|-------|-------|-------|-------|-------|-------|-------|
| AAA11 | 111.5 | 82.4 | 94.8 | 209.0 | 113.6 | 146.6 |
| AAA12 | 112.9 | 83.7 | 100.3 | 199.2 | 112.5 | 160.8 |
| AAA13 | 118.3 | 74.5 | 97.3 | 254.1 | 132.2 | 200.3 |
| AAA14 | 134.8 | 128.6 | 131.8 | 168.6 | 84.2 | 127.3 |
| AAA15 | 118.7 | 76.5 | 103.7 | 248.5 | 113.4 | 172.5 |
| AAA16 | 122.7 | 76.3 | 108.5 | 318.7 | 158.3 | 244.1 |
| AAA17 | 136.1 | 95.9 | 118.0 | 231.3 | 105.0 | 166.4 |
| AAA18 | 138.7 | 96.7 | 112.0 | 298.4 | 165.6 | 219.4 |
| AAA19 | 122.4 | 76.0 | 104.6 | 274.2 | 130.5 | 204.4 |
| AAA20 | 122.8 | 86.1 | 100.9 | 255.4 | 131.5 | 186.3 |
| AAA21 | 123.4 | 99.4 | 115.1 | 281.5 | 159.1 | 213.0 |
| MEAN | 126.2 | 93.9 | 112.4 | 265.1 | 152.2 | 205.8 |
| SEM | 2.2 | 3.8 | 2.8 | 12.3 | 14.9 | 14.0 |

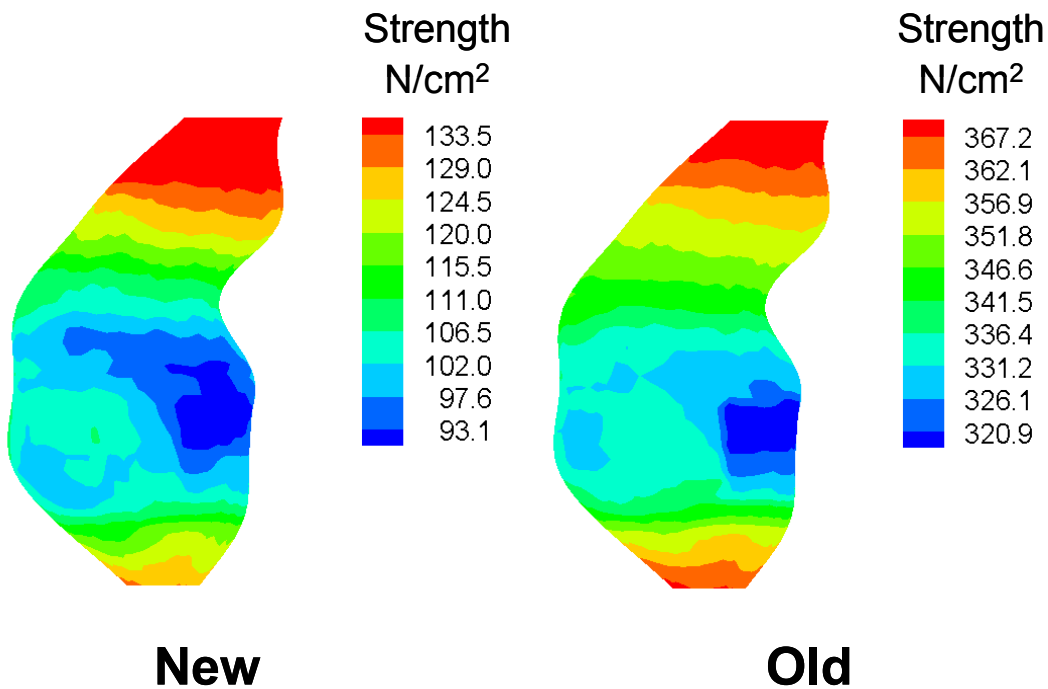


Figure 6-15: A representative 3D distribution of AAA wall strength for the new and old methods for predicting AAA wall strength

6.4.7 Ruptured Versus Non-ruptured AAAs

In order to investigate the differences in AAA wall strength between ruptured and non-ruptured AAAs the peak, minimum, and mean wall strengths for both the old ([Table 6-8](#)) and new methods ([Table 6-9](#)) was calculated for each of the 5 non-ruptured and 9 ruptured AAA models described in [Section 5.2.5](#). A representative comparison between a ruptured and non-ruptured AAA using the new method of wall strength estimation is shown in [Figure 6-16](#) for N3 and R15.

The mean peak wall strength using the old method for AAA wall strength estimation was 253.60 ± 12.96 and 263.28 ± 22.16 N/cm² for the ruptured and non-ruptured AAA models, respectively ($p = 0.69$). The mean minimum wall strength using the old method for AAA wall strength estimation was 110.96 ± 12.72 and 151.41 ± 11.39 N/cm² for the ruptured and non-ruptured AAA models, respectively ($p = 0.06$). The mean average wall strength using the old method for AAA wall strength estimation was 179.57 ± 13.42 and 202.90 ± 12.94 N/cm² for the ruptured and non-ruptured AAA models, respectively ($p = 0.28$).

The mean peak wall strength using the new method for AAA wall strength estimation was 119.41 ± 4.48 and 137.06 ± 1.49 N/cm² for the ruptured and non-ruptured AAA models, respectively ($p = 0.02$). The mean minimum wall strength using the new method for AAA wall strength estimation was 81.18 ± 3.45 and 108.33 ± 10.18 N/cm² for the ruptured and non-ruptured AAA models, respectively ($p = 0.03$). The mean average wall strength using the new method for AAA wall strength estimation was 103.04 ± 3.02 and 124.52 ± 5.84 N/cm² for the ruptured and non-ruptured AAA models, respectively ($p = 0.003$). It should be noted that there were no statistical differences in the maximum cross-sectional diameters between ruptured and non-ruptured AAAs (7.10 ± 0.38 vs. 6.14 ± 0.54 , $p = 0.17$).

Table 6-8: Strength values using the old statistical model for ruptured and non-ruptured AAAs

| NR AAA | Old Strength (N/cm ²) | | | RAAA | Peak | Min | Mean |
|--------|-----------------------------------|-------|-------|------|-------|-------|-------|
| | Peak | Min | Mean | | | | |
| N1 | 247.3 | 150.8 | 191.9 | R1 | 169.5 | 87.3 | 122.6 |
| N2 | 249.7 | 139.1 | 206.8 | R2 | 254.3 | 191.1 | 211.8 |
| N3 | 206.1 | 130.5 | 164.6 | R3 | 213.7 | 61.2 | 108.6 |
| N4 | 272.4 | 141.6 | 206.6 | R4 | 273.7 | 120.2 | 187.8 |
| N5 | 340.9 | 195.1 | 244.6 | R5 | 277.2 | 135.5 | 196.2 |
| | | | | R6 | 297.0 | 129.2 | 230.3 |
| | | | | R7 | 256.7 | 93.8 | 170.5 |
| | | | | R8 | 274.0 | 92.4 | 204.5 |
| | | | | R9 | 266.4 | 87.9 | 183.6 |
| MEAN | 263.3 | 151.4 | 202.9 | MEAN | 253.6 | 111.0 | 179.6 |
| SEM | 22.2 | 11.4 | 12.9 | SEM | 13.0 | 12.7 | 13.4 |

Table 6-9: Strength values using the new statistical model for ruptured and non-ruptured AAAs (*,+,# p < 0.05)

| NR AAA | New Strength (N/cm ²) | | | RAAA | Peak | Min | Mean |
|--------|-----------------------------------|--------------------|--------------------|------|--------|-------------------|--------------------|
| | Peak | Min | Mean | | | | |
| N1 | 131.4 | 90.6 | 108.2 | R1 | 116.0 | 89.5 | 99.5 |
| N2 | 138.2 | 130.7 | 135.3 | R2 | 90.9 | 85.1 | 87.0 |
| N3 | 137.1 | 132.8 | 134.7 | R3 | 136.4 | 95.7 | 113.4 |
| N4 | 139.9 | 104.6 | 131.8 | R4 | 134.4 | 81.5 | 105.2 |
| N5 | 138.8 | 82.9 | 112.6 | R5 | 111.9 | 68.8 | 91.4 |
| | | | | R6 | 116.0 | 68.5 | 101.7 |
| | | | | R7 | 121.6 | 70.5 | 107.6 |
| | | | | R8 | 123.1 | 92.4 | 111.1 |
| | | | | R9 | 124.3 | 78.8 | 110.4 |
| MEAN | 137.1* | 108.3 ⁺ | 124.5 [#] | MEAN | 119.4* | 81.2 ⁺ | 103.0 [#] |
| SEM | 1.5 | 10.2 | 5.8 | SEM | 4.5 | 3.5 | 3.0 |

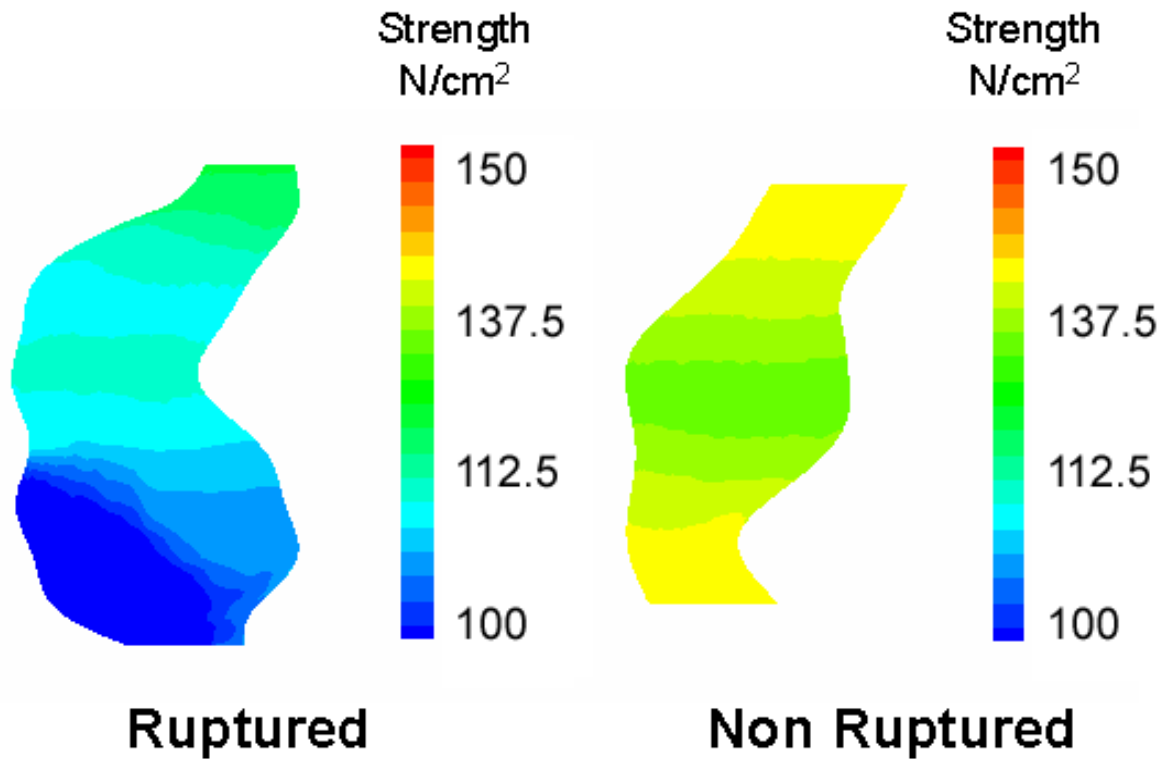


Figure 6-16: 3D strength distribution on a representative ruptured and non-ruptured AAA using the current wall statistical model

6.4.8 Discussion

Rupture of an individual AAA, like failure of any loaded structure, occurs when the local stress applied to the wall exceeds the local strength of the tissue. In order to evaluate the risk of rupture for a given AAA, information on both local stress and local strength are required. Our results demonstrate that local wall strength may be predicted by certain clinical noninvasively-measurable parameters via equation [6.10](#). This model contains four, non-invasively measurable

predictors: the square root of local ILT thickness, normalized local diameter, patient's sex, and the patient's family history of AAA. The noninvasive statistical model for predicting AAA wall strength derived here predicted a statistically weaker wall for ruptured AAAs than for non-ruptured AAAs. In fact, the current model performed better than either the previously derived AAA wall strength model or the clinically utilized maximum cross sectional diameter in identifying ruptured AAAs.

The traditional approach of using AAA size to guide decisions for elective AAA repair has faced strong challenge because of its inability to accurately predict rupture for all AAA [170, 200]. Recent studies have been focused on studying in vivo stress levels in AAA [28, 34, 35, 40, 55] and it has been shown that aneurysms smaller than a certain size threshold can experience higher peak stress than larger aneurysms [28, 34, 35, 40, 55]. While these studies have suggested that using peak wall stress to predict the rupture potential for individual AAA would be an improvement over using maximum diameter alone, stress is only one of two factors that dictate the failure of a material, including the AAA wall. For example, two aneurysms with the same peak stress levels but different wall strength distributions might have a different rupture potential. In order to most accurately predict the rupture potential for each individual AAA, therefore, both the stress and strength distributions are necessary. By combining the technique reported here for predicting in vivo wall strength distribution with our companion method of 3D AAA wall stress analysis [28, 55], a new and improved means to predict the rupture potential for individual AAA may be possible. It is important to note that the strength prediction model derived here is noninvasive in nature. Each of the predictor variables - patient's sex, normalized local AAA diameter, family history, and local ILT thickness - are noninvasively obtainable.

Therefore, in vivo AAA wall strength distribution for any given patient is clinically feasible and cost effective.

Previous work in our laboratory resulted in a statistical model for wall strength using multiple linear regression techniques [39, 40]. This statistical model consisted of four variables and took the form

$$\text{STRENGTH} = 141.26 - 17.16 * \text{ILT} + 3.39 * \text{AGE} - 257.30 * \text{NORD} - 69.5 * \text{HIST} \quad (6.11)$$

where ILT is the thickness of intra-luminal thrombus (cm), AGE is the patient's age (years), NORD is the local diameter normalized to the maximum diameter, and HIST is the patient's family history of aneurysm. As can be seen from **Figure 6-15** and **Tables 7-9**, this model resulted in larger stress values than for the currently developed model. This difference is most likely due to the correction made for the sample thickness in the strength measurements (uniaxial testing, [Section 6.3.3](#)). The previous model also predicted an increase in wall strength for increasing age. This result was not found in the current study, which may have been due to the large increase in sample size for the current model compared to the previous model (39 versus 11 patients, respectively). It is also interesting to note that the current model predicted a significant decrease in mean AAA wall strength for ruptured versus non-ruptured AAAs, while the previous model did not ([Figure 6-17](#)).

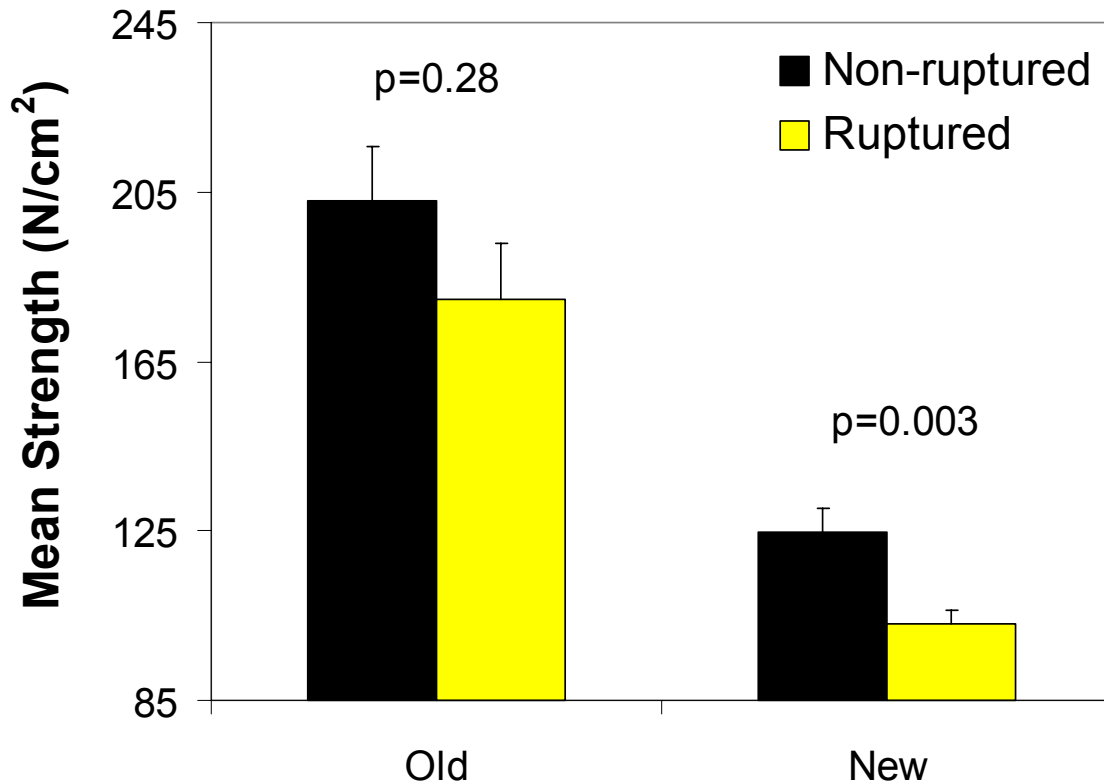


Figure 6-17: Mean AAA wall strength using the old and new models for ruptured vs. non-ruptured AAAs

The currently accepted for criterion for determining a given AAAs risk of rupture is the maximum cross sectional diameter. While a surgeon will not decide to perform surgery based *solely* on the maximum diameter (there are other factors taken into account), a diameter greater than 5.5 cm remains the globally accepted quantitative criteria for determining a given aneurysm’s risk of rupture. The current method for quantitatively assessing an individuals rupture risk includes the maximum cross sectional diameter in the independent variable NORD, while also including other patient-specific predictors such as gender, family history, and the presence and amount of ILT present. The fact that the patient’s sex remained in the current statistical model for AAA wall strength is not surprising given the recent reports that women

have recently been reported as having a higher growth and rupture rate than men [176, 201, 202]. Similarly, a recent investigation by Hans et al. showed that rupture risk of AAAs may be associated with the AAA volume, which supports our finding that ILT is an important predictor of AAA strength [203].

As with any modeling technique, there are certain limitations that should be kept in mind regarding the statistical model derived here. Due to restrictions associated with open surgical procedures, we were limited to AAA wall samples from the anterior region of AAA only. Ideally, samples would be obtained from the anterior, posterior and both lateral regions of AAA. This limitation should be kept in mind whenever utilizing the proposed statistical model. The use of an estimated nonaneurysmal diameter to normalize the local diameter was used for two reasons: CT scans were not available for all patients, and the authors believe that the proximal aorta of each AAA may not serve as an appropriate measure of the nonaneurysmal aorta, since this region can often times be dilated as well. It should also be noted that the local cross sectional diameter was measured as the average of two orthogonally oriented diameter measurements. Therefore, this reflects only the average of circumferential radius of curvature when in reality the AAA wall also has a longitudinal radius of curvature and both radii can vary spatially [204].

An important constraint of the statistical model (6.10) is that the range of the original data from which it was constructed limits its application. For example, if one would like to predict the wall strength distribution for a AAA which contained an ILT thickness greater than 3.6 cm, the strength model derived from Group C can not be used reliably since this ILT thickness is outside of the range utilized in its derivation. In addition, using a “worst-case scenario” from the entire dataset (SEX=Female=-0.5, HIS=Positive=0.5, $ILT^{1/2}=1.9$, NORD=3.92), the strength calculated

is -3.59 N/cm^2 . While negative wall strength is not physically reasonable, this occurs simply due a lack of a strength measurement with these worst-case scenario parameter values used in the derivation of the model. However, since for 38 patients and 81 specimens, no such combination exists, we would expect this occurrence to be of relatively low probability. In order to avoid this issue completely, a very large number of patients covering the entire range of possible predictor variables would be required, a task which lies outside the scope of the current work.

It is also important to note that in the present work it is assumed that the failure criterion of the AAA wall (its strength) can be adequately measured and modeled using uniaxial techniques. The fact that the aorta itself is a complex composite of collagen and elastin fibers suggests that assuming this material fails in a manner similar to a typical engineering material (e.g., steel etc.) may not be correct. In fact, a recent report by Ohashi et al. has shown that the biaxial inflation of human thoracic aneurysms results in a preferential tearing of the aortic wall in the longitudinal direction [205]. The actual failure mechanisms responsible for AAA rupture remain unknown. An alternative mathematical description of the gradual dilation and failure of AAAs has recently been derived by Watton et al. [206]. In this work the AAA is modeled as a two-layered cylindrical membrane using nonlinear elasticity and physiologically realistic constitutive relations to mathematically model the growth of a AAA in-vivo. While it is clear that the gradual expansion of a AAA corresponds with a reorganization of the extracellular matrix, it remains unclear which of the structural components (e.g., collagen) may be primarily responsible for the eventual failure of the AAA wall. The structural changes of the extracellular matrix present in AAAs have not been included in the current estimations of either stress or strength. Identifying these changes and how they correlate with the gradual dilation of the abdominal aorta may elucidate whether the inclusion of such information would benefit the estimations of stress

and strength in our current RPI. In addition, taking a closer look at the structural changes present in specimens received from ruptured AAAs may provide evidence for the prevailing mechanisms involved in AAA rupture.

In summary, a four-parameter statistical model has been successfully developed to noninvasively estimate wall strength distribution of any AAA. Despite the noted limitations, the current model predicts local AAA wall strength moderately well ([Figure 6-13](#)). Results here also suggest that the newly developed model for estimating AAA wall strength may identify those AAAs at high risk of rupture better than the clinically accepted maximum transverse diameter criterion. By combining this technique with the AAA wall stress calculation technique developed in our laboratory, a more accurate assessment for AAA rupture potential may be possible. The successful implementation of such a technique would likely benefit the management of patients with AAA.

7.0 RUPTURE POTENTIAL INDEX

7.1 INTRODUCTION

Abdominal aortic aneurysms are characterized by the structural remodeling resulting in the gradual weakening and expansion of the aortic wall. This disease occurs over the time course of several years and can typically remain quiescent until the strength of the aortic wall is unable to withstand the forces acting on it as a result of the luminal blood pressure – resulting in AAA rupture. Since the development and progression of AAAs can often times be asymptomatic, rupture of AAA can often times go unnoticed. The clinical treatment of those patients whose AAA is diagnosed presents a unique dilemma for the surgeon: surgery should only be recommended when the risk of rupture of the AAA outweighs the risks associated with the surgical procedure.

This unique clinical situation has led researchers to investigate several different predictors of AAA rupture. The most common clinical quantitative measure of aneurysm rupture risk has been the maximum transverse diameter [202]. Some of the other predictors proposed in the literature include cyclic strain via ultrasound [148], ILT volume [203], and growth rate [207, 208] among others. For example, Fillinger et al. also recently utilized the finite element method to demonstrate that peak wall stress as opposed to maximum diameter may better identify those

AAAs at high risk [33]. This study utilized techniques for noninvasively estimating wall stress previously derived in our laboratory which have since been improved with the inclusion of ILT [55] and anisotropy ([Chapter 5](#)). Clearly these estimations of wall stress represent improvements over previous predictions of wall stress based on the Law of LaPlace, hypothetical AAA geometries, and linear material properties [95, 127, 128, 145, 146, 149, 209]. Wang et al. first developed a statistical model for noninvasively predicting AAA wall strength. This model has been improved in the present work with the addition of data as well as several other notable improvements ([Table 6-1](#)).

Since AAA rupture occurs when the stress acting on the wall exceeds its strength, the prediction of AAA rupture should include both of these mechanical parameters. The techniques utilized in the current work for stress ([Chapter 5](#)) and strength ([Chapter 6](#)) estimation can be combined such that a rupture potential index (RPI) can be defined which represents the spatial distribution of rupture potential on a patient-specific basis. The RPI is therefore proposed here to be a more dependable criterion for rupture potential than the clinically accepted maximum transverse diameter.

7.2 METHODS

7.2.1 Rupture Potential Index Calculation

The rupture potential index (RPI) is defined as the ratio of local wall stress to local wall strength:

$$\text{RPI}_i = \frac{\text{Stress}_i}{\text{Strength}_i}. \quad (7.1)$$

The subscript i in equation (7.1) corresponds to a given (X,Y,Z) location on the AAA wall. Once the stress for a given node in the finite element simulation was determined (Chapter 5), the locally acting wall strength was calculated for this node using equation (6.10). The 3D distribution of RPI is then calculated by dividing each node's stress and strength values. The calculation of the locally acting RPI for a given AAA was done in the Matlab script described in [Section 6.4.5](#) (Appendix L).

7.2.2 Comparison of Old versus New RPI Techniques

In order to compare the RPI using the previously methods of stress and strength versus those derived in the current work, the RPI was calculated using each method for all 21 electively AAAs described in [Section 5.2.5](#).

7.2.3 Ruptured versus Electively Repaired AAAs

The ability of the RPI to predict AAAs who are at high risk of rupture was analyzed by calculating the RPI for all 5 non-ruptured and 9 ruptured AAAs described in [Section 5.2.5](#). The improvements in rupture prediction using the current versus previous model of RPI were also

investigated by comparing the ruptured and non-ruptured RPI values using both methods. The new method of RPI was also compared to the maximum transverse diameter criterion for rupture prediction.

7.3 RESULTS AND DISCUSSION

The stress, strength, and RPI for a representative AAA using the methods derived in [Chapter 5](#) and [6](#) is shown in [Figure 7-1](#). The current approach to assessing this AAA’s risk of rupture would suggest this aneurysm is at 32% of its capacity to withstand rupture.

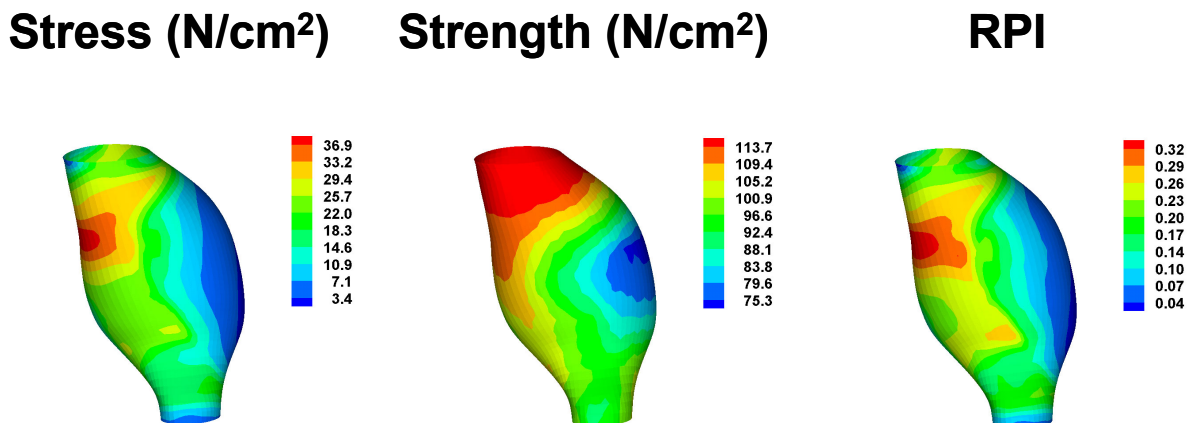


Figure 7-1: Noninvasively predicted stress, strength and RPI using the current techniques for stress and strength estimation

7.3.1 Comparison of Old versus New RPI Techniques

The peak and mean RPI values for each of the electively repaired AAAs are shown in [Table 7-1](#).

The peak RPI values for the new RPI were statistically larger than that utilized for the previous

method (0.34 ± 0.03 vs. 0.22 ± 0.03 , $p < 0.001$). In addition, the mean RPI values for the new RPI were statistically larger than that utilized for the previous method (0.14 ± 0.01 vs. 0.10 ± 0.01 , $p < 0.001$). A representative comparison of the previous and current RPI predictions is shown in [Figure 7-2](#) for AAA16.

Table 7-1: Peak and Mean RPI values for all electively repaired AAAs

| Aneurysm | New RPI | | Old RPI | |
|----------|---------|------|---------|------|
| | Peak | Mean | Peak | Mean |
| AAA1 | 0.39 | 0.18 | 0.39 | 0.18 |
| AAA2 | 0.35 | 0.13 | 0.21 | 0.09 |
| AAA3 | 0.45 | 0.18 | 0.21 | 0.10 |
| AAA4 | 0.62 | 0.30 | 0.34 | 0.16 |
| AAA5 | 0.29 | 0.13 | 0.09 | 0.04 |
| AAA6 | 0.53 | 0.22 | 0.37 | 0.17 |
| AAA7 | 0.35 | 0.11 | 0.19 | 0.05 |
| AAA8 | 0.28 | 0.08 | 0.10 | 0.03 |
| AAA9 | 0.12 | 0.03 | 0.07 | 0.02 |
| AAA10 | 0.52 | 0.22 | 0.37 | 0.16 |
| AAA11 | 0.41 | 0.13 | 0.22 | 0.10 |
| AAA12 | 0.29 | 0.13 | 0.17 | 0.09 |
| AAA13 | 0.19 | 0.07 | 0.10 | 0.04 |
| AAA14 | 0.40 | 0.25 | 0.52 | 0.28 |
| AAA15 | 0.35 | 0.14 | 0.25 | 0.10 |
| AAA16 | 0.35 | 0.14 | 0.17 | 0.07 |
| AAA17 | 0.34 | 0.12 | 0.27 | 0.10 |
| AAA18 | 0.21 | 0.06 | 0.12 | 0.04 |
| AAA19 | 0.33 | 0.12 | 0.15 | 0.07 |
| AAA20 | 0.19 | 0.07 | 0.10 | 0.05 |
| AAA21 | 0.28 | 0.16 | 0.15 | 0.09 |
| MEAN | 0.34 | 0.14 | 0.22 | 0.10 |
| SEM | 0.03 | 0.01 | 0.03 | 0.01 |

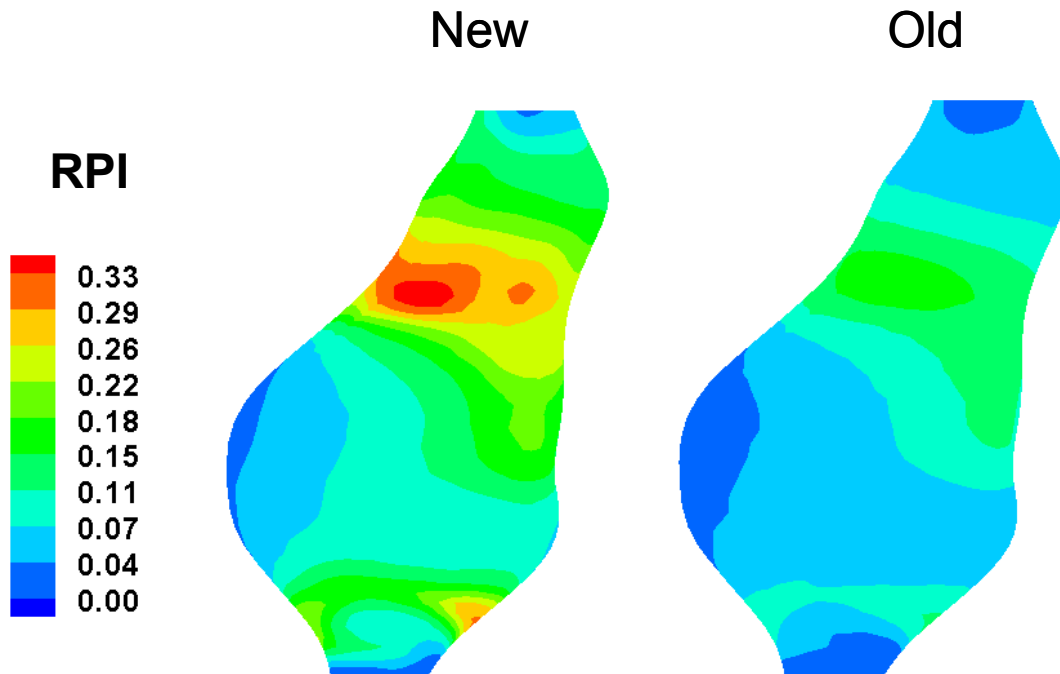


Figure 7-2: Comparison of old versus new techniques for RPI for a representative electively repaired AAA (AAA16)

7.3.2 Ruptured versus Non-ruptured AAAs

The peak and mean RPI values derived from the old method for stress and strength estimation are shown in [Table 7-2](#). [Table 7-3](#) lists the RPI values for the current estimations of stress and strength. The differences between the ruptured and non-ruptured peak RPI values were larger for the current RPI as compared to the previously developed RPI technique ($p = 0.10$ vs. $p = 0.79$, respectively). These differences were not as prominent when comparing the mean RPI values between the two groups ($p = 0.35$ vs. $p = 0.58$, respectively). A representative comparison of RPI for a ruptured (R8, maximum diameter = 5.20 cm) and non-ruptured (N4, maximum diameter = 5.23 cm) AAA is shown in [Figure 7-3](#). There was no significant

difference between the maximum transverse diameter of the ruptured and non-ruptured AAAs (7.10 ± 0.38 vs. 6.14 ± 0.54, respectively, p = 0.17).

Table 7-2: RPI values derived from the old stress and strength estimation techniques (* p = 0.79 ; + p = 0.58)

| NR AAA | Old RPI | | | | Peak | Mean |
|--------|---------|-------------------|------|-------|-------------------|------|
| | Peak | Mean | RAAA | Peak | | |
| N1 | 0.25 | 0.09 | R1 | 0.23 | 0.07 | |
| N2 | 0.22 | 0.12 | R2 | 0.28 | 0.14 | |
| N3 | 0.37 | 0.15 | R3 | 0.71 | 0.26 | |
| N4 | 0.23 | 0.11 | R4 | 0.22 | 0.10 | |
| N5 | 0.19 | 0.08 | R5 | 0.32 | 0.13 | |
| | | | R6 | 0.19 | 0.07 | |
| | | | R7 | 0.40 | 0.20 | |
| | | | R8 | 0.20 | 0.10 | |
| | | | R9 | 0.20 | 0.07 | |
| MEAN | 0.25* | 0.11 ⁺ | MEAN | 0.30* | 0.13 ⁺ | |
| SEM | 0.03 | 0.01 | SEM | 0.06 | 0.02 | |

Table 7-3: RPI values derived from the new stress and strength estimation techniques (* p = 0.10; + p = 0.35)

| NR AAA | New RPI | | | | Peak | Mean |
|--------|---------|-------------------|------|-------|-------------------|------|
| | Peak | Mean | RAAA | Peak | | |
| N1 | 0.41 | 0.14 | R1 | 0.31 | 0.07 | |
| N2 | 0.31 | 0.18 | R2 | 0.64 | 0.37 | |
| N3 | 0.44 | 0.18 | R3 | 0.51 | 0.22 | |
| N4 | 0.27 | 0.16 | R4 | 0.42 | 0.16 | |
| N5 | 0.38 | 0.15 | R5 | 0.55 | 0.24 | |
| | | | R6 | 0.57 | 0.16 | |
| | | | R7 | 0.60 | 0.29 | |
| | | | R8 | 0.38 | 0.17 | |
| | | | R9 | 0.28 | 0.13 | |
| MEAN | 0.36* | 0.16 ⁺ | MEAN | 0.47* | 0.20 ⁺ | |
| SEM | 0.03 | 0.01 | SEM | 0.04 | 0.03 | |

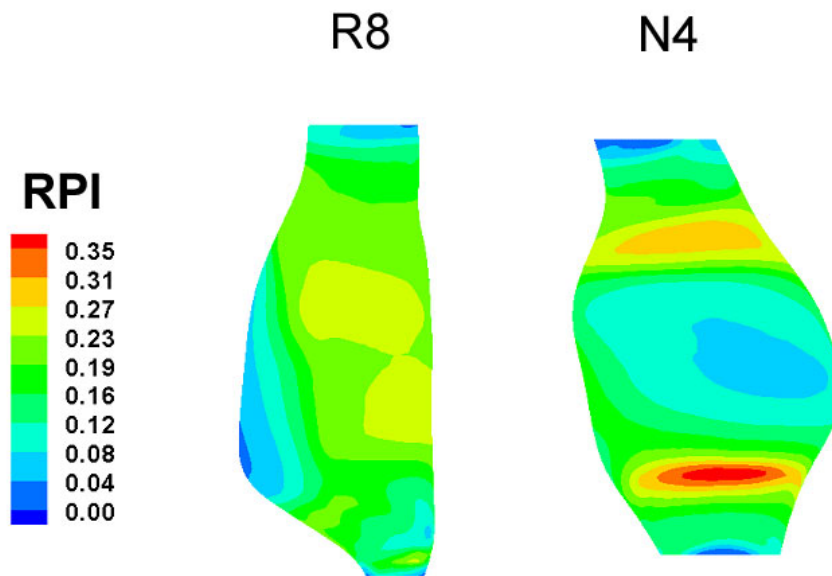


Figure 7-3: Representative comparison of the current RPI between a ruptured (R8, maximum diameter = 5.20) and non-ruptured AAA (N4, maximum diameter = 5.23 cm)

7.3.3 Summary

The currently developed techniques resulted in an increased mean and peak value of RPI for a set of electively repaired AAAs in comparison to the previously developed RPI technique [40]. In addition, comparisons of peak RPI values for ruptured and non-ruptured AAAs suggest an improvement in rupture prediction utilizing the current methodology as opposed to the previously developed RPI as well as the maximum diameter criterion.

A graphical depiction of the improvements in identifying AAAs who are at high risk of rupture is shown in [Figure 7-4](#). In this figure the Old RPI AAAs represent the rupture potential index as calculated using the previously derived isotropic constitutive relation for the AAA wall

stress as well as the previously developed noninvasive technique for wall strength. These results suggest that both the maximum diameter and the currently developed RPI provide an improved prediction of rupture potential as compared to the previously defined RPI technique [40]. While this figure suggests an improvement of the current RPI over the maximum diameter criterion ($p = 0.1$ vs. $p = 0.17$), more AAAs are needed to accurately test this hypothesis.

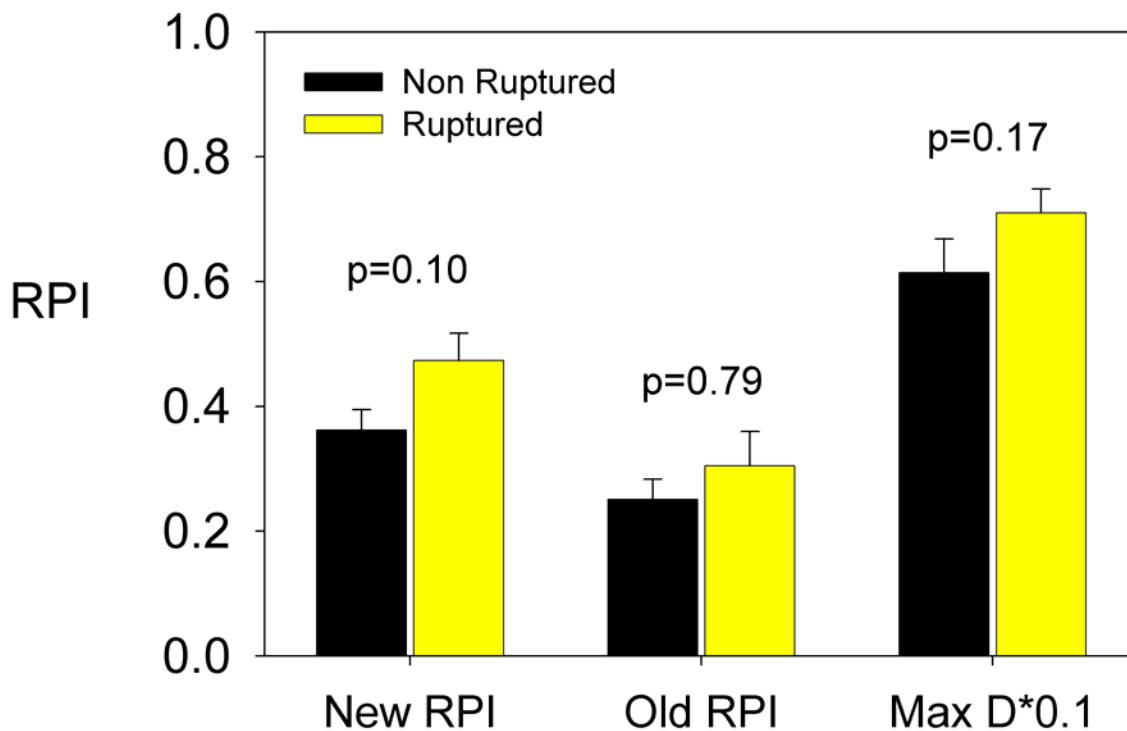


Figure 7-4: Improvement in rupture potential prediction by using the currently developed RPI methodology (n=5 for non-ruptured, n=9 for ruptured)

8.0 DISCUSSION

8.1 RELATION TO PREVIOUS WORK

The locally acting AAA wall stress divided by the local AAA wall strength, termed the rupture potential index (RPI), has been introduced as an alternative to the more commonly accepted maximum diameter criterion for predicting the rupture of abdominal aortic aneurysms. Improvements in the estimation of stress have been made including the replacement of a previously derived isotropic constitutive relationship for the AAA wall [38] by the anisotropic constitutive relationship derived ([Chapter 3](#)) and implemented ([Chapter 5](#)) in the current work. In addition, the statistical model for noninvasive estimation of AAA wall strength has been improved with several notable enhancements some of which include a larger construction data set ([Section 6.2](#)) and a CT-based method of local diameter measurement ([Section 6.3.2.2](#)). The currently developed estimations of wall stress and strength were significantly different than the previously defined estimations ([Section 5.3.3](#) and [6.4.6](#)), suggesting that an improved rupture potential index may result. In fact, when retrospectively comparing peak and mean RPI values between ruptured and non-ruptured AAAs, the currently developed RPI resulted in an improved ability to differentiate those AAAs which eventually rupture ([Section 7.3.2](#), [Figure 7-4](#)). The currently proposed technique for noninvasively predicting the rupture potential of a AAA may benefit the surgical decision making and clinical management of AAA patients.

The most commonly used criterion for AAA rupture prediction is the maximum diameter criterion, which is typically based on a cut-off value of 5.5cm. Other parameters that have been proposed as potential predictors of AAA rupture include the AAA expansion rate [201, 210, 211], wall stiffness [148], increase in intra-luminal thrombus (ILT) thickness [212], volume of ILT [203], wall tension [27], and peak AAA wall stress [33, 34]. All of these approaches are empirical in nature, and as such fail to take into account the physical aspects which control AAA development and rupture. Described in this section are the most common criteria utilized for the clinical management of AAA and the shortcomings associated with their use.

Maximum Diameter

The maximum transverse diameter of an aneurysm has become the mainstay for determining a given AAAs risk of rupture. The definition of this criterion for rupture prediction most likely stems from the Law of LaPlace, which states that the stress acting on a pressurized sphere is a function of its internal pressure, the radius of the sphere, and the thickness of the walls of the sphere. Utilizing this method of stress estimation therefore assumes the AAA is spherical in nature. Translating this technique to AAAs would suggest that the peak stress acting on a given aneurysm would:

- 1) occur exclusively at the level of maximum diameter
- 2) be the same for two AAAs of equal diameter but largely different local curvatures and 3D tortuosity and
- 3) require the direct measurement of the wall thickness within a AAA.

There have been several studies investigating the effect of non-spherical geometry on the peak wall stress in AAAs which show the peak stress may and often-times does not occur at the level of maximum diameter [28, 33-35, 55, 93-95, 111, 127, 146]. The presence of unique distributions of first and second principal curvatures within AAAs has been quantified in the literature [110, 147, 213]. These major and minor curvatures occurring regularly within AAA suggest may play a more prominent role on local wall stress than diameter alone. The effect of wall thickness on the patient-specific wall stress has largely been ignored in the literature. This primarily stems from the inability to noninvasively measure this quantity using the medical imaging techniques typically used in AAA patient management (CT, ultrasound). A recent report has investigated the effect of localized changes in wall thickness on AAA wall stresses. This study implemented localized AAA wall thickness measurements taken from a fully intact ruptured AAA from autopsy into a patient-specific finite element analysis and found the peak stress correlated with the point of AAA rupture [109]. Clearly the ability to noninvasively predict the three dimensional distribution of AAA wall thickness would greatly improve the estimation of wall stress.

Perhaps the most convincing evidence that the maximum diameter of a AAA is unable to predict rupture is given in a study by Darling et al. [23]. They studied records from 24,000 consecutive, non-specific autopsies performed over a 23-year period. They found 473 non-resected AAA, of which 118 were ruptured. Fifteen percent of AAA under 5 cm in diameter ruptured, and 66% of the aneurysms between 5 cm and 10 cm (including 54% of those between 7.1 cm and 10 cm) never ruptured. These findings question the maximum diameter criterion to assess AAA severity. If a 5cm criterion were followed strictly for the 473 subjects with AAA studied by Darling and his associates, 7% (34/473) of them would have succumbed to rupture

before surgical repair was offered since their AAA was "too small" (<5cm). Likewise, 25% (116/473) of them would have undergone major surgery, perhaps unnecessarily since their aneurysm may not have ruptured if left untreated. Darling et al.'s study has also recently been supported by Hall et al. who summarized a group of studies indicating that up to 23% of AAAs rupture at a diameter less than 5 cm [27]. All of these studies indicate that maximum diameter itself is unable to reliably predict AAA rupture.

Wall Stress Alone

There have been a few studies in the literature that have suggested the use of peak AAA wall stress alone as an improvement in AAA rupture prediction over the commonly accepted maximum diameter criterion. Hall et al. [27] described the relationship between aortic wall stress predicted using the Law of LaPlace (i.e., based on maximum AAA diameter) and risk of AAA rupture. In their study of 40 AAA patients, they suggested that there exists a threshold tension after which rupture was imminent. However, it has been shown by our laboratory [28, 55, 93, 111] and others [33-35] that the stresses acting on a AAA are not evenly distributed, and cannot be adequately described by the Law of LaPlace (see also previous section). Fillinger et al. also found a significant increase in peak wall stress when comparing ruptured AAAs to those who remained quiescent [33]. A more recent study by Venkatasubramaniam et al. also found similar results, while also showing that the location of AAA rupture correlated with the location of peak wall stress [34]. It should be noted that both of these studies neglected the presence of mechanical anisotropy, utilizing the isotropic constitutive relationship developed previously in our laboratory [38]. Another investigation that has recently been added to the literature also investigates the use of stress prediction in AAA patient management [214].

While the peak stress is an important component in determining the mechanical failure of the AAA wall, this measure alone is unable to account for differences in wall strength from patient to patient as well as within a given patient. Thubrikar recently reported the important conclusion that the yield stress within a given AAA varies spatially [54]. These results are in support of work done by Raghavan et al. who have also shown a 3D variation in wall strength in a AAA excised from autopsy [109]. The degradation of the AAA wall has also recently been shown to vary spatially within a given AAA [215], also suggesting that the wall strength varies as a function of location within a AAA. All of these studies as well as recent work in our laboratory [216] provide evidence that the local wall strength is equally important in determining a given AAAs risk of rupture.

Other Potential Predictors of Rupture

The expansion rate (change in maximum diameter over time) has been suggested as a potential predictor of AAA rupture by a few researchers [201, 211, 217]. While it stands to reason that the risk of rupture of a given AAA is related to its growth rate, the use of a noninvasive predictor that is a function of time is troublesome. This is primarily due to the fact that a patient's maximum diameter history must be known in order to make a clinical assessment on rupture potential. Since AAAs can often-times be asymptomatic, the diagnosis of a significant number of AAAs occurs as a result of investigating other comorbid conditions. For these patients, no prior knowledge of AAA growth rate is known and therefore it is impossible to assess their rupture risk using expansion rate.

Another potential rupture risk indicator that has been proposed in the literature is the mechanical properties of the AAA wall as measured noninvasively using ultrasonography. The

beta stiffness (β) and pressure-strain elastic modulus (E_p) are typically used in such studies to quantify the mechanical behavior of arterial tissue. Sonesson et al. measured the beta stiffness of ruptured and non-ruptured AAAs and found there to be no correlation between beta stiffness in those AAAs who eventually ruptured as compared to those who remained quiescent [148]. Wilson et al. investigated the relationship between AAA wall compliance, maximum diameter and growth rate in a series of patients with non-operated, asymptomatic AAAs [175]. Their results suggest that if aortic wall compliance is related to rupture then its use may augment the ability to effectively manage the AAA patient population. The use of a noninvasive estimate of aneurysmal mechanical behavior may or may not prove to be statistically correlated with the rupture of AAAs. From a mechanical point of view, however, the compliance, beta stiffness, and pressure-strain modulus fail to take into account the mechanical *failure* of the wall, which is a function of its strength and the stress acting on it. That is not to say, however, that the patient-specific mechanical behavior of a AAA does not effect its risk of rupture. In fact, the currently developed RPI includes information regarding the anisotropic mechanical behavior of the AAA wall; however this is a population-wide model and is not patient-specific. The use of noninvasive medical imaging techniques to determine the mechanical properties on a patient-specific basis may vastly improve the prediction of stress in AAAs and therefore aide in rupture prediction.

The presence, amount, and location of intra-luminal thrombus have also been proposed as means of directing AAA patient management. Stenbaek et al. [212] investigated the increase of relative ILT volume as a potential rupture risk predictor and concluded that a rapid increase may be a better predictor of AAA rupture than an increase in maximal diameter. Hans et al. has also recently provided evidence that ILT is important in rupture prediction [203]. Their

study revealed that ruptured AAAs are larger in diameter and have a greater volume of thrombus compared with intact AAAs. This difference disappeared, however, when the ILT volume was normalized to AAA volume. This group also showed that the location (anterior and eccentric) of ILT between ruptured and non-ruptured AAAs did not significantly differ. While the presence and location of ILT within an AAA may correlate with its peak stress, analyzing this parameter alone may lead to large errors in rupture assessment as this measure is not based on sound physical principles.

The accurate prediction of the rupture potential of an AAA remains an unrequited clinical dilemma whose solution would prove beneficial to the management and treatment of AAA patients. The current work focuses on a mechanically-based rupture potential index that may fill this vacancy. The primary advantages of the currently developed RPI are that it

- is patient-specific
- is noninvasively attainable
- varies with increases or decreases in AAA wall stress
- includes the mechanical anisotropy known to be present in the AAA wall
- varies with the strength of the AAA wall as determined from a patients medical history, sex, local ILT thickness, and local normalized diameter, and
- is based on estimating those factors which influence the *mechanical failure* of the AAA wall.

While the currently proposed RPI is encouraging in its promise, there remain several ways in which it could be improved, some of which are discussed in the following section.

8.2 LIMITATIONS AND FUTURE WORK

8.2.1 Estimation of Wall Stress

The estimation of AAA wall stress using the finite element method has made several incremental improvements over the past few decades. Current computed-tomography imaging techniques have allowed the implementation of patient-specific geometry in AAA finite element simulations, which is thought to be an improvement over the Law of La Place [27] or other hypothetical geometries used for wall stress estimation [95]. Recent work in our laboratory has also shown the importance of including the ILT in AAA finite element simulations [55]. While the stresses estimated in the current work included the presence of the ILT as well as mechanical anisotropy, there are several key assumptions made here that leave room for improvement. One of these assumptions is that the AAA wall acts as a mechanically homogenous material. The atherosclerotic nature of aneurysm formation results in the calcification of the aneurysmal wall. The inclusion of this hardened plaque into finite element simulations of AAA and shown to alter the location and magnitude of wall stresses [98]. The presence and amount of calcification within the AAA wall should therefore be included in future stress simulations of AAA.

Another assumption that requires future investigation is the boundary conditions applied to the AAA finite element simulations. As stated in [Section 5.2.1](#), the AAA is in a complex mechanical environment in the abdominal cavity including contact with the spinal column posteriorly as well as being tethered via arteries bifurcating from the AAA sac. The influences of such mechanical boundaries were neglected in the current study and require further examination.

The effect of the ILT on AAA wall stresses has been shown in our laboratory to effect the location and magnitude of the peak wall stresses acting on AAAs [55]. The ILT has also been investigated with respect to its role in the weakening of the wall [31], which may be a result of the hypoxia caused by the hindrance of luminal blood supply due to the ILT. In terms of its mechanical significance, the ILT has been assumed to act as a *purely* solid continuum in the current work. The large water content and microstructure of the ILT [59, 152] suggests that this assumption may be invalid. In fact, Takagi et al. recently investigated the changes in pressure dissipation through the ILT thickness and found that the thrombus of an aneurysm does not significantly decrease the pressure on the aneurysmal wall [150]. Future work should investigate the porous nature of the ILT and how this may affect its mechanical and physiological role in the development and rupture of AAA.

8.2.2 Estimation of Wall Strength

The development of the noninvasive method for estimating AAA wall strength in the current work also has its limitations. As with any statistical regression model, the application of any statistical regression model is limited by the range of independent variables used in its derivation (see [Section 6.4.8](#)). The fact that only anterior samples of wall strength were used in the model derivation should also be kept in mind when utilizing this model. This limitation was unavoidable in the current work as the procurement of specimens from three-dimensionally random was impossible.

Perhaps the most concerning limitation of the statistical model is the relatively small number (seven) of variables chosen as potential predictors of AAA wall strength. In reality, there may be a very large number of factors that influence local wall strength. The use of the

potential predictors chosen in this study was based primarily on the evidence provided for each in the literature as well as their noninvasive attainability. For example, one variable that may be important in the degradation of extracellular proteins within the AAA wall is the local acting stresses [218-221]. Indeed, the local stresses acting at a specific location of the AAA wall is a major focus of the current work and has been proven to be noninvasively attainable. In fact, plotting the peak wall strength (from uniaxial tests) versus wall stress (as determined from [stress analyses](#) and IMA correlation technique described in [Section 6.3.2.2](#)) suggests that there may be a relationship between these two variables (**Figure 8-1**). Future studies should investigate this relationship further, being sure to test whether local wall stress should be included in the statistical model for wall strength. Other variables that may prove to be important and should therefore be included in future studies are the presence and amount of calcification [98] as well as the volume of ILT [203, 212].

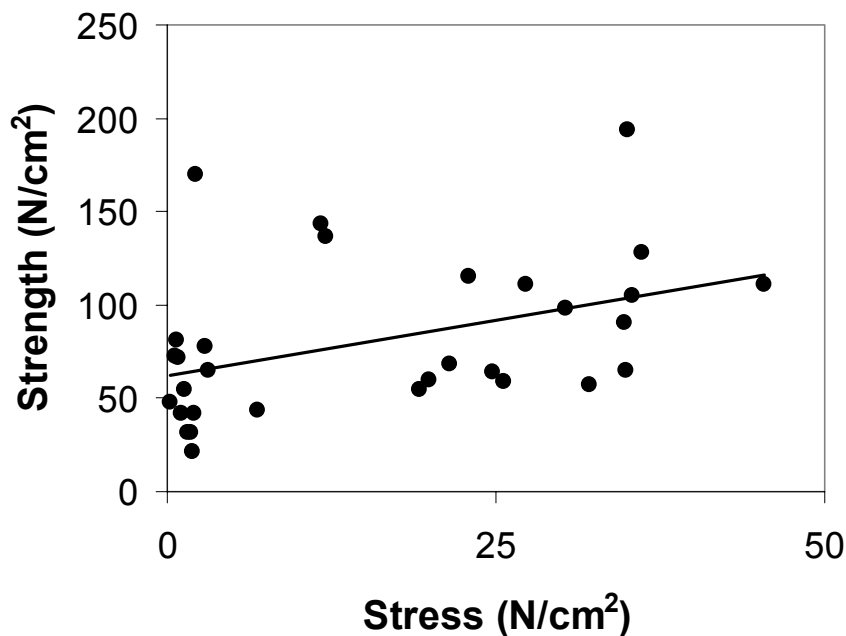


Figure 8-1: Preliminary relationship between AAA wall strength and locally acting wall stress

8.2.3 RPI in the Clinic

Of course, the fallacy of the maximum diameter criterion and its replacement by the RPI will only prove to be clinically meaningful with a prospective randomized study which displays an improved management of AAA patients using the RPI. This may be a tricky study to perform, since surgeons will most likely not be able to create two experimental arms, basing a surgical decision primarily on either maximum diameter or RPI. A more realistic study would be to retrospectively compare the RPI and rate of RPI with the maximum diameter and rate of maximum diameter for a randomized set of AAA patients. Correlating the outcomes of these patients with the two proposed criteria would provide evidence for their comparison. This has been performed in the current study, however the dataset was relatively small (n=5 non-ruptured, n=9 ruptured). In addition, the RPI and maximum diameter were measured *after* the clinical outcome of the patient was determined.

8.3 CONCLUSION

The formation of aneurysm within the abdominal aorta presents a unique clinical dilemma, requiring surgeons to intervene when the risks of rupture outweigh those associated with repairing the AAA. The current work describes the continued improvement of a rupture potential index which involves the noninvasive estimation of those factors influencing the *mechanical failure* of the AAA wall. The clinical relevance of this method for rupture assessment has yet to be validated, however its success will undoubtedly aid surgeons in clinical decision making and AAA patient management.

APPENDIX A

AVERAGING OF BIAXIAL TENSILE TESTING DATA

```
% These files are called (ave data.m, new_post_ave_data.m)
clear;
% this program requires there to be zeros so all cols are
% the same length
load l6a_2dir.txt
data=l6a_2dir;

output='constants.txt';
fod=fopen(output,'w');

% m is the # of rows, n is the # of cols
[m,n]=size(data);
flag=0;
test=0;
% these are column titles
%fprintf(fod,'%s','Specimen');
%fprintf(fod,' %s','a');
%fprintf(fod,' %s\n','b');

for i=1:2:n
    x=data(:,i);
    y=data(:,i+1);
    len=m;
    for j=1:m
        test=abs(x(j))+abs(y(j));
        if flag==1;
            if test==0;
                flag=0;
                len=j-2;
                test=1;
            %         j=m;
```

```

        break;
    else
        flag=0;
    end
end
end
if test==0
    flag=1;
end
end
newx=x(1:len);
newy=y(1:len);

ln_y=log(newy);
coeff=polyfit(newx,ln_y,1);
a=coeff(1);
b=coeff(2);
c=exp(b);

fprintf(fod,'%g',i);
fprintf(fod,'    %g',c);
fprintf(fod,'    %g\n',a);
end
fclose(fod);

load constants.txt
cterm=constants(:,2);
expterm=constants(:,3);

numsamples=length(cterm);

temp=0.001:2:121;
temp=temp';

colincr=1;
for i=1:numsamples
    %stuff(:,colincr)=temp;    %tension
    stuff(:,colincr)=(1/expterm(i)).*log(temp./cterm(i)); %strain
    colincr=colincr+1;
end

save ave_data_l6a_2.txt stuff -ASCII -TABS

%%%%%%%%%%

% First, combine all data for EITHER 1 or 2 directions so that they are consecutively next to
eachother

```

```

% in the following order l2a_i, l3a_i, l4d_i, l5a_i, l6a_i where i indicates the direction
% For example, if you have 8 specimens, you should have a total of 8x5=40 columns of data
% call this file comb_data_1.txt or comb_data_2.txt

```

```

load comb_data_1.txt
data=comb_data_1;

```

```

% m is the # of rows, n is the # of cols
[m,n]=size(data);
numsp = n/5;
thick=1.32;
in_ten=0.001;
ten_stp=2;

```

```

% this section was added just before submission of the AAA paper
% due to Dr. Sacks' request to use the sum of inverse of thicknesses as
% opposed to an average thickness
load specimen_thicknesses.txt
thickdata=specimen_thicknesses;
invthick=1./thickdata;
newthick=(1/numsp)*(sum(invthick));

```

```

% lets split up each protocol..it'll be easier that way
% the i index below references which protocol you are using

```

```

for i=1:5
    for j=1:m
        for k=1:numsp
            threeD_data1(i,j,k)=data(j,(i-1)*numsp+k);
        end
    end
end

```

```

for i=1:5
    for j=1:m
        aveE11(j,i)=mean(threeD_data1(i,j,:));
        stdev11(j,i)=(std(threeD_data1(i,j,:)))/sqrt(numsp);
    end
end

```

```

for i=1:m
    tension1(i) = in_ten;
    in_ten=in_ten+2;
end

```

```
aveE11(1,:)=0;
stdev11(1,:)=0;
tension1=tension1';
```

```
for j=1:5
    for i=1:m
        S11(i,j)=(newthick.*tension1(i))*(1/(2*aveE11(j)+1));
    end
end
```

```
%%%%%%%%%%%%%%%%%%%%%%%%%%%%%%%%%%%%%%%%%%%%%%%%%%%%%%%%%%
%%%%%%%%%%%%%%%%%%%%%%%%%%%%%%%%%%%%%%%%%%%%%%%%%%%%%%%%%%
%%%%%%%%%%%%%%%%%%%%%%%%%%%%%%%%%%%%%%%%%%%%%%%%%%%%%%%%%%
%%%%%%%%%%%%%%%%%%%%%%%%%%%%%%%%%%%%%%%%%%%%%%%%%%%%%%%%%%
% NOW FOR THE 2 DIRECTION
```

```
load comb_data_2.txt
data2=comb_data_2;
```

```
% m is the # or rows, n is the # of cols
[m,n]=size(data2);
numsp = n/5;
in_ten=0.001;
ten_stp=2;
```

```
% lets split up each protocol..it'll be easier that way
% the k index below references which protocol you are using
```

```
for i=1:5
    for j=1:m
        for k=1:numsp
            threeD_data2(i,j,k)=data2(j,(i-1)*numsp+k);
        end
    end
end
```

```
for i=1:5
    for j=1:m
        aveE22(j,i)=mean(threeD_data2(i,j,:));
        stdev22(j,i)=(std(threeD_data2(i,j,:)))/sqrt(numsp);
    end
end
```

```

end

for i=1:m
    tension2(i) = in_ten;
    in_ten=in_ten+2;
end

aveE22(1,:)=0;
stdev22(1,:)=0;
tension2=tension2';

for j=1:5
    for i=1:m
        S22(i,j)=(newthick.*tension2(i))*(1/(2*aveE22(j)+1));
    end
end

%%%%%%%%%%%%%%%%%%%%%%%%%%%%%%%%%%%%%%%%%%%%%%%%%%%%%%%%%%%%%%%%%%%%%%%%
%%%%%%%%%%%%%%%%%%%%%%%%%%%%%%%%%%%%%%%%%%%%%%%%%%%%%%%%%%%%%%%%%%%%%%%%
% now ceate the fung 4 param stresses using the averaged Eij's
% we need to create a strain space that will allow us to cover
% the stress space adequately
%%%%%%%%%%%%%%%%%%%%%%%%%%%%%%%%%%%%%%%%%%%%%%%%%%%%%%%%%%%%%%%%%%%%%%%%
%%%%%%%%%%%%%%%%%%%%%%%%%%%%%%%%%%%%%%%%%%%%%%%%%%%%%%%%%%%%%%%%%%%%%%%%

modelE11=zeros(100,5);
modelE22=zeros(100,5);

modelE11(:,1)=linspace(0,max(aveE11(:,1))+0.009,100)';
modelE11(:,2)=linspace(0,max(aveE11(:,2))+0.009,100)';
modelE11(:,3)=linspace(0,max(aveE11(:,3))+0.009,100)';
modelE11(:,4)=linspace(0,max(aveE11(:,4))+0.009,100)';
modelE11(:,5)=linspace(0,max(aveE11(:,5))+0.009,100)';
modelE22(:,1)=linspace(0,max(aveE22(:,1))+0.009,100)';
modelE22(:,2)=linspace(0,max(aveE22(:,2))+0.009,100)';
modelE22(:,3)=linspace(0,max(aveE22(:,3))+0.009,100)';
modelE22(:,4)=linspace(0,max(aveE22(:,4))+0.009,100)';
modelE22(:,5)=linspace(0,max(aveE22(:,5))+0.009,100)';

c=0.621;
a1=142.859;
a2=127.222;
a3=40.136;

Q=a1*modelE11.^2+a2*modelE22.^2+2*a3.*modelE11.*modelE22;
modelS11=(c.*exp(Q).*(a1.*modelE11+a3.*modelE22));

```

```

modelS22=(c.*exp(Q).*(a1.*modelE22+a3.*modelE11));

%%%%%%%%%%%%%%%%%%%%%%%%%%%%%%%%%%%%%%%%%%%%%%%%%%%%%%%%%%%%%%%%%%%%%%%%
% now for some plots of this data
%%%%%%%%%%%%%%%%%%%%%%%%%%%%%%%%%%%%%%%%%%%%%%%%%%%%%%%%%%%%%%%%%%%%%%%%

figure
subplot(1,2,1);
plot(aveE11(:,1),S11(:,1),'k. ');
axis([0 max(max(max(aveE11,aveE22)))+0.01 0 max(max(max(S11,S22)))+10]);
hold on;
plot(aveE11(:,2),S11(:,2),'k. ');
hold on;
plot(aveE11(:,3),S11(:,3),'k. ');
hold on;
plot(aveE11(:,4),S11(:,4),'k. ');
hold on;
plot(aveE11(:,5),S11(:,5),'k. ');
hold on;
plot(modelE11(:,1),modelS11(:,1),'-k');
hold on;
plot(modelE11(:,2),modelS11(:,2),'-k');
hold on;
plot(modelE11(:,3),modelS11(:,3),'-k');
hold on;
plot(modelE11(:,4),modelS11(:,4),'-k');
hold on;
plot(modelE11(:,5),modelS11(:,5),'-k');
title('S11 vs E11')
xlabel('E11')
ylabel('S11')

subplot(1,2,2);
plot(aveE22(:,1),S22(:,1),'b. ');
axis([0 max(max(max(aveE11,aveE22)))+0.01 0 max(max(max(S11,S22)))+10]);
hold on;
plot(aveE22(:,2),S22(:,2),'b. ');
hold on;
plot(aveE22(:,3),S22(:,3),'b. ');
hold on;
plot(aveE22(:,4),S22(:,4),'b. ');
hold on;
plot(aveE22(:,5),S22(:,5),'b. ');
hold on;

```

```

plot(modelE22(:,1),modelS22(:,1),'-k');
hold on;
plot(modelE22(:,2),modelS22(:,2),'-k');
hold on;
plot(modelE22(:,3),modelS22(:,3),'-k');
hold on;
plot(modelE22(:,4),modelS22(:,4),'-k');
hold on;
plot(modelE22(:,5),modelS22(:,5),'-k');
title('S22 vs E22')
xlabel('E22')
ylabel('S22')

```

```

% figure
% plot(aveE11(:,1),tension1(:,1),'r. ');
% hold on;
% plot(aveE11(:,2),tension1(:,1),'r. ');
% hold on;
% plot(aveE11(:,3),tension1(:,1),'r. ');
% hold on;
% plot(aveE11(:,4),tension1(:,1),'r. ');
% hold on;
% plot(aveE11(:,5),tension1(:,1),'r. ');

```

```

% figure
% plot(aveE22(:,1),tension2(:,1),'g. ');
% hold on;
% plot(aveE22(:,2),tension2(:,1),'g. ');
% hold on;
% plot(aveE22(:,3),tension2(:,1),'g. ');
% hold on;
% plot(aveE22(:,4),tension2(:,1),'g. ');
% hold on;
% plot(aveE22(:,5),tension2(:,1),'g. ');

```

```

clear i;
clear j;
clear k;
clear n;

```

```

%%%%%%%%%%
%%%%%%%%%%
%%%%%%%%%%
%%%%%%%%%%

```

```
% NOW TO OUTPUT A FILE FOR SIGMASTAT FUNG 4 REGRESSION FIT
```

```
for i=1:(m*10)
    for j=1:4
        output(i,j)=0;
    end
end
```

```
for i=1:m
    output(i,1)=1;
end
```

```
for i=m+1:2*m
    output(i,1)=2;
end
```

```
for i=2*m+1:3*m
    output(i,1)=1;
end
```

```
for i=3*m+1:4*m
    output(i,1)=2;
end
```

```
for i=4*m+1:5*m
    output(i,1)=1;
end
```

```
for i=5*m+1:6*m
    output(i,1)=2;
end
```

```
for i=6*m+1:7*m
    output(i,1)=1;
end
```

```
for i=7*m+1:8*m
    output(i,1)=2;
end
```

```
for i=8*m+1:9*m
    output(i,1)=1;
end
```

```

for i=9*m+1:10*m
    output(i,1)=2;
end

%%%%%%%%%%
%%%%%%%%%%
% put stresses in column 4

for i=1:m
    output(i,2)=aveE11(i,1);
    output(i,3)=aveE22(i,1);
    output(i,4)=S11(i,1);

end

for i=m+1:2*m
    output(i,2)=aveE11(i-(1*m),1);
    output(i,3)=aveE22(i-(1*m),1);
    output(i,4)=S22(i-(1*m),1);
end

for i=2*m+1:3*m
    output(i,2)=aveE11(i-(2*m),2);
    output(i,3)=aveE22(i-(2*m),2);
    output(i,4)=S11(i-(2*m),2);
end

for i=3*m+1:4*m
    output(i,2)=aveE11(i-(3*m),2);
    output(i,3)=aveE22(i-(3*m),2);
    output(i,4)=S22(i-(3*m),2);
end

for i=4*m+1:5*m
    output(i,2)=aveE11(i-(4*m),3);
    output(i,3)=aveE22(i-(4*m),3);
    output(i,4)=S11(i-(4*m),3);
end

for i=5*m+1:6*m
    output(i,2)=aveE11(i-(5*m),3);
    output(i,3)=aveE22(i-(5*m),3);
    output(i,4)=S22(i-(5*m),3);
end

for i=6*m+1:7*m

```

```

    output(i,2)=aveE11(i-(6*m),4);
    output(i,3)=aveE22(i-(6*m),4);
    output(i,4)=S11(i-(6*m),4);
end

for i=7*m+1:8*m
    output(i,2)=aveE11(i-(7*m),4);
    output(i,3)=aveE22(i-(7*m),4);
    output(i,4)=S22(i-(7*m),4);
end

for i=8*m+1:9*m
    output(i,2)=aveE11(i-(8*m),5);
    output(i,3)=aveE22(i-(8*m),5);
    output(i,4)=S11(i-(8*m),5);
end

for i=9*m+1:10*m
    output(i,2)=aveE11(i-(9*m),5);
    output(i,3)=aveE22(i-(9*m),5);
    output(i,4)=S22(i-(9*m),5);
end

%%%%%%%%%%%%%%%%%%%%%%%%%%%%%%%%%%%%%%%%%%%%%%%%%%%%%%%%%%%%%%%%%%%%%%%%
%%%%%%%%%%%%%%%%%%%%%%%%%%%%%%%%%%%%%%%%%%%%%%%%%%%%%%%%%%%%%%%%%%%%%%%%
% now lets calculate the MTM for each direction for the equibiaxial protocol
%%%%%%%%%%%%%%%%%%%%%%%%%%%%%%%%%%%%%%%%%%%%%%%%%%%%%%%%%%%%%%%%%%%%%%%%
%%%%%%%%%%%%%%%%%%%%%%%%%%%%%%%%%%%%%%%%%%%%%%%%%%%%%%%%%%%%%%%%%%%%%%%%

for j=1:numsp
    MTMcirc(j)=(S11(m,3)-S11((m-10),3))/(threeD_data1(3,m,j)-threeD_data1(3,m-10,j));
    MTMlong(j)=(S22(m,3)-S22((m-10),3))/(threeD_data2(3,m,j)-threeD_data2(3,m-10,j));
    MTMcirc=MTMcirc';
    MTMlong=MTMlong';
end

save presigmastat.txt output -ASCII -TABS
save aveE11.txt aveE11 -ASCII -TABS
save aveE22.txt aveE22 -ASCII -TABS
save S11.txt S11 -ASCII -TABS
save S22.txt S22 -ASCII -TABS
save stdev11.txt stdev11 -ASCII -TABS
save stdev22.txt stdev22 -ASCII -TABS
save modelS11.txt modelS11 -ASCII -TABS
save modelS22.txt modelS22 -ASCII -TABS
save modelE11.txt modelE11 -ASCII -TABS

```

```
save modelE22.txt modelE22 -ASCII -TABS
save MTMcirc.txt MTMcirc -ASCII -TABS
save MTMlong.txt MTMlong -ASCII -TABS
```

```
clear Q;
clear a1;
clear a2;
clear a3;
clear c;
clear i;
clear j;
clear m;
clear in_ten;
clear numsp;
clear ten_stp;
clear thick;
clear data;
clear data2;
clear tension1;
clear tension2;
```

APPENDIX B

PREPROCESSING OF 2D SLICE DATA

% This file is called recon3D.txt and is written in Mathematica

```
FExt=".txt";FileOut="Out.txt";Spc="  ";
```

```
MainDat=ReadList[FileInput,String];  
StrLngMin3=StringLength[MainDat[[1]]]-4;  
LastStr[J_,N_]:=StringTake[MainDat[[J]],-N];  
MainPath=StringTake[FileInput,StringLength[FileInput]-9];  
InpFil=StringTake[MainDat[[1]],StrLngMin3];  
FPath=StringJoin[MainPath,InpFil];
```

```
NL=ToExpression[LastStr[1,3]];  
Z={ToExpression[LastStr[2,3]]};  
Do[Z=AppendTo[Z,ToExpression[LastStr[J,3]]],  
  {J,3,NL+1}];
```

```
NZ=Quotient[NL,3];  
RZ=Mod[NL,3];
```

```
If[Z[[1]]==0,NumChar=".000",  
  {Num=N[Z[[1]]/1000,3];  
  If[StringLength[ToString[Num]]==4,  
    NumChar=StringJoin[StringTake[ToString[N[Z[[1]]/1000,  
      3]],-3],"0"],  
    NumChar=StringTake[ToString[N[Z[[1]]/1000,3]],-4]};  
FName={StringJoin[FPath,NumChar]};  
Do[{If[Z[[J]]==0,NumChar=".000",  
  {Num=N[Z[[J]]/1000,3];  
  If[StringLength[ToString[Num]]==4,
```

```

    NumChar=StringJoin[StringTake[ToString[N[Z[[J]]/1000,
        3]],-3],"0"],
        {If[StringLength[ToString[Num]]==3,
            NumChar=StringJoin[StringTake[ToString[
                N[Z[[J]]/1000,3]],-2],"00"],
            NumChar=StringTake[ToString[N[Z[[J]]/1000,3]],-4]}}];
    FName=AppendTo[FName,StringJoin[FPath,NumChar]],
    {J,2,NL}];

TL=0;
Do[
Lst[J]=ReadList[FName[[J]],Number,RecordLists->True];
    EL[J]=Length[Lst[J]];TL=TL+EL[J],{J,1,NL}];

Do[Lst[J]=Append[Lst[J],Lst[J][[1]],{J,1,NL}];

Do[{AA=0;
Do[{DX=(Lst[J][[L+1]][[1]]-Lst[J][[L]][[1]])*MulFac;
    DY=(Lst[J][[L+1]][[2]]+Lst[J][[L]][[2]])*MulFac;
    AA=AA+0.5*DX*DY},
    {L,1,EL[J]}];
DA[J]=Abs[AA]},{J,1,NL}]

Vol:=0;
Do[Vol+=DA[J],{J,1,NL}];

Coords=Table[{0.0,0.0,0.0},[11]];

K=1;FileXYZ=OpenWrite[StringJoin[FPath,FileOut],FormatType->
    OutputForm];
Do[{AX=0;AY=0;
Do[{Coords[[K]]=Append[Table[Lst[J][[L]]*MulFac,-0.1*Z[[J]];
    DX=(Lst[J][[L+1]][[1]]-Lst[J][[L]][[1]])*MulFac;
    DY=(Lst[J][[L+1]][[2]]-Lst[J][[L]][[2]])*MulFac;
    TX=(Lst[J][[L+1]][[1]]+Lst[J][[L]][[1]])*MulFac;
    TY=(Lst[J][[L+1]][[2]]+Lst[J][[L]][[2]])*MulFac;
    AX=AX+TX*DX*TY;AY=AY+TY*DY*TX;
    Write[FileXYZ,Coords[[K]][[1]]," ",Coords[[K]][[2]]," ",
        Coords[[K]][[3]];K=K+1},
    {L,1,EL[J]}];
Write[FileXYZ,Coords[[K-EL[J]][[1]]," ",
    Coords[[K-EL[J]][[2]]," ",Coords[[K-EL[J]][[3]]];
CX[J]=Abs[AX/(4.0*DA[J]);
CY[J]=Abs[AY/(4.0*DA[J])],
    {J,1,NL}];Close[FileXYZ];

```

```
Do[Pol[J]=Table[{0,0},{L,1,EL[J]},{J,1,NL}]
```

```
Do[Pol[J]=Sort[Table[{Which[
  (Lst[J][[L]][[1]]*MulFac-CX[J])>=0 &&
  (Lst[J][[L]][[2]]*MulFac-CY[J])>=0,
    90.-ArcTan[(Lst[J][[L]][[1]]*MulFac-CX[J]),
    (Lst[J][[L]][[2]]*MulFac-CY[J])*180./N[Pi],
  (Lst[J][[L]][[1]]*MulFac-CX[J])>=0 &&
  (Lst[J][[L]][[2]]*MulFac-CY[J])<0,
    90.-ArcTan[(Lst[J][[L]][[1]]*MulFac-CX[J]),
    (Lst[J][[L]][[2]]*MulFac-CY[J])*180./N[Pi],
  (Lst[J][[L]][[1]]*MulFac-CX[J])<=0 &&
  (Lst[J][[L]][[2]]*MulFac-CY[J])>=0,
    450.-ArcTan[(Lst[J][[L]][[1]]*MulFac-CX[J]),
    (Lst[J][[L]][[2]]*MulFac-CY[J])*180./N[Pi],
  (Lst[J][[L]][[1]]*MulFac-CX[J])<=0 &&
  (Lst[J][[L]][[2]]*MulFac-CY[J])<0,
    90.-ArcTan[(Lst[J][[L]][[1]]*MulFac-CX[J]),
    (Lst[J][[L]][[2]]*MulFac-CY[J])*180./N[Pi]],
  Sqrt[(Lst[J][[L]][[1]]*MulFac-CX[J])^2+
  (Lst[J][[L]][[2]]*MulFac-CY[J])^2}],
{L,1,EL[J]},{J,1,NL}]
```

```
Do[Bfr[J]=ListPlot[Append[Lst[J]*MulFac,{CX[J],
  CY[J]}],PlotRange->Automatic,Ticks->None,AspectRatio->1,
  DisplayFunction->Identity,PlotJoined->True},{J,1,NL}];
```

```
DT=5;K=1;RTheta=Table[{0,0},{360/DT*NL}];
```

```
Do[{TX=0;L=1;
  While[TX<360 && L<EL[J],
    {T1=Pol[J][[L]][[1]];T2=Pol[J][[L+1]][[1]];
    R1=Pol[J][[L]][[2]];R2=Pol[J][[L+1]][[2]];
    Which[TX<=T1,
      {T1=Pol[J][[EL[J]][[1]]-360;R1=Pol[J][[EL[J]][[2]];
      T2=Pol[J][[L]][[1]]; R2=Pol[J][[1]][[2]];
      RTheta[[K]]={TX,(TX-T1)/(T2-T1)*(R2-R1)+R1};
      K=K+1;TX=TX+DT},
    TX>T1 && TX<=T2,
      {TM=T1+0.5*(T1+T2);RM=(R1+R2)/2;
      RTheta[[K]]={TX,(TX-T1)/(T2-T1)*(R2-R1)+R1};
      K=K+1;TX=TX+DT},
    TX>T2,L=L+1}];
  While[TX<360,
    {T1=Pol[J][[EL[J]][[1]];T2=Pol[J][[1]][[1]];
    R1=Pol[J][[EL[J]][[2]];R2=Pol[J][[1]][[2]];
    TM=T1+0.5*(T1+T2);RM=(R1+R2)/2;
```

```

RTheta[[K]]= {TX,(TX-T1)/(T2-T1)*(R2-R1)+R1};
K=K+1;
TX=TX+DT}}, {J,1,NL}];

Do[RTB[J]=ListPlot[Pol[J],PlotJoined->True,Ticks->None,
  DisplayFunction->Identity,PlotRange->Automatic,
  GridLines->Automatic], {J,1,NL}];

Do[RTA[J]=ListPlot[Table[RTheta[[J-1]*360/DT+L]],
  {L,1,360/DT}],Ticks->None,PlotJoined->True,
  DisplayFunction->Identity,PlotRange->Automatic,
  GridLines->Automatic], {J,1,NL}];

FileEvn=OpenWrite[StringJoin[FPath,"XYZ.txt"],FormatType->
  OutputForm];
XYZ=Table[{0,0},{360/DT*NL}];K=1;
Do[
Do[{XYZ[[K]]={CX[J]+RTheta[[K]][[2]]*Sin[RTheta[[K]][[1]]*
  N[Pi]/180.],
  CY[J]+RTheta[[K]][[2]]*Cos[RTheta[[K]][[1]]*N[Pi]/180],
  -.1*Z[[J]]};
  Write[FileEvn,XYZ[[K]][[1]]," ",XYZ[[K]][[2]]," ",
    slicethick*XYZ[[K]][[3]]];
  K=K+1},{L,1,360/DT}],
{J,1,NL}];Close[FileEvn];

TT=0;
Do[Aft[J]=ListPlot[Table[{XYZ[[J-1]*360/DT+K]][[1]],
  XYZ[[J-1]*360/DT+K]][[2]],{K,1,360/DT}],DisplayFunction->Identity,
  AspectRatio->1,PlotJoined->True,PlotRange->Automatic,
  Ticks->None],
{J,1,NL}];

FileXYZ=OpenRead[StringJoin[FPath,FileOut]];
aneu=ReadList[FileXYZ,Point[{Number,Number,Number}],
  RecordLists -> True];Close[FileXYZ];

FileEvn=OpenRead[StringJoin[FPath,"XYZ.txt"]];
even=ReadList[FileEvn,Number,RecordLists -> True];Close[FileEvn];

v1=Show[Graphics3D[Line[even],Boxed->True, Axes->True, AxesLabel->{x,y,z}],
  ViewPoint->{-3,-5,5},DisplayFunction->Identity];
v2=Show[Graphics3D[Line[even],Boxed->True, Axes->True, AxesLabel->{x,y,z}],
  ViewPoint->{5,-3,5},DisplayFunction->Identity];
v3=Show[Graphics3D[Line[even],Boxed->True, Axes->True, AxesLabel->{x,y,z}],

```

```

ViewPoint-> {-3,5,5},DisplayFunction->Identity];

vx=Show[Graphics3D[Line[even],Boxed->True, Axes->True, AxesLabel->{x,y,z}],
ViewPoint-> {0,-5,0},DisplayFunction->Identity];
vy=Show[Graphics3D[Line[even],Boxed->True, Axes->True, AxesLabel->{x,y,z}],
ViewPoint-> {-5,0,0},DisplayFunction->Identity];

Needs["Graphics`Animation`"]

Do[vk[J]=Show[Graphics3D[Line[even],SphericalRegion->True,
Boxed->True, Axes->True, AxesLabel->{x,y,z}],ViewPoint->{J-3,-3,2},
DisplayFunction->$DisplayFunction],{J,0,6}];
Do[vk[J+6]=Show[Graphics3D[Line[even],SphericalRegion->True,
Boxed->True, Axes->True, AxesLabel->{x,y,z}],ViewPoint->{3,J-3,2},
DisplayFunction->$DisplayFunction],{J,1,6}];
Do[vk[J+12]=Show[Graphics3D[Line[even],SphericalRegion->True,
Boxed->True, Axes->True, AxesLabel->{x,y,z}],ViewPoint->{3-J,3,2},
DisplayFunction->$DisplayFunction],{J,1,6}];
Do[vk[J+18]=Show[Graphics3D[Line[even],SphericalRegion->True,
Boxed->True, Axes->True, AxesLabel->{x,y,z}],ViewPoint->{-3,3-J,2},
DisplayFunction->$DisplayFunction],{J,1,5}];

Show[Graphics3D[Line[even],Boxed->True, Axes->True, AxesLabel->{x,y,z}],
ViewPoint->{5,0,0}];

```

APPENDIX C

ILD TO 3D SMOOTHING MATLAB FUNCTION

```
function idl2dsmith = idl2dsmith(n1,n2,fname);

%FUNCTION idl2dsmith creates input.dat file in a specified format
% as well as calling Mathematica to run recon2.nb. It then creates
% the .dat file needed by david smith programs
%
% Syntax: function idl2dsmith[c] = idl2dsmith(n1,n2,fname);
%
% INPUTS:n1,n2 are start and end indexes of file extensions
%      fname = filename as a string (single quotes) without the extension (usually 'Draw0' etc)

%%%%%%%%%%%%%%%%%%%%%%%%%%%%%%%%%%%%%%%%%%%%%%%%%%%%%%%%%%%%%%%%%%%%%%%%
%%%%%%%%%%%%%%%%%%%%%%%%%%%%%%%%%%%%%%%%%%%%%%%%%%%%%%%%%%%%%%%%%%%%%%%%
% this portion of the code creates an input.dat file
% suitable to be used by the Mathematica program recon2.nb
fid = fopen('input.dat','wt');
if n1==0
    nslices=n2-n1;
else
    nslices=n2-n1+1;
end
if nslices<10
    fmt = '%s%s %i\n';
elseif nslices>9 & nslices<100
    fmt = '%s%s %i\n';
end
c= n2-n1+1;
fprintf(fid,fmt,fname,',',c);
fmt2 = '%s%s %i\n';
```

```

fmt3 = '%s%s %i\n';
for i = n1:n2,
    if i<10
        fprintf(fid,fmt2,fname,',',i);
    else
        fprintf(fid,fmt3,fname,',',i);
    end
end
fclose(fid)

% RUN MATHEMATICA
system('C:\Program Files\Wolfram Research\Mathematica\5.0\Mathematica.exe');

pause
%%%%%%%%%%%%%%%%%%%%%%%%%%%%%%%%%%%%%%%%%%%%%%%%%%%%%%%%%%%%%%%%%%%%%%%%%%%%%%
%%%%%%%%%%%%%%%%%%%%%%%%%%%%%%%%%%%%%%%%%%%%%%%%%%%%%%%%%%%%%%%%%%%%%%%%%%%%%%
% now we need to read in the Draw0XYZ.txt file and edit
% it to a .dat file that can be used by David Smiths programs
s=pwd;
cd(s);
xyz=load(strcat(fname,'XYZ.txt'));
name=input('Please enter the name of the file -> dsmith (.dat assumed,8 CHARS OR LESS):
','s');
fid5=fopen(strcat(name,'.dat'),'w');
fprintf(fid5,'%s %i %s\n','1',length(xyz),'1');
fprintf(fid5,'%s %s\n','1','1');
for i=1:length(xyz)
    fprintf(fid5,'%6.4f %6.4f %4.2f\n',xyz(i,1),xyz(i,2),xyz(i,3));
end
fclose(fid5);
%
```

APPENDIX D

3D SMOOTHING TO IGES CREATION MATLAB SCRIPT

```
function dsmith2iges = dsmith2iges(fname2);

%FUNCTION dsmith2iges reads in the .plt file from dsmith
% and creates .gambit files used by IGES.exe. IGES.exe is
% called at the end of this program
%
% Syntax: function dsmith2iges[c] = idl2dsmith(fname2);
%
% INPUTS:fname2 = filename of .plt file (.plt assumed, e.g. 'wall' etc)

%%%%%%%%%%%%%%%%%%%%%%%%%%%%%%%%%%%%%%%%%%%%%%%%%%%%%%%%%%%%%%%%%%%%%%%%
% read in the plt file
fid1=fopen(strcat(fname2,'.plt'));
a=fscanf(fid1,'%6s',40);
size_a=size(a);
fclose(fid1);
%%%%%%%%%%%%%%%%%%%%%%%%%%%%%%%%%%%%%%%%%%%%%%%%%%%%%%%%%%%%%%%%%%%%%%%%
%determine where the N= portion of the file is
for i=1:size_a(2)
    if (a(i)=='N') & (a(i+1)=='=')
        begofnum=i+2;
    else
        jon=7;
    end
end
%%%%%%%%%%%%%%%%%%%%%%%%%%%%%%%%%%%%%%%%%%%%%%%%%%%%%%%%%%%%%%%%%%%%%%%%
% determine the number of nodes in the file
for i=begofnum:begofnum+6
    if a(i)=='='
        lengthofnumnodes=i-begofnum;
    end
end
```

```

        comma=i;
    end
end
nodes_str=a(begofnum);
for j=begofnum:comma-2
    nodes_str=strcat(nodes_str,a(j+1));
end
nodes=str2num(nodes_str);
%%%%%%%%%%%%%%%%%%%%%%%%%%%%%%%%%%%%%%%%%%%%%%%%%%%%%%%%%%%%%%%%%%%%%%%%
% determine the number of elements in the file
if a(comma+3)==' '
    comma2=comma+3;
elseif a(comma+4)==' '
    comma2=comma+4;
elseif a(comma+5)==' '
    comma2=comma+5;
elseif a(comma+6)==' '
    comma2=comma+6;
elseif a(comma+7)==' '
    comma2=comma+7;
end
begofel=comma+3;
el_str=a(begofel);
for j=begofel:comma2-2
    el_str=strcat(el_str,a(j+1));
end
elements=str2num(el_str);
%%%%%%%%%%%%%%%%%%%%%%%%%%%%%%%%%%%%%%%%%%%%%%%%%%%%%%%%%%%%%%%%%%%%%%%%
% open the entire file
fid3=fopen(strcat(fname2,'.plt'));
all_data=fscanf(fid3,'%6s');
endofheader=comma2+21;
newb=all_data(endofheader+1:length(all_data));
clear all_data;
%%%%%%%%%%%%%%%%%%%%%%%%%%%%%%%%%%%%%%%%%%%%%%%%%%%%%%%%%%%%%%%%%%%%%%%%
%%
% find the end of the data we are interested in
all_es=findstr('e',newb);
lastindex=max(all_es);
clear all_es;
endofdata=lastindex+3;
just_data=newb(1:endofdata);
clear newb;
i=1;
z=0;
while i<length(just_data)-5

```

```

if just_data(i)=='-'
i=i+13;
z=z+1;
else
i=i+12;
z=z+1;
end
end
array=zeros(1,z);
i=1;
z=1;
while i<length(just_data)-5
if just_data(i)=='-'
array(z)=str2num(just_data(i:i+12));
i=i+13;
z=z+1;
else
array(z)=str2num(just_data(i:i+11));
i=i+12;
z=z+1;
end
end

array2=zeros(length(array)/11,11);
for i=1:length(array2)
for j=1:11
array2(i,j)=array((i-1)*11+j);
end
end
%%%%%%%%%%%%%%%%%%%%%%%%%%%%%%%%%%%%%%%%%%%%%%%%%%%%%%%%%%%%%%%%%%%%%%%%
% load wall_plt.txt;
% data=wall_plt;
file_size=size(array2);
% xyz_data=zeros(file_size(1),3);
xyz_data=array2(:,1:3);
tmp=xyz_data(1,3);

% find out how many pts are in each slice (npps)
for i=2:150
if xyz_data(i,3)~=tmp
npps=i-1;
break
else
jon=7;
end

```

```

end

% find out how many slices there are
file_size=size(array2);
num_slices=file_size(1)/npps;

% open all the files for writing
for i=1:num_slices
    title=strcat(fname2,num2str(i),'.gambit');
    fid2=fopen(title,'w');
    for j=1:npps
        fprintf(fid2,'%s','vertex create coordinates ');
        fprintf(fid2,'%6.3f      %6.3f      %6.3f\n',xyz_data(i*npps-npps+j,1),xyz_data(i*npps-
npps+j,2),xyz_data(i*npps-npps+j,3));
    end
    fclose(fid2);
end

system('C:\Documents and Settings\Jonathan\Desktop\recon\IGES.exe');

```

APPENDIX E

CREATION OF ABAQUS INPUT FILE FROM TRUE GRID FILE

```
%TruGrid_2_ABAQUS_with_ILT.m
close all
clear all
clc
% read in the data file from True Grid
fname1=input('Please enter the name of the WALL mesh file from TrueGrid including the
extension: ','s');
data=textread(fname1,'%s','delimiter','');
data1=char(data);
clear data;

% Find the indexes of important keywords
k=1;
j=1;
for i=1:length(data1)
    if data1(i,1:5)=='*NODE'
        nodeindex=i+2;
    end
    if data1(i,1:6)=='*SHELL'
        endnodeindex=i-1;
    end
    if data1(i,1:8)=='*ELEMENT'
        elementindex=i+3;
    end
    if data1(i,1:6)=='*ELSET'
        elsetindex(k)=i;
        k=k+1;
    end
    if data1(i,1:5)=='*NSET'
        nsetindex(j)=i;
    end
end
```

```

        j=j+1;
    end
end
numelsets=k-1;
numnsets=j-1;

% find endelementindex, the index corresponding to the end of the connectivity
if numelsets==0 & numnsets==0
    endelementindex=length(data1);
elseif numelsets>=1 & numnsets==0
    endelementindex=elsetindex(1)-1;
elseif numelsets==0 & numnsets>=1
    endelementindex=nsetindex(1)-1;
else
    firstsetindex=min([elsetindex(1) nsetindex(1)]);
    endelementindex=firstsetindex-1;
end

% here we will create elset1, which is the first elset.
k=1;
for i=elsetindex(1)+2:1:length(data1)
    if (data1(i,1:3)==' ')
        jon=5;
    else
        data2(k,:)=data1(i,:);
        elset1(k,:)=str2num(data2(k,:));
        k=k+1;
    end
end
clear data2;
clear jon;

% First, lets find the total number of nodes and then save the node numbers to nodenums
% Then lets get the x,y, and z values
k=1;
for i=nodeindex:4:endnodeindex
    nodenums(k)=str2num(data1(i,:));
    x(k)=str2num(data1(i+1,:));
    y(k)=str2num(data1(i+2,:));
    z(k)=str2num(data1(i+3,:));
    k=k+1;
end

% First, lets find the total number of elements and then save the element numbers to elnums
% Then, lets get the nodes in locations one through four of the wall connectivity
numels=(endelementindex-elementindex+1)/5;

```

```

k=1;
for i=elementindex:5:endelementindex
    elnums(k)=str2num(data1(i,:));
    one_nodes(k)=str2num(data1(i+1,:));
    two_nodes(k)=str2num(data1(i+2,:));
    three_nodes(k)=str2num(data1(i+3,:));
    four_nodes(k)=str2num(data1(i+4,:));
    k=k+1;
end

% Concatenate the nodes and xyz coordinates into one array called nodes_xyz
nodes_xyz=[nodenums; x; y; z];
nodes_xyz=nodes_xyz';

% Concatenate the connectivity into one array called connectivity
connectivity=[elnums; one_nodes; two_nodes; three_nodes; four_nodes];
connectivity=connectivity';

% Lets first ascertain how many divisions there are in the theta direction
% The easiest way to do this is to isolate all the points at one end of the
% AAA.
bottomz=min(nodes_xyz(:,4));
topz=max(nodes_xyz(:,4));
lengthz=topz-bottomz;
numnodesbottom=length(find(nodes_xyz(:,4)<=bottomz+0.005 & nodes_xyz(:,4)>=bottomz-
0.005));%CHANGED!!
numnodestop=length(find(nodes_xyz(:,4)<=topz+0.005 & nodes_xyz(:,4)>=topz-
0.005));%CHANGED!!
numzslices=numels/numnodesbottom+1;
numzsegments=numzslices-1;
zslicedist=lengthz/(numzsegments);

sorted_xyz=sortrows(nodes_xyz,4);
% now change to descending instead of ascending
j=1;
for i=length(sorted_xyz):-1:1
    sorted_xyz2(j,:)=sorted_xyz(i,:);
    j=j+1;
end
sorted_xyz=sorted_xyz2;
clear sorted_xyz2;

for i=1:numzslices
    sort_label(i,1:numnodesbottom)=sorted_xyz(numnodesbottom*(i-1)+1:numnodesbottom*i,1)';
end

```

```

for i=1:numzslices
slices(:,i)=nodes_xyz(sort_label(i,:),:);
end

```

% Now lets calculate the center of mass of each slice

```

for i=1:numzslices
    %x=mean(slices(:,2,i));
    x=min(slices(:,2,i))+((max(slices(:,2,i))-min(slices(:,2,i)))/2);
    %y=mean(slices(:,3,i));
    y=min(slices(:,3,i))+((max(slices(:,3,i))-min(slices(:,3,i)))/2);
    z=mean(slices(:,4,i));
    centerpt(i,:)=[x y z];
end

```

% Here is the part where I fit two fourth order poly's to x
% versus z and y versus z....

```

xparams=polyfit(centerpt(:,3),centerpt(:,1),3);
yparams=polyfit(centerpt(:,3),centerpt(:,2),3);
x=polyval(xparams,centerpt(:,3));
y=polyval(yparams,centerpt(:,3));

```

% This calculates meanx, meany, and meanz, each 1D vectors of length numel that contain
% the mean location of each element

```

for i=1:numel
    meanx(i)= (nodes_xyz(connectivity(i,2),2) + nodes_xyz(connectivity(i,3),2) + ...
    nodes_xyz(connectivity(i,4),2) + nodes_xyz(connectivity(i,5),2))/4;

    meany(i)= (nodes_xyz(connectivity(i,2),3) + nodes_xyz(connectivity(i,3),3) + ...
    nodes_xyz(connectivity(i,4),3) + nodes_xyz(connectivity(i,5),3))/4;

    meanz(i)= (nodes_xyz(connectivity(i,2),4) + nodes_xyz(connectivity(i,3),4) + ...
    nodes_xyz(connectivity(i,4),4) + nodes_xyz(connectivity(i,5),4))/4;
end

```

% Now lets get the element sets for each z region we are interested in

```

orient_elsets=zeros(numzsegments,500);
k=1;
for i=1:numzsegments
    index=find(meanz<=(topz-(i-1)*zslicedist) & meanz>=(topz-(i)*zslicedist));
    orient_elsets(k,1:length(index))=index;
    k=k+1;
end

```

%Plot the points of the mesh along with the centerline calculated above

% for i=1:numzslices

```

% zvector(:,i)=bottomz+(i-1)*zsllicedist.*(ones(length(slices),1));
% end
% for i=1:numzslices
% plot3(slices(:,2,i),slices(:,3,i),slices(:,4,i),'k.');
```

% hold on

```

% end
% hold on
% plot3(x,y,centerpt(:,3),'-b');
```

% hold on

```

% plot3(centerpt(:,1),centerpt(:,2),centerpt(:,3),'or');
```

%%%%%%%%%

% LOAD IN THE ILT FILE AND PREPARE IT FOR PRINTING OUT

%%%%%%%%%

```

% read in the ilt data file from True Grid
fname2=input('Please enter the name of the ILT mesh file from TrueGrid including the
extension: ','s');
iltdata=textread(fname2,'%s','delimiter',' ');
iltdata1=char(iltdata);
clear iltdata;
```

```

% Find nodeindex, the index of the first node in the node list
% Find endnodeindex, the index corresponding to the end of the nodelist.
% Find elementindex, the index of the first element in the element list
% Lets find out if there are any element sets in the file (*ELSET)
% Lets find out if there are any node sets sets in the file (*NSET)
k=1;
j=1;
for i=1:length(iltdata1)
    if iltdata1(i,1:5)=='*NODE'
        iltnodeindex=i+2;
    end
    if iltdata1(i,1:4)=='****'
        iltendnodeindex=i-1;
    end
    if iltdata1(i,1:8)=='*ELEMENT'
        iltelementindex=i+3;
    end
    if iltdata1(i,1:6)=='*ELSET'
        iltelsetindex(k)=i;
        k=k+1;
    end
end

```

```

end
if iltdata1(i,1:5)=='*NSET'
    iltndata1(i,1:5)=='*NSET'
    iltndata1(i,1:5)=='*NSET'
    iltndata1(i,1:5)=='*NSET'
    iltndata1(i,1:5)=='*NSET'
end
end
iltnumelsets=k-1;
iltndata1sets=j-1;

% find endelementindex, the index corresponding to the end of the connectivity
if iltnumelsets==0 & iltndata1sets==0
    iltndata1sets=length(iltndata1);
elseif iltnumelsets>=1 & iltndata1sets==0
    iltndata1sets=iltndata1sets(1)-1;
elseif iltnumelsets==0 & iltndata1sets>=1
    iltndata1sets=iltndata1sets(1)-1;
else
    iltndata1sets=min([iltndata1sets(1) iltndata1sets(1)]);
    iltndata1sets=iltndata1sets-1;
end

% First, lets find the total number of nodes and then save the node numbers to nodenums
% Then, lets get the x,y, and z values
k=1;
iltndata1nodes=(iltndata1nodeindex-iltndata1nodeindex+1)/4;
for i=iltndata1nodeindex:4:iltndata1nodeindex
    iltndata1nodes(k)=str2num(iltndata1(i,:));
    iltndata1x(k)=str2num(iltndata1(i+1,:));
    iltndata1y(k)=str2num(iltndata1(i+2,:));
    iltndata1z(k)=str2num(iltndata1(i+3,:));
    k=k+1;
end

% First, lets find the total number of elements and then save the element numbers to elnums.
% Then less get the nodes in locations one through eight of ilt connectivity
k=1;
iltndata1elems=(iltndata1elementindex-iltndata1elementindex+1)/9;
for i=iltndata1elementindex:9:iltndata1elementindex
    iltndata1elems(k)=str2num(iltndata1(i,:));
    iltndata1one_nodes(k)=str2num(iltndata1(i+1,:));
    iltndata1two_nodes(k)=str2num(iltndata1(i+2,:));
    iltndata1three_nodes(k)=str2num(iltndata1(i+3,:));
    iltndata1four_nodes(k)=str2num(iltndata1(i+4,:));
    iltndata1five_nodes(k)=str2num(iltndata1(i+5,:));
    iltndata1six_nodes(k)=str2num(iltndata1(i+6,:));
    iltndata1seven_nodes(k)=str2num(iltndata1(i+7,:));

```

```

    iltheight_nodes(k)=str2num(iltdata1(i+8,:));
    k=k+1;
end

% Concatenate the nodes and xyz coordinates into one array called nodes_xyz
iltnodes_xyz=[iltnodenums; iltx; ilty; iltz];
iltnodes_xyz=iltnodes_xyz';

% Concatenate the connectivity into one array called connectivity
iltconnectivity=[iltelnums; iltone_nodes; ilttwo_nodes; iltthree_nodes; iltfour_nodes;
iltfive_nodes; ...
    iltsix_nodes; iltseven_nodes; iltheight_nodes];
iltconnectivity=iltconnectivity';

% This section finds the element set corresponding to the wall with no ILT
% It first finds the outside elements of the ILT, then transforms these into
% a cylindrical coordinate system, assigning a value of theta to each of these
% elements. then finds elements of the wall corresponding to this value of theta
% this portion assumes that there are 4 elements through the thickness of the ILT.
erase=input('Please enter the number of elements through the thickness of the ILT: ','s');
elthick=str2num(erase);

iltbottomz=min(iltnodes_xyz(:,4));
ilttopz=max(iltnodes_xyz(:,4));
iltinels=iltconnectivity(elthick:elthick:length(iltconnectivity),:);
iltoutels=iltconnectivity(1:elthick:length(iltconnectivity),:);
% %
% %
% This section isolates the nodes on the inside of the ilt
isubset1=horzcat(iltnodes_xyz(iltinels(:,2),1),                iltnodes_xyz(iltinels(:,2),2),
iltnodes_xyz(iltinels(:,2),3), iltnodes_xyz(iltinels(:,2),4));
isubset2=horzcat(iltnodes_xyz(iltinels(:,5:6),1),            iltnodes_xyz(iltinels(:,5:6),2),
iltnodes_xyz(iltinels(:,5:6),3), iltnodes_xyz(iltinels(:,5:6),4));
isubset3=horzcat(iltnodes_xyz(iltinels(:,9),1),              iltnodes_xyz(iltinels(:,9),2),
iltnodes_xyz(iltinels(:,9),3), iltnodes_xyz(iltinels(:,9),4));
erase=union(isubset1,isubset2,'rows');
ilt_xyz_inside_nodes=union(erase,isubset3,'rows');
clear isubset* erase
% plot3(ilt_xyz_inside_nodes(:,2),ilt_xyz_inside_nodes(:,3),ilt_xyz_inside_nodes(:,4),'r*');
% hold on;
%
plot3(iltnodes_xyz(iltinels(:,2:9),2),iltnodes_xyz(iltinels(:,2:9),3),iltnodes_xyz(iltinels(:,2:9),4),'b
o')

% this then isolates the middle slice of the inside of the ilt and calculates the center of mass
mid=ilttopz-abs((iltbottomz-ilttopz)/2);

```

```

middleiltslice=find(ilt_xyz_inside_nodes(:,4)<mid+0.1 & ilt_xyz_inside_nodes(:,4)>mid-0.1);
middleiltslice=ilt_xyz_inside_nodes(middleiltslice,:);
ilt_centerx=mean(middleiltslice(:,2));
ilt_centery=mean(middleiltslice(:,3));
ilt_centerz=mean(middleiltslice(:,4));
%clear ilt_xyz_inside_nodes;
% plot3(middleiltslice(:,2),middleiltslice(:,3),middleiltslice(:,4),'r*')
% hold on;
% plot3(ilt_centerx,ilt_centery,ilt_centerz,'bo');

osubset1=horzcat(iltnodes_xyz(iltoutels(:,3:4),1),           iltnodes_xyz(iltoutels(:,3:4),2),
iltnodes_xyz(iltoutels(:,3:4),3), iltnodes_xyz(iltoutels(:,3:4),4));
osubset2=horzcat(iltnodes_xyz(iltoutels(:,7:8),1),         iltnodes_xyz(iltoutels(:,7:8),2),
iltnodes_xyz(iltoutels(:,7:8),3), iltnodes_xyz(iltoutels(:,7:8),4));
ilt_xyz_outside_nodes=union(osubset1,osubset2,'rows');
clear osub*;
%

% Now lets get the element sets for each z region we are interested in
num_sections=input('How many sections would you like to use to section the ILT (50 for full
length ILT)? :','s');
num_sections=str2num(num_sections);

iltzslicedist=abs(iltbottomz-ilttopz)/num_sections;
iltnumzsegments=num_sections;

temp=find(nodes_xyz(:,4)>ilttopz+0.01);
temp2=nodes_xyz(temp,:);

% This portion is added because the case where the ilt is completely cylindrical yet does not
% cover the entire wall was not covered before. The code from the next line to the line reading
% xyz2=[]; was inserted afterwards to take this into account
erase3=input('Is the ILT perfectly tubular with a flat top and bottom? (Y=1, N=0):','s');
check3=str2num(erase3);
if check3==1
    check1=0;
    erase4=input('Does the wall extend above (1) or below (2) the ILT or both (3)?','s');
    check4=str2num(erase4);
    if check4==3
        t3=find(nodes_xyz(:,4)<iltbottomz-0.05 | nodes_xyz(:,4)>ilttopz+0.05);
        t3=nodes_xyz(t3,:);
        nodes3=t3(:,1);
        wall_no_ilt_elset2=[];
        for g=1:length(nodes3)
            wall_no_ilt_elset=find(connectivity(:,2)==nodes3(g) | connectivity(:,3)==nodes3(g) | ...

```

```

        connectivity(:,4)==nodes3(g) | connectivity(:,5)==nodes3(g));
aa=connectivity(wall_no_ilt_elset,1);
wall_no_ilt_elset2=[wall_no_ilt_elset2;aa];
clear aa
end
wall_no_ilt_elset2=unique(wall_no_ilt_elset2);
elseif check4==1
t3=find(nodes_xyz(:,4)>ilttopz+0.05);
t3=nodes_xyz(t3,:);
nodes3=t3(:,1);
wall_no_ilt_elset2=[];
for g=1:length(nodes3)
    wall_no_ilt_elset=find(connectivity(:,2)==nodes3(g) | connectivity(:,3)==nodes3(g) | ...
        connectivity(:,4)==nodes3(g) | connectivity(:,5)==nodes3(g));
    aa=connectivity(wall_no_ilt_elset,1);
    wall_no_ilt_elset2=[wall_no_ilt_elset2;aa];
    clear aa
end
wall_no_ilt_elset2=unique(wall_no_ilt_elset2);
else
t3=find(nodes_xyz(:,4)<ilttopz-0.05);
t3=nodes_xyz(t3,:);
nodes3=t3(:,1);
wall_no_ilt_elset2=[];
for g=1:length(nodes3)
    wall_no_ilt_elset=find(connectivity(:,2)==nodes3(g) | connectivity(:,3)==nodes3(g) | ...
        connectivity(:,4)==nodes3(g) | connectivity(:,5)==nodes3(g));
    aa=connectivity(wall_no_ilt_elset,1);
    wall_no_ilt_elset2=[wall_no_ilt_elset2;aa];
    clear aa
end
wall_no_ilt_elset2=unique(wall_no_ilt_elset2);
end
else
xyz2=[];
wall_sec3=temp2;
clear temp temp2
ilt_sec3=[];
erase2=input('Does the ILT cover the ENTIRE aneurysm? (Y=1, N=0): ','s');
check1=str2num(erase2);

if check1==1
    donothing=1;
else
    for i=1:iltnumzsegments

```

```

% isolate ilt nodes within z range
ilt_sec=find((ilt_xyz_outside_nodes(:,4)<ilttopz-(i-1)*iltzslicedist+iltzslicedist) &
(ilt_xyz_outside_nodes(:,4)>ilttopz-(i-1)*iltzslicedist-iltzslicedist));
ilt_sec=ilt_xyz_outside_nodes(ilt_sec,:);
wall_sec=find((nodes_xyz(:,4)<ilttopz-(i-1)*iltzslicedist+iltzslicedist) &
(nodes_xyz(:,4)>ilttopz-(i-1)*iltzslicedist-iltzslicedist));
wall_sec=nodes_xyz(wall_sec,:);

% in this section lets locate the elset corresponding to wall with no ilt
meanofslice=[mean(ilt_sec(:,2));mean(ilt_sec(:,3));mean(ilt_sec(:,4))];
X=meanofslice(1)+zeros(length(wall_sec),1);
Y=meanofslice(2)+zeros(length(wall_sec),1);
Z=meanofslice(3)+zeros(length(wall_sec),1);
nothing=zeros(length(wall_sec),1);
array=horzcat(nothing,X,Y,Z);
wall_sec2=wall_sec-array;
X=meanofslice(1)+zeros(length(ilt_sec),1);
Y=meanofslice(2)+zeros(length(ilt_sec),1);
Z=meanofslice(3)+zeros(length(ilt_sec),1);
nothing=zeros(length(ilt_sec),1);
array=horzcat(nothing,X,Y,Z);
ilt_sec2=ilt_sec-array;

[th,r,z]=cart2pol(ilt_sec2(:,2),ilt_sec2(:,3),ilt_sec2(:,4));
ilt_pol=horzcat(ilt_sec(:,1),th,r,z);
[wth,wr,wz]=cart2pol(wall_sec2(:,2),wall_sec2(:,3),wall_sec2(:,4));
wall_pol=horzcat(wall_sec(:,1),wth,wr,wz);
% EVERYTHING IS GOOD TO HERE...

% the resulting thetas range from -3.142 rad to +3.142 rad
% basically there are four cases. case 1 is the ilt encompasses all values of theta.
% case 2 and 3 are where either one end or the other of the ilt stops at pos or neg
% 3.142. case 4 is where the max and min ilt fall somewhere in the interior of the range
%of theta
margin=3.0;
thetadiff=0.3;
if(min(ilt_pol(:,2))<-margin & max(ilt_pol(:,2))>margin)
%aaaa=1;
b=ilt_pol(:,2);
b2=sort(b);
for j=1:length(b2)-1
if(abs(b2(j+1)-b2(j))>thetadiff)
%bbbb=1;
bottom_no_ilt_bound=b2(j);
top_no_ilt_bound=b2(j+1);
answer=6;

```

```

        break
    else
        %cccc=1;
        answer=5;
    end
end
if(answer==5)
    %dddd=1;
    wall_no_ilt=0; %the ilt covers the whole wall
else %isolate the wall where there is no ilt
    %eeee=1;
    temp=find((wall_pol(:,2)>bottom_no_ilt_bound+0.11)
wall_pol(:,2)<top_no_ilt_bound-0.11);
    wall_no_ilt=wall_pol(temp,:);
    clear check
    check=wall_pol(temp,:);
end
elseif(min(ilt_pol(:,2))<-margin & max(ilt_pol(:,2))<margin)
    %ffff=1;
    temp=find((wall_pol(:,2)<3.142) & wall_pol(:,2)>max(ilt_pol(:,2))+0.11);
    wall_no_ilt=wall_pol(temp,:);
elseif(min(ilt_pol(:,2))>-margin & max(ilt_pol(:,2))>margin)
    %gggg=1;
    temp=find((wall_pol(:,2)>-3.142) & wall_pol(:,2)<min(ilt_pol(:,2))+0.11);
    wall_no_ilt=wall_pol(temp,:);
else
    %hhhh=1;
    temp=find((wall_pol(:,2)<min(ilt_pol(:,2))-0.11) & wall_pol(:,2)>-3.142)
(wall_pol(:,2)>max(ilt_pol(:,2))+0.11 & wall_pol(:,2)<3.142));
    wall_no_ilt=wall_pol(temp,:);
end

if (wall_no_ilt~=0)
    %iiii=1;
    [noiltx,noilty,noiltz]=pol2cart(wall_no_ilt(:,2),wall_no_ilt(:,3),wall_no_ilt(:,4));
    noiltx=noiltx+meanofslice(1);
    noilty=noilty+meanofslice(2);
    noiltz=noiltz+meanofslice(3);
    xyz=horzcat(wall_pol(temp),noiltx,noilty,noiltz); %IM NOT SURE TEMP IS WHAT I
WANT HERE!!!!???
    xyz2=[xyz2;xyz];
    wall_sec3=[wall_sec3;wall_sec];
    ilt_sec3=[ilt_sec3;ilt_sec];
    if (i==iltnumzsegments)
        %kkkk=1;
        t=find(nodes_xyz(:,4)<iltbottomz-0.01);

```

```

        t=nodes_xyz(t,:);
        wall_sec3=[wall_sec3;t];
        clear t;
    end
    %clear noiltx noilty noiltz temp ilt_pol wall_pol
    h=plot3(xyz2(:,2),xyz2(:,3),xyz2(:,4),'g*');
    hold on;
    plot3(wall_sec3(:,2),wall_sec3(:,3),wall_sec3(:,4),'bo')
    hold on;
    plot3(ilt_sec3(:,2),ilt_sec3(:,3),ilt_sec3(:,4),'r+')
    axis equal;
    saveas(h,strep('fig$', '$',int2str(i)), 'bmp');
    pause;
    close all;
end
end
t=find(nodes_xyz(:,4)<iltbottomz-0.05 | nodes_xyz(:,4)>ilttopz+0.05);
t=nodes_xyz(t,:);
wall_no_ilt=[xyz2;t];
nodes=wall_no_ilt(:,1);
wall_no_ilt_elset2=[];
for g=1:length(nodes)
    wall_no_ilt_elset=find(connectivity(:,2)==nodes(g) | connectivity(:,3)==nodes(g) | ...
        connectivity(:,4)==nodes(g) | connectivity(:,5)==nodes(g));
    aa=connectivity(wall_no_ilt_elset,1);
    wall_no_ilt_elset2=[wall_no_ilt_elset2;aa];
    clear aa
end
wall_no_ilt_elset2=unique(wall_no_ilt_elset2);
end

end

%
%
%%%%%%%%%%
%%%%%%%%%%
%%%%%%%%%%
% PRINT OUT THE ABAQUS FILE
%%%%%%%%%%
%%%%%%%%%%
%%%%%%%%%%
outputstring=fname1(1:length(fname1)-4);
outputstring=strcat(outputstring, '.inp');
fid=fopen(outputstring, 'w');

```

```

%PRINT THE FILE HEADER
fprintf(fid,'%s\n%s\n%s\n%s\n%s\n%s\n%s\n%s\n','*Heading','*Preprint,echo=NO,model=NO,histor
y=NO,contact=NO',...
    '*Part, name=THRINST','*End Part','*Part, name=WALLINST','*End Part','*Assembly,
name=Assembly');
fprintf(fid,'%s\n%s\n','*Instance, name=WALLINST, part=WALLINST','*Node');

%PRINT THE WALL NODES
for i=1:length(nodes_xyz)
fprintf(fid,'%i%%s%%6.3f%%s%%6.3f%%s%%6.3f\n', nodes_xyz(i,1), ' ', nodes_xyz(i,2),' ',
nodes_xyz(i,3),' ', nodes_xyz(i,4));
end

%PRINT THE WALL ELEMENTS
fprintf(fid,'%s\n','*Element, type=S4R');
for i=1:length(connectivity)
fprintf(fid,'%i%%s%%i%%s%%i%%s%%i%%s%%i\n', connectivity(i,1), ' ', connectivity(i,2),' ',
connectivity(i,3),' ', ...
    connectivity(i,4),' ',connectivity(i,5));
end

%PRINT THE ELSETS
fprintf(fid,'%s\n%i%%s%%i%%s%%i\n','*Elset, elset=WALLSHELL, internal, generate',1,', ', 'numels,',
',1);

%PRINT THE ELSETS FOR USE IN THE *SHELL SECTION ASSIGNMENT
[a b]=size(orient_elsets);
for i=1:a
    if i>1
        fprintf(fid,'\n');
    end
    fprintf(fid,'%s\n',strrep('*Elset, elset=wall$, internal, instance=WALLINST','$',num2str(i)));
    for j=1:max(find(orient_elsets(i,:)))
        if rem(j,15)==0
            fprintf(fid,'\n');
        end
        if orient_elsets(i,j)~=0
            fprintf(fid,'%i%%s ',orient_elsets(i,j),' ');
        else
            break
        end
    end
end
end
fprintf(fid,'\n')

```

```
%PRINT THE SHELL SECTION FOR THE WALL AND THE TRANSVERSE SHEAR
STIFFNESS LINES
```

```
for i=1:numzslices-1
    fprintf(fid,'%s%s%s%s\n%f%s%i\n',strrep('*Shell Section, elset=wall$', '$',num2str(i)),
material=wall',',',...
        strep('orientation=cylcoord$', '$',num2str(i)),0.13,',',5);
    fprintf(fid,'%s\n%s\n',*Transverse shear stiffness',500, 500, 500');
end
```

```
%PRINT THE ORIENTATION DEFINITIONS
```

```
for i=1:numzslices-1
    fprintf(fid,'%s\n %f%s %f%s %f%s %f%s %f\n %i %s %i\n',...
    strep('*Orientation, name=cylcoord$, definition=coordinates,
system=cylindrical', '$',num2str(i)),x(i),',',y(i),',',...
centerpt(i,3),',',x(i+1),',',y(i+1),',',centerpt(i+1,3),1,',',0);
end
```

```
fprintf(fid,'%s\n',*End Instance');
```

```
% PRINT OUT THE INSTANCE (NODES AND CONNECTIVITY) OF THE ILT
```

```
fprintf(fid,'%s\n%s\n',*Instance, name=THRINST, part=THRINST',*Node');
```

```
%PRINT THE ILT NODES
```

```
for i=1:length(iltnodes_xyz)
    fprintf(fid,'%i%s%6.3f%s%6.3f%s%6.3f\n', iltnodes_xyz(i,1), ', ', iltnodes_xyz(i,2), ', ',
iltnodes_xyz(i,3), ', ', iltnodes_xyz(i,4));
end
```

```
%PRINT THE ILT ELEMENTS
```

```
fprintf(fid,'%s\n',*Element, type=C3D8H');
for i=1:length(iltconnectivity)
    fprintf(fid,'%i%s%i%s%i%s%i%s%i%s%i%s%i\n', iltconnectivity(i,1), ', ',
iltconnectivity(i,2), ', ', iltconnectivity(i,3), ', ', ...
    iltconnectivity(i,4), ', ', iltconnectivity(i,5), ', ', iltconnectivity(i,6), ', ', iltconnectivity(i,7), ',
',iltconnectivity(i,8)...
    ', ', iltconnectivity(i,9));
end
```

```
fprintf(fid,'%s\n',*Elset, elset=ilt, internal, generate');
fprintf(fid,'%s%i%s\n',1, ',iltnumels,', 1 ');
fprintf(fid,'%s\n',*Solid Section, elset=ilt, material=ILT');
fprintf(fid,'%s\n',1.,');
```

```
fprintf(fid,'%s\n',*End Instance');
```

```

%%
%%
%% ENTER ELSETS AND SURFACES FOR TIE CONTACT HERE
%%
fprintf(fid,'%s\n','*Elset, elset=walltie, internal, instance=WALLINST, generate');
fprintf(fid,'%s%i%s\n',1, ' ',numels, ' 1 ');
fprintf(fid,'%s\n','*Surface, type=ELEMENT, name=insideofwall');
fprintf(fid,'%s\n','walltie, SNEG');

fprintf(fid,'%s\n','*Elset, elset=outside_ilt_elset, internal, instance=THRINST');
outside_ilt=iltoutels(:,1);
for i=1:length(outside_ilt)
    if mod(i,10)==0
        fprintf(fid,'\n');
    end
    fprintf(fid,'%i%s ',outside_ilt(i),',');
end
fprintf(fid,'\n');

fprintf(fid,'%s\n','*Surface, type=ELEMENT, name=outside_ilt_surface');
fprintf(fid,'%s\n','outside_ilt_elset, S6');

if check1==0
    fprintf(fid,'%s\n','*Elset, elset=wallnoilt_elset, internal, instance=WALLINST');
    for i=1:length(wall_no_ilt_elset2)
        if mod(i,10)==0
            fprintf(fid,'\n');
        end
        fprintf(fid,'%i%s ',wall_no_ilt_elset2(i),',');
    end
    fprintf(fid,'\n');
    fprintf(fid,'%s\n','*Surface, type=ELEMENT, name=wallnoilt_surface');
    fprintf(fid,'%s\n','wallnoilt_elset, SNEG');
end

inside_ilt=iltinels(:,1);
fprintf(fid,'%s\n','*Elset, elset=inside_ilt, internal, instance=THRINST');
for i=1:length(inside_ilt)
    if mod(i,10)==0
        fprintf(fid,'\n');
    end
    fprintf(fid,'%i%s ',inside_ilt(i),',');
end
fprintf(fid,'\n');

```

```
fprintf(fid,'%s\n','*Surface, type=ELEMENT, name=inside_ilt_surface');
fprintf(fid,'%s\n','inside_ilt, S4');
```

```
bottomnset=find(nodes_xyz(:,4)>=bottomz-0.001
nodes_xyz(:,4)<=bottomz+0.001);%CHANGED!!
fprintf(fid,'%s\n','*Nset, nset=bottomnodeset, instance=WALLINST');
for i=1:length(bottomnset)
    if mod(i,10)==0
        fprintf(fid,'\n');
    end
    fprintf(fid,'%i%s ',bottomnset(i),');
end
fprintf(fid,'\n');
```

&

```
topnset=find(nodes_xyz(:,4)>=topz-0.001 & nodes_xyz(:,4)<=topz+0.001);%CHANGED!!
fprintf(fid,'%s\n','*Nset, nset=topnodeset, instance=WALLINST');
for i=1:length(topnset)
    if mod(i,10)==0
        fprintf(fid,'\n');
    end
    fprintf(fid,'%i%s ',topnset(i),');
end
fprintf(fid,'\n');
```

```
fprintf(fid,'%s\n','*Tie, name=tiecontact, adjust=yes, position tolerance=0');
fprintf(fid,'%s\n','outside_ilt_surface, insideofwall');
```

```
fprintf(fid,'%s\n','*End Assembly');
fprintf(fid,'%s\n','*****');
```

% MATERIAL DEFINITIONS

```
fprintf(fid,'%s\n','*Material, name=wall');
fprintf(fid,'%s\n','*User Material, constants=8');
fprintf(fid,'%s\n','0.014, 477, 416.4, 408.3, 100., 40, 40, 40. ');
fprintf(fid,'%s\n','*****');
```

```
fprintf(fid,'%s\n','*Material, name=ILT');
fprintf(fid,'%s\n','*Hyperelastic, n=2');
fprintf(fid,'%s\n','0., 2.804, 0., 0., 2.858, 0., 0. ');
fprintf(fid,'%s\n','*****');
```

% STEP DEFINITION

```
fprintf(fid,'%s\n','*Step, name=Step1, nlgeom=YES');
fprintf(fid,'%s\n','*Static');
```

```

fprintf(fid,'%s\n','0.01, 1., 1e-06, 0.4');
fprintf(fid,'%s\n','*****');

% BOUNDARY CONDITIONS
fprintf(fid,'%s\n','*Boundary');
fprintf(fid,'%s\n','bottomnodeset, 1, 3');
fprintf(fid,'%s\n','topnodeset, 1, 3');
fprintf(fid,'%s\n','*****');

% LOADS
if check1==0
    fprintf(fid,'%s\n','*Dload');
    fprintf(fid,'%s\n','wallnoilt_surface, P, 1.6');
end
fprintf(fid,'%s\n','*Dload');
fprintf(fid,'%s\n','inside_ilt_surface, P, 1.6');

% OUTPUT REQUESTS
fprintf(fid,'%s\n','*Restart, write, frequency=1');
fprintf(fid,'%s\n','*Output, field');
fprintf(fid,'%s\n','*Node Output');
fprintf(fid,'%s\n','COORD, U');
fprintf(fid,'%s\n','*Element Output');
fprintf(fid,'%s\n','3');
fprintf(fid,'%s\n','EE, S');
fprintf(fid,'%s\n','*Output, history, variable=PRESELECT');
fprintf(fid,'%s\n','*El Print, freq=999999');
fprintf(fid,'%s\n','*Node Print, freq=999999');

fprintf(fid,'%s\n','*CONTROLS, PARAMETERS=TIME INCREMENTATION');
fprintf(fid,'%s\n','7, 10, 9, 25, 10, 7, 12, 8, 6, 3');
fprintf(fid,'%s\n','0.10, 0.5, 0.75, 0.85, 0.25, 0.75, 1.75, 0.75');
fprintf(fid,'%s\n','0.8, 1.5, 1.25, 2, 0.95, 0.1, 1, 0.95');

fprintf(fid,'%s\n','*End Step');

clear data1 iltdata1 numelsets meanx numels meany meanz iltthree_nodes
clear iltseven_nodes iltone_nodes ilttwo_nodes iltfour_nodes iltfive_nodes iltsix_nodes
clear x y z iltx ilty iltz slices subset* xparams yparams ilteight_nodes iltnodenums
clear sort_label sorted_xyz

fclose(fid);
fprintf('%s','ALL                                     DONE!');

```

APPENDIX F

EXERPTS FROM A SAMPLE INPUT FILE

```
*Heading
*Preprint,echo=NO,model=NO,history=NO,contact=NO
*Part, name=THRINST
*End Part
*Part, name=WALLINST
*End Part
*Assembly, name=Assembly
*Instance, name=WALLINST, part=WALLINST
*Node
1, 21.510, 21.964, 0.000
2, 21.620, 22.258, -0.296
3, 21.736, 22.593, -0.543
4, 21.858, 22.949, -0.757
5, 21.984, 23.310, -0.957
...
...
...
2010, 22.742, 24.273, -9.893
2011, 22.649, 24.094, -10.112
2012, 22.555, 23.909, -10.325
2013, 22.461, 23.726, -10.537
2014, 22.370, 23.546, -10.750
*Element, type=S4R
1, 1, 2, 18, 17
2, 17, 18, 34, 33
3, 33, 34, 50, 49
4, 49, 50, 66, 65
5, 65, 66, 82, 81
6, 81, 82, 98, 97
...
```

```

...
...
1954, 1936, 1937, 1948, 1947
1955, 1947, 1948, 1959, 1958
1956, 1958, 1959, 1970, 1969
1957, 1969, 1970, 1981, 1980
1958, 1980, 1981, 1992, 1991
1959, 1991, 1992, 2003, 2002
1960, 2002, 2003, 2014, 2013
1961, 2013, 2014, 416, 415
*Elset, elset=WALLSHELL, internal, generate
1, 1961, 1
*Elset, elset=wall1, internal, instance=WALLINST
1, 2, 3, 4, 5, 6, 7, 8, 9, 10, 11, 12, 13, 14,
519, 520, 521, 522, 523, 524, 525, 526, 527, 528, 529, 926, 927, 928, 929,
930, 931, 932, 933, 934, 935, 936, 937, 938, 939, 1444, 1445, 1446, 1447, 1448,
1449, 1450, 1451, 1452, 1453, 1454, 1455, 1456, 1457,
*Elset, elset=wall2, internal, instance=WALLINST
15, 16, 17, 18, 19, 20, 21, 22, 23, 24, 25, 26, 27, 28,
530, 531, 532, 533, 534, 535, 536, 537, 538, 539, 540, 940, 941, 942, 943,
944, 945, 946, 947, 948, 949, 950, 951, 952, 953, 1458, 1459, 1460, 1461, 1462,
1463, 1464, 1465, 1466, 1467, 1468, 1469, 1470, 1471,
...
...
...
*Elset, elset=wall37, internal, instance=WALLINST
505, 506, 507, 508, 509, 510, 511, 512, 513, 514, 515, 516, 517, 518,
915, 916, 917, 918, 919, 920, 921, 922, 923, 924, 925, 1430, 1431, 1432, 1433,
1434, 1435, 1436, 1437, 1438, 1439, 1440, 1441, 1442, 1443, 1948, 1949, 1950, 1951, 1952,
1953, 1954, 1955, 1956, 1957, 1958, 1959, 1960, 1961,
*Shell Section, elset=wall1, material=wall, orientation=cylcoord1
0.130000, 5
*Transverse shear stiffness
100,100,100
*Shell Section, elset=wall2, material=wall, orientation=cylcoord2
0.130000, 5
...
...
...
*Shell Section, elset=wall37, material=wall, orientation=cylcoord37
0.130000, 5
*Transverse shear stiffness
100,100,100
*Orientation, name=cylcoord1, definition=coordinates, system=cylindrical
21.300244, 20.654832, -0.000000, 21.452739, 20.980064, -0.288287
1 0

```

```

*Orientation, name=cylcoord2, definition=coordinates, system=cylindrical
21.452739, 20.980064, -0.288287, 21.584740, 21.260887, -0.558157
1 0
...
...
...
*Orientation, name=cylcoord37, definition=coordinates, system=cylindrical
21.748014, 22.038184, -10.491524, 21.696035, 21.974308, -10.750000
1 0
*End Instance
*Instance, name=THRINST, part=THRINST
*Node
1, 24.512, 24.084, -2.202
2, 24.487, 24.342, -2.270
3, 24.458, 24.597, -2.350
4, 24.428, 24.846, -2.445
5, 24.397, 25.087, -2.558
...
...
...
1222, 21.861, 19.688, -4.667
1223, 22.092, 19.660, -4.854
1224, 22.358, 19.658, -4.987
*Element, type=C3D8H
1, 2, 32, 37, 7, 1, 31, 36, 6
2, 32, 62, 67, 37, 31, 61, 66, 36
3, 7, 37, 42, 12, 6, 36, 41, 11
4, 37, 67, 72, 42, 36, 66, 71, 41
...
...
...
733, 1168, 1192, 1196, 1172, 1167, 1191, 1195, 1171
734, 1192, 1216, 1220, 1196, 1191, 1215, 1219, 1195
735, 1172, 1196, 1200, 1176, 1171, 1195, 1199, 1175
736, 1196, 1220, 1224, 1200, 1195, 1219, 1223, 1199
*Elset, elset=ilt, internal, generate
1, 736, 1
*Solid Section, elset=ilt, material=ILT
1.,
*End Instance
*Elset, elset=walltie, internal, instance=WALLINST, generate
1, 1961, 1
*Surface, type=ELEMENT, name=insideofwall
walltie, SNEG
*Elset, elset=outside_ilt_elset, internal, instance=THRINST
1, 3, 5, 7, 9, 11, 13, 15, 17,

```

19, 21, 23, 25, 27, 29, 31, 33, 35, 37,
 39, 41, 43, 45, 47, 49, 51, 53, 55, 57,
 59, 61, 63, 65, 67, 69, 71, 73, 75, 77,
 ...
 ...
 ...
 639, 641, 643, 645, 647, 649, 651, 653, 655, 657,
 659, 661, 663, 665, 667, 669, 671, 673, 675, 677,
 679, 681, 683, 685, 687, 689, 691, 693, 695, 697,
 699, 701, 703, 705, 707, 709, 711, 713, 715, 717,
 719, 721, 723, 725, 727, 729, 731, 733, 735,
 *Surface, type=ELEMENT, name=outside_ilt_surface
 outside_ilt_elset, S6
 *Elset, elset=wallnoilt_elset, internal, instance=WALLINST
 1, 2, 3, 4, 5, 6, 7, 8, 9,
 10, 11, 12, 13, 14, 15, 16, 17, 18, 19,
 20, 21, 22, 23, 24, 25, 26, 27, 28, 29,
 30, 31, 32, 33, 34, 35, 36, 37, 38, 39,
 40, 41, 42, 43, 44, 45, 46, 47, 48, 49,
 50, 51, 52, 53, 54, 55, 56, 57, 58, 59,
 60, 61, 62, 63, 64, 65, 66, 67, 68, 69,
 ...
 ...
 ...
 1918, 1919, 1920, 1921, 1922, 1923, 1924, 1925, 1926, 1927,
 1928, 1929, 1930, 1931, 1932, 1933, 1934, 1935, 1936, 1937,
 1938, 1939, 1940, 1941, 1942, 1943, 1944, 1945, 1946, 1947,
 1948, 1949, 1950, 1951, 1952, 1953, 1954, 1955, 1956, 1957,
 1958, 1959, 1960, 1961,
 *Surface, type=ELEMENT, name=wallnoilt_surface
 wallnoilt_elset, SNEG
 *Elset, elset=inside_ilt, internal, instance=THRINST
 2, 4, 6, 8, 10, 12, 14, 16, 18,
 20, 22, 24, 26, 28, 30, 32, 34, 36, 38,
 40, 42, 44, 46, 48, 50, 52, 54, 56, 58,
 60, 62, 64, 66, 68, 70, 72, 74, 76, 78,
 ...
 ...
 ...
 640, 642, 644, 646, 648, 650, 652, 654, 656, 658,
 660, 662, 664, 666, 668, 670, 672, 674, 676, 678,
 680, 682, 684, 686, 688, 690, 692, 694, 696, 698,
 700, 702, 704, 706, 708, 710, 712, 714, 716, 718,
 720, 722, 724, 726, 728, 730, 732, 734, 736,
 *Surface, type=ELEMENT, name=inside_ilt_surface
 inside_ilt, S4

```

*Nset, nset=bottomnodeset, instance=WALLINST
416, 427, 438, 449, 460, 471, 482, 493, 504,
515, 526, 537, 548, 559, 570, 878, 889, 900, 911,
922, 933, 944, 955, 966, 977, 988, 1377, 1388, 1399,
1410, 1421, 1432, 1443, 1454, 1465, 1476, 1487, 1498, 1509,
1520, 1882, 1893, 1904, 1915, 1926, 1937, 1948, 1959, 1970,
1981, 1992, 2003, 2014,
*Nset, nset=topnodeset, instance=WALLINST
1, 17, 33, 49, 65, 81, 97, 113, 129,
145, 161, 177, 193, 209, 225, 571, 587, 603, 619,
635, 651, 667, 683, 699, 715, 731, 989, 1005, 1021,
1037, 1053, 1069, 1085, 1101, 1117, 1133, 1149, 1165, 1181,
1197, 1521, 1537, 1553, 1569, 1585, 1601, 1617, 1633, 1649,
1665, 1681, 1697, 1713,
*Tie, name=tiecontact, adjust=yes, position tolerance=0
outside_ilt_surface, insideofwall
*End Assembly
*****
*Material, name=wall
*User Material, constants=8
0.014, 477, 416.4, 408.3, 100.
*****
*Material, name=ILT
*Hyperelastic, n=2
0., 2.804, 0., 0., 2.858, 0., 0.
*****
*Step, name=Step1, nlgeom=YES
*Static
0.0001, 1., 1e-05, 0.1
*****
*Boundary
bottomnodeset, 1, 3
topnodeset, 1, 3
*****
*Dload
wallnoilt_surface, P, 1.6
*Dload
inside_ilt_surface, P, 1.6
*Restart, write, frequency=1
*Output, field
*Node Output
COORD, U
*Element Output
3
E, S
*Output, history, variable=PRESELECT

```

*El Print, freq=999999
*Node Print, freq=999999
*EndStep

APPENDIX G

ABAQUS UMAT SUBROUTINE FOR ANISOTROPIC IMPLEMENTATION

```
SUBROUTINE UMAT(STRESS,STATEV,DDSDDE,SSE,SPD,SCD,  
1 RPL,DDSDDT,DRPLDE,DRPLDT,STRAN,DSTRAN,  
2 TIME,DTIME,TEMP,DTEMP,PREDEF,DPRED,MATERL,NDI,NSHR,NTENS,  
3 NSTATV,PROPS,NPROPS,COORDS,DROT,PNEWDT,CELENT,  
4 DFGRD0,DFGRD1,NOEL,NPT,KSLAY,KSPT,KSTEP,KINC)  
C  
C   INCLUDE 'ABA_PARAM.INC'  
C  
C   CHARACTER*8 MATERL  
C   DIMENSION STRESS(NTENS),STATEV(NSTATV),  
C   1 DDSDDE(NTENS,NTENS),DDSDDT(NTENS),DRPLDE(NTENS),  
C   2 STRAN(NTENS),DSTRAN(NTENS),DFGRD0(3,3),DFGRD1(3,3),  
C   3 TIME(2),PREDEF(1),DPRED(1),PROPS(NPROPS),COORDS(3),DROT(3,3)  
C  
C   LOCAL ARRAYS  
C -----  
C   BBAR - DEVIATORIC RIGHT CAUCHY-GREEN TENSOR  
C   DISTGR - DEVIATORIC DEFORMATION GRADIENT (DISTORTION TENSOR)  
C -----  
C  
C   DIMENSION BBAR(6),DISTGR(3,3)  
C  
C   PARAMETER(ZERO=0.D0, ONE=1.D0, TWO=2.D0, THREE=3.D0, FOUR=4.D0)  
C  
C -----  
C -----  
C   UMAT FOR FUNG 5 MODEL HYPERELASTICITY  
C  
C   WRITTEN BY:
```

```

C   JONATHAN P. VANDE GEEST
C   PH.D CANDIDATE
C   ADVISOR: DR. DAVID VORP
C   COMPUTATIONAL VASCULAR BIOMECHANICS LABORATORY
C   DEPT OF SURGERY AND BIOENGINEERING
C   UNIVERSITY OF PITTSBURGH
C   DATE: NOV 2004

```

```

C -----

```

```

C   To run the program:
c   put below lines into your model for material definition:
c   *MATERIAL,NAME=AAA
c   ** Fung 5 parameter model
c   *USER MATERIAL,CONSTANTS=5
c

```

```

c -----

```

```

C   ELASTIC PROPERTIES

```

```

C -----

```

```

C   PROPS(1) - C
C   PROPS(2) - A1
C   PROPS(3) - A2
C   PROPS(4) - A3
C   PROPS(5) - A4 - the shear term
C   PROPS(6) - u11
C   PROPS(6) - u22
C   PROPS(6) - u12

```

```

C -----

```

```

C

```

```

C   ELASTIC PROPERTIES

```

```

C

```

```

real*8 C, A1, A2, A3, A4, DET, SCALE, E11, E12, E22, S11, S22, S12
real*8 J1, J2, J3, J4, J5, J6, J7, J8, J9
real*8 l1sqrd, l2sqrd, l3sqrd, l1
REAL*8 F1, F2, K1, K2
real*8 u11, u22, u12
c   integer u

```

```

C =PROPS(1)
A1=PROPS(2)
A2=PROPS(3)
A3=PROPS(4)
A4=PROPS(5)
u11=PROPS(6)
u22=PROPS(7)
u12=PROPS(8)

```

```

C
C  JACOBIAN AND DISTORTION TENSOR
C
  DET=DFGRD1(1, 1)*DFGRD1(2, 2)*DFGRD1(3, 3)
1  -DFGRD1(1, 2)*DFGRD1(2, 1)*DFGRD1(3, 3)
  IF(NSHR.EQ.3) THEN
    DET=DET+DFGRD1(1, 2)*DFGRD1(2, 3)*DFGRD1(3, 1)
1    +DFGRD1(1, 3)*DFGRD1(3, 2)*DFGRD1(2, 1)
2    -DFGRD1(1, 3)*DFGRD1(3, 1)*DFGRD1(2, 2)
3    -DFGRD1(2, 3)*DFGRD1(3, 2)*DFGRD1(1, 1)
  END IF
  SCALE=DET**(-ONE/THREE)
  DO K1=1, 3
    DO K2=1, 3
      DISTGR(K2, K1)=SCALE*DFGRD1(K2, K1)
    END DO
  END DO

C
C  CALCULATE LEFT CAUCHY-GREEN TENSOR
C
  BBAR(1)=DISTGR(1, 1)**2+DISTGR(1, 2)**2+DISTGR(1, 3)**2
  BBAR(2)=DISTGR(2, 1)**2+DISTGR(2, 2)**2+DISTGR(2, 3)**2
  BBAR(3)=DISTGR(3, 3)**2+DISTGR(3, 1)**2+DISTGR(3, 2)**2
  BBAR(4)=DISTGR(1, 1)*DISTGR(2, 1)+DISTGR(1, 2)*DISTGR(2, 2)
1  +DISTGR(1, 3)*DISTGR(2, 3)
  IF(NSHR.EQ.3) THEN
    BBAR(5)=DISTGR(1, 1)*DISTGR(3, 1)+DISTGR(1, 2)*DISTGR(3, 2)
1  +DISTGR(1, 3)*DISTGR(3, 3)
    BBAR(6)=DISTGR(2, 1)*DISTGR(3, 1)+DISTGR(2, 2)*DISTGR(3, 2)
1  +DISTGR(2, 3)*DISTGR(3, 3)
  END IF

C
C  CALCULATE THE STRAIN
C
  E11=0.5*(DFGRD1(1, 1)**2+DFGRD1(2, 1)**2-1)
  E22=0.5*(DFGRD1(1, 2)**2+DFGRD1(2, 2)**2-1)
  E12=0.5*(DFGRD1(1, 1)*DFGRD1(1, 2)+DFGRD1(2, 2)*DFGRD1(2, 1))
  E21=0.5*(DFGRD1(1, 2)*DFGRD1(1, 1)+DFGRD1(2, 2)*DFGRD1(2, 1))
  E33=ZERO

c    Fung 5 parameter strain energy function

```

$$Q=A1*E11**2+A2*E22**2+2*A3*E11*E22+A4*E12**2$$

$$D1=2*(A1*E11+A3*E22)$$

$$D2=2*(A2*E22+A3*E11)$$

$$D3=2*(A4*E12)$$

$$S11= 2*u11*E11 + C*(A1*E11*EXP(0.5*A1*E11**2)+A3*E22*EXP(A3*E11*E22))$$

$$S22= 2*u22*E22 + C*(A2*E22*EXP(0.5*A2*E22**2)+A3*E11*EXP(A3*E11*E22))$$

$$S12= 2*u12*E12 + C*(A4*E12*EXP(0.5*A4*E12**2))$$

$$S33= ZERO$$

C S11= 2*u11*E11 + 0.5*C*D1*EXP(Q)

C S22= 2*u22*E22 + 0.5*C*D2*EXP(Q)

C S33= ZERO

C S12=0.5*C*D3*EXP(Q)

C OUTPUT TO VALIDATE DATA FILE

c write(unit=u,fmt="(E,E,E,E,E,E)")E11,E22, E12

c 1,S11,S22, S12

C OUTPUT TO DAT FILE

C write(unit=u,fmt="(E,E,E,E,E,E)")E11, E12, E22

C 1,S11, S12, S22

$$F1=DFGRD1(1, 1)$$

$$F2=DFGRD1(2, 2)$$

$$K1=0.5*(DFGRD1(1, 2)+DFGRD1(2,1))$$

$$K2=K1$$

C CALCULATE THE STRESS

$$STRESS(1)=(F1*S11+K1*S12)*F1+(F1*S12+K1*S22)*K2$$

$$STRESS(2)=(S11*K2+S12*F2)*K1+(K2*S12+F2*S22)*F2$$

$$STRESS(3)=(S11*K2+S12*F2)*F1+(K2*S12+F2*S22)*K2$$

$$J1=2*u11 + C*(A1*EXP(0.5*A1*E11**2) + EXP(0.5*A1*E11**2)*(A1*E11)**2 + EXP(A3*E11*E22)*(A3*E22)**2)$$

$$J2=2*u22 + C*(A2*EXP(0.5*A2*E22**2) + EXP(0.5*A2*E22**2)*(A2*E22)**2 + EXP(A3*E11*E22)*(A3*E11)**2)$$

$$J3=2*u12 + C*(A4*EXP(0.5*A4*E12**2) + EXP(0.5*A4*E12**2)*(A4*E12))$$

C J4 is dS11/dE22, which is equivalent to J7 = dS22/dE11

$$J4=C*(A3*A3*E11*E22*EXP(A3*E11*E22) + A3*EXP(A3*E11*E22))$$

C J5 is dS12/dE11

$$J5=0$$

C J5= 0.5*C*EXP(Q)*(D1*D3)

```

C J6 is dS12/dE22
  J6=0
C   J6= 0.5*C*EXP(Q)*(D2*D3)
  J7=J4
  J8=J5
  J9=J6

C   J1= 0.5*C*EXP(Q)*((2*A1)+D1**2)
C   J2= 0.5*C*EXP(Q)*((2*A2)+D2**2)
C   J3= 0.5*C*EXP(Q)*((2*A4)+D3**2)
C   J4= 0.5*C*EXP(Q)*((2*A3)+D1*D2)
C   J5= 0.5*C*EXP(Q)*(D1*D3)
C   J6= 0.5*C*EXP(Q)*(D2*D3)
C   J7= J4
C   J8= J5
C   J9= J6
C
C CALCULATE THE STIFFNESS MATRIX
C
DDSDDE(1, 1)= 2*F1*S11+F1*F1*J1+K1*S12+F1*K1*J8+
  1          K1*S12+F1*K1*J8+K1*K1*J7

DDSDDE(2, 2)= K2*K2*J4+K2*S12+F2*K2*J9+K2*S12+
  1          F2*K2*J9+2*F2*S22+F2*F2*J2

DDSDDE(3, 3)= F1*S11+F1*K2*J5+F1*F2*J3+2*K1*S12
  1          +K1*K2*J3+F2*S22+K1*F2*J6

DDSDDE(1, 2)= F1*F1*J4+F1*K1*J9+K1*F1*J9+K1*K1*J2

DDSDDE(1, 3)= F1*F1*J5+F1*S12+K1*F1*J3+F1*S12+K1*F1*J3
  1          +2*K1*S22+K1*K1*J6

DDSDDE(2, 3)= 2*K2*S11+K2*K2*J5+F2*S12+K2*F2*J3+F2*S12
  1          +K2*F2*J3+F2*F2*J6

DDSDDE(2, 1)= DDSDDE(1, 2)

DDSDDE(3, 1)= K2*S11+F1*K2*J1+F2*S12+F1*F2*J8+K1*K2*J8
  1          +K1*F2*J7

DDSDDE(3, 2)= F1*K2*J4+F1*S12+F1*F2*J9+K1*K2*J9
  1          +K1*S22+K1*F2*J2
C   close(u)
C
RETURN

```

END

APPENDIX H

MATLAB FUNCTION TO CREATE BIAxIAL SPECIMEN SIMULATIONS

```
function create_nodeset = findnodes(ofname,ifname,seed,depthnode,length,step,numnodes);
% function create_nodeset = findnodes(ofname,ifname,seed,depthnode,length,step,numnodes);
% ofname and ifname should be written 'filename.txt'
% this program assumes you are using a first order element
%
% seed = global element size as defined when seeding mesh in Abaqus
% depthnode = number of nodes user wants to leave open from edges
% length = length in mm specimen must be square dimensions
% step = number of nodes between each chosen node
% numnodes = number of nodes wanted in each displacement nodeset

%load input file *.txt
eval(strrep('load j','j',ifname))
data=eval(strrep(ifname,'.txt',''));

fod=fopen(ofname,'w');

% m is the # of rows, n is the # of cols
[m,n]=size(data);

% This program needs node number in column 1, x in column 2, and y in column 3
% The nodes sets are labeled counterclockwise starting with node set one on the right
% The output is nodesets 1,2,3,4 in columns 5,6,7,8 respectively

%CALCULATIONS

halflength = length / 2;
depthlength = depthnode * seed;
dimensionb = halflength - depthlength;
increment = seed * step;
```

```
%FINDING NODESETS
```

```
%NODESET ONE
```

```
x1 = dimensionb;
```

```
a = linspace(increment*(numnodes-1)/2,-1*increment*(numnodes-1)/2,numnodes)';
```

```
node=data(:,1);
```

```
x=data(:,2);
```

```
y=data(:,3);
```

```
for i = 1:4,
```

```
eval(strrep('cell$(1:m,1)=0;','$',int2str(i)));
```

```
end
```

```
for j=1:numnodes
```

```
    for k = 1:m
```

```
        if (x(k)==x1 & y(k)==a(j))
```

```
            cell1(k,1)=node(k,1);
```

```
        end
```

```
    end
```

```
end
```

```
%NODESET TWO
```

```
y2 = dimensionb;
```

```
for j2 = 1:numnodes
```

```
    for k2 = 1:m
```

```
        if (y(k2)==y2 & x(k2)==a(j2))
```

```
            cell2(k2,1)=node(k2,1);
```

```
        end
```

```
    end
```

```
end
```

```
%NODESET THREE
```

```
x3 = -1*dimensionb;
```

```
for j3 = 1:numnodes
```

```
    for k3 = 1:m
```

```
        if (x(k3)==x3 & y(k3)==a(j3))
```

```
            cell3(k3,1)=node(k3,1);
```

```
        end
```

```
    end
```

```
end
```

```
%NODESET FOUR
```

```
y4 = -1*dimensionb;
```

```

for j4 = 1:numnodes
    for k4=1:m
        if (y(k4)==y4 & x(k4)==a(j4))
            cell4(k4,1)=node(k4,1);
        end
    end
end

for i = 1:4,
eval(strrep('indice$=find(cell$(:,1)~=0);','$',int2str(i)))
end

for i=1:size(indice1),
    fprintf(fod,'%i %i %i %i\n',indice1(i),indice2(i),indice3(i),indice4(i));
end

plot(data(indice1,2),data(indice1,3),'b.')
hold on;
plot(data(indice2,2),data(indice2,3),'b.')
hold on;
plot(data(indice3,2),data(indice3,3),'b.')
hold on;
plot(data(indice4,2),data(indice4,3),'b.')
fclose(fod);

```

APPENDIX I

POST PROCESSING MATLAB FUNCTION FOR STRESS GRADIENTS

```
function postprocessing
% This is the main function which calls all other functions

close all
clear all
%%%%%%%%%%%%%%%%%%%%%%%%%%%%%%%%%%%%%%%%%%%%%%%%%%%%%%%%%%%%%%%%%%%%%%%%
%%%%%%%%%%%%%%%%%%%%%%%%%%%%%%%%%%%%%%%%%%%%%%%%%%%%%%%%%%%%%%%%%%%%%%%%
%
% read in the user defined output data file...which is saved to the array abaqus_data
filename=uigetfile('*.txt','Please choose a AAA by choosing one of its results files: ');
age=input('Please enter the age of the Patient: ');
sex=input('Please enter sex (0.5 for male, -0.5 for female): ');
hist=input('Please enter hist (0.5 if yes, -0.5 if no): ');
%abaqus_data=read_results(filename);
%%%%%%%%%%%%%%%%%%%%%%%%%%%%%%%%%%%%%%%%%%%%%%%%%%%%%%%%%%%%%%%%%%%%%%%%
%%%%%%%%%%%%%%%%%%%%%%%%%%%%%%%%%%%%%%%%%%%%%%%%%%%%%%%%%%%%%%%%%%%%%%%%
%
% read in the wall mesh file for the undeformed nodes and the connectivity
for i=1:length(filename)
    if filename(i)=='_'
        endoftag=i-1;
        break
    end
end
tag=filename(1:endoftag);
filename2=[tag '_wall.txt'];
[undeformed_mesh,undeformed_connectivity]=read_wall_mesh(filename2);
clear i endoftag filename2
fname1=strcat(tag,'_ANI_ISO.txt');fname2=strcat(tag,'_ISO_ISO.txt');
fname3=strcat(tag,'_ANI_ANI.txt');fname4=strcat(tag,'_ANI_NOILT.txt');
```

```

fname5=strcat(tag,'_ISO_NOILT.txt');
ani_iso=read_results(fname1);
iso_iso=read_results(fname2);
ani_ani=read_results(fname3);
ani_noilt=read_results(fname4);
iso_noilt=read_results(fname5);
%%%%%%%%%%%%%%%%%%%%%%%%%%%%%%%%%%%%%%%%%%%%%%%%%%%%%%%%%%%%%%%%%%%%%%%%
%%%%%%%%%%%%%%%%%%%%%%%%%%%%%%%%%%%%%%%%%%%%%%%%%%%%%%%%%%%%%%%%%%%%%%%%
% read in the DSMITH plt file ...contains local curvatures
filename3=[tag '_wall.plt'];
[dsmith_data]=read_dsmith(filename3,ani_iso); % here the choice of ani_iso is arbitrary
clear filename3
%%%%%%%%%%%%%%%%%%%%%%%%%%%%%%%%%%%%%%%%%%%%%%%%%%%%%%%%%%%%%%%%%%%%%%%%
%%%%%%%%%%%%%%%%%%%%%%%%%%%%%%%%%%%%%%%%%%%%%%%%%%%%%%%%%%%%%%%%%%%%%%%%
% read in the ilt mesh file from TrueGrid
filename4=[tag '_ilt.txt'];
[iltnodes_xyz,iltconnectivity,l_nodes]=read_ilt_mesh(filename4);
clear filename4
%%%%%%%%%%%%%%%%%%%%%%%%%%%%%%%%%%%%%%%%%%%%%%%%%%%%%%%%%%%%%%%%%%%%%%%%
%%%%%%%%%%%%%%%%%%%%%%%%%%%%%%%%%%%%%%%%%%%%%%%%%%%%%%%%%%%%%%%%%%%%%%%%
% We need to update ani_iso, etc. so that X Y and Z correspond to the
% undeformed config!
jon=undeformed_mesh(:,2:4);
ani_iso(:,2:4)=jon;
iso_iso(:,2:4)=jon;
ani_ani(:,2:4)=jon;
ani_noilt(:,2:4)=jon;
iso_noilt(:,2:4)=jon;
%%%%%%%%%%%%%%%%%%%%%%%%%%%%%%%%%%%%%%%%%%%%%%%%%%%%%%%%%%%%%%%%%%%%%%%%
%%%%%%%%%%%%%%%%%%%%%%%%%%%%%%%%%%%%%%%%%%%%%%%%%%%%%%%%%%%%%%%%%%%%%%%%
% Use old_RPI to calculate local diameter, old RPI, etc.
% final_mesh is Node X Y Z Stress ILT_thick old_NORD old_Strength old_RPI
% global_new_mesh is needed in new_RPI
[final_mesh1,global_new_mesh1,m_use1,age]=old_RPI(ani_iso,l_nodes,age);
[final_mesh2,global_new_mesh2,m_use2,age]=old_RPI(iso_iso,l_nodes,age);
[final_mesh3,global_new_mesh3,m_use3,age]=old_RPI(ani_ani,l_nodes,age);
[final_mesh4,global_new_mesh4,m_use4,age]=old_RPI_noilt(ani_noilt,l_nodes,age);
[final_mesh5,global_new_mesh5,m_use5,age]=old_RPI_noilt(iso_noilt,l_nodes,age);
%%%%%%%%%%%%%%%%%%%%%%%%%%%%%%%%%%%%%%%%%%%%%%%%%%%%%%%%%%%%%%%%%%%%%%%%
%%%%%%%%%%%%%%%%%%%%%%%%%%%%%%%%%%%%%%%%%%%%%%%%%%%%%%%%%%%%%%%%%%%%%%%%
% Use new_RPI to calculate the new Strength and RPI values. It also
% outputs the old (D Wang) strength values
% The format of these arrays is:

```

```

%      Node,X,Y,Z,PrinE,E11,E22,Mises,MPrincS,S11,S22,newStrength,newRPI,old_Strength,
oldRPI
%
[ani_iso]=new_RPI(final_mesh1,global_new_mesh1,ani_iso,age,m_use1,sex,hist);
[iso_iso]=new_RPI(final_mesh2,global_new_mesh2,iso_iso,age,m_use2,sex,hist);
[ani_ani]=new_RPI(final_mesh3,global_new_mesh3,ani_ani,age,m_use3,sex,hist);
[ani_noilt]=new_RPI_noilt(final_mesh4,global_new_mesh4,ani_noilt,age,m_use4,sex,hist);
[iso_noilt]=new_RPI_noilt(final_mesh5,global_new_mesh5,iso_noilt,age,m_use5,sex,hist);
new=iso_iso(:,9)/iso_iso(:,14);
iso_iso=[iso_iso new];
new2=zeros(length(ani_iso),1);
ani_iso=[ani_iso new2];
ani_ani=[ani_ani new2];
ani_noilt=[ani_noilt new2];
iso_noilt=[iso_noilt new2];
clear m_ * ilt* l_ * new final_ * global_ * new2

%%%%%%%%%%%%%%%%%%%%%%%%%%%%%%%%%%%%%%%%%%%%%%%%%%%%%%%%%%%%%%%%%%%%%%%%
% calculate gradients here and append them to the data arrays ani_iso etc.
% now ani_iso is (where g stands for gradients)
% Node,X,Y,Z, PrinE, E11, E22, Mises, MPrincS, S11, S22, newStrength, newRPI,
old_Strength, oldRPI
%      gPrinE, gE11, gE22, gMises, gMPrincS, gS11, gS22, gnewStrength, gnewRPI,
gold_Strength, goldRPI
data = ['ani_iso ','iso_iso ','ani_ani ','ani_noilt','iso_noilt'];
celldata = cellstr(data);
for i=1:5
    [a,b]=size(eval(char(celldata(i))));
    temp1=zeros(a,b-4);
    for j=5:b
        temp2=global_gradients(eval(char(celldata(i))),j);
        temp1(:,j-4)=temp2;
    end
    eval(strrep('data%=[eval(char(celldata(i))) temp1];','% ',num2str(i)));
end
ani_iso=data1; iso_iso=data2; ani_ani=data3; ani_noilt=data4; iso_noilt=data5;
clear data* temp* a b data celldata
%%%%%%%%%%%%%%%%%%%%%%%%%%%%%%%%%%%%%%%%%%%%%%%%%%%%%%%%%%%%%%%%%%%%%%%%
% Print out results summary file...must also calculate gradients here
printoutsummary(tag,ani_iso,iso_iso,ani_ani,ani_noilt,iso_noilt);
%%%%%%%%%%%%%%%%%%%%%%%%%%%%%%%%%%%%%%%%%%%%%%%%%%%%%%%%%%%%%%%%%%%%%%%%
% Print out results to one PLT file
printoutPLT(fname1,undeformed_mesh,ani_iso,undeformed_connectivity);

```

```

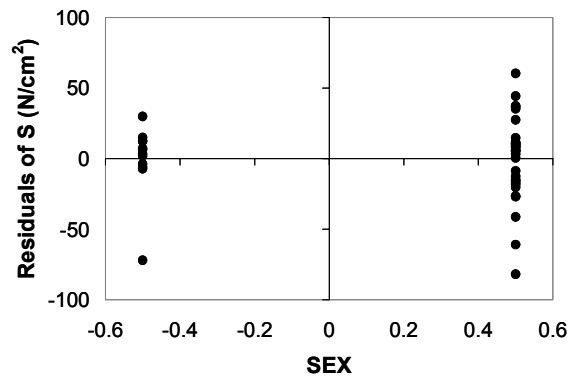
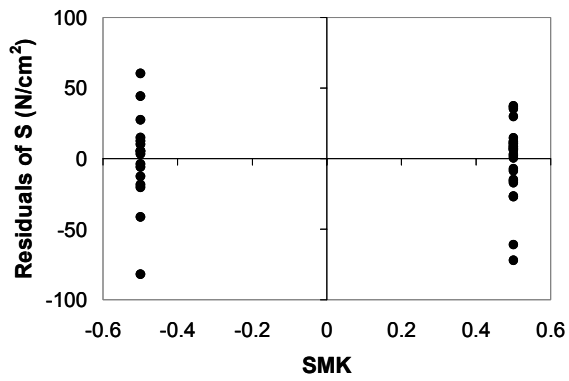
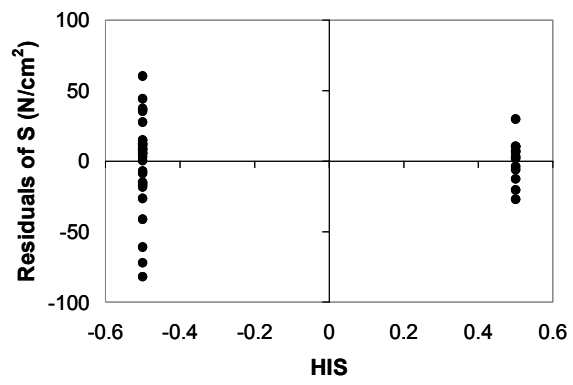
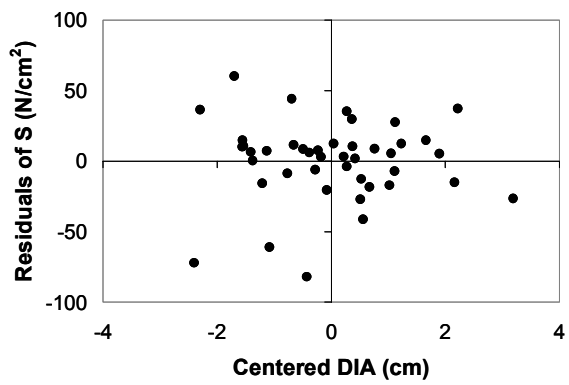
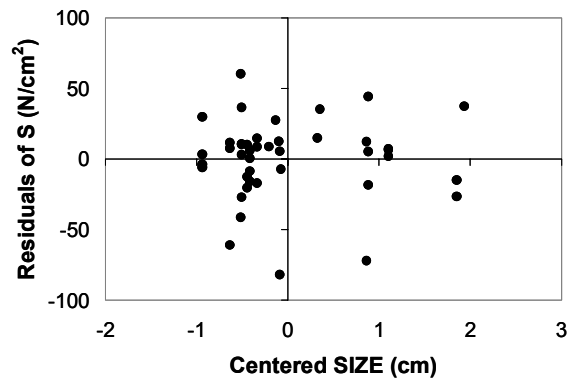
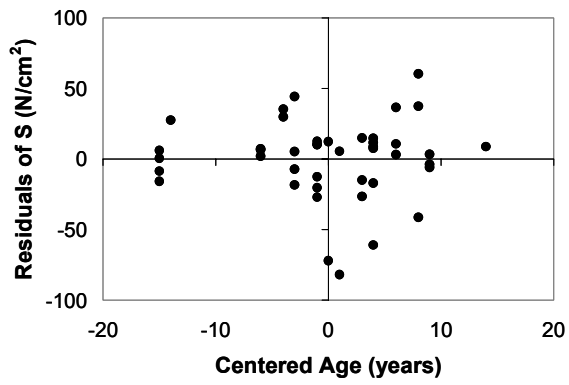
printoutPLT(fname2,undeformed_mesh,iso_iso,undeformed_connectivity);
printoutPLT(fname3,undeformed_mesh,ani_ani,undeformed_connectivity);
printoutPLT(fname4,undeformed_mesh,ani_noilt,undeformed_connectivity);
printoutPLT(fname5,undeformed_mesh,iso_noilt,undeformed_connectivity);
clear fname* i j filename
%%%%%%%%%%%%%%%%%%%%%%%%%%%%%%%%%%%%%%%%%%%%%%%%%%%%%%%%%%%%%%%%%%%%%%%%
%%%%%%%%%%%%%%%%%%%%%%%%%%%%%%%%%%%%%%%%%%%%%%%%%%%%%%%%%%%%%%%%%%%%%%%%
% Print out gradient file
%%%%%%%%%%%%%%%%%%%%%%%%%%%%%%%%%%%%%%%%%%%%%%%%%%%%%%%%%%%%%%%%%%%%%%%%
%%%%%%%%%%%%%%%%%%%%%%%%%%%%%%%%%%%%%%%%%%%%%%%%%%%%%%%%%%%%%%%%%%%%%%%%
outputgradientfile(tag,ani_iso,iso_iso,ani_ani,ani_noilt,iso_noilt);
eval(strrep('save %_FINAL_RESULTS','% ',tag))
%
%%%%%%%%%%%%%%%%%%%%%%%%%%%%%%%%%%%%%%%%%%%%%%%%%%%%%%%%%%%%%%%%%%%%%%%%
%%%%%%%%%%%%%%%%%%%%%%%%%%%%%%%%%%%%%%%%%%%%%%%%%%%%%%%%%%%%%%%%%%%%%%%%
% % The portion of code below prompts the user for a location of
% interest, it has been commented out for simplicity If you uncomment
% it it will need to be updated as the variable names have changed
% % prompt the user for the value of z in which the IMA stitch was
% located...to determine the values of stress etc at that level
%
% fprintf('The top and bottom of the AAA are: ');
% topz
% botz
% zofinterest=input('Please enter the value of z for which you would like to calculate the values
of stress, curvature, and strain:');
%
% a=find(dsmith_data(:,4)>zofinterest-0.4 & dsmith_data(:,4)<zofinterest+0.4);
% answer=dsmith_data(a,:);
%
% % the columns of abaqus_data are Node coord1 coord2 coord3 maxprinE E11 E22 Mises
maxprinS S11 S22 strength rpi
%
% vonmises_stress=mean(answer(:,8));
% maxprinc_stress=mean(answer(:,9));
% maxprinc_strain=mean(answer(:,5));
% E11=mean(answer(:,6));
% E22=mean(answer(:,7));
%
% b=find(curv_values(:,3)>zofinterest-0.2 & curv_values(:,3)<zofinterest+0.2);
% answer2=curv_values(b,:);
% firstprincurv=mean(answer2(:,4));
% secondprincurv=mean(answer2(:,8));

%clear topz botz a b
%
```

APPENDIX J

RESIDUALS VERSUS EACH INDEPENDENT VARIABLE

The residuals of each independent strength variable are displayed on the following page.



APPENDIX K

MATLAB FUNCTION CALCULATING RPI

```
function
[abaqus_data]=new_RPI(final_mesh,global_new_mesh,abaqus_data,age,m_use,sex,hist)

%Computes the strength and RPI of FE models of AAA
%conn is a variable containing the connectivity of the triangular wall mesh (n by 3)
%nodes: n*5 matrix of node x y z stress for the nodes just on the wall
%extras is a variable of size (n X 4), where n is the number of nodes in the wall mesh
%this array consists of the ILT NORD STRENGTH RPI from davids results
%age is the age of the patient in years - used to determine the nonaneurysmal diameter
%sex is the sex of the patient (sex=0.5 for males and sex=-0.5 for females)
%hist is the family history of the patient (hist=0.5 if yes, hist=-0.5 if no)
%final is the returned value which is an array of size n*7, where col 1=node number,
%col 2-4 = x y z, col 5 = stress, col 6 = strength, col 7 = rpi
ilt=final_mesh(:,6);
%Diameter
loc_diameter=global_new_mesh(:,3);

max_dia=2*max(global_new_mesh(:,3));
%ilt=extras(:,1);
%nord=extras(:,2);
%old_strength=extras(:,3);
%old_rpi=extras(:,4);
%loc_diameter=nord*max_dia;
sqrt_ilt=sqrt(ilt);
%stress=nodes(:,5);
stress=final_mesh(:,5);

%Normalized Diameter

if sex==0.5
```

```

    prox=0.0127*age+1.1673;
else
    prox=0.0065*age+1.2342;
end

norm_loc=loc_diameter/prox;

for i =1:size(final_mesh(:,1)),
    final_mesh(i,10)=72.9-33.5*(sqrt_ilt(i)-0.79)-12.3*(norm_loc(i)-2.31)-24*hist+15*sex;
    %column 10 is strength;
end

final_mesh=final_mesh(m_use,:);

window=1.5;
for i=1:length(abaqus_data)
    matchingrows=find((abs(abaqus_data(i,2)-final_mesh(:,2))<window) &...
        (abs(abaqus_data(i,3)-final_mesh(:,3))<window) &...
        (abs(abaqus_data(i,4)-final_mesh(:,4))<window));
    % col 12 is new strength
    abaqus_data(i,12)=mean(final_mesh(matchingrows,10));
    % col 13 is new rpi
    abaqus_data(i,13)=abaqus_data(i,9)/abaqus_data(i,12);
    % col 14 is the old strength
    abaqus_data(i,14)=mean(final_mesh(matchingrows,8));
    %check=notfinishedyet;
end

```

BIBLIOGRAPHY

1. Sonesson, B., T. Lanne, F. Hansen, and T. Sandgren, *Infrarenal aortic diameter in the healthy person*. Eur J Vasc Surg, 1994. **8**(1): p. 89-95.
2. Al-Omran, M., S. Verma, T.F. Lindsay, R.D. Weisel, and Y. Sternbach, *Clinical decision making for endovascular repair of abdominal aortic aneurysm*. Circulation, 2004. **110**(23): p. e517-23.
3. *Deaths, percent of total deaths and death rates for the 15 leading causes of death: United States and each state, 2000*, N.C.f.H. Statistics, Editor. 2000.
4. Cronenwett, J., W. Krupski, and R. Rutherford, *Abdominal aortic and iliac aneurysms in vascular surgery*. 5th ed. ed. 2000, Philadelphia: WB Saunders.
5. Vardulaki, K.A., N.M. Walker, N.E. Day, S.W. Duffy, H.A. Ashton, and R.A. Scott, *Quantifying the risks of hypertension, age, sex and smoking in patients with abdominal aortic aneurysm*. British Journal of Surgery, 2000. **87**(2): p. 195-200.
6. Brown, L.C. and J.T. Powell, *Risk factors for aneurysm rupture in patients kept under ultrasound surveillance. UK Small Aneurysm Trial Participants*. Annals of Surgery, 1999. **230**(3): p. 289-96; discussion 296-7.
7. Huber, T.S., J.G. Wang, A.E. Derrow, D.A. Dame, C.K. Ozaki, G.B. Zelenock, T.C. Flynn, and J.M. Seeger, *Experience in the United States with intact abdominal aortic aneurysm repair*. Journal of Vascular Surgery, 2001. **33**(2): p. 304-10; discussion 310-1.
8. Dubost, C., M. Allary, and N. Oeconomos, *Resection of an Aneurysm of the Abdominal Aorta: Reestablishment of the Continuity by a Preserved Human Arterial Graft, with result after five months*. Arch. Surg., 1952. **64**: p. 405-408.
9. Rinckenbach, S., O. Hassani, F. Thaveau, Y. Bensimon, X. Jacquot, S.E. Tally, B. Geny, B. Eisenmann, A. Charpentier, N. Chakfe, and J.G. Kretz, *Current outcome of elective open repair for infrarenal abdominal aortic aneurysm*. Annals of Vascular Surgery, 2004. **18**(6): p. 704-9.

10. Johansen, K., *Ruptured abdominal aortic aneurysm: how should recent outcome studies impact current practices?* Semin Vasc Surg, 1995. **8**(2): p. 163-7.
11. Johansen, K., T.R. Kohler, S.C. Nicholls, R.E. Zierler, A.W. Clowes, and A. Kazmers, *Ruptured abdominal aortic aneurysm: the Harborview experience.* J Vasc Surg, 1991. **13**(2): p. 240-5; discussion 245-7.
12. Ouriel, K., K. Geary, R.M. Green, W. Fiore, J.E. Geary, and J.A. DeWeese, *Factors determining survival after ruptured aortic aneurysm: the hospital, the surgeon, and the patient.* J Vasc Surg, 1990. **11**(4): p. 493-6.
13. Parodi, J., J. Palmaz, and H. Baroni, *Transfemoral Intraluminal Graft Implantation of Abdominal Aortic Aneurysms.* Ann. Vasc. Surg., 1991. **5**: p. 491-499.
14. Ghansah, J.N. and J.T. Murphy, *Complications of major aortic and lower extremity vascular surgery.* Semin Cardiothorac Vasc Anesth, 2004. **8**(4): p. 335-61.
15. Rigberg, D.A., A. Dorafshar, A. Sridhar, W. Quinones-Baldrich, and W.S. Moore, *Abdominal aortic aneurysm: stent graft vs clinical pathway for direct retroperitoneal repair.* Arch Surg, 2004. **139**(9): p. 941-4; discussion 945-6.
16. Zeebregts, C.J., R.H. Geelkerken, J. van der Palen, A.B. Huisman, P. de Smit, and R.J. van Det, *Outcome of abdominal aortic aneurysm repair in the era of endovascular treatment.* Br J Surg, 2004. **91**(5): p. 563-8.
17. Greenberg, R.K., T.A. Chuter, W.C. Sternbergh, 3rd, and N.E. Fearnot, *Zenith AAA endovascular graft: intermediate-term results of the US multicenter trial.* J Vasc Surg, 2004. **39**(6): p. 1209-18.
18. Verhoeven, E.L., T.R. Prins, I.F. Tielliu, J.J. van den Dungen, C.J. Zeebregts, R.G. Hulsebos, M.G. van Andringa de Kempnaer, M. Oudkerk, and R. van Schilfgaarde, *Treatment of short-necked infrarenal aortic aneurysms with fenestrated stent-grafts: short-term results.* Eur J Vasc Endovasc Surg, 2004. **27**(5): p. 477-83.
19. Sampaio, S.M., J.M. Panneton, G.I. Mozes, J.C. Andrews, T.C. Bower, M. Karla, A.A. Noel, K.J. Cherry, T. Sullivan, and P. Gloviczki, *Proximal type I endoleak after endovascular abdominal aortic aneurysm repair: predictive factors.* Ann Vasc Surg, 2004. **18**(6): p. 621-8.
20. Sternbergh, W.C., 3rd, G. Carter, J.W. York, M. Yoselevitz, and S.R. Money, *Aortic neck angulation predicts adverse outcome with endovascular abdominal aortic aneurysm repair.* Journal of Vascular Surgery, 2002. **35**(3): p. 482-6.
21. Wolf, Y.G., M. Tillich, W.A. Lee, G.D. Rubin, T.J. Fogarty, and C.K. Zarins, *Impact of aortoiliac tortuosity on endovascular repair of abdominal aortic aneurysms: evaluation of 3D computer-based assessment.* Journal of Vascular Surgery, 2001. **34**(4): p. 594-9.

22. White, G.H., J. May, R.C. Waugh, X. Chaufour, and W. Yu, *Type III and type IV endoleak: toward a complete definition of blood flow in the sac after endoluminal AAA repair*. J Endovasc Surg, 1998. **5**(4): p. 305-9.
23. Darling, R.C., C.R. Messina, D.C. Brewster, and L.W. Ottinger, *Autopsy study of unoperated abdominal aortic aneurysms. The case for early resection*. Circulation, 1977. **56**(3 Suppl): p. II161-4.
24. Dryjski, M., R.C. Driscoll, M.A. Blair, M.A. McGurrin, F.J. Dagher, M. Ceraolo, O'Donnell, and W. Blackshear, *The small abdominal aortic aneurysm: the eternal dilemma*. Journal of Cardiovascular Surgery, 1994. **35**: p. 95-100.
25. Geroulakos, G. and A. Nicolaides, *Infrarenal abdominal aortic aneurysms less than five centimetres in diameter: the surgeon's dilemma*. European Journal of Vascular Surgery, 1992. **6**(6): p. 616-22.
26. Choksy, S.A., A.B. Wilmlink, and C.R. Quick, *Ruptured abdominal aortic aneurysm in the Huntingdon district: a 10-year experience*. Annals of the Royal College of Surgeons of England, 1999. **81**(1): p. 27-31.
27. Hall, A.J., E.F.G. Busse, D.J. McCarville, and J.J. Burgess, *Aortic Wall tension as a predictive factor for abdominal aortic aneurysm rupture: improving the selection of patients for abdominal aortic aneurysm repair*. Annals of Vascular Surgery, 2000. **14**(2): p. 152-157.
28. Raghavan, M.L., D.A. Vorp, M.P. Federle, M.S. Makaroun, and M.W. Webster, *Wall stress distribution on three-dimensionally reconstructed models of human abdominal aortic aneurysm*. Journal of Vascular Surgery, 2000. **31**(4): p. 760-769.
29. Vorp, D.A., J.D. Trachtenberg, and M.W. Webster, *Arterial hemodynamics and wall mechanics*. Seminars in Vascular Surgery, 1998. **11**(3): p. 169-80.
30. Raghavan, M.L., M.W. Webster, and D.A. Vorp, *Ex-vivo Biomechanical Behavior of Abdominal Aortic Aneurysm: Assessment Using a New Mathematical Model*. Annals of Biomedical Engineering, 1996. **24**: p. 573-582.
31. Vorp, D.A., P.C. Lee, D.H.J. Wang, M.S. Makaroun, E.M. Nemoto, S. Ogawa, and M.W. Webster, *Association Of Intraluminal Thrombus in Abdominal Aortic Aneurysm With Local Hypoxia and Wall Weakening*. Journal of Vascular Surgery, 2001. **34**(2): p. 291-9.
32. Vorp, D.A., M.L. Raghavan, S.C. Muluk, M.S. Makaroun, D.L. Steed, R. Shapiro, and M.W. Webster, *Wall strength and stiffness of aneurysmal and nonaneurysmal abdominal aorta*. Annals of the New York Academy of Sciences, 1996. **800**: p. 274-6.

33. Fillinger, M.F., S.P. Marra, M.L. Raghavan, and F.E. Kennedy, *Prediction of rupture risk in abdominal aortic aneurysm during observation: wall stress versus diameter*. Journal of Vascular Surgery, 2003. **37**(4): p. 724-32.
34. Venkatasubramaniam, A.K., M.J. Fagan, T. Mehta, K.J. Mylankal, B. Ray, G. Kuhan, I.C. Chetter, and P.T. McCollum, *A comparative study of aortic wall stress using finite element analysis for ruptured and non-ruptured abdominal aortic aneurysms*. European Journal of Vascular & Endovascular Surgery, 2004. **28**(2): p. 168-76.
35. Fillinger, M.F., M.L. Raghavan, S.P. Marra, J.L. Cronenwett, and F.E. Kennedy, *In vivo analysis of mechanical wall stress and abdominal aortic aneurysm rupture risk*. Journal of Vascular Surgery, 2002. **36**(3): p. 589-97.
36. Sacks, M.S., *A method for planar biaxial mechanical testing that includes in-plane shear*. Journal of Biomechanical Engineering, 1999. **121**(5): p. 551-5.
37. Sacks, M.S., *Biaxial Mechanical Evaluation of Planar Biologocial Materials*. Journal of Elasticity, 2000. **61**: p. 199-246.
38. Raghavan, M.L. and D.A. Vorp, *Toward a biomechanical tool to evaluate rupture potential of abdominal aortic aneurysm: identification of a finite strain constitutive model and evaluation of its applicability*. Journal of Biomechanics, 2000. **33**: p. 475-482.
39. Wang, D., M. Makaroun, and D. Vorp. *Noninvasive Estimation of Wall Strength Distribution in Human Abdominal Aortic Aneurysm*. in *ASME-IMECE Proceedings*. 2001: ASME.
40. Wang, D.H., *Noninvasive Biomechanical Assessment of the Rupture Potential of Abdominal Aortic Aneurysms*, in *Bioengineering*. 2002, University of Pittsburgh: Pittsburgh, PA. p. 244.
41. Lanir, Y. and Y.C. Fung, *Two-dimensional mechanical properties of rabbit skin. I. Experimental system*. Journal of Biomechanics, 1974. **7**(1): p. 29-34.
42. Lanir, Y. and Y.C. Fung, *Two-dimensional mechanical properties of rabbit skin. II. Experimental results*. Journal of Biomechanics, 1974. **7**(2): p. 171-82.
43. Boriek, A.M., N.G. Kelly, J.R. Rodarte, and T.A. Wilson, *Biaxial constitutive relations for the passive canine diaphragm*. Journal of Applied Physiology, 2000. **89**(6): p. 2187-90.
44. Zhou, J. and Y.C. Fung, *The degree of nonlinearity and anisotropy of blood vessel elasticity*. Proceedings of the National Academy of Sciences of the United States of America, 1997. **94**(26): p. 14255-60.

45. Brossollet, L.J. and R.P. Vito, *The effects of cryopreservation on the biaxial mechanical properties of canine saphenous veins*. Journal of Biomechanical Engineering, 1997. **119**(1): p. 1-5.
46. Debes, J.C. and Y.C. Fung, *Biaxial mechanics of excised canine pulmonary arteries*. American Journal of Physiology, 1995. **269**(2 Pt 2): p. H433-42.
47. Sacks, M.S. and D.C. Gloeckner, *Quantification of the fiber architecture and biaxial mechanical behavior of porcine intestinal submucosa*. Journal of Biomedical Materials Research, 1999. **46**(1): p. 1-10.
48. Gloeckner, D.C., K.L. Billiar, and M.S. Sacks, *Effects of mechanical fatigue on the bending properties of the porcine bioprosthetic heart valve*. ASAIO Journal, 1999. **45**(1): p. 59-63.
49. Gloeckner, D.C., M.S. Sacks, M.O. Fraser, G.T. Somogyi, W.C. de Groat, and M.B. Chancellor, *Passive biaxial mechanical properties of the rat bladder wall after spinal cord injury*. Journal of Urology, 2002. **167**(5): p. 2247-52.
50. Mohan, D. and J.W. Melvin, *Failure properties of passive human aortic tissue. II-- Biaxial tension tests*. Journal of Biomechanics, 1983. **16**(1): p. 31-44.
51. Schulze-Bauer, C.A. and G.A. Holzapfel, *Passive biaxial mechanical response of aged human iliac arteries*. J Biomech, 2003. **125**(3): p. 395-406.
52. Okamoto, R.J., J.E. Wagenseil, W.R. DeLong, S.J. Peterson, N.T. Kouchoukos, and T.M.r. Sundt, *Mechanical properties of dilated human ascending aorta*. Annals of Biomedical Engineering, 2002. **30**(5): p. 624-35.
53. He, C.M. and M.R. Roach, *The composition and mechanical properties of abdominal aortic aneurysms*. Journal of Vascular Surgery, 1994. **21**: p. 6-13.
54. Thubrikar, M.J., M. Labrosse, F. Robicsek, J. Al-Soudi, and B. Fowler, *Mechanical properties of abdominal aortic aneurysm wall*. Journal of Medical Engineering & Technology, 2001. **25**(4): p. 133-42.
55. Wang, D.H.J., M.S. Makaroun, M.W. Webster, and D.A. Vorp, *Effect of intraluminal thrombus on wall stress in patient specific models of abdominal aortic aneurysm*. Journal of Vascular Surgery, 2002. **136**(3): p. 598-604.
56. Vande Geest, J.P., M.S. Sacks, and D.A. Vorp, *Age dependency of the biaxial biomechanical behavior of human abdominal aorta*. Journal of Biomechanical Engineering, 2004. **126**(6): p. 815-822.

57. Vande Geest, J.P., M.S. Sacks, and D.A. Vorp, *The effect of aneurysm on the biaxial mechanical behavior of human abdominal aorta*. Journal of Biomechanics, 2004. **in press**.
58. Sacks, M.S. and W. Sun, *Multiaxial mechanical behavior of biological materials*. Annu Rev Biomed Eng, 2003. **5**: p. 251-84.
59. Wang, D.H., M. Makaroun, M.W. Webster, and D.A. Vorp, *Mechanical properties and microstructure of intraluminal thrombus from abdominal aortic aneurysm*. Journal of Biomechanical Engineering, 2001. **123**(6): p. 536-9.
60. Medynsky, A.O., D.W. Holdsworth, M.H. Sherebrin, R.N. Rankin, and M.R. Roach, *The effect of storage time and repeated measurements on the elastic properties of isolated porcine aortas using high resolution x-ray CT*. Canadian Journal of Physiology & Pharmacology, 1998. **76**(4): p. 451-6.
61. Sacks, M.S., *A method for planar biaxial mechanical testing that includes in-plane shear*. J Biomech Eng, 1999. **121**(5): p. 551-5.
62. Patel, D.J., J.S. Janicki, and T.E. Carew, *Static anisotropic elastic properties of the aorta in living dogs*. Circulation Research, 1969. **25**(6): p. 765-79.
63. Ling, S.a.A., HB, *A nonlinear analysis of pulsatile flow in arteries*. Journal of Fluid Mechanics, 1972. **55**(3): p. 493-511.
64. Rivlin, R.S., Saunders, D W, *Large elastic deformations of isotropic materials, VII. Experiments on the deformation of rubber*. Philos. Trans. Roy. Soc. London Ser. A, 1951. **243**: p. 251-288.
65. Nicosia, M.A., J.S. Kasalko, R.P. Cochran, D.R. Einstein, and K.S. Kunzelman, *Biaxial mechanical properties of porcine ascending aortic wall tissue*. J Heart Valve Dis, 2002. **11**(5): p. 680-6; discussion 686-7.
66. Fung, Y.C., *Biomechanics --Mechanical Properties of Living tissue*. 2 ed. 1993: Springer.
67. Sherebrin, M.H., J.E. Hegney, and M.R. Roach, *Effects of age on the anisotropy of the descending human thoracic aorta determined by uniaxial tensile testing and digestion by NaOH under load*. Can J Physiol Pharmacol, 1989. **67**(8): p. 871-8.
68. Angouras, D., D.P. Sokolis, T. Dosios, N. Kostomitsopoulos, H. Boudoulas, G. Skalkeas, and P.E. Karayannacos, *Effect of impaired vasa vasorum flow on the structure and mechanics of the thoracic aorta: implications for the pathogenesis of aortic dissection*. Eur J Cardiothorac Surg, 2000. **17**(4): p. 468-73.

69. Tsatsaris, A., D. Iliopoulos, A. Baldoukas, D. Triantafyllou, N. Berketis, and N. Kavantzias, *Effect of an experimental stenosis in the porcine descending thoracic aorta*. *Artif Organs*, 2004. **28**(11): p. 987-92.
70. Okamoto, R.J., J.E. Wagenseil, W.R. DeLong, S.J. Peterson, N.T. Kouchoukos, and T.M. Sundt, 3rd, *Mechanical properties of dilated human ascending aorta*. *Ann Biomed Eng*, 2002. **30**(5): p. 624-35.
71. Monson, K.L., W. Goldsmith, N.M. Barbaro, and G.T. Manley, *Significance of source and size in the mechanical response of human cerebral blood vessels*. *Journal of Biomechanics*, 2005. **38**(4): p. 737-744.
72. Vorp, D.A., W.A. Mandarino, M.W. Webster, and J. Gorcsan, 3rd, *Potential influence of intraluminal thrombus on abdominal aortic aneurysm as assessed by a new non-invasive method*. *Cardiovascular Surgery*, 1996. **4**(6): p. 732-9.
73. Stergiopoulos, N., S. Vulliamoz, A. Rachev, J.J. Meister, and S.E. Greenwald, *Assessing the homogeneity of the elastic properties and composition of the pig aortic media*. *Journal of Vascular Research*, 2001. **38**(3): p. 237-46.
74. Fung, Y.C., *Elasticity of soft tissue in simple elongation*. *Am. J. Physiol.*, 1967. **213**: p. 1532-1544.
75. Humphrey, J.D. and F.C. Yin, *On constitutive relations and finite deformation of passive cardiac tissue I: A pseudostrain-energy function*. *J. Biomech. Eng.*, 1987. **109**: p. 298-304.
76. Humphrey, J.D., *An evaluation of pseudoelastic descriptors used in arterial mechanics*. *Journal of Biomechanical Engineering*, 1999. **121**(2): p. 259-62.
77. Sacks, M.S. and C.J. Chuong, *Orthotropic mechanical properties of chemically treated bovine pericardium*. *Annals of Biomedical Engineering*, 1998. **26**(5): p. 892-902.
78. Chuong, C.J. and Y.C. Fung, *Compressibility and constitutive equation of arterial wall in radial compression experiments*. *J. of Biomech.*, 1984. **17**(1): p. 35-40.
79. Patel, D.J. and D.L. Fry, *The elastic symmetry of arterial segments in dogs*. *Circulation Research*, 1969. **24**(1): p. 1-8.
80. Vito, R.P. and J. Hickey, *The mechanical properties of soft tissue II: the elastic response of arterial segments*. *J. Biomech.*, 1980.
81. Vorp, D.A., K.R. Rajagopal, P.J. Smolinski, and H.S. Borovetz, *Identification of elastic properties of homogeneous orthotropic vascular segments in distention*. *Journal of Biomechanics*, 1995. **28**: p. 501-412.

82. Girerd, X.J., C. Acar, J.J. Mourad, P. Boutouyrie, M.E. Safar, and S. Laurent, *Incompressibility of the human arterial wall: an in vitro ultrasound study*. J Hypertens Suppl, 1992. **10**(6): p. S111-4.
83. Sun, W., M.S. Sacks, T.L. Sellaro, W.S. Slaughter, and M.J. Scott, *Biaxial mechanical response of bioprosthetic heart valve biomaterials to high in-plane shear*. J Biomech Eng, 2003. **125**(3): p. 372-80.
84. Rivlin, R.S. and D.W. Saunders, *Large elastic deformation of isotropic material, VII. Experiments on the deformation of rubber*. Phil. Trans. Roy. Soc., 1951. **A243**(251-288).
85. Yin, F.C., H.A. Spurgeon, and C.H. Kallman, *Age-associated alterations in viscoelastic properties of canine aortic strips*. Circ Res, 1983. **53**(4): p. 464-72.
86. Choi, H.S. and R.P. Vito, *Two-dimensional stress-strain relationship for canine pericardium*. Journal of Biomechanical Engineering, 1990. **112**(2): p. 153-9.
87. Baxter, T.B. and B.G. Halloran, *Matrix metabolism in abdominal aortic aneurysms*, in *Aneurysms: new findings and treatments*, P.W. Yao JST, Editor. 1994, Appleton and Lange: East Norwalk, Conn. p. 25-34.
88. Sakalihasan, N., A. Heyeres, B.V. Nussgens, R. Limet, and C.M. Lapiere, *Modifications of the extracellular matrix of aneurysmal abdominal aorta as a function of their size*. European Journal of Vascular Surgery, 1993. **7**: p. 633-37.
89. Raghavan, M.L., M.W. Webster, and D.A. Vorp, *Ex vivo biomechanical behavior of abdominal aortic aneurysm: assessment using a new mathematical model*. Annals of Biomedical Engineering, 1996. **24**(5): p. 573-82.
90. Criscione, J.C., M.S. Sacks, and W.C. Hunter, *Experimentally tractable, pseudo-elastic constitutive law for biomembranes: I. Theory*. Journal of Biomechanical Engineering, 2003. **125**(1): p. 94-9.
91. Criscione, J.C., M.S. Sacks, and W.C. Hunter, *Experimentally tractable, pseudo-elastic constitutive law for biomembranes: II. Application*. Journal of Biomechanical Engineering, 2003. **125**(1): p. 100-5.
92. Di Martino, E., S. Mantero, F. Inzoli, G. Melissano, D. Astore, R. Chiesa, and R. Fumero, *Biomechanics of abdominal aortic aneurysm in the presence of endoluminal thrombus: experimental characterisation and structural static computational analysis*. European Journal of Vascular & Endovascular Surgery, 1998. **15**(4): p. 290-9.
93. Di Martino, E. and D. Vorp, *Effect of variation in intraluminal thrombus constitutive properties on abdominal aortic aneurysm wall stress*. Ann Biomed Eng, 2003. **31**(7): p. 804-9.

94. Di Martino, E.S., G. Guadagni, A. Fumero, G. Ballerini, R. Spirito, P. Biglioli, and A. Redaelli, *Fluid-structure interaction within realistic three-dimensional models of the aneurysmatic aorta as a guidance to assess the risk of rupture of the aneurysm*. Medical Engineering & Physics, 2001. **23**(9): p. 647-55.
95. Mower, W.R., W.J. Quinones, and S.S. Gambhir, *Effect of intraluminal thrombus on abdominal aortic aneurysm wall stress*. Journal of Vascular Surgery: Official Publication, the Society For Vascular Surgery [and] International Society For Cardiovascular Surgery, North American Chapter, 1997. **26**(4): p. 602-8.
96. Wang, D.H., *Noninvasive Biomechanical Assessment of the Rupture Potential of Abdominal Aortic Aneurysms*, in *Bioengineering*. 2002, University of Pittsburgh: Pittsburgh.
97. Sacks, M.S., *Incorporation of SALS-derived fiber orientation data into a structural constitutive model for planar collagenous tissues*. Journal of Biomechanical Engineering, 2003. **25**: p. 280-87.
98. Speelman, L., A. Bohra, and D.A. Vorp. *Implementation of wall calcification in patient-specific finite element analyses of abdominal aortic aneurysms*. in *2005 ASME Summer Bioengineering Conference*. 2005. Vail, CO.
99. Yin, F.C.P., P.H. Chew, and S.L. Zeger, *An approach to quantification of biaxial tissue stress-strain data*. Journal of Biomechanics, 1986. **19**(1): p. 27-37.
100. Abramowitch, S.D. and S.L. Woo, *An improved method to analyze the stress relaxation of ligaments following a finite ramp time based on the quasi-linear viscoelastic theory*. Journal of Biomechanical Engineering, 2004. **126**(1): p. 92-97.
101. Braccini, G. and O. Salvetti, *Morphometric analysis of sonographic images by spatial geometric modeling*. Comput Med Imaging Graph, 1992. **16**(2): p. 93-108.
102. Raghavan, M.L., S. Trivedi, A. Nagaraj, D.D. McPherson, and K.B. Chandran, *Three-dimensional finite element analysis of residual stress in arteries*. Ann Biomed Eng, 2004. **32**(2): p. 257-63.
103. Lanning, C., S.Y. Chen, A. Hansgen, D. Chang, K.C. Chan, and R. Shandas, *Dynamic three-dimensional reconstruction and modeling of cardiovascular anatomy in children with congenital heart disease using biplane angiography*. Biomed Sci Instrum, 2004. **40**: p. 200-5.
104. Antiga, L., B. Ene-Iordache, and A. Remuzzi, *Computational geometry for patient-specific reconstruction and meshing of blood vessels from MR and CT angiography*. IEEE Trans Med Imaging, 2003. **22**(5): p. 674-84.

105. Chen, S.J., Y.W. Li, J.K. Wang, I.S. Chiu, C.T. Su, J.C. Hsu, and H.C. Lue, *Three-dimensional reconstruction of abnormal ventriculoarterial relationship by electron beam CT*. J Comput Assist Tomogr, 1998. **22**(4): p. 560-8.
106. Smith, D.B., M.S. Sacks, D.A. Vorp, and M. Thornton, *Surface geometric analysis of anatomic structures using biquintic finite element interpolation*. Annals of Biomedical Engineering, 2000. **28**(6): p. 598-611.
107. Smith, D., M. Sacks, D. Vorp, and M. Thornton, *Surface geometric analysis of anatomic structures using biquintic finite element interpolation*. Ann Biomed Eng, 2000. **28**(6): p. 598-611.
108. Di Martino, E.S., S. Yamakawa, K. Shimada, and D. Vorp. *Requirements for mesh size and mesh type in non linear computational finite element method structural analyses*. in *Second MIT Conference on Computational Fluid and Solid Mechanics*. 2003. Cambridge, MA: MIT.
109. Raghavan, M.L., J. Kratzberg, and E.S. DaSilva. *Heterogeneous, variable wall-thickness modeling of a ruptured abdominal aortic aneurysm*. in *2004 ASME International Mechanical Engineering Conference*. 2004. Anaheim, CA.
110. Smith, D.B., M.S. Sacks, M.L. Raghavan, M.P. Federle, M.W. Webster, and D.A. Vorp. *A biquintic hermite finite element for surface geometric analysis of abdominal aortic aneurysms*. in *Proc. 3rd World Congress fo Biomechanics*. 1998.
111. Vorp, D.A., M.L. Raghavan, and M.W. Webster, *Mechanical wall stress in abdominal aortic aneurysm: influence of diameter and asymmetry*. Journal of Vascular Surgery, 1998. **27**(4): p. 27.
112. Brusseau, E., C.L. de Korte, F. Mastik, J. Schaar, and A.F. van der Steen, *Fully automatic luminal contour segmentation in intracoronary ultrasound imaging--a statistical approach*. IEEE Trans Med Imaging, 2004. **23**(5): p. 554-66.
113. McInerney, T. and D. Terzopoulos, *Deformable models in medical image analysis: a survey*. Med Image Anal, 1996. **1**(2): p. 91-108.
114. Pardo, X.M., P. Radeva, and D. Cabello, *Discriminant snakes for 3D reconstruction of anatomical organs*. Med Image Anal, 2003. **7**(3): p. 293-310.
115. Sebbahi, A., A. Herment, A. de Cesare, and Mousseaux, *Multimodality cardiovascular image segmentation using a deformable contour model*. Comput Med Imaging Graph, 1997. **21**(2): p. 79-89.
116. Terzopoulos, D. and T. McInerney, *Deformable models and the analysis of medical images*. Stud Health Technol Inform, 1997. **39**: p. 369-78.

117. Tolxdorff, T. and C. Derz, *3D reconstruction of organ surfaces using model-based snakes*. Stud Health Technol Inform, 2003. **94**: p. 360-6.
118. Wei, M., Y. Zhou, and M. Wan, *A fast snake model based on non-linear diffusion for medical image segmentation*. Comput Med Imaging Graph, 2004. **28**(3): p. 109-17.
119. Lehmann, T.M., H.P. Meinzer, and T. Tolxdorff, *Advances in biomedical image analysis-past, present and future challenges*. Methods Inf Med, 2004. **43**(4): p. 308-14.
120. Thubrikar, M.J., J. J Al-Soudi, and F. Robicsek, *Wall Stress Studies of Abdominal Aortic Aneurysm in a Clinical Model*. Annals of Vascular Surgery, 2001. **15**(3): p. 355-366.
121. Stringfellow, M.M., P.F. Lawrence, and R.G. Stringfellow, *The influence of aorta-aneurysm geometry upon stress in the aneurysm wall*. Journal of Surgical Research, 1987. **42**(4): p. 425-33.
122. Raghavan, M.L., D.A. Vorp, M.P. Federle, M.S. Makaroun, and M.W. Webster, *Wall stress distribution on three-dimensionally reconstructed models of human abdominal aortic aneurysm*. J Vasc Surg, 2000. **31**(4): p. 760-9.
123. Mower, W.R., L.J. Baraff, and J. Sneyd, *Stress distributions in vascular aneurysms: factors affecting risk of aneurysm rupture*. The Journal of Surgical Research, 1993. **55**(2): p. 155-61.
124. Hua, J. and W.R. Mower, *Simple geometric characteristics fail to reliably predict abdominal aortic aneurysm wall stresses*. Journal of Vascular Surgery, 2001. **34**(2): p. 308-15.
125. Fillinger, M.F., M.L. Raghavan, S.P. Marra, J.L. Cronenwett, and F.E. Kennedy, *In vivo analysis of mechanical wall stress and abdominal aortic aneurysm rupture risk*. J Vasc Surg, 2002. **36**(3): p. 589-97.
126. DiMartino, E.S. and D.A. Vorp, *Effect of Variation in Intraluminal Thrombus Constitutive Properties on Abdominal Aortic Aneurysm Wall Stress*. Ann Biomed Eng, 2003. **31**: p. 804-809.
127. Elger, D.F., D.M. Blackketter, R.S. Budwig, and K.H. Johansen, *The influence of shape on the stresses in model abdominal aortic aneurysms*. Journal of Biomechanical Engineering, 1996. **118**(3): p. 326-32.
128. Hua, J. and W.R. Mower, *Simple geometric characteristics fail to reliably predict abdominal aortic aneurysm wall stress*. Journal of Vascular Surgery, 2001. **34**: p. 308-15.

129. Kyriacou, S.K. and J.D. Humphrey, *Influence of size, shape and properties on the mechanics of axisymmetric saccular aneurysms*. Journal of Biomechanics, 1996. **29**(8): p. 1015-22.
130. Crawford, C.M., K. Hurtgen-Grace, E. Talarico, and J. Marley, *Abdominal aortic aneurysm: an illustrated narrative review*. J Manipulative Physiol Ther, 2003. **26**(3): p. 184-95.
131. Patel, D.J. and D.L. Fry, *Longitudinal tethering of arteries in dogs*. Circ Res, 1966. **19**(6): p. 1011-21.
132. Patel, D.J. and D.L. Fry, *The elastic symmetry of arterial segments in dogs*. Circ Res, 1969. **24**(1): p. 1-8.
133. Tanaka, T.T. and Y.C. Fung, *Elastic and inelastic properties of the canine aorta and their variation along the aortic tree*. J Biomech, 1974. **7**(4): p. 357-70.
134. Chuong, C.J. and Y.C. Fung, *On residual stress in arteries*. ASME J. Biomech. Engr., 1984. **108**: p. 189-192.
135. Delfino, A., N. Stergiopoulos, J.E. Moore, and J.-J. Meister, *Residual strain effects on the stress field in a thick wall finite element model of the human carotid bifurcation*. Journal of Biomechanics, 1997. **30**(8): p. 777-786.
136. Han, H.C. and Y.C. Fung, *Direct measurement of transverse residual strains in aorta*. Am J Physiol, 1996. **270**(2): p. H750-9.
137. Vaishnav, R.N. and J. Vossoughi, *Residual stress and strain in aortic segments*. J. Biomech., 1987. **20**(235-239).
138. Vossoughi, J., Z. Hedjazi, and F.S. Borris. *intimal residual stress and strain in large arteries*. in *1993 ASME Advances in bioengineering*. 1993.
139. Finol, E.A. and C.H. Amon, *Flow dynamics in anatomical models of abdominal aortic aneurysms: computational analysis of pulsatile flow*. Acta Cient Venez, 2003. **54**(1): p. 43-9.
140. Finol, E.A. and C.H. Amon, *Flow-induced wall shear stress in abdominal aortic aneurysms: Part II--pulsatile flow hemodynamics*. Comput Methods Biomech Biomed Engin, 2002. **5**(4): p. 319-28.
141. Finol, E.A. and C.H. Amon, *Flow-induced wall shear stress in abdominal aortic aneurysms: Part I--steady flow hemodynamics*. Comput Methods Biomech Biomed Engin, 2002. **5**(4): p. 309-18.

142. Finol, E.A. and C.H. Amon, *Blood flow in abdominal aortic aneurysms: pulsatile flow hemodynamics*. J Biomech Eng, 2001. **123**(5): p. 474-84.
143. Finol, E.A., K. Keyhani, and C.H. Amon, *The effect of asymmetry in abdominal aortic aneurysms under physiologically realistic pulsatile flow conditions*. J Biomech Eng, 2003. **125**(2): p. 207-17.
144. Hibbitt, K.S., Inc., *Abaqus User's Manuals*. 2002.
145. Inzoli, F., F. Boschetti, M. Zappa, T. Longo, and R. Fumero, *Biomechanical factors in abdominal aortic aneurysm rupture*. European Journal of Vascular Surgery, 1993. **7**: p. 667-74.
146. Stringfellow, M.M., P.F. Lawrence, and R.G. Stringfellow, *The influence of aorta-aneurysm geometry upon stress in the aneurysm wall*. Journal of Surgical Research, 1987. **42**: p. 425-33.
147. Sacks, M.S., D.A. Vorp, M.L. Raghavan, M.P. Federle, and M.W. Webster, *In vivo three-dimensional surface geometry of abdominal aortic aneurysms*. Annals of Biomedical Engineering, 1999. **27**(4): p. 469-79.
148. Sonesson, B., T. Sandgren, and T. Lanne, *Abdominal aortic aneurysm wall mechanics and their relation to risk of rupture*. European Journal of Vascular & Endovascular Surgery, 1999. **18**(6): p. 487-93.
149. Thubrikar, M.J., F. Robicsek, M. Labrosse, V. Chervenkov, and B.L. Fowler, *Effect of thrombus on abdominal aortic aneurysm wall dilation and stress*. J Cardiovasc Surg (Torino), 2003. **44**(1): p. 67-77.
150. Takagi, H., S. Yoshikawa, Y. Mizuno, Y. Matsuno, Y. Umeda, Y. Fukumoto, and Y. Mori, *Intrathrombotic pressure of a thrombosed abdominal aortic aneurysm*. Ann Vasc Surg, 2005. **19**(1): p. 108-12.
151. Marra, S.P., M.L. Raghavan, D.R. Whittaker, M.F. Fillinger, D.T. Chen, J.M. Dwyer, M.J. Tsapakos, and F.E. Kennedy. *Estimation of the zero-pressure geometry of abdominal aortic aneurysms from dynamic magnetic resonance imaging*. in *2005 Summer Bioengineering Conference*. 2005. Vail, CO: ASME.
152. Adolph, R., D.A. Vorp, D.L. Steed, M.W. Webster, M.V. Kameneva, and S.C. Watkins, *Cellular content and permeability of intraluminal thrombus in abdominal aortic aneurysm*. Journal of Vascular Surgery, 1997. **25**(5): p. 916-26.
153. Vorp, D.A., D.H. Wang, M.W. Webster, and W.J. Federspiel, *Effect of intraluminal thrombus thickness and bulge diameter on the oxygen diffusion in abdominal aortic aneurysm*. Journal of Biomechanical Engineering, 1998. **120**(5): p. 579-83.

154. Wang, D.H.J., M.S. Makaroun, M.W. Webster, and D.A. Vorp, *Mechanical Properties and Microstructure of Intraluminal Thrombus from Abdominal Aortic Aneurysm*. Journal of biomechanical Engineering, 2001. **123**: p. 536-539.
155. Facchiano, A., F. De Marchis, E. Turchetti, F. Facchiano, M. Guglielmi, A. Denaro, R. Palumbo, M. Scoccianti, and M.C. Capogrossi, *The chemotactic and mitogenic effects of platelet-derived growth factor-BB on rat aorta smooth muscle cells are inhibited by basic fibroblast growth factor*. J. Cell Sci., 2000. **113**(16): p. 2855-2863.
156. Lindblad, B., G. Borner, and A. Gottsater, *Factors Associated with Development of Large Abdominal Aortic Aneurysm in Middle-aged Men*. Eur J Vasc Endovasc Surg, 2005.
157. Wanhainen, A., D. Bergqvist, K. Boman, T.K. Nilsson, J. Rutegard, and M. Bjorck, *Risk factors associated with abdominal aortic aneurysm: a population-based study with historical and current data*. J Vasc Surg, 2005. **41**(3): p. 390-6.
158. Alcorn, H.G., S.K. Wolfson, and K. Sutton-Tyrrell, *Risk factors for abdominal aortic aneurysms in older adults enrolled in the Cardiovascular Health Study*. Arterioscler Thromb Vasc Biol, 1996. **16**: p. 963-70.
159. Cole, W.C., G.B. Hill, and A.G. Bouchard, *Are aortic aneurysms caused by atherosclerosis? Atherosclerotic risk factors in abdominal aortic aneurysm and peripheral vascular occlusive disease*, 1994. **Chronic Dis Can**(15): p. 120-2.
160. Powell, J.T., P. Worrell, S.T.R. MacSweeney, P.J. Franks, and R.M. Greenhalgh, *Smoking as a risk factor for abdominal aortic aneurysm*. Ann. N.Y. ACAD. Sci., 1996. **800**: p. 246-248.
161. Strachan, D.P., *Predictors of death from aortic aneurysm among middle-aged men; the Whitehall study*. Br. J Surg, 1991. **79**: p. 401-404.
162. Blanchard, J.F., *Epidemiology of Abdominal Aortic Aneurysms*. Epidemiologic Reviews, 1999. **21**(2): p. 207-221.
163. Cohen, J.R., I. Sarfati, and L. Wise, *The effect of cigarette smoking on rabbit aortic elastase activity*. J Vasc Surg, 1989. **9**(4): p. 580-2.
164. Nordskog, B.K., A.D. Blixt, W.T. Morgan, W.R. Fields, and G.M. Hellmann, *Matrix-degrading and pro-inflammatory changes in human vascular endothelial cells exposed to cigarette smoke condensate*. Cardiovasc Toxicol, 2003. **3**(2): p. 101-17.
165. Carmo, M., L. Colombo, A. Bruno, F.R. Corsi, L. Roncoroni, M.S. Cuttin, F. Radice, E. Mussini, and P.G. Settembrini, *Alteration of elastin, collagen and their cross-links in abdominal aortic aneurysms*. Eur J Vasc Endovasc Surg, 2002. **23**(6): p. 543-9.

166. Webster, M.W., C.E. McAuley, D.L. Steed, D.D. Miller, and C.H. Evans, *Collagen stability and collagenolytic activity in the normal and aneurysmal human abdominal aorta*. American Journal of Surgery, 1991. **161**(6): p. 635-8.
167. Wilson, K.A., J.S. Lindholt, P.R. Hoskins, L. Heickendorff, S. Vammen, and A.W. Bradbury, *The relationship between abdominal aortic aneurysm distensibility and serum markers of elastin and collagen metabolism*. European Journal of Vascular & Endovascular Surgery, 2001. **21**(2): p. 175-8.
168. Cole, C.W., G.G. Barber, and A.G. Bouchard, *Abdominal aortic aneurysm: consequences of a positive family history*. Can J Surg, 1989. **32**: p. 117-20.
169. Webster, M.W., P.L. St. Jean, and D.L. Steed, *Abdominal aortic aneurysm: results of a family study*. J Vasc Surg, 1991(13): p. 366-72.
170. Darling, R.C., D.C. Brewster, and G.m. LaMuaglia, *Are familial abdominal aortic aneurysm different?* J Vasc Surg, 1989. **10**: p. 39-43.
171. Fitzgerald, P., D. Ramsbottom, and P. Burke, *Abdominal aortic aneurysm in the Irish population: a familial screening study*. Br J Surg, 1989. **32**: p. 117-20.
172. Johansen, K. and T. Koepsell, *Familial tendency for abdominal aortic aneurysms*. JAMA, 1986. **256**: p. 1934-6.
173. Bengtsson, H., B. Sonesson, and D. Bergqvist, *Incidence and prevalence of abdominal aortic aneurysms, estimated by necropsy studies and population screening by ultrasound*. Annals of the New York Academy of Sciences, 1996. **800**: p. 1-24.
174. Lillienfeld, D.E., P.D. Gunderson, J.M. Sprafka, and C. Vargas, *Epidemiology of aortic aneurysms. I. Mortality trends in the United State, 1951 to 1981*. Atherosclerosis, 1987. **7**: p. 637-643.
175. Wilson, K.A., A.J. Lee, P.R. Hoskins, F.G. Fowkes, C.V. Ruckley, and A.W. Bradbury, *The relationship between aortic wall distensibility and rupture of infrarenal abdominal aortic aneurysm*. Journal of Vascular Surgery, 2003. **37**(1): p. 112-7.
176. Solberg, S., K. Singh, T. Wilsgaard, and B.K. Jacobsen, *Increased growth rate of abdominal aortic aneurysms in women. The Tromso study*. Eur J Vasc Endovasc Surg, 2005. **29**(2): p. 145-9.
177. Ailawadi, G., J.L. Eliason, K.J. Roelofs, I. Sinha, K.K. Hannawa, E.P. Kaldjian, G. Lu, P.K. Henke, J.C. Stanley, S.J. Weiss, R.W. Thompson, and G.R. Upchurch, Jr., *Gender differences in experimental aortic aneurysm formation*. Arterioscler Thromb Vasc Biol, 2004. **24**(11): p. 2116-22.

178. Di Martino, E., A. Bohra, J. Vande Geest, N. Gupta, M. Makaroun, and D. Vorp. *Biomechanical properties of ruptured versus non-ruptured Abdominal Aortic Aneurysm wall tissue*. in *Biomedical Engineering Society Annual Fall Meeting*. 2004. Philadelphia, PA.
179. Jacob, M.P., B.-C. C, V. Fontaine, Y. Benazzoug, L. Feldman, and J.B. Michel, *Extracellular matrix remodeling in the vascular wall*. *Pathol Biol*, 2001. **49**(4): p. 326-32.
180. Lakatta, E.G., J.H. Mitchell, A. Pomerance, and G. Rowe, *Human aging: changes in structure and function*. *J Am Coll Cardiol*, 1987. **10**: p. 42A-47A.
181. Lakatta, E.G.M., *Cardiovascular Aging Research: The Next Horizons*. *Journal of the American Geriatrics Society*, 1999. **47**(5): p. 613-625.
182. McNulty, M., P. Spiers, E. McGovern, and J. Feely, *Aging is associated with increased matrix metalloproteinase-2 activity in the human aorta*. *Am J Hypertens*, 2005. **18**(4 Pt 1): p. 504-9.
183. Dobrin, P.B., *Pathophysiology and pathogenesis of aortic aneurysms. Current concepts*. *Surgical Clinics of North America*, 1989. **69**: p. 687-703.
184. Kazi, M., T. J., P. Religa, J. Roy, P. Eriksson, U. Hedin, and J. Swedenborg, *Influence of intraluminal thrombus on structural and cellular composition of abdominal aortic aneurysm wall*. *Journal of Vascular Surgery*, 2003. **38**(6): p. 1283-92.
185. Kazi, M., C. Zhu, J. Roy, G. Paulsson-Berne, A. Hamsten, J. Swedenborg, U. Hedin, and P. Eriksson, *Difference in Matrix-Degrading Protease Expression and Activity Between Thrombus-Free and Thrombus-Covered Wall of Abdominal Aortic Aneurysm*. *Arterioscler Thromb Vasc Biol*, 2005.
186. Menashi, S., J.S. Campa, and R.M. Geenhalgh, *Collegan in abdominal aortic aneurysm: typing, content, and degradation*. *J. Vas. Surg.*, 1987. **6**: p. 578-82.
187. Bengtsson, H. and D. Bergqvist, *Ruptured abdominal aortic aneurysm: a population-based study*. *J Vasc Surg*, 1993. **18**: p. 74-80.
188. Limet, R., N. Sakalihassan, and A. Albert, *Determination of the expansion rate and incidence of rupture of abdominal aortic aneurysms*. *Journal of Vascular Surgery: Official Publication, the Society For Vascular Surgery [and] International Society For Cardiovascular Surgery, North American Chapter*, 1991. **14**(4): p. 540-8.
189. Papalambros, E., F. Sigala, S. Georgopoulos, C. Menekakos, A. Giatromanolaki, E. Bastounis, and E. Sivridis, *Immunohistochemical expression of metalloproteinases MMP-2 and MMP-9 in abdominal aortic aneurysms: correlation with symptoms and aortic diameter*. *Int J Mol Med*, 2003. **12**(6): p. 965-8.

190. Aiken, L.S. and S.G. West, *Multiple regression: testing and interpreting interactions*. 1991, Newbury Park, Calif.: Sage Publications. xi, 212.
191. Cohen, J. and J. Cohen, *Applied multiple regression/correlation analysis for the behavioral sciences*. 3rd ed. 2003, Mahwah, N.J.: L. Erlbaum Associates. xxviii, 703.
192. Sonesson, B., F. Hansen, H. Stale, and T. Lanne, *Compliance and diameter in the human abdominal aorta-the influence of age and sex*. *Eur J Vasc Surg*, 1993. 7: p. 690-7.
193. Cohen, J. and P. Cohen, *Applied multiple regression/correlation analysis for the behavioral sciences*. 1992, Hillsdale, NJ: Lawrence Erlbaum Associates, Inc.
194. Draper, N.R. and H. Smith, *Applied regression analysis*. 1967: John Wiley & Sons, Inc. 238.
195. Draper, N.R. and H. Smith, *Applied Regression Analysis*. 2nd ed. 1981, New York: Wiley. 417.
196. Chatterjee, S. and B. Price, *Regression analysis by example*. 1977: John Wiley & Sons.
197. Hutcheson, G. and N. Sofroniou, *The multivariate social scientist: Introductory statistics using generalized linear models*. 1999, Thousand Oaks, CA: Sage Publications.
198. Brown, H. and R. Prescott, *Applied Mixed Models in Medicine*. 1999, Chichester, England: John Wiley & Sons.
199. Pinheiro, J.C. and D.M. Bates, *Mixed-Effects Models in S and S-PLUS*. 2000, New York: Springer-Verlag.
200. da Silva, E.S., A.J. Rodrigues, E.M.C. de Tolosa, C.J. Rodrigues, G. Villas Boas do Prado, and J.C. Nakamoto, *Morphology and Diameter of Infrarenal Aortic Aneurysms: A Prospective Autopsy Study*. *Cardiovascular Surgery*, 2000. 8(7): p. 526-532.
201. Brown, P.M., D.T. Zelt, and B. Sobolev, *The risk of rupture in untreated aneurysms: the impact of size, gender, and expansion rate*. *Journal of Vascular Surgery*, 2003. 37(2): p. 280-4.
202. Participants, U.S.A.T., *Long-term outcomes of immediate repair compared with surveillance of small abdominal aortic aneurysms*. *N Engl J Med*, 2002. 346(19): p. 1445-52.
203. Hans, S.S., O. Jareunpoon, M. Balasubramaniam, and G.B. Zelenock, *Size and location of thrombus in intact and ruptured abdominal aortic aneurysms*. *J Vasc Surg*, 2005. 41(4): p. 584-8.

204. Sacks, M.S., D.A. Vorp, M.L. Raghavan, M.P. Federle, and M.W. Webster. *A noninvasive surface geometric analysis of in-vivo abdominal aortic aneurysm*. in *Proc. Summer Bioengineering Conference*. 1997.
205. Ohashi, T., S. Sugita, T. Matsumoto, K. Kumagai, H. Akimoto, K. Tabayashi, and M. Sato. *Measurement of rupture properties of thoracic aortic aneurysms using pressure-imposed test*. in *Proceedings of Int. Cong. Biol. and Med. Eng.* 2002. Singapore.
206. Watton, P.N., N.A. Hill, and M. Heil, *Mathematical model for the growth of the abdominal aortic aneurysm*. *Biomechanics and Modeling in Mechanobiology*, 2004. **3**(2): p. 98-113.
207. Lobato, A.C. and P. Puech-Leao, *Predictive factors for rupture of thoracoabdominal aortic aneurysm*. *J Vasc Surg*, 1998. **27**(3): p. 446-53.
208. Vardulaki, K.A., T.C. Prevost, N.M. Walker, N.E. Day, A.B.M. Wilmink, C.R.G. Quick, H.A. Ashton, and R.A.P. Scott, *Growth rates and risk of rupture of abdominal aortic aneurysms*. *British Journal of Surgery*, 1998. **85**(12): p. 1674-1680.
209. Thubrikar, M.J., J. al-Soudi, and F. Robicsek, *Wall stress studies of abdominal aortic aneurysm in a clinical model*. *Annals of Vascular Surgery*, 2001. **15**(3): p. 355-66.
210. Hatakeyama, T., S. Hiroshi, and M. Tetsuichiro, *Risk factors for rupture of abdominal aortic aneurysm based on three-dimensional study*. *Journal of Vascular Surgery*, 2001. **33**(3): p. 453-461.
211. Lederle, F.A., G.R. Johnson, S.E. Wilson, D.J. Ballard, W.D. Jordan, Jr., J. Blebea, F.N. Littooy, J.A. Freischlag, D. Bandyk, J.H. Rapp, A.A. Salam, and I. Veterans Affairs Cooperative Study, *Rupture rate of large abdominal aortic aneurysms in patients refusing or unfit for elective repair*. *Journal of the American Medical Association*, 2002. **287**(22): p. 2968-72.
212. Stenbaek, J., B. Kalin, and J. Swedenborg, *Growth of thrombus may be a better predictor of rupture than diameter in patients with abdominal aortic aneurysms*. *European Journal of Vascular & Endovascular Surgery*, 2000. **20**(5): p. 466-9.
213. Smith, D.B., M.S. Sacks, D.A. Vorp, and M. Thorton, *Surface Geometric Analysis of Anatomic Structures Using Biquintic Finite Element Interpolation*. *Ann Biomed Eng*, 2000. **28**: p. 598-611.
214. Li, Z. and C. Kleinstreuer, *A new wall stress equation for aneurysm-rupture prediction*. *Ann Biomed Eng*, 2005. **33**(2): p. 209-13.
215. Vallabhaneni, S.R., G.L. Gilling-Smith, T.V. How, S.D. Carter, J.A. Brennan, and P.L. Harris, *Heterogeneity of tensile strength and matrix metalloproteinase activity in the wall of abdominal aortic aneurysms*. *J Endovasc Ther*, 2004. **11**(4): p. 494-502.

216. Vande Geest, J.P., D.H. Wang, S.R. Wisniewski, M. Makaroun, and D.A. Vorp, *A noninvasive method for determination of patient-specific wall strength distribution in abdominal aortic aneurysms*. submitted to *Annals of Biomechanical Engineering*, 2005.
217. Limet, R.N. and A.A. Sakalishasan, *Determination of the expansion rate and incidence of rupture of abdominal aortic aneurysm*. *J vasc Surg*, 1991. **14**: p. 540-548.
218. James, T.E., R. Wagner, L.A. White, and Z. RM, *Induction of collagenase and stromelysin gene expression by mechanical injury in a vascular smooth muscle-derived cell line*. *Journal of Cellular Physiology*, 1993. **157**(2): p. 426-37.
219. Redmond, E.M., P.A. Cahill, M. Hirsch, Y.N. Wang, J.V. Sitzmann, and S.S. Okada, *Effect of pulse pressure on vascular smooth muscle cell migration: the role of urokinase and matrix metalloproteinase*. *Thrombosis & Haemostasis.*, 1999. **81**(2): p. 293-300.
220. Tyagi, S.C., K. Lewis, D. Pikes, A. Marcello, V.S. Mujumdar, L.M. Smiley, and C.K. Moore, *Stretch-induced membrane type matrix metalloproteinase and tissue plasminogen activator in cardiac fibroblast cells*. *Journal of Cellular Physiology.*, 1998. **176**(2): p. 374-82.
221. Yoshida, M., N. Sagawa, H. Itoh, S. Yura, M. Takemura, Y. Wada, T. Sato, A. Ito, and S. Fujii, *Prostaglandin F(2alpha), cytokines and cyclic mechanical stretch augment matrix metalloproteinase-1 secretion from cultured human uterine cervical fibroblast cells*. *Molecular Human Reproduction.*, 2002. **8**(7): p. 681-7.